WTS-1 b: the first extrasolar planet detected in the WFCAM Transit Survey

Michele Cappetta

München 2012

WTS-1 b: the first extrasolar planet detected in the WFCAM Transit Survey

Michele Cappetta

Dissertation
an der Fakultät für Physik
der Ludwig–Maximilians–Universität
München

vorgelegt von
Michele Cappetta
aus Bolzano, Italien

München, den 19. Dezember 2012

Erstgutachter: R. P. Saglia
Zweitgutachter: B. Ercolano
Tag der mündlichen Prüfung: 5. Februar 2013

Contents

List of Figures

List of Tables

Acronyms

2MASS Two Micron All Sky Survey

ADU Analog-to-Digital Unit

AGB Asymptotic Giant Branch

AU Astronomic Unit

BD Brown Dwarf

BS Bisector Spans

CASU Cambridge Astronomical Survey Unit

CC Cross-Correlation

CF Correlation Function

CCD Charge Coupled Device

CR Cosmic Rays

CV Cataclysmic Variable

DA Data Analysis

DF Dispersion Function

DR Data Reduction

EChO Exoplanet Characterisation Observatory

EHJ Extremely Hot Jupiters

ESA European Space Agency

ESO European Southern Observatory

EW Equivalent Width

FAP False Alarm Probability

FSR Free Spectral Range

FWHM Full Width Half Maximum

Gaia Global Astrometric Interferometer for Astrophysics

HARPS High Accuracy Radial velocity Planet Searcher

HET Hobby-Eberly Telescope

HJ Hot Jupiter

HRS High-resolution Spectrograph

IAU International Astronomical Union

INT Isaac Newton Telescope

ISIS Intermediate dispersion Spectrograph and Imaging System

JD Julian Days

KPNO Kitt Peak National Observatory

LC Light Curve

LRS Low-resolution Spectrograph

LTE Local Thermodynamic Equilibrium

MAD Median Absolute Deviation

MRS Medium-resolution Spectrograph

NASA National Aeronautics and Space Administration

NIR Near Infrared

PDF Probability Density Function

PI Principal Investigator

PPD Proto-planetary Disk

PSF Point Spread Function

RMS Root Mean Square

RGB Red Giant Branch

RoPACS Rocky Planets Around Cool Stars

RV Radial Velocity

SDSS Sloan Digital Sky Survey

SE Super Earth

SED Spectral Energy Distribution

SNDM Solar Nebular Disk Model

SNR Signal-to-Noise Ratio

SS Solar System

TAC Telescope Allocation Committee

ThAr Thorium-Argon

TSL Target Submission Language

TTV Transit Timing Variation

UKIRT United Kingdom Infrared Telescope

UV Ultra Violet

UVES Ultraviolet and Visual Echelle Spectrograph

VHJ Very Hot Jupiters

VLT Very Large Telescope

VOSA Virtual Observatory SED Analyser

WD White Dwarf

WFC Wide Field Camera

WFCAM Wide Field Camera

WFS Wide Field Survey

WGESP Working Group on Extrasolar Planets

WHT William Herschel Telescope

WISE Wide-field Infrared Survey Explorer

WTS WFCAM Transit Survey

Zusammenfassung

Ende des zwanzigsten Jahrhunderts erlebte unser Verständnis von Planetensystemen eine Revolution. Die Entdeckung des ersten extrasolaren Planeten im Jahr 1992 markierte den Beginn einer Ära und veränderte unser Bild von Planeten und Planetensystemen grundlegend. In den darauf folgende Jahren wurde viele weitere Detektionen erzielt, die eine außerordentliche Vielfalt an Planetensystemen mit unterschiedlichen physikalischen Eigenschaften aufdeckten welche fortan neue Fragen auf dem Gebiet der Planetologie aufwerfen. Bis heute wurden mehr als 800 extrasolare Planeten nachgewiesen die einen weiten Bereich an Massen abdecken, der von wenigen Erdmassen bis zu ein paar Dutzend Jupitermassen reicht.

Die vorliegende Ph.D. Thesis behandelt die Bestätigung von Planetenkandidaten mit Hilfe von Radialgeschwindigkeitsmessungen. Gefunden wurden die Kandidaten im Rahmen des WFCAM Transit Surveys (WTS) - einer photometrische Suchkampagne mit der Wide Field Camera am United Kingdom Infrared Telescope auf dem Mauna Kea (Hawaii, USA). Der WTS und diese Arbeit wurden im Rahmen des siebten Programms der Europäischen Kommission von der RoPACS (Rocky Planets Around Cool Stars) Gruppe, einem Marie Curie Initial Training Network, unterstützt. Da der WTS in erster Linie konzipiert wurde, um Planeten um M-Zwerge zu finden, wurden die Beobachtungen im J-Band bei ca. $1.25\,\mu$m aufgenommen. Diese Wellenlänger ist in der Nähe des Maximum der spektralen Energiverteilung eines M-Zwerges. Simulationen zeigen, dass Beobachtungen im J-Band die Effekte von stellarer Variabilität verringern, welche stärker im optischen Spektrum von kühlen Sternen auftreten.

Die J-Band Lichtkurven, die einen periodischen Helligkeitsabfall zeigen und die Selektionskriterien erfüllen, wurden in der folgenden Bestätigungs-Phase weiter untersucht. Nach einem Konsistenz-Check der Transittiefe mit Hilfe von photometrischen Nachbeobachtungen im i'-Band wurden Fehldetektionen in Form von Bedeckungsveränderlichen mit Spektren mittlerer Auflösung ausgeschlossen. Danach wurden hochauflösende Spektren aufgenommen, um die WTS-Kandidaten mit der Radialgeschwindigkeits-Methode als Planeten zu bestätigen. Diese hochauflösenden Spektren wurden mit dem High Resolution Spectrograph am 9.2-m Hobby-Eberly Telescope (HET) in Texas, USA, aufgenommen.

Die Daten-Analyse Pipeline für die Auswertung der HET Spektren wurde im Rahmen dieser Arbeit entwickelt. Fehlersuche, Optimierungen und Tests der gesamten Prozedur wurden mit Hilfe von Beobachtungen von mehreren Sternen mit unterschiedlicher scheinbaren Helligkeit und unterschiedlichem Spektraltypen durchgeführt. Dies erlaubte es, die

Präzision der Radialgeschwindigkeitsmessungen für unterschiedliche Sterne zu bestimmen. Demnach sind Fehlerbalken von $\sim$10 m s^{-1} für sonnenähnliche Sterne mit Helligkeiten bis m_V=10 und SNR der beobachteten Spektren von $\gtrsim$150 zu erwarten. Spektren mit einem SNR von $\sim$30 können für schwache M-Sterne ($m_V\sim$14) gemessen werden, für welche eine Radialgeschwindigkeitsgenauigkeit von 60 m s^{-1} erreicht wird. Des weiteren wurde ein technisches Problem identifiziert und behoben, welches für bestimmte Konfigurationen des Spektrographen auftritt. Damit wurde eine systematische Fehlerquelle für alle folgenden Beobachtungen eliminiert. Schlussendlich wurde ein Nullpukts-Offset für Daten des HARPS-Spektrographen bestimmt, welcher es erlaubt, die HET Daten mit Messungen von anderen Spektrographen, die im Prozess der Nachbeobachtungen beteiligt waren, zu kombinieren.

Die Radialgeschwindigkeiten, welche aus den hochauflösenden HET Spektren bestimmt wurden, haben zur Bestätigung der ersten beiden Detektionen von extrasolaren Planeten im WTS geführt. `WTS1 b` ist ein $\sim$4 M_J Planet welcher in 3.35 Tagen einen späten F-Stern mit möglicherweise geringfügig subsolarer Metallizität umkreist. Mit einem Radius von 1.49 $R_J$ist er der drittgrösste von allen bisher gefundenen extrasolaren Planet im Massenbereich von 3-5 M_J. Der ungewöhlich grosse Radius kann nicht durch die etablierten Standardentwicklungstheorien erklärt werden, selbst wenn man die starke Einstrahlung berücksichtigt, die der Planet von seinem Mutterstern empfängt. Der Mechanismus des Ohm'schen Heizens könnte Energie in die tieferen Schichten von `WTS1 b` bringen und damit den anomalen Radius erklären. `WTS2 b` ist ein $\sim$1 M_J Planet, welcher einen frühen K-Sterne in etwa 1 Tag umrundet. Messungen der sekundären Bedeckung im Ks-Band werden es erlauben, die thermische Strahlung dieses besonderen Planeten zu messen, der Einfluss der starken Einstrahlung seines nahen Muttersterns steht, welcher aber deutlich kühler ist, als die Muttersterne anderer bekannter Hot Jupiter. Dies wird darüber Aufschluss geben, welchen Einfluss das stellare Spektrum auf die Zusammensetzung und den Aufbau von Hot Jupiter Atmosphären hat. Zusäzlich zum RoPACS Programm wurde die in dieser Arbeit entwickelte Daten-Analyse Pipeline für die Auswertung von Radialgeschwindigkeits Beobachtungen des Weissen Zwerg Sterns `NLTT 5306` verwendet, welche die Existenz eines Braunen Zwerges mit 56$\pm$3 M_J bestätigte, der den Weissen Zwerg in nur $\sim$102 Minuten umkreist. Dies ist die kürzeste Periode, die bislang in solchen Systemen beobachtet wurde.

Die Entdeckungen von `WTS1 b` und `WTS2 b` zeigen, dass der WTS Planeten finden kann, und das obwohl er als back-up Programm für schlechte Beobachtungsbedingen betrieben wird was zu einer mehr oder minder zufälligen Abfolge der Beobachtungen führt. Die beiden detektierten Planeten sind sogenannte Hot-Jupiter die einen F- bzw. einen K-Stern umrunden. Diese Sterne sind heisser als M-Zwerge, welche das Hauptziel des WTS sind.

Wie in Kovacs et al. (2012, MNRAS submitted) beschrieben, wurden bislang im WTS keine Planeten um M-Zwerge mit Helligkeiten von m_V<17 und Perioden kürzer als 10 Tagen gefunden. Aufgrund dieser Ergebnisse, konnte eine Obergrenze für die Planetenhäufigkeit von Jupiterähnlichen Planeten um M-Zwerge bestimmt werden. Diese Obergrenze liegt bei 0.017 und ist damit präziser als die zuvor auf dem *Kepler* M-Zwerg Datensatz bestimmte Grenze von 0.04.

Summary

The end of the twentieth century saw a revolution in our knowledge of planetary systems. The detection of the first extrasolar planet in 1992 marked the beginning of a modern era and changed our idea of planets and planetary systems. The discoveries continue rapidly and reveal an extraordinary diversity of planetary systems and physical properties of the exoplanets, raising new questions in the field of planetary science. So far, more than 800 extrasolar planets have been detected, spanning a wide range of masses from a few Earth masses to a few tens of Jupiter masses.

This Ph.D. Thesis is devoted to the confirmation via radial velocity follow-up of the candidate planets detected by the WFCAM Transit Survey (WTS), which is an on-going photometric monitoring campaign using the Wide Field Camera on the United Kingdom Infrared Telescope at Mauna Kea (Hawaii, USA). The WTS and the present work were supported by the RoPACS (Rocky Planets Around Cool Stars) group, a Marie Curie Initial Training Network funded by the Seventh Framework Programme of the European Commission. Since the WTS was primarily designed to find planets transiting M-dwarf stars, the observations are obtained in the J-band (1.25 μm). This wavelength is near to the peak of the spectral energy distribution of a typical M-dwarf. Simulations show that operating in the J-band reduces the effects of stellar variability, which became important at optical wavelengths in cool stars. The J-band light curves that show a periodic drop and pass all the selection criteria, progress to the candidate confirmation phase. After a transit depth consistency check performed with i'-band observations, intermediate resolution spectra enable to rule out false-positive eclipsing binaries scenarios. Finally, high-resolution spectroscopic follow-up is performed to confirm, by the radial velocity method, the planetary nature of the stellar companion detected by the WTS. The spectra employed in this phase were observed with the High Resolution Spectrograph (HRS) housed in the basement of the 9.2-m Hobby-Eberly Telescope (HET) in Texas, USA.

The pipeline for the reduction and analysis of the HET spectra has been created. Debug, optimization and test of the whole procedure were performed observing several target stars with different apparent magnitude and spectral type. These observations allowed to estimate the precision on the velocity measures for different targets. Errorbars of $\sim$10 m s^{-1} are expected for solar type stars of magnitude up to m_V=10 and SNR of the observed spectra $\gtrsim$150. Spectra with a SNR of $\sim$30 can be measured for faint ($m_V\sim$14) M stars, leading to a final radial velocity uncertainty of about 60 m s^{-1}. Furthermore, a technical problem occurring under given instrumental configurations could be identified

and fixed, removing a possible source of systematic from any later observation. Finally, the zero-point offset with respect to the HARPS data was computed allowing the comparison of the HET measures with those related to any other instruments involved in radial velocity follow-up.

The radial velocities computed from the HET high-resolution spectra allowed to confirm the detection of the first two extrasolar planet performed by the WTS. `WTS1 b` is a $\sim$4 M_J planet orbiting in 3.35 days a late F-star with possibly slightly sub-solar metallicity. With a radius of 1.49,R_J, it is the third largest planet of the known extrasolar planets in the mass range 3-5 M_J. Its unusual large radius can not be explained within the standard evolution models, even considering the strong radiation that the planet receives from the parent star. Ohmic heating could be a possible mechanism able to bring energy in the deeper layers of `WTS1 b` and hence explaining its radius anomaly. `WTS2 b` is instead a $\sim$1 M_J planet orbiting an early K-star in about 1 day only. The measure of its secondary eclipses in the Ks-band will allow to study a highly irradiated planet around a cool star, cooler than many of the currently known very hot-Jupiters host star. This will provide an insight to the effect of the stellar spectrum on the composition and structure of hot-Jupiter atmospheres.

Beyond the RoPACS program, the pipeline has been employed in the radial velocity follow-up of the white dwarf `NLTT 5306`, confirming the presence of a brown dwarf companion of 56$\pm$3 M_J orbiting its host star in $\sim$102 minutes, the shortest period ever observed in such systems.

The discoveries of `WTS1 b` and `WTS2 b` demonstrate the capability of WTS to find planets, even if it operates in a back-up mode during dead time on a queue-schedule telescope and despite of the somewhat randomised observing strategy. Moreover, the two new discovered planets are hot-Jupiters orbiting an F-star and a K-star. Both are hotter than an M-dwarf, the main target sample of the WTS.

As described in Kovacs et al. (2012, MNRAS submitted), no planets around M-dwarf stars monitored by the WTS (m_V<17) with period shorter than 10 days have been found. According to these results, the upper limit of the very hot-Jupiter planetary occurrence around M-stars can be estimated. The resulting value of 0.017 is a stricter constraint than the one derived for the *Kepler* M-dwarfs sample (0.04).

Chapter 1

Extrasolar planets

We are not more central then any other point in the Universe.

G. Bruno

Figure 1.1: Statue of Giordano Bruno erected at Campo de' Fiori, Rome. M. Cappetta©

1.1 Introduction

An extrasolar planet, or exoplanet, is a planet orbiting a star different from the Sun and detectable outside the Solar System (SS). As of November 1^{st}, 2012[1], a total of 843 extrasolar planets have been identified. They were detected in 665 planetary systems, 126 of which are multiple planetary systems. Most of the Sun-like stars host at least one planet as strongly suggested by estimates of the systems frequency (Mayor et al., 2011).

The existence of planets hosted by other stars was supposed in the past by many philosophers and then scientists. Giordano Bruno was an Italian philosopher in the 16^{th} century. He supported the Copernican theory, in which is the Earth (with the other planets) orbiting the Sun. Furthermore, he forwarded the view that the fixed stars are similar to the Sun and are likewise accompanied by planets. He was burned at the stake by the Roman inquisition in 1600 in Campo de' Fiori, Rome (see Figure 1.1). Later in the 18^{th} century, Isaac Newton mentioned in the 'General Scholium', that concludes his 'Principia', the same possibility making a comparison to the SS planets. He wrote: "And if the fixed stars are the centres of similar systems, they will all be constructed according to a similar design and subject to the dominion of One". Of course there were no possibilities to know how common or how similar to the planets of the SS such extrasolar planets could have been.

The discovery of several Earth-masses planets orbiting the pulsar `PSR B1257+12` represented the first confirmed detection in 1992 (Wolszczan & Frail, 1992). Three years later, the first exoplanet orbiting a main-sequence star was confirmed: a giant planet was found in a 4 day orbit around `51 Pegasi` (Mayor & Queloz, 1995). Since then, the number of detections has increased rapidly year after year due to improved observational techniques. Some exoplanets have been directly seen nearby the parent star observed with a telescope (Chauvin et al., 2004; Marois et al., 2008). Nevertheless, most of the detection have been performed through indirect methods, in particular radial velocity (RV, Mayor & Queloz, 1995) and transit (Charbonneau et al., 2000).

As massive planets are more easily observed, most of the known exoplanets are gas-giant planets similar to Neptune or Jupiter. Despite such sampling bias, some relatively lightweight exoplanets, only a few times more massive than the Earth (known by the term Super-Earth, SE), have been discovered in the last few years. Statistical studies now indicate that the number of SE is actually larger than that of gas-giant planets (Borucki et al., 2010).

The statistical sample of extrasolar planets has now been enlarged by the recent discoveries of Earth-sized (or smaller) planets and tens that show properties similar to the Earth (Fressin et al., 2012). Planetary-mass objects were found also around Brown Dwarfs (BDs) and several planetary-mass objects that do not orbit any star have been reported too (Marsh et al., 2010). The term *planet* is not always applied in this last case. Such objects were probably ejected from their planetary system at which they may have once

[1] *http://exoplanet.eu/catalog/*

belonged.

An increment of the interest in the search for extraterrestrial life took place after the discovery of the first extrasolar planets orbiting in the habitable zone. In particular, some of them were detected in a particular region of the habitable zone where liquid water (ergo also life) can exist on the surface of the planet. Thus, the study of planetary habitability, which considers a wide range of factors that determine the suitability for hosting life, is included in the search for extrasolar planets.

The International Astronomical Union (IAU) uses an official definition of *planet* that actually covers the SS only (Shaver, 2006). An old working definition of SS planet has been hence modified accordingly to the new discovered extrasolar planets. Rather than try to construct a detailed definition of a planet which is designed to cover all future possibilities, the Working Group on Extrasolar Planets (WGESP) of the IAU has agreed to restrict itself to developing a working definition applicable to the cases where there already are claimed detections[2].

The following criteria are considered in the newer definition:

- objects with true masses below the smaller mass required for the ignition of the deuterium-burning ($13\,M_J$ for solar metallicity objects) orbiting stars (or stellar remnants) are 'planets'. The different formation processes are not considered;
- sub-stellar objects with true masses above the limiting mass for thermonuclear fusion of deuterium are 'BD'. The different formation processes and the position of such objects within their own systems are not considered;
- free-floating objects in young star clusters with masses below the limiting mass for thermonuclear fusion of deuterium are not planets, but are 'sub-BD'.

However, such working definition is not generally recognized. An alternative is that, depending on the object formation, planets and BD should be distinguished. It is believed that gas-giant planets form through core accretion (see Section 1.3). That process may sometimes produce planets with masses higher than the value of mass required for the ignition of the deuterium-burning (Mordasini et al., 2007; Baraffe et al., 2008). Such scenario also comprehends the existence of sub-BDs, which have planetary masses but form like stars from the direct collapse of clouds of gas (see Section 1.3). Moreover, no precise physical significance is joined to the $13\,M_J$ limit. Even the core of objects with mass below that cut-off can host nuclear fusion where the Deuterium is destroyed. The rate of this fusion depends on the composition of the object too (Spiegel et al., 2010). The 'Extrasolar Planets Encyclopaedia' includes objects up to $25\,M_J$ saying: "The fact that there is no special feature around $13\,M_J$ in the observed mass spectrum reinforces the choice to forget this mass limit" (Schneider et al., 2011), and the Exoplanet Data Explorer includes objects up to $24\,M_J$ with the advisory: "The $13\,M_J$ distinction by the WGESP is physically unmotivated for planets with rocky cores, and observationally problematic due to the $sin(i)$ ambiguity" (Wright et al., 2011).

[2] *http://www.dtm.ciw.edu/boss/definition.html*

1.2 Detection methods

Planets are very dim objects, and their direct observation is an extremely difficult task. Even Jupiter, the biggest planet in our own SS, has only $\sim 10^{-6}$ times the luminosity of the sun, making a similar exoplanet unobservable to us by present techniques (Beaugé et al., 2007). All the planets directly imaged so far are both massive (several Jupiter masses) and with a separation from their parent star of the order of tens AUs. Due to their high temperature, most of them emit intense infrared radiation. Hence, such planets are brighter than they are at visible wavelengths, making their detection much easier (Absil & Mawet, 2010). Most of the known extrasolar planets have only been detected through indirect methods. The basic idea is that, even if invisible, the presence of a planet may affect the luminosity of the star, or its motion with respect to background objects. Thus, the existence of a planet may be deduce by analysing changes in some observable aspect of the parent star in an exoplanetary system.

The following are the major indirect methods employed for the detection and/or the confirmation of the extrasolar planets:

- **Radial velocity or Doppler method**: in a planetary system, both the planet and its parent star orbit around the common centre of mass. The star moves in its own orbit with a semi-major axis much smaller than the one of the planet. Variations in the stellar RV (that is, the speed with which it moves towards or away from Earth) can be detected from displacements of the absorption lines in stellar spectral due to

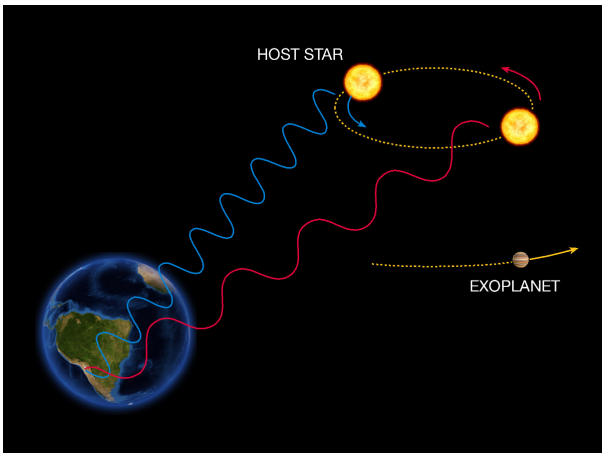

(a) The radial velocity method to detect exoplanet is based on the detection of variations in the velocity of the parent star along the line of sight, due to the changing direction of the gravitational pull from an exoplanet as it orbits the star. Eso© press photo.

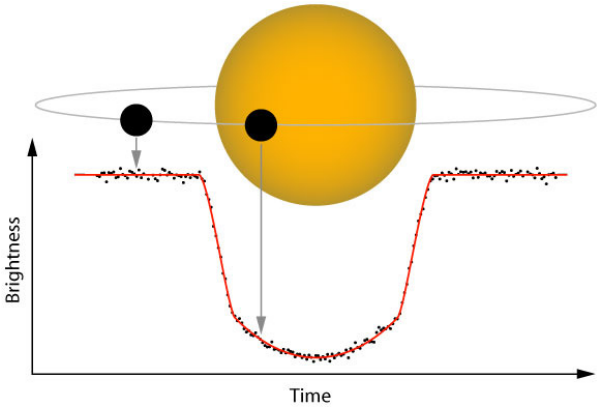

(b) The transit method to detect exoplanet is based on the drop of the flux coming from a star due to the passage (transit) of the planet and the consequent occultation of part of the disk of the star. The amount by which the star dims depends on both the stellar and planetary sizes.

Figure 1.2: Detection methods: radial velocity and transit.

the Doppler effect (see Figure 1.2a). Nowadays, extremely small RV variations can be observed, of the order of $\sim 1\,\mathrm{m\ s^{-1}}$ or even somewhat less (Pepe et al., 2011). Most of the known planets have been detected with this method so far (490 planets as of November 1^{st}, 2012). It has the advantage of being applicable to stars with a wide range of characteristics (spectral class and magnitude). One of its disadvantages is that alone it can not determine the true mass of the detected planet. Only a lower limit on the planetary mass can be estimate because only the projection of the velocity along the line of sight can be measured. However, if the RV of both the star and the planet itself can be measured, then the true masses of both can be determined (Rodler et al., 2012).

- **Transit method**: the method consists in detecting the shallow dim in a stellar light curve (LC, see Figure 1.2b) when a planet, during its revolution, crosses the line of sight between the Earth and the host star (Moutou & Pont, 2006). The amount by which the star dims depends on both the stellar and planetary sizes among other factors (impact parameter, limb darkening, etc.). This has been the second most productive method of detection (288 planets as of November 1^{st}, 2012). However, a significant number of eclipsing binaries false-positives can contaminate the detections and confirmation from another method is usually required. The transit method

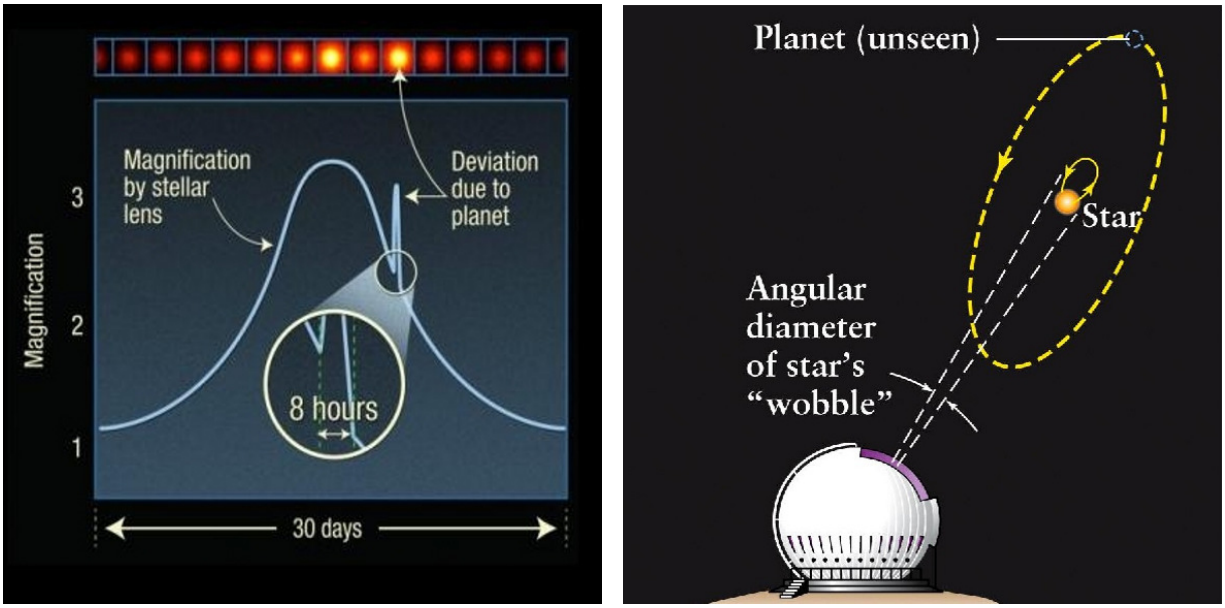

(a) Example of the brightness magnification of a background source due to gravitational microlensing. NASA©, courtesy A. Feild.

(b) The gravitational influence of a planet generates the motion of the parent star which can be detected as changes in the position of the star.

Figure 1.3: Detection methods: gravitational microlensing and astrometry.

reveals the radius of a planet. Sometimes, the atmosphere of transiting planets can be studied through spectroscopy. In order to be detectable with this method, the inclination of the planetary orbit must be higher then $\sim 80\,^{\circ}$.

- **Gravitational microlensing**: a microlensing event consists in the magnification of the light from a distant background star due to the gravitational field of a star that acts like a lens (see Figure 1.3a). Planets orbiting the star that act as a lens can cause detectable anomalies in such magnification. Such anomaly varies over time (Gould & Loeb, 1992). This method has resulted in only 16 detections as of November 1^{st}, 2012. Anyway, its advantage consists in being more sensible to planets at large separations (few AU) from their parent stars.

- **Astrometry**: astrometry consists of precisely measuring the star position in the sky and observing the changes in that position over time (Unwin et al., 1997). The motion of a star can be due to the gravitational influence of an invisible planet and may be observable (see Figure 1.3b). As the motion caused by a planet is small, the method resulted in only 1 planet detected as of November 1^{st}, 2012. Revolutionary results are expected by the 'Global Astrometric Interferometer for Astrophysics' (Gaia) survey (Sozzetti, 2012) as complementary detection method to transit and Doppler methods.

- **Transit Timing Variation (TTV)**: when two or more planets are present in a planetary system, each one introduces small perturbations in the orbits of the others. Small variations in the times of transit of a planet can hence suggest the presence of a new unknown planet. Such new planet can even not transit the parent star. For example, variations in the transits of the planet `WASP-3b` allowed to discover the existence of a second planet in the system, the non-transiting `WASP-3c` (Maciejewski et al., 2010). An alternative version of the method allows to detect the presence of outer planets that orbit binary systems timing the eclipses in an eclipsing binary star.

- **Pulsar timing**: a pulsar, the remnant of a star after it phase as supernovae, emits radio waves with extremely well defined period as it rotates. If planets orbit around a pulsar, they will cause slight variations in the timing of its observed pulses in the radio domain. The first confirmed discovery of an extrasolar planet was made using this method (Wolszczan & Frail, 1992). As of November 1^{st}, 2012, 17 planets have been found in that way.

1.3 Planet formation

1.3.1 The Solar Nebular Model

The solar nebula theory, also known as the 'nebular hypothesis', is the most widely accepted model explaining the formation and evolution of our SS. It was originally applied to our SS only, but this method of planetary system formation is now thought to hold true throughout the universe (Montmerle et al., 2006). The widely accepted modern variant of the nebular hypothesis is the 'Solar Nebular Disk Model' (SNDM) or simply 'Solar Nebular Model' (Woolfson, 1993).

According to SNDM stars form in massive, dense clouds of molecular hydrogen called giant molecular clouds. These clouds are gravitationally unstable, and matter coalesces into smaller, denser clumps inside. These clouds then collapse and form stars. Star formation is a complex process which produces a gaseous Proto-planetary Disk (PPD) around the young star. This can give birth to planets under the right circumstances. The formation of planetary systems is hence thought to be a natural result of star formation. A sun-like star usually takes around 10^8 yrs to form.

The PPD is an accretion disk which continues to feed the central star. At the beginning the disk is very hot and subsequently cools in the so called `T tauri` stage. In the inner part of the PPD, the temperature is high enough to prevent condensation of water ice. This results in the coagulation of purely rocky grains and later into the formation of rocky planetesimals of $\sim 1\,\mathrm{km}$ size. If the disk is massive enough the run-away accretions begin. Growth accelerates as mass accumulates, resulting in the rapid formation of 'oligarchs' ($\sim 10^3\,\mathrm{km}$ size). This leads to the growth of larger bodies by the destruction of smaller bodies. Next, oligarch accretion begins leading the the formation of Moon-size and Mars-size bodies called 'embryos'. The last merger phase begins when such objects become massive enough to perturb each other causing their orbits to become chaotic. This forms a limited number of Earth sized bodies.

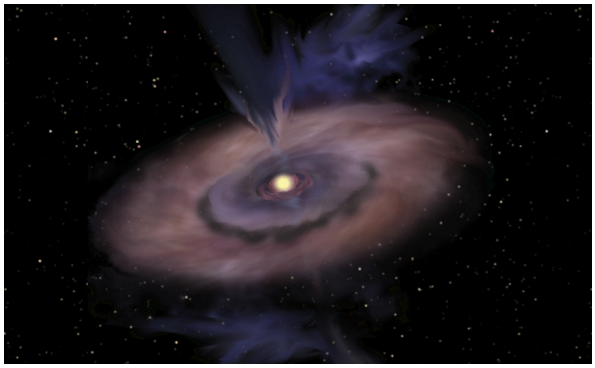

Figure 1.4: Artistic vision of a T-Tauri star with a circumstellar proto-planetary accretion disc. Courtesy S. Bowers.

A more complicated process leads to the formation of giant planets. It is thought to occur beyond the so-called 'snow line' (also know as frost line, see Figure 1.5), where planetary embryos are mainly made of various ices. As a result they are several times more massive than in the inner part of the PPD. Some embryos appear to continue to grow and eventually reach 5-10 $M_\oplus$, starting the accretion of the hydrogenhelium gas from the disk. The accumulation of gas by the rocky-icy core is a slow process at the begin. After the mass of the protoplanet reaches about 30 $M_\oplus$, it accelerates and proceeds in a

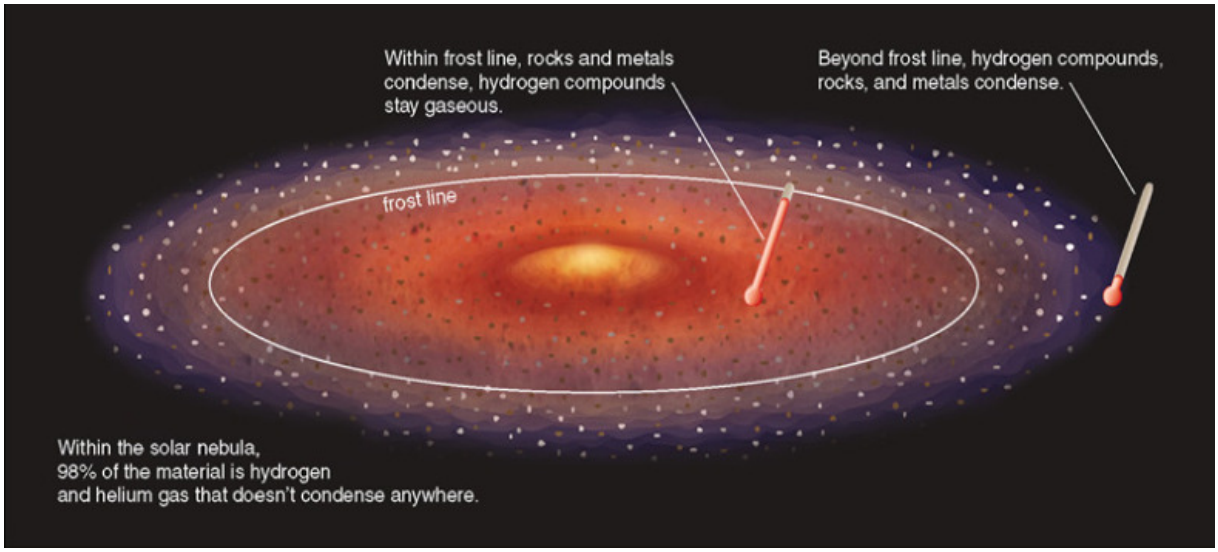

Figure 1.5: Hydrogen compounds, such as water and methane, typically condense at low temperatures, and remain gaseous inside the frost line where temperatures are higher. The heavier rocky and metallic materials condense instead at higher temperatures. Thus, the inner planets are made almost entirely of rocks and metals. Courtesy Pearson Educucation Inc.©

runaway manner. The exhaustion of the gas in the disk stops the accretion. The so formed gaseous planets can then migrate after their formation. The ice giants, like Uranus and Neptune, are thought to be failed cores, which formed too late when the disk had almost disappeared. A detailed description of rocky and gaseous planets formation is given in the following sections[3].

1.3.2 Rocky planets formation

According to the SNDM, the inner part of the PPD within the snow line (see Figure 1.5) hosts the formation of the rocky planets. In this region the temperature is high enough to impede the condensation of water ice and other substances into grains. In these circumstances, pure rocky grains only can coagulate and later form rocky planetesimals (Raymond et al., 2007). Such conditions are thought to exist in the inner 3-4 AU part of the disk of a sun-like star (Montmerle et al., 2006).

After small planetesimals (~ 1 km in diameter) have formed, run-away accretion begins (Kokubo & Ida, 2002). It is called run-away as the mass growth rate goes as $R^3 \cdot M^{4/3}$, where R and M are the radius and mass of the growing body (Thommes et al., 2003). The larger is the mass, the higher is the growth rate, leading to the preferential growth of larger bodies at the expense of the smaller ones. The run-away accretion lasts between 10^4 to 10^5 yrs until the largest bodies exceed approximately 10^3 km in diameter. The gravitational

[3]Based on Armitage (2010).

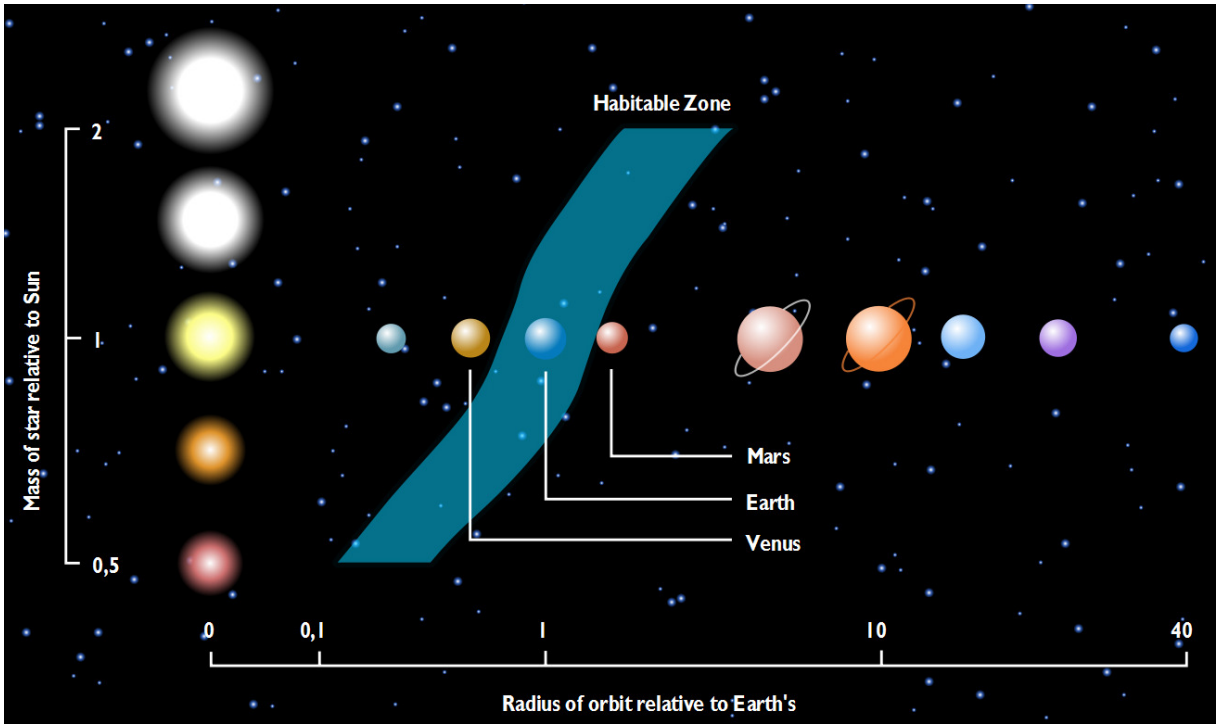

Figure 1.6: The size or mass of a star determine the boundaries of the habitable zone. Only when a planetary orbit falls within this zone, water can exist on its surface in liquid form over a long period of time. Courtesy GFDL©.

perturbations by the larger bodies on the remaining planetesimals cause a decreasing of the growth rate.

The abundance and the following dominance of several hundred of the largest bodies (called 'oligarchs') characterize the next stage, called oligarchic accretion. No other bodies other than the oligarchs can grow, continuing to slowly accrete planetesimals (Kokubo & Ida, 2002). The accretion rate is proportional to R^2 at this stage, which is derived from the geometrical cross-section of an oligarch (Thommes et al., 2003). The specific accretion rate is instead proportional to $M^{-1/3}$. As it decreases with the mass of the body, smaller oligarchs are allowed to merge into larger ones. The oligarchs continue to accrete (two nearby oligarchs can merge too) until no more planetesimals are present in the disk around them (Kokubo & Ida, 2002). The distance from the central star and the planetesimals surface density determine the value of the final mass of an oligarch (Thommes et al., 2003). This is up to $0.1\,M_\oplus$ in case of rocky planets (Montmerle et al., 2006). The result of the oligarchic accretion stage (which is thought to last a few 10^5 yrs, Kokubo & Ida, 2002) is the formation of ∼100 Moon-sized to Mars-sized planetary 'embryos' (Raymond et al., 2006). They are thought to lie inside gaps in the disk and to be separated by rings of planetesimals survived to the previous merge into the oligarchs.

The last stage of rocky planet formation begins when only a small number of planetesimals remains and embryos become massive enough to gravitationally perturb each other

(Montmerle et al., 2006). The orbits of the embryos become thus chaotic (Raymond et al., 2006) while the remaining planetesimals are expelled from the disk or collide with each other. Mars and Mercury may be considered remaining embryos that survived this phase (Bottke et al., 2005). This process lasts for 10^7 to 10^8 yrs and leads to the formation of a limited number of Earth-sized bodies. Simulations show that the number of surviving planets is on average from 2 to 5 (Montmerle et al., 2006; Raymond et al., 2006; Bottke et al., 2005; Petit et al., 2001). The Earth and Venus can represent the result of this merging phase in the SS (Raymond et al., 2006). Their formation required the merging of approximately 10-20 embryos, while an equal number of them were probably ejected from the SS (Bottke et al., 2005). Some of the embryos, which originated in the asteroid belt, are thought to have brought water to Earth (Raymond et al., 2007). Only the rocky planets that lie in the habitable zones can keep water in the liquid phase on their surface. The habitable zones boundaries depend on the mass of the parent star (see Figure 1.6). Rocky planets settle into more or less stable orbits as time passes, explaining why planetary systems are generally packed to the limit (*i. e.* why they always appear to be at the edge of instability, Raymond et al., 2006).

1.3.3 Gas-giant planets formation

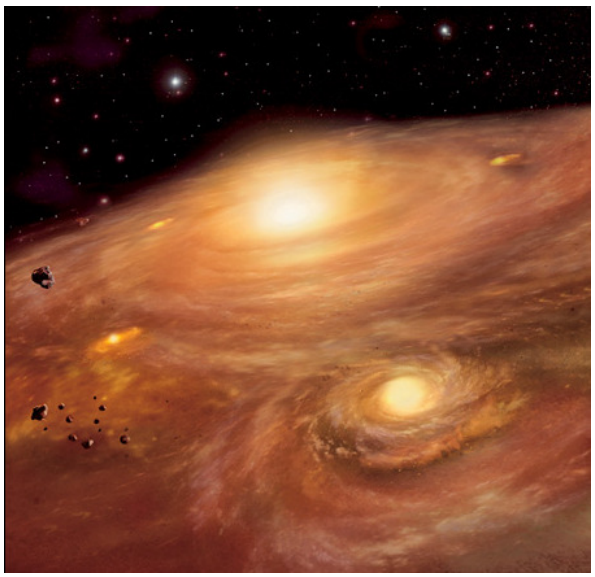

Figure 1.7: Artistic vision showing the core collapse model of gas-giant planets formation. Gravity instability causes the PPD of gas and dust circling the star to collapse into several dense clouds, shown as bright clumps in this drawing. NGC©, courtesy *Moonrunner*.

In the framework of the SNDM two theories for the formation of gas-giant planets exist. The 'disk instability' model states that giant planets form in the massive PPD as a result of its gravitational fragmentation (Boss, 2003) (see Figure 1.7). The second possibility is the 'core accretion' model, also known as the nucleated instability model (Hubickyj et al., 2005). This second scenario seems to be the most promising one as it can explain the formation of the giant planets in relatively low mass disks (less than $0.1\,M_\odot$). Over the last decade, several evidences have been presented showing that core accretion is most likely the dominant mechanism for the close-in population of planets probed by radial velocity and transits (Janson et al., 2011).

Two phases characterize the formation of a gas-giant planet in the core accretion model: i) the creation of a $\sim 10\,M_\oplus$ core via embryos merging and ii) the following accretion of gas from the PPD (Montmerle et al., 2006). The formation of giant planet core is similar to a terrestrial planet creation (Kokubo & Ida, 2002). As described in the

previous section, such process begins with the run-away growth of planetesimals, followed by the slower oligarchic stage (Thommes et al., 2003). The probability of collisions between planetary embryos is lower in the outer part of planetary systems (Thommes et al., 2003). As a consequence, no embryos merging stage is expected. An additional difference is the composition of the planetesimals. In this case, they form beyond the snow line (see Figure 1.5) and therefore consist mainly of ice. As the ice to rock abundance ratio is about 4 to 1 (Inaba et al., 2003), the mass of planetesimals is enhanced fourfold.

However, only a 1-2 $M_\oplus$ cores at the distance of Jupiter (5 AU) can be formed within 10^7 yrs in a minimum mass PPD capable of terrestrial planet formation (Thommes et al., 2003). The value of 10^7 yrs is the average lifetime of gaseous disks around Sun-like stars (Haisch et al., 2001). Several solutions were proposed: mass of the disk increased by a factor 10 (Thommes et al., 2003); migration of the proto-planet, allowing so the embryo to accrete more planetesimals (Inaba et al., 2003); improvement of the accretion due to gas drag in the gaseous envelopes of the embryos (Inaba et al., 2003; Fortier et al., 2007). The core formation of a gas giant planet (such as Jupiter and perhaps Saturn too) can be explained by a combination of the previous reported ideas.

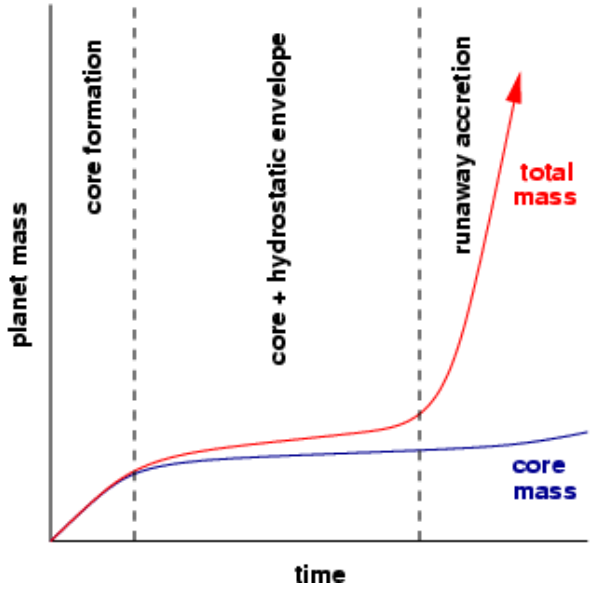

Figure 1.8: Schematic illustration showing how the core mass (blue line) and total mass (core + envelope: red line) grow in a calculation of giant planet formation via core accretion. The formation of a $\sim$10 $M_\oplus$ core is followed first by slow quasi-static growth of an envelope, before finally run-away gas accretion ensues. The time scale of the slow phase of growth is a few million years. Courtesy P. Armitage.

More problematic is the explanation of the formation of planets like Uranus and Neptune. Indeed, no theory has been capable to provide the in situ formation of their cores at the distance of 20-30 AU from the central star (Montmerle et al., 2006). A possible solution is that they initially accreted in the Jupiter-Saturn region, to be then scattered to their present location after a migration phase (Thommes et al., 1999). Once the cores were sufficiently massive (5-10 $M_\oplus$), they started to accrete gas from the surrounding disk (Montmerle et al., 2006). Initially it was a slow process, increasing the core masses up to 30 $M_\oplus$ in a few million years (Inaba et al., 2003; Fortier et al., 2007). After that, the accretion rates suddenly increased in a run-away process. The remaining 90% of the mass accumulated in approximately 10^4 yrs (Fortier et al., 2007) (see Figure 1.8). As the gas falls onto the forming gaseous planet, the formation of a gap in the PPD can occur (Papaloizou et al., 2007). Furthermore, the dimension of such gap in the disk is increased by the torque that the planet exerts on the gas in its vicinity via gravitational

interaction. When the gas is exhausted, the gas accretion of the planet stops. Giants planets like Uranus and Neptune represent failed cores within this model. The cores began too late the gas accretion stage, when almost all gas had already disappeared.

The formation of terrestrial planets can be significantly influenced by the presence of gas-giant planets. It tends in fact to increase eccentricities and inclinations of planetesimals and embryos in the terrestrial planet region (inside 4 AU in the SS) via Kozai mechanism (Bottke et al., 2005; Petit et al., 2001). Moreover, the planet accretion in the inner part of the PPD can be reduced or even prevented in case giant planets form too early. If their formation occurs roughly at the end of the oligarchic stage, as probably happened in the SS, it will influence the planetary embryos merge making it more violent (Bottke et al., 2005). A decrease of the number of terrestrial planets, which will be more massive, is a possible consequence (Levison & Agnor, 2003).

Concerning our SS, the influence of giant planets (that of Jupiter in particular) is thought to have been limited by the distance from the terrestrial planets (Levison & Agnor, 2003). In the region of a planetary system adjacent to the giant planets, the eccentricities of embryos can increase due to the gravitation perturbation. The embryos that pass close to a giant planet may be ejected from the system (Bottke et al., 2005; Petit et al., 2001). If all embryos are removed, then no planets will form in this region (Petit et al., 2001). A further consequence is that a large number of small planetesimals can remain as giant planets are incapable to accrete all of them without the help of embryos. Such a region will eventually evolve into an asteroid belt (a full analogue of the asteroid belt in the SS) located 2-4 AU from the Sun (Bottke et al., 2005; Petit et al., 2001).

1.4 Planet evolution

The detection of `51 Peg-b` (Mayor & Queloz, 1995), a $0.468\,M_J$ gaseous planet, significantly increased the interest in mechanisms for planetary migration. The orbital period of 4.2 days only places the planet so close to its parent star to make highly unlikely that its formation took place in situ. Early on, the hypothesis that planetary orbits could be modified after the formation of a planet was recognized by Goldreich & Tremaine, 1980. Three main hypothesis for planetary migration have been studied: the interaction of a planet with i) the remnant gas in the disk, ii) with planetesimal that survived to the planet formation stage and iii) with the other planets. The following sections[4] are devoted to the analysis of these three mechanisms.

1.4.1 Gas disk migration

A planet gravitationally perturbs the residual gas in the PPD along its orbit. Density waves can be generated at orbital radii where the gas is in resonance with the planet. Energy and angular momentum are hence transferred between the planet and the surrounding gas through such waves. This results in a variation of the semi-major axis a (causing the planetary migration) and possibly the orbital eccentricity e.

Gas disk migration has been divided in two main regimes (Goldreich & Tremaine, 1980; Lin & Papaloizou, 1986; Ward, 1997). Low-mass planets are involved in the so called *type-I migration*. The planets only weakly perturb the surface density profile of the gas disk. The migration rate is proportional to the planetary mass. As the planet remains entirely embedded within the gas, the most important resonances are those located close to the planet. The interaction with the gas disk interior to the planetary orbit adds angular momentum to the planet, while the interaction with the exterior disk removes angular momentum. The planet migration, inward or outward, depends upon the balance of the two effects. Theoretical calculations suggest that the planet migrates inward in almost all circumstances, potentially on a short time scale (Tanaka et al., 2002, estimate a migration time scale for a $1\,M_\oplus$ planet at 5 AU as

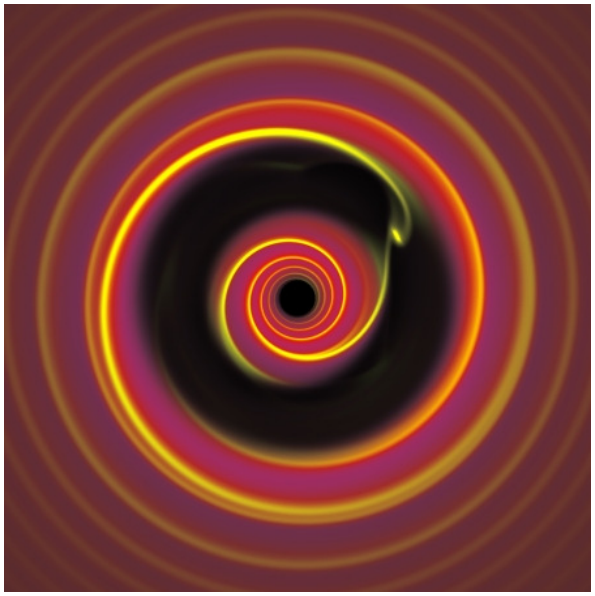

Figure 1.9: The surface density from a numerical simulation of the interaction between a massive planet and the proto-planetary gas disk. Courtesy P. Armitage.

[4]Based on Armitage (2010).

only $\sim 10^6$ yrs). In a highly turbulent disk, type-I migration may be closer to a random walk than a smooth inward migration. Type-I migration may be a relatively minor effect for terrestrial planets due to their low masses, but type-I migration is likely to affect the formation of giant planets in the core accretion model (see Section 1.3).

On the other hand, massive planets strongly perturb the gas disk. The exchange of angular momentum between the planet and the disk tends to reject gas from the planetary orbit neighbourhood, creating an annular gap with a lower surface density of the gas (see Figure 1.9). Orbital migration direction and rate depend on how rapidly the gas of the disk, accordingly to the processes of its own internal angular momentum transport, tries to flow back filling again the gap. In this regime, known as *type-II migration*, the orbit of the planet and the viscous evolution of the disk are directly joined. In the regions of the disk where the gas is flowing inward, the planet moves inward too and vice versa. Type-II migration is typically slower than type-I migration. The boundary between type-I and type-II migration is not sharp. In between these regimes, non-linear effects become important. These effects are poorly quantified at present, but numerical models suggest planetary migration may slow down or even change direction for intermediate-mass planets. Planets that have formed a gap continue to accrete some gas via narrow streams of material that cross the gap. However, the rate of gas accretion declines as the planet grows more massive and the gap becomes deeper.

Although there is no direct observational evidence for gas disk migration, it is widely believed that this mechanism explains the existence of the so called hot-Jupiters (HJs, see also Section 1.5.1). These gas-giant planets have very short-period orbits, such as `51 Pegasi-b`, which are likely to have stopped their migration when they reached the inner edge in the PPD (Papaloizou et al., 2007). Ford & Rasio (2006) used the observed distribution of HJs to constrain the location of the inner edge in the mass-period diagram (see Section 1.5). They found that the edge corresponds to a separation close to twice the Roche limit, as expected if the planets started on highly eccentric orbits that were later circularized. In contrast, any migration scenario would predict an inner edge right at the Roche limit, which applies to planets approaching on nearly circular orbits. It has been suggested that gas disk migration may also excite planetary eccentricity (thereby providing a simultaneous explanation for the wide spread of eccentricity observed among extrasolar planets).

1.4.2 Planetesimal-driven migration

Planets migrate also due to the interaction with smaller bodies (planetesimals) in their vicinity. Ejecting a planetesimal from the planetary system, a planet must give up energy. As a consequence it moves closer toward the star (this occurs, with negligible effects, when spacecrafts are boosted making use of the gravitational slingshots from the giant planets). Instead, if planetesimals are scattered into shorter period orbits, a planet gains energy, and migrates outward. A planet will suffer a substantial change to its orbit if it interacts with a mass of planetesimals that is comparable to its own mass. Since the mass of the condensed matter is ~ 5 times larger than the gas mass in typical PPD, this condition is

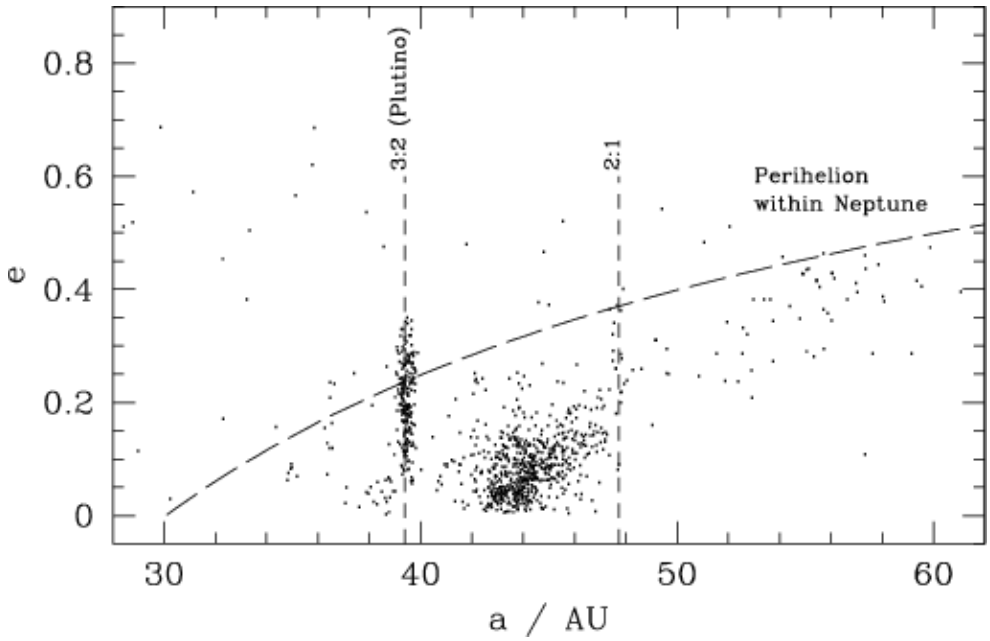

Figure 1.10: The distribution of known trans-Neptunian objects in semi-major axis a and eccentricity e. Note the concentration of bodies in 3:2 resonance with Neptune (the *Plutinos*). Courtesy P. Armitage.

easier to meet for ice giants, which have accreted relatively modest gaseous envelopes, than for very massive planets with near stellar composition. Such effects of planetesimal-driven migration have been mostly explored through N-body studies (Hahn & Malhotra, 1999; Kirsh et al., 2009; Bromley & Kenyon, 2011; Capobianco et al., 2011).

The distribution of trans-Neptunian objects provides strong evidence for planetesimal migration having occurred early in SS history. In addition to Pluto itself, a large number of other bodies (called *Plutinos*) are observed to be trapped in 3:2 resonance with Neptune (see Figure 1.10). Some of these bodies have eccentricities high enough that they cross Neptune orbit. This unusual distribution is likely the result of the outward migration of Neptune (Malhotra, 1995), driven by the scattering of a disk of planetesimals inward into orbits that eventually led to encounters with Jupiter and ejection from the SS. Simultaneously, the slow outward motion of Neptune captured Pluto and other bodies into the 3:2 resonance (a process known as resonant capture) and excited their eccentricity.

Although the evidence is less direct, it is also possible that all the gas-giant planets in the SS originated in a more compact configuration, which then evolved under the action of planetesimal scattering to its current state. The *Nice model*, proposed by Tsiganis et al. (2005), suggests that this evolution included a crossing of the 2:1 resonance between Jupiter and Saturn, and links this crossing to the late heavy bombardment (a transient spike in the cratering rate, Gomes et al., 2005) on the Moon.

1.4.3 Planet-planet scattering

Interactions between planets can also occur after both the gas and planetesimal disks have been lost or depleted to a dynamically negligible level (Rasio & Ford, 1996; Lin & Ida, 1997; Ford et al., 2001; Marzari & Weidenschilling, 2002; Ford et al., 2003). No general stability criteria is known for a planetary system with more than two planets, so numerical N-body experiments are needed to study the evolution of such systems. An initially unstable planetary system can evolve via:

- ejection of one or more planets (typically the lightest);
- an increase in the orbital separation of the planets, toward a more stable configuration;
- physical collisions between planets, or between a planet and the star.

The relative probability of these channels depends upon the orbital radii and masses of the planets, and so no blanket statement about the outcome of planet-planet scattering is possible. However, typically the survivors after scattering have migrated modestly inward, and gained significant eccentricity (Adams & Laughlin, 2003; Veras & Armitage, 2006; Ford & Rasio, 2008; Raymond et al., 2011). Numerical calculations have shown that planet-planet scattering can reproduce the observed eccentricity distribution of massive extrasolar planets, and as a result this mechanism is the leading candidate for explaining why extrasolar planets frequently have non-circular orbits.

1.5 Extrasolar planets properties

The known extrasolar planets have led to a new era in the study of planetary systems. For example, the traditional theory for the formation of the SS does not likely explain certain structures of extrasolar planetary systems. This is due to the properties discovered in extrasolar planetary systems being quite unlike our own. Many detailed simulations and mechanisms have been proposed to explore these important issues (Jiang & Ip, 2001; Kinoshita & Nakai, 2001; Armitage et al., 2002; Ji et al., 2003; Jiang & Yeh, 2004a,b; Boss, 2005; Jiang & Yeh, 2007; Rice et al., 2008). As the number of detected exoplanets keeps increasing, the statistical properties of exoplanets have become more meaningful.

Figure 1.11 shows the frequency histograms of the main properties of the known extrasolar planets. According to the method employed for the discovery and characterization of a planet, some of the quantities here reported could be unknown for some planets. So, the frequency distribution of a give parameter is computed taking into account all the planets for which that parameter is known and not all the 834 planets discovered so far. Both the planetary mass (actually M sin(i)) and the orbital period frequency distributions (left hand side panels) suggest a power-low probability density function (PDF) (Armitage et al., 2002; Jiang et al., 2009, 2010). For both these quantities, the trend followed by the data are not a direct consequence of any detection method bias. Higher mass planets produce higher, and therefore much easily detectable, indirect effects (reflex motion of the parent star, gravitation microlensing, etc.). This bias makes statistical analysis difficult, but it appears that lower-mass planets are actually more common than higher-mass ones, at least within a broad mass range that includes all giant planets. In addition, the discovery of several planets only a few times more massive than Earth, despite the great difficulty of detecting them, indicates that such planets are fairly common. As of September 2012[5], nearly 50% of the known exoplanets have a mass smaller than $1\,M_J$, that is the mass of the heavier planet in the SS. Moreover, the baseline length of the different surveys (performing mainly photometric and spectroscopic observations) is nowadays sufficiently long to place a limit on the detectable period well beyond the period range shown in Figure 1.11 (bottom-left panel). In the same panel, a sub-plot shows a zoom of the period histogram considering values up to 10 days. The frequency peak visible in the histograms, the so called ~ 3 days *pile-up*, corresponds to the planets who experienced inward migration and orbit now at a distance to the host star representing the inner edge of the PPD (see Section 1.4). The power-law PDFs of the planetary mass and orbital period histograms are also recognisable in Figure 1.12. Here, the occurrence frequency of mass and period are reported in logarithmic scales. The black bin-filling is drawn with respect to a linear regression of the logarithm of the quantities along the X-axis (mass and period) and Y-axis (occurrence frequency). As it can be seen, a linear regression represents a good approximation of the data. This trend corresponds to a power-low in the linear representation.

The distribution of the planetary radius occurrences (Figure 1.11 top-right panel) clearly shows two distinct planet populations. A first peak is centred at $\sim 0.2\,R_J$ (equiv-

[5] *http://exoplanet.eu/*

alent to $\sim 2.2\,R_\oplus$); it corresponds to the population of rocky planets (also called *super-Earths*). The second one is located at larger radii; its maximum is located at $\sim 1.2\,R_J$ as it represents the population of gas-giant planets. The large-radius tail of this second distribution originates in the so called *radius anomaly* (see next section).

The eccentricity histogram reported in Figure 1.11, bottom-right panel, shows how peculiar is our SS where almost all the planets have a very low eccentric orbit. The orbit of Pluto[6] has an eccentricity of ~ 0.25 and, as of September 2012, 52% of the known

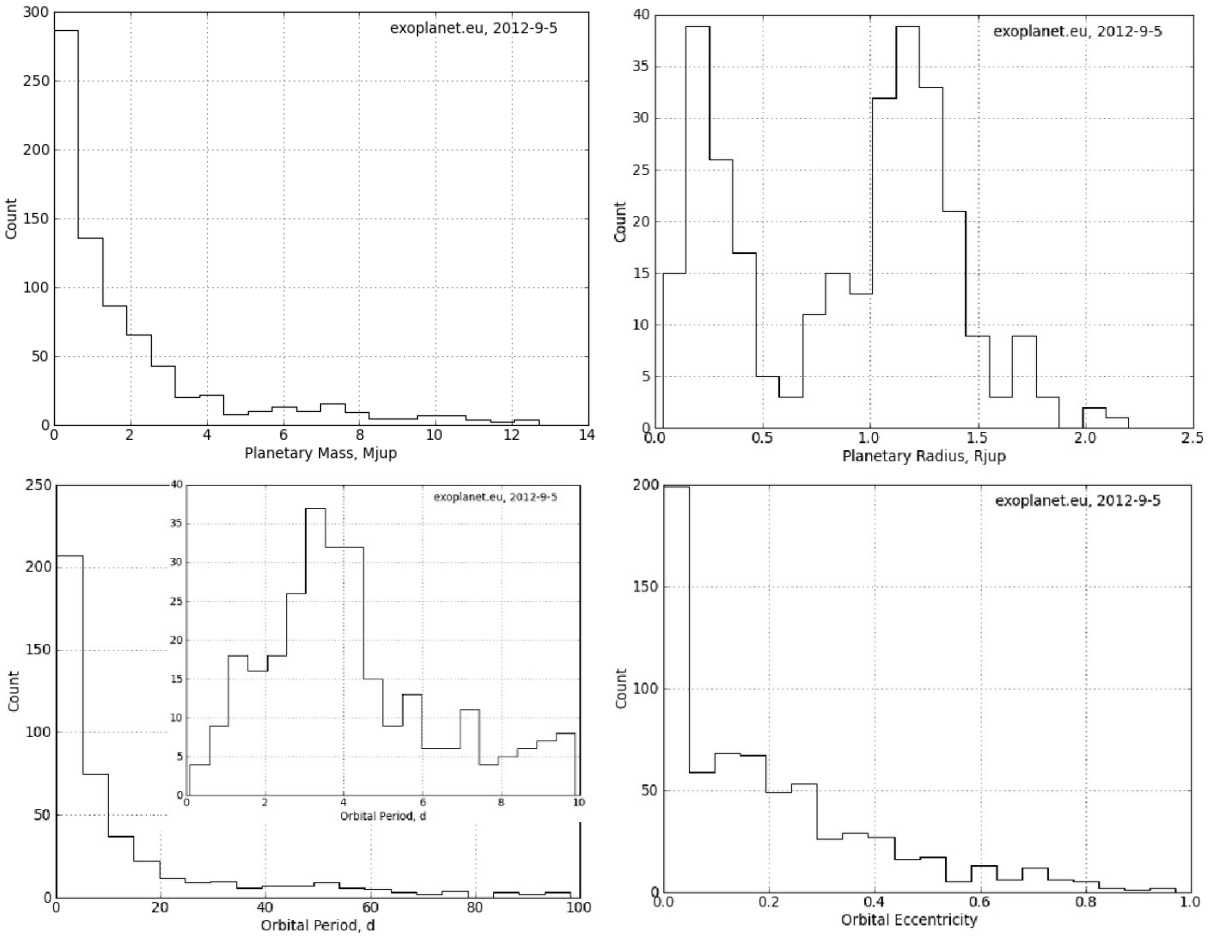

Figure 1.11: Frequency histograms of the main properties of the known extrasolar planets. The frequency distribution of a give parameter is computed taking into account all the planets for which that parameter is known. From top-left, clockwise direction: planetary mass (M sin(i)), planetary radius, orbital eccentricity and orbital period. In the sub-plot of the period histogram, a zoom at smaller values is reported in order to show the ~ 3 days pile-up. The frequency distribution is nearly flat up to ~ 2000 days. Analogous zoom plots for mass and eccentricity histograms are not reported as the trends are basically the same at smaller values. Data and plots from *http://exoplanet.eu/*.

[6]Originally classified as the ninth planet from the Sun, Pluto was recategorized as a dwarf planet and

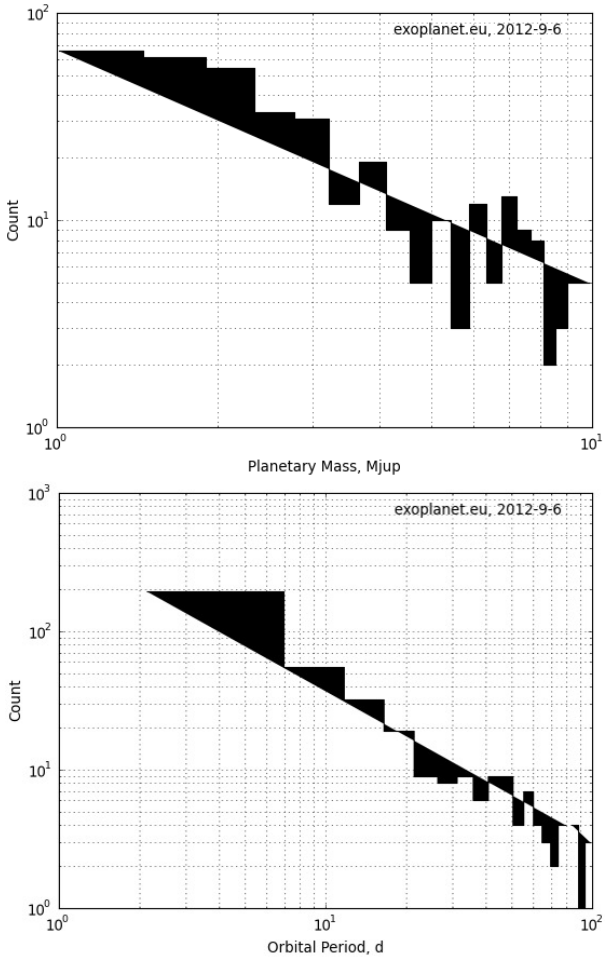

Figure 1.12: Frequency histograms of planetary mass (M sin(i), left) and orbital period (right) of the detected extrasolar planets. Logarithmic scales are employed for both X and Y-axis. The bins are filled in black with respect a linear regression of the data (actually the logarithm of the X and Y values). The ranges of mass and period are limited in order to highlight the power-low shape of the probability density functions of the two distributions. Data and plots from *http://exoplanet.eu/*.

extrasolar planets have greater eccentricities. The prevalence of elliptical orbits is a major puzzle, since current theories of planetary formation strongly suggest planets should form with circular orbits (Boss, 2009). The prevalence of eccentric orbits may also indicate that the SS is unusual, since all of its planets except for Mercury and Pluto have near-circular orbits (Marcy et al., 2005). However, it is suggested that some of the high eccentricity values reported for exoplanets may be overestimates, since simulations show that many observations are also consistent with two planets on circular orbits. Reported observations

'plutoid', owing to the discovery that it is only one of several large bodies within the Kuiper belt (Voelzke & de Araújo, 2010).

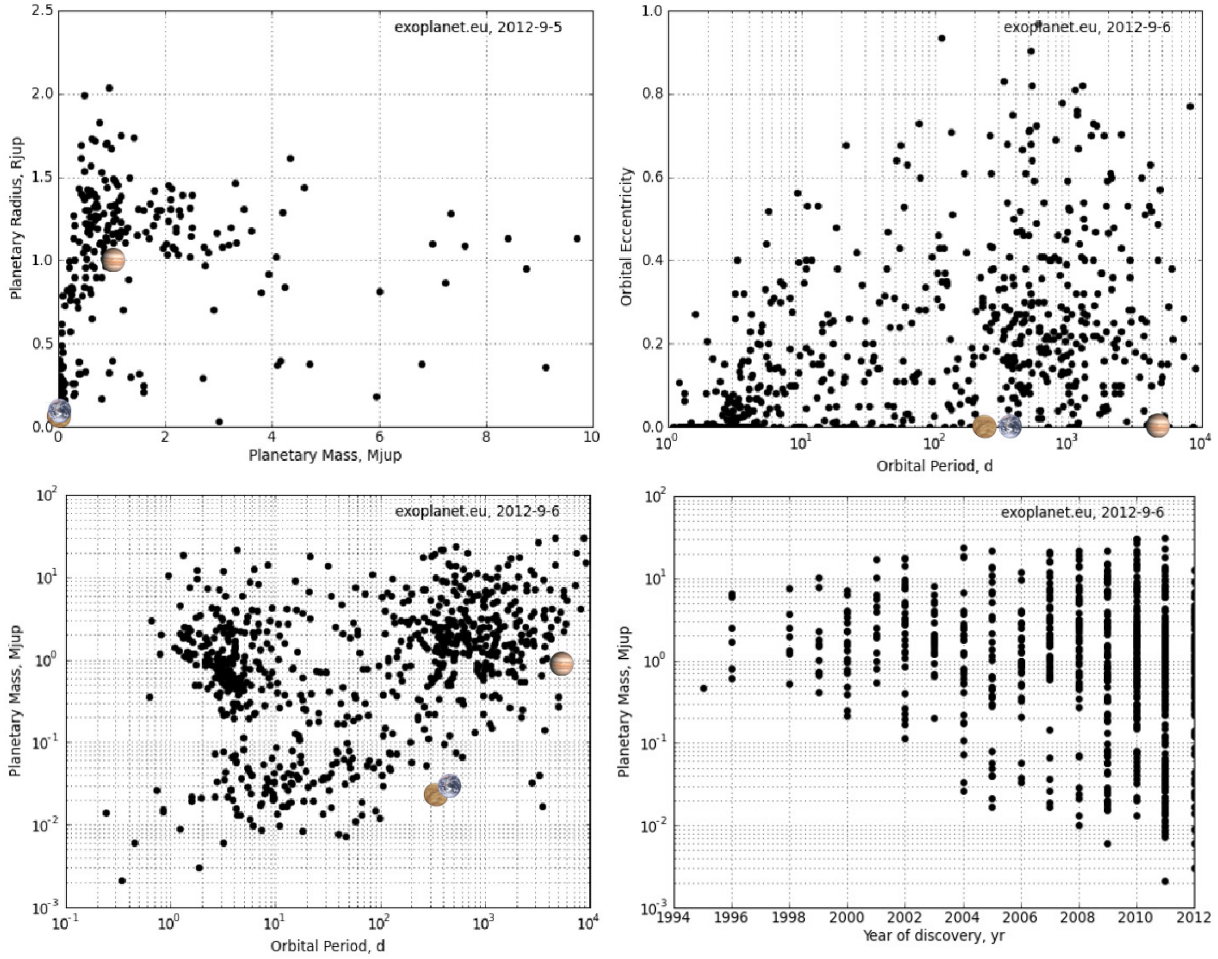

Figure 1.13: Correlation plots of the properties of the known extrasolar planets. From top-left, clockwise direction: M sin(i) - radius, period - eccentricity, discovery year - M sin(i) and period - M sin(i) diagrams. The locations of the Earth, Venus and Jupiter are marked with a relative image of the three planets. Data and plots from *http://exoplanet.eu/*.

of single planets in moderately eccentric orbits have about a 15% chance of being a pair of planets (Rodigas & Hinz, 2009). This misinterpretation is especially likely if the two planets orbit with a 2:1 resonance. Anglada-Escudé et al. (2010) have concluded that:

- around 35% of the published eccentric one-planet solutions are statistically indistinguishable from planetary systems in 2:1 orbital resonance;
- another 40% cannot be statistically distinguished from a circular orbital solution;
- planets with masses comparable to Earth could be hidden in known orbital solutions of eccentric super-Earths and Neptune mass planets.

The correlation diagrams of the measured properties allow to understand further features of the extrasolar planets. One of the most interesting plot is the planetary mass -

radius diagram (Figure 1.13, top-left panel). The radius of a planet depends on its mass and on its composition/structure. The Earth-like planets are those with $M_p < 15\,M_\oplus$, such that no primordial atmosphere of H_2 and He is retained by the planet (Wuchterl et al., 2000). Neptune-like planets have a M_p of $\sim 20\,M_\oplus$ (Santos et al., 2004; McArthur et al., 2004; Butler et al., 2004). The Jupiter-like planets class comprehends all the gas-giant planets in a much larger mass range ($M_p \sim 1\,M_J$and more). Despite the boundaries between the classes are not so well defined, these are commonly employed for the identification of the new discovered extrasolar planets. Within this basic class division, many models have been proposed for the structure and the composition of the planetary interior (e.g. Wuchterl et al., 2000; Valencia et al., 2006; Fortney et al., 2007; Sotin et al., 2007; Baraffe et al., 2008; Wagner et al., 2012) and their atmosphere (e.g. Baraffe et al., 2004; Fortney et al., 2008, 2011). One of the major open problem in this field of astrophysics is the radius anomaly shown by many HJs. It arose with the discovery that the measured radii of transiting gas-giant planets are significantly larger than what structural evolutionary models would expect. The first planet showing such anomaly is `HD 209458-b` (Charbonneau et al., 2000). A decade of additional discoveries has made it clear that the radius anomaly of `HD 209458-b` is by no means anomalous, and the status of discussion in the field is well covered in the recent reviews by Showman et al. (2009); Burrows & Orton (2009); Baraffe et al. (2010). The extraordinary variation in observed radii in the planetary population is visible in the mass - radius diagram for $M_p > 1\,M_J$. The radius anomaly is profusely discussed in the following section.

Most exoplanets with orbital periods of just few days show near-circular orbits, i.e. very low eccentricity (see Figure 1.13, top-right panel). That is believed to be due to tidal circularization: reduction of eccentricity over time due to gravitational interaction between two bodies (Ivanov & Papaloizou, 2007; Rodríguez et al., 2011). By contrast, most known exoplanets with longer orbital periods have quite eccentric orbits. As of September 2012, 52% of such exoplanets have eccentricities greater than 0.2 while 17% have eccentricities greater than 0.5[7]. This is not an observational selection effect, since a planet can be detected almost equally well regardless of the eccentricity of its orbit.

In the period - mass diagram (Figure 1.13, bottom-left panel) the distribution of points can be divided in three parts. In the lower part of the figure ($M_P < 0.1\,M_J$) the planets seem to be uniformly distributed in the range 1 to 100 days; at higher periods the selection effects of the different methods limit the number of discovered planets. For example, Venus and the Earth ($M_p \sim 3 \cdot 10^{-3}\,M_J$, 224 and 365 days respectively) lie in this empty portion of the diagram. A crowded blob of data points lies in the upper-left part of the plot: it corresponds to the pile-up at ~ 3 days discussed above and visible in the bottom-left panel of Figure 1.11. A period of ~ 3 days corresponds to ~ 0.04 AU (for a solar-type host star) and represents the limit of the inward migration of the HJs (see Section 1.4). Accordingly to Ford & Rasio (2006), this population of planets is located at roughly twice the star-planet Roche limit. The Jupiter-like planets with orbital period between 10^2 and 10^4 days (0.5 to 10 AU) represent the variety of gas-giant planets formed via gravitational fragmentation or

[7] *http://exoplanet.eu/catalog/*

core accretion (see Section 1.3) and migrating inward or outward accordingly to the type-I and II migration (see Section 1.4). Jupiter ($M_p = 1\,M_J$, 4333 days) lies on the right side of this cloud of points.

In the fourth correlation diagram, Figure 1.13 bottom-right panel, the mass of the planets and the related year of the discovery is reported. The progressive and continuous increase of the surveys sensitivity to detect lighter and lighter planets can be appreciated. A gain of nearly two order of magnitudes is obtained over a decade. This results is mainly due to the efforts spent to make spectroscopic observation more precise and the instruments more stable over a time-scale of several years.

1.5.1 Radius anomaly of the hot-Jupiters

The existence of highly-irradiated, gas-giants planets orbiting within < 0.1 AU of their host stars, and the unexpected large radii of many of them, is an unresolved problem in the theory of planet formation and evolution (Baraffe et al., 2010). Their prominence amongst all the confirmed exoplanets is unsurprising; their large radii, large masses, and short orbital periods make them readily accessible to ground-based transit and radial velocity

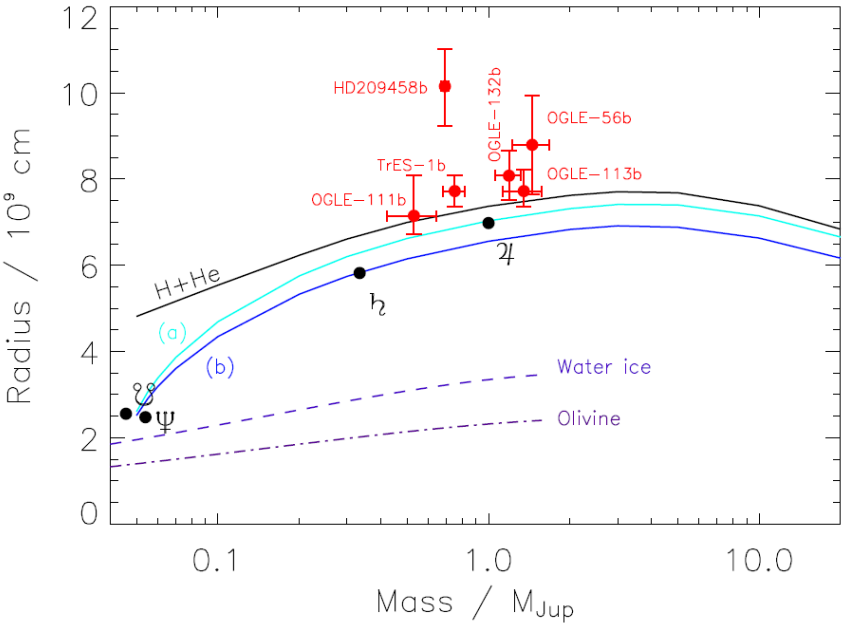

Figure 1.14: Radius versus mass for giant planets after 4.5 Gyrs of evolution compared to measured values for the four giant planets in the SS and four known extrasolar planets. The lines correspond to: a pure hydrogen-helium composition (Y=0.25); (a): a model with Y=0.30 and a 15 $M_\oplus$ core; (b): the same model but with Y=0.36. An approximate mass-radius relation for zero-temperature water and olivine planets is shown as dashed and dash-dotted lines, respectively. The locations of the SS planets Jupiter, Saturn, Uranus and Neptune are marked too. Courtesy of W.B. Hubbard.

surveys, on account of the comparatively large flux variations and reflex motions that they cause. Exoplanet searches often focus on the detection of small Earth-like exoplanets, but understanding the formation mechanism and evolution of the giant planets, particularly in the overlap mass regime with BD, is a key question in astrophysics.

Theoretical models of isolated giant planets predict an almost constant radius for pure H+He objects in the mass range $0.5-10\,M_J$ as a result of the equilibrium between the electron degeneracy in the core and the pressure support in the external gas layers (Zapolsky & Salpeter, 1969; Guillot, 2005; Seager et al., 2007; Baraffe et al., 2010). Hence the larger radii of many HJs must arise from other factors. Due to the proximity of these planets to their host star, the irradiation of the surface of the planet is thought to play a major role in the so-called *radius anomaly*, by altering the thermal equilibrium and delaying the Kelvin-Helmholtz contraction of the planet from birth (e.g. Showman & Guillot, 2002). This is supported by a correlation between the mean planetary density and the incident stellar flux (Laughlin et al., 2011; Demory & Seager, 2011; Enoch et al., 2012). However, it has been shown that this cannot be the only explanation for the radius anomaly (Burrows et al., 2007), and other sources must contribute to the large amount of energy required to keep gas giants radii above $\sim 1.2\,R_J$ (Baraffe et al., 2010).

There are a number of physical mechanisms thought to be responsible for radius inflation, including (but not limited to): tidal heating due to the circularisation of close-in orbits (Bodenheimer et al., 2001, 2003; Jackson et al., 2008), reduced heat loss due to enhanced opacities in the outer layers of the planetary atmosphere (Burrows et al., 2007), double-diffusive convection leading to slower heat transportation (Chabrier & Baraffe, 2007; Leconte & Chabrier, 2012), increased heating via Ohmic dissipation in which ionised atoms interact with the planetary magnetic field as they move along strong atmospheric winds (Batygin & Stevenson, 2010a), and a slower cooling rate due to the mechanical greenhouse effect in which turbulent mixing drives a downwards flux of heat simulating a more intense incident irradiation (Youdin & Mitchell, 2010). A radically different explanation has been proposed by Martin et al. (2011) who point out a correlation between radius anomaly and tidal decay timescale and suggest that inflated HJs are actually young because they have recently formed as a result of binary mergers. Studying the radius anomaly in higher mass HJs ($> 3\,R_J$) is useful as they are perhaps more resilient to atmospheric loss due to their larger Roche lobe radius.

Chapter 2

WFCAM Transit Survey[†]

Figure 2.1: The United Kingdom Infrared Telescope. JAC©

[†]Based on Kovacs et al. (2012), MNRAS submitted.

This chapter introduces the WFCAM Transit Survey (WTS), the first published wide-field near-infrared back-up program, searching for short period (< 10 days) transiting systems around M-dwarfs. The observing strategy of the survey is discussed in Section 2.1, while the pipeline employed for the reduction of the photometric data is shown in Section 2.2. After the illustration of the method used for the detection of the transits in the light curves (LCs, Section 2.3), the efficiency of the transits detection is analysed in Section 2.4. A comparison between the expected results and the discoveries performed along the first five years of the survey can be find in Section 2.5. The WTS is an on-going photometric monitoring campaign using the Wide Field Camera (WFCAM, Casali et al., 2007) on the United Kingdom Infrared Telescope (UKIRT, see Figure 2.1) at Mauna Kea, Hawaii, and has been in operation since August 2007. The survey observes at infrared wavelengths (J-band, 1.25 μm) and its main science goals are two: provide stringent constraints on planet formation theory by determining the giant planet fraction for a large sample of M-dwarfs (Kovacs et al., 2012); constrain low-mass stellar evolution models by measuring fundamental stellar parameters in M-dwarf eclipsing binaries (Birkby et al., 2012).

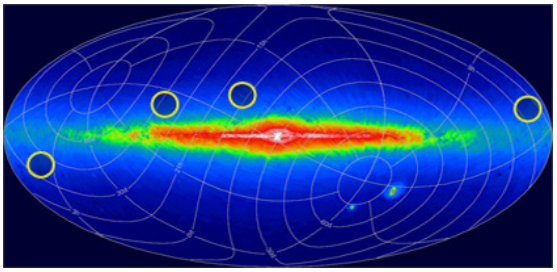

Figure 2.2: Illustration of the four selected target fields (circles) shown in a Galactic projection of the 2MASS sky.

The WTS LCs are observed at infrared wavelengths in order to maximise sensitivity to photons from M-dwarfs, which have a spectral energy distribution that peaks at longer wavelengths with respect to the F, G and K stars. However, for such hotter stars in the WTS fields, infrared observations have the added advantage of being less sensitive to low-level star-spot modulation, thus providing more stable light curves in which to hunt for planets (Goulding et al., 2012). The WTS covers four fields distributed in RA so that at least one field is always visible within 15 ° of zenith from Mauna Kea. The fields are distributed seasonally in right ascension at 03, 07, 17 and 19 hours to allow year-round visibility. In Figure 2.2 the four selected target fields are shown in a Galactic projection of the Two Micron All Sky Survey (2MASS) sky. As of June 16, 2011, the 19 hour field (hereafter, the 19hr field) has approximately 1145 epochs which is close to completion, the other ones are less complete. The year-round visibility of the fields is key to the survey observing strategy as it operates as a back-up program in the highly efficiently queue-scheduled operational mode, observing in sky conditions that the UKIRT large programs, such as UKIDSS (Lawrence et al. 2007), cannot use e.g. a seeing $> 1.3''$. Consequently, the majority of the WTS observations are taken in the first hour of the night when the atmosphere is still cooling and settling. However, the back-up nature of the program serves to randomise the WTS observing pattern. The exact field locations were chosen to minimise giant contamination, while maximising the number of early M-dwarfs and maintaining E(B-V) < 0.1, which keeps them at b > 5 °. The four fields were also observed once in all other WFCAM bands (Z, Y, H and K) at the beginning of the survey (the photometric system is described in Hodgkin et al., 2009).

2.1 Observing strategy

The four fields were chosen to be reasonably close to the galactic plane to maximize stellar density but high enough on the galactic plane ($b > 5\,^{\circ}$) to keep giant contamination and reddening at an acceptable level ($E(B-V) < 0.1$) and to avoid over-crowding. Note that this field is very close to, but does not overlap with, the *Kepler* field (Batalha et al., 2006), but it is promising that recent work showed the giant contamination in the *Kepler* field for magnitudes in a comparable range to our survey was low ($7 \pm 3\,\%$ M-giant fraction for K_P >14, Mann et al., 2012).

The WFCAM comprises four Rockwell Hawaii-II PACE arrays, with $2k \times 2k$ pixels each covering 13.65′ x 13.65′ at a plate scale of 0.4″/pixel. The detectors are placed in the four corners of a square with a separation of 12.83′ between the chips, corresponding to 94% of a chip width. This pattern is called a *pawprint*. Each field of the WTS, covering $1.6\,deg^2$, is made up of 8 pawprints observation sequence with slightly overlapping regions at the edges of the pawprints (see Figure 2.3). Observations are carried out using 10 s exposures in a jitter pattern of 9 pointings. It takes 15 minutes to observe an entire WTS field ($9 \times 10s \times 8$ + overheads). In this way, the NIR light-curves (LCs) have an average cadence of 4 data points per hour.

As already said, the WTS is primarily designed to find planets transiting M-dwarf stars. The observations are hence obtained in the J-band, which effective wavelength ($\sim$1.25 μm) is near to the peak of the SED of a typical M-dwarf. Interestingly, the photometric monitoring of hotter stars at NIR wavelengths may have the advantage as it is potentially less susceptible to the effect of star-spot induced variability (Goulding et al., 2012).

The back-up nature of the program allows the observation of a given field only in bad seeing conditions (> 1.3″). Hence, the observations are randomly distributed throughout

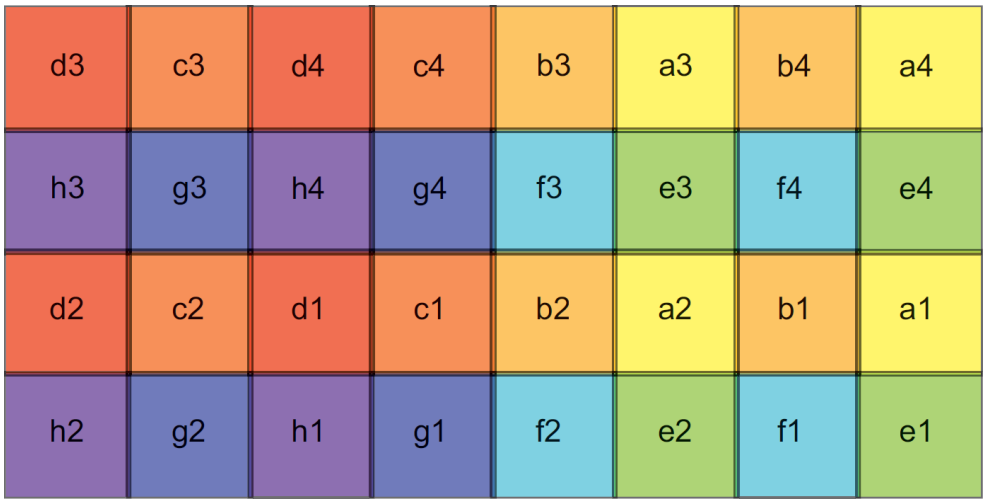

Figure 2.3: Observation sequence of the WTS. A field of $1.6\,deg^2$ consists of 8 pawprints (a-h), each pawprint is built up from the simultaneous exposures of the four (numbered) detectors.

a given night, but on average occur in a one hour block at its beginning or end. Seasonal visibility also leaves long gaps when no observations are possible (Kovacs et al., 2012). This has a dominant effect on the detectable transiting systems. In Figure 2.4 a simple sensitivity diagram is presented considering only the distribution of observational epochs over time. We use simulated transiting systems from the Neptune-size planets around an M0-dwarf scenario (M0+N) and compare the simulated transit times with our real observational epochs. The simulated systems represent an unbiased sample of different transit lengths and time offsets derived from random geometric orientations within the transiting inclination range (allowing for grazing). A system is considered detectable here if at least 5, 10 or 15 in-transit observational epochs occur. The fraction of detectable systems has an obvious strong dependence on the period of the transiting system and the required number of in-transit observational epochs as well. Of course, it depends on the noise properties of the data how many in-transit observations are necessary for detecting a transit event. Typical transit times for a Neptune mass and radius planet around an M0 and M4.5 dwarf vary between 60-120 minutes to 40-90 minutes respectively (edge on, circular orbit, 1-10 days orbital period). A detailed and complete discussion of the transit recovery ratios concerning other different scenarios can be found in the Section 2.4.

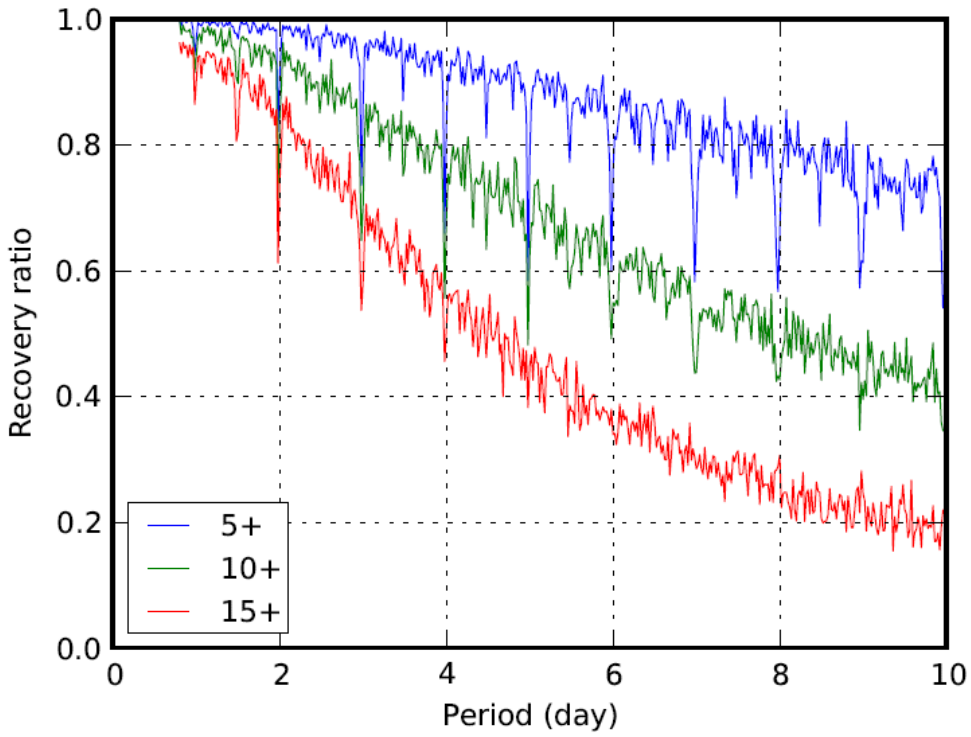

Figure 2.4: Influence of the observation strategy on the survey sensitivity for transiting systems. The fraction of simulated transiting systems is shown where at least 5, 10 or 15 in-transit observational epochs occur in the survey.

2.2 Reduction pipeline

The WTS uses aperture photometry to construct LCs from individual data frames. All images taken with WFCAM are processed using an image reduction pipeline operated by the Cambridge Astronomical Survey Unit (CASU[1]). The pipeline is a successor of the INT WFS (Irwin & Lewis, 2001a) and Monitor (Irwin et al., 2007) pipelines and implements the methods presented in Irwin (1985). This is a standardized procedure for all projects using the WFCAM instrument on UKIRT. Only a brief overview of the image processing steps are given. Images are converted into multi extension *fits* format, containing the data of the 4 detectors in one pawprint as extensions. Other data products from the pipeline (catalogues, LCs) are also stored in binary *fits* table files. A series of instrumental correction steps is performed: linearity, reset, dark, flat, de-fringing and sky subtraction. The sky subtraction removes spatial variation of the sky background but keeps its mean level. Object detection, astrometry, photometry and object classification are also performed for each frame. Astrometry and photometric calibration are based on matching a set of bright objects with the 2MASS (Skrutskie et al., 2006) point source catalogue. The astrometry of data frames are described by a cubic radial distortion factor (zenithal polynomial transformation) and a six coefficient linear transformation allowing for scale, rotation, shear and coordinate offset corrections. Header keywords in *fits* files follow the system presented in Greisen & Calabretta (2002); Calabretta & Greisen (2002). In the photometry step, object fluxes are measured by aperture photometry using a series of soft-edged apertures (i.e. pro-rata division of counts at pixels divided by the aperture edge). In the sequence of apertures, the area is doubled in each step. For WFCAM, the smallest aperture is r_{core}=1.4″(0.4″/pixel). Morphological object classification and derived aperture corrections are based on analysis of the curve of growth of the object flux in the series of apertures.

Next, master images are created for each pawprint by stacking the 20 best seeing photometric frames. The master images play dual roles: they give the catalogue of objects of the survey for each pawprint and help reaching better accuracy for aperture photometry. WTS objects are identified and numbered according to these master frames. Having better signal-to-noise ratio (SNR) levels on the stacked image, the catalogue may include objects on the faint end that could not be identified on individual frames. As it is discussed in Irwin et al. (2007), positioning error of aperture placements is a source of error in aperture photometry. Determining object centroid positions on a frame by frame basis would reduce the accuracy of aperture positions of fainter objects. To refine aperture locations in the WTS, astrometry is re-run on the master catalogues. These object positions are then fixed for the survey. In the photometry step, object fluxes are measured at these fixed locations on each frame using a series of soft apertures. By fixing object positions on the master frame, remaining errors in aperture locations will typically be mapping errors that affect all stars in the same way or vary smoothly across frames. This could be corrected by the normalization procedure.

[1] *http://casu.ast.cam.ac.uk/surveys-projects/wfcam*

Table 2.1: LC quality in the WTS. Median LC RMS (mmag) as a function of object magnitudes using different pipeline options in the 19a pawprint.

J =	11-12	12-13	13-14	14-15	15-16	16-17
constant normalization	11.7	8.5	6.9	6.8	9.6	18.3
quadratic normalization	11.0	7.9	6.0	5.9	9.0	18.0
+ outlier filtering	11.0	7.8	5.9	5.7	8.7	17.4
+ seeing correction	8.6	5.9	5.0	5.5	8.4	16.8

Subsequently, sky background is estimated using a coarse grid of 64×64 pixels over the data frames. Sky level are calculated by a robust $k\sigma$ clipped median estimator of the pixel counts for each bin in the grid[2]. The sky background map is filtered by 2D bilinear and median filters to avoid sky level shifting in bins dominated by bright objects. For each object, sky level is determined by evaluating a bilinear interpolation of the coarse sky map at the objects position. For further details we refer to Irwin (1985, 1997).

Although the photometry of each frame is calibrated individually to 2MASS sources (Hodgkin et al., 2009), these values can be refined for better photometric accuracy. LCs constructed of magnitudes by using photometric scales determined for each frame individually have typical RMS at the few percent level ($J < 16$). To reach a better accuracy, an iterative normalization algorithm is used to correct magnitude offsets on each frame also allowing for a smooth spatial variation. In each iteration, LCs are constructed for all stellar objects and a set of bright stars selected ($13 < J < 17$) excluding the most variable decile of the group based on their (actual iteration) LC RMS. Then for each frame, a polynomial fit is performed on the magnitude differences between the given frame magnitudes and the corresponding median (LC) magnitude for the selected objects. The polynomial order is kept at 0 (constant) until the last iteration. In the last iteration, a second order 2D polynomial is fitted as a function of image coordinates. For each frame, the best fit polynomial magnitude correction is applied for all objects and the loop starts again until there is no further improvement. Multiple iterations of the constant correction step help to separate inherently variable objects from non-variable ones initially hidden by LC scatter caused by magnitude scale differences. The smooth spatial component during the last iteration accounts for the effects of differential extinction, as well as possible residuals from non-uniformity in the point spread function (PSF) across the field of view. It is also found that LC noise correlates with observational seeing. In the seeing-correction final post-processing step, for each object, a second order polynomial is fitted to differences from median magnitude as a function of observational seeing values. Magnitude values are then corrected by this function on a per-star basis.

Bad observational epochs (frames) are then removed as they could add outlier data

[2]The median absolute deviation (MAD) is used as a robust estimator of the root mean square (RMS) in most pipeline components both during processing individual frames and LCs. For normal distribution, RMS=1.48·MAD.

points for a significant number of objects in any chip of a pawprint. For each epoch (frame), those objects are marked where the given epoch is a 3σ outlier in the object LC. Frames exceeding 30% of marked objects are removed from the LCs. Our rejection threshold is a compromise between the number of affected frames and frame quality. At the threshold of 0.3, 4% of the frames are removed in the 19hr field.

Each step of the reduction pipeline contributes to reduce the final RMS of the data (see Table 2.1). The normalization procedure of the photometric scale by per-frame constant offsets, the quadratic spatial correction during the normalization, the bad epoch filtering and the seeing correction give an improvement at the $0.5 - 1$ mmag level. In Figure 2.5 a theoretical noise model curve consisting of Poisson noise, sky noise and a constant residual are drawn. According to this model, in the J=13-15 magnitude range a ~ 3 mmag of residuals dominates. Some saturation appears and makes LC RMS worse for objects brighter than J=13 while for the faint end, the sky noise is the primary noise component.

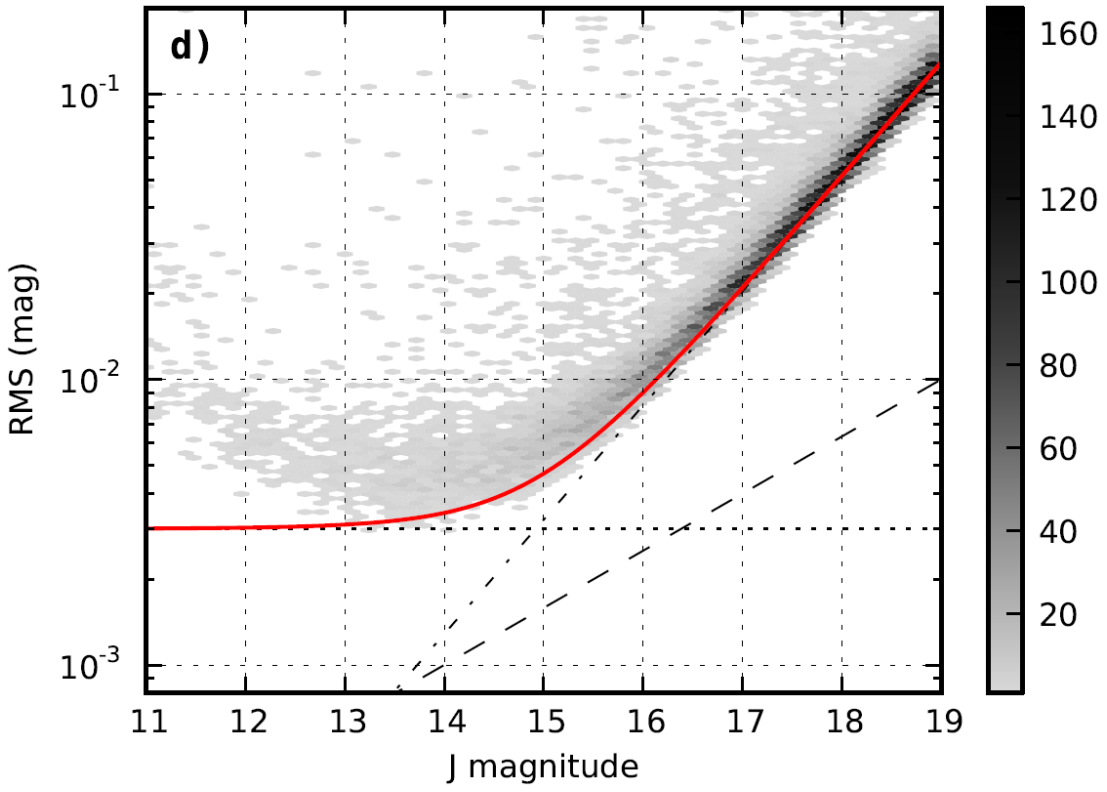

Figure 2.5: RMS of stellar objects in the 19a pawprint with seeing correction. Noise model (solid line) consisting of Poisson noise (dashed line), sky noise (dash-dotted line) and systematic noise of 3 mmag (dotted line) is drawn.

2.3 Transit detection algorithm

The transit candidates are identified in the J-band LCs by using the Box-Least-Squares transit search algorithm OCCFIT, as described in Aigrain & Irwin (2004), which takes a maximum likelihood approach to fitting generalized periodic step functions. Before inspecting transit candidates by eye, several criteria to speed up the detection process are employed . The first is a magnitude cut, in which all sources fainter than $J = 17$ mag are removed. It is also required that the source have an image morphology consistent with stellar sources (Irwin et al., 2007). Despite the attempts to remove systematic trends in the LCs, they invariably suffer from residual correlated red noise, so the detection significance statistic, S, from OCCFIT is modified according to the prescription of Pont et al. (2006) (equation 4), to obtain S_{red}. The transit candidates must then have $S_{red} \geq 5$ to survive, although this is more permissive with respect to the limit recommended by Pont and collaborators ($S_{red} \geq 7$). Any detections with a period in the range 0.99 <P< 1.005 days are further discarded, in order to avoid the common ∼1 day alias of the ground-based photometric surveys. An example of a phase folded J-band LC that passed all these criteria is shown in Figure 2.6.

Next, as fully described in Birkby et al. (2012), the WFCAM $ZYJHK$ single epoch photometry are combined with five more optical photometric data points ($ugriz$ bands) available for the 19hr field from the Sloan Digitized Sky Survey archive (SDSS 7^{th} release, Nash, 1996) to create an initial spectral energy distribution (SED). The SEDs of the transiting candidate objects are fitted with the NextGen models (Baraffe et al., 1998) in order to estimate effective temperatures and hence a stellar radius for each source. A final threshold on the detected transit depths can then be imposed, by rejecting those that corresponded to a planetary radius greater than $2\,R_J$. It is worth noting that OCCFIT tends to under-estimate transit depths because it does not consider limb-darkening effects and the trapezoidal shape of the transits. Moreover, the NextGen models systematically under-estimate the temperature of solar-like stars (Baraffe et al., 1998), so the initial radius estimates are also under-predicted. Hence, the genuine HJ transit events are unlikely to be removed in this final threshold cut. As a result, the transits detection procedure is conservative. Many of the ∼3 500 phase-folded LCs which satisfied the selection criteria just described were false-positives arising from nights of bad data or single bad frames. Others were binary systems, folded on half the true orbital period. A more detailed analysis of the candidate selection procedure and of advanced selection steps in the survey can be found in Sipocz et al. (2012).

The J-band LCs that pass all these selection criteria progress to the following phases of candidate confirmation. Optical photometric follow-up are conduced in the i'-band using the Wide Field Camera (WFC) on the 2.5-m Isaac Newton Telescope (INT) at Roque de Los Muchachos, La Palma. The data are reduced with the CASU INT/WFC data reduction pipeline as described in detail by Irwin & Lewis (2001b) and Irwin et al. (2007). The pipeline performs a standard CCD reduction, including bias correction, trimming of the overscan and non-illuminated regions, a non-linearity correction, flat-fielding and defringing, followed by astrometric and photometric calibration. A master catalogue for the

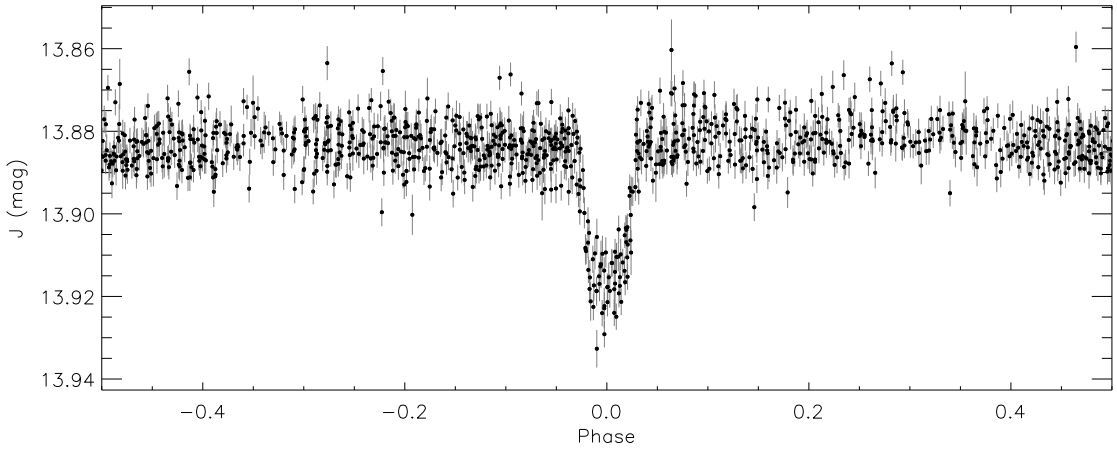

Figure 2.6: Example of a phase folded LC showing a transit detected among the raw thousands of J-band LCs measured within the WTS.

i'-band filter was then generated by stacking 20 frames taken under the best conditions (seeing, sky brightness and transparency) and running source detection software on the stacked image. The extracted source positions are used to perform variable aperture photometry on all of the images, resulting in a time-series of differential photometry. Such observation allows to prove the real presence of the transit and check the transit depth consistency between the infrared and optical bands.

In order to exclude any false-positive eclipsing binaries or grazing binaries scenarios, intermediate-resolution spectroscopic observation of the candidates are then conduced using the William Herschel Telescope (WHT) at Roque de Los Muchachos, La Palma. These spectra allow the identification of any giant contaminants via gravity sensitive spectral features and provide an upper limit on the mass of the transiting companion of the host star. Finally, high-resolution spectra of a planetary candidate are observed with the High Resolution Spectrograph mounted in the basement of the Hobby-Eberly Telescope at the McDonald Observatory, Texas, USA. The fit of the high precision RV measurements, related to the different epochs of the observations, allows to precisely estimate the mass of the planetary candidate and, in case, confirms the planetary nature of the parent star companion. Constrains on the eccentricities of the orbit of the new detected planet could be fixed too. Another set of properties of the star-planet system can be achieved fitting the transit shape in the LCs. The simultaneous fit of both the J- and i'-band LCs allow a better estimation of the free parameters employed for modelling the transit. Orbital period, transit epoch, planet - star radius ratio (R_p/R_s), mean stellar density and impact parameter can be estimated in such a way (see Sections 5.2 and 5.3). The full set of parameters, completed by the planetary mass, permits to fully characterized the new discovered planet and allows to place it (for example) in the correlation plots shown in Section 1.5 in order to better understand the nature of the planet (super-Earth, Jupiter-like, HJ, etc.).

2.4 Transit recovery ratios

As already introduced in Section 2.1, transiting systems were simulated in order to quantify the efficiency of the observations (according to the back-up nature of the program) coupled with the transit detection algorithm. To determine our transit recovery ratios (P_r), an iteration loop was used to generate mock LCs in different scenarios: M0+J (M0-dwarfs+Jupiter), M0+N, M2+J and M2+N. In each iteration, a transiting planetary system is created with parameters randomly drawn from fixed prior distributions as detailed below and its simulated transiting signal is added to a randomly selected (real) LC. It is then tried to recover the generated system using the survey transit detection algorithm (see Section 2.3). P_r is estimated as the ratio between successful transit recoveries and the total number of iterations. The sensitivity of the survey is studied by using different definitions of signal recovery success. Systems in circular orbits only are considered. A set of flat M-dwarf LCs in the 19hr field that serves as input in the iteration loop are identified. Flatness means that the LCs are originally not recognized as candidates by searching for transits in them. They contain all the other noise features, systematics except for transit signals. By adding noise free signals to these LCs and recovering them from the noisy data, the effect of noise on P_r can be quantified.

The iteration loop consists of three steps:

- generation of parameters for a random transiting planetary system in the investigated star-planet scenario and selection of a flat LC;
- modification of the LC by adding an artificial transit signal to it;
- performing the transit detection step of the survey to recover the generated system from the modified data.

The period value (T) is drawn from a uniform distribution in the range of 0.8 to 10 days. The source distribution of the periods in the iteration loop carries no physical meaning. The period value determines the semi-major axis (a) of the system. A randomly oriented system is uniformly distributed in $\cos(i)$ where i is its orbital inclination. The random inclination is chosen to satisfy $0 \leq \cos(i) \leq (R_\star + R_p) = a$ to yield a transiting system. This also allows for grazing orientations. The phase of the transit is also drawn uniformly within the orbital period. As a last step, a LC is chosen from the set of flat LCs. Having all the system parameters generated, observational epochs from the target LC are compared with transit events. If there is no observational epoch affected the iteration loop ends and the generated parameters are recorded. Otherwise, a realistic, quadratic limb darkening model is used with coefficients from Claret (2000) to calculate brightness decrease at in-transit observational epochs (Mandel & Agol, 2002; Pál, 2008). This artificial signal is added to the LC magnitude values. Then the box fitting transit detection algorithm (see Section 2.3) is run on the modified LC and both generated and detected transit parameters are recorded for the iteration. The transit detection algorithm gives the computationally most intensive step in the loop.

Moreover, an 'optimistic' and 'pessimistic' approach in calculating P_r are introduced to consider the quality of detections. In the optimistic case, a transit recovery step is considered successful if the SNR threshold is met. In the pessimistic case, we require in addition that the discovered period value matches (or be a harmonic of) the generated period. This step uses external information thus it has no analogous check in the real survey. The true value of P_r should be between these two approaches. We show results of P_r as a function of stellar magnitude and simulated period. We adopt 0.8-3.0, 3.0-5.0, 5.0-10.0 days ranges following the definition of Hartman et al. (2009) for extremely hot-Jupiters (EHJ), very hot-Jupiters (VHJ), hot-Jupiters (HJ) respectively. The recovery ratio for Jupiter and Neptune size planets around M0 and M2 stars can be seen in Figures 2.7 and 2.8.

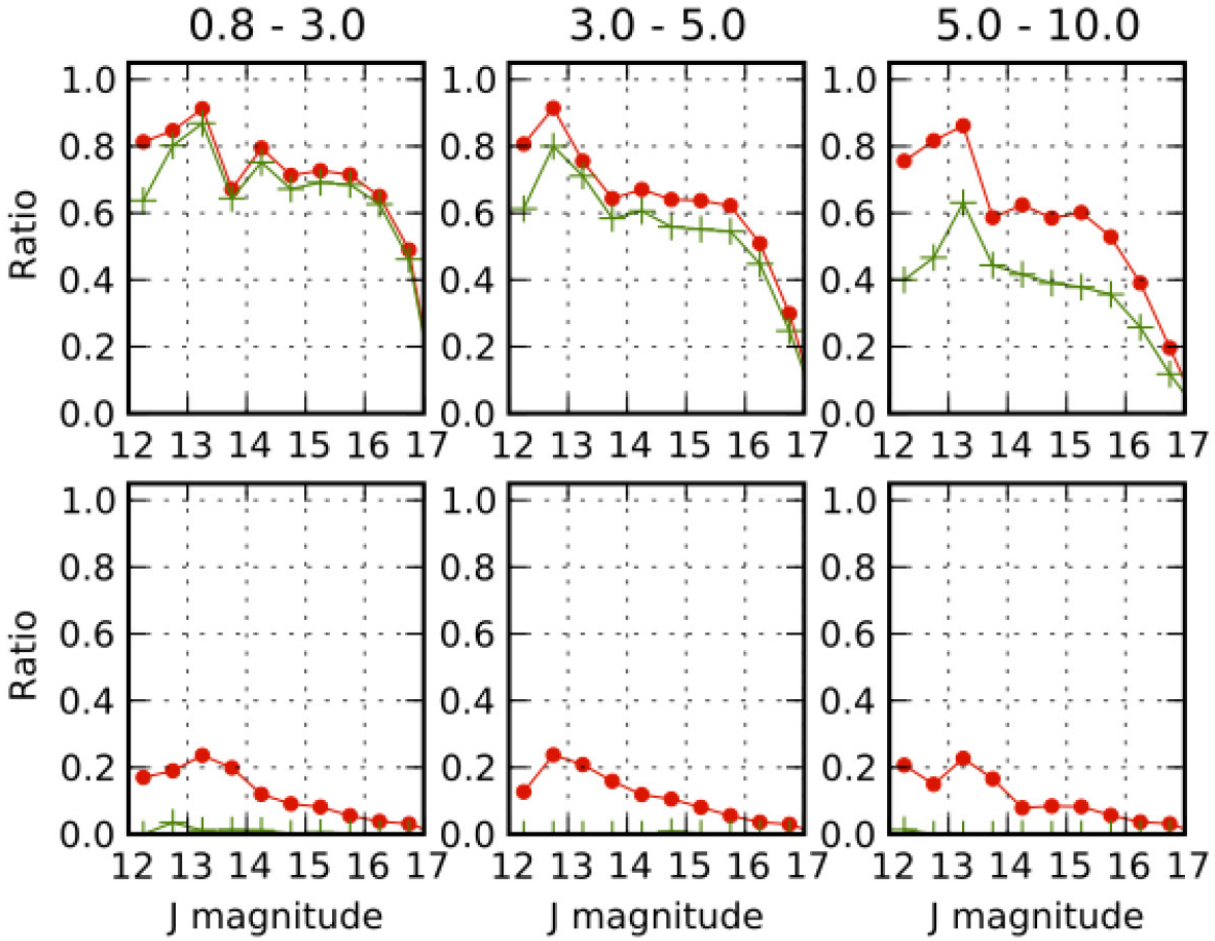

Figure 2.7: Recovery ratios (P_r) of simulated transiting system for M0+Jupiter (upper row) and M0+Neptune (lower row) scenarios in three period ranges as a function of stellar brightness. Filled circles (•) and crosses (+) represent the optimistic and pessimistic ratio respectively.

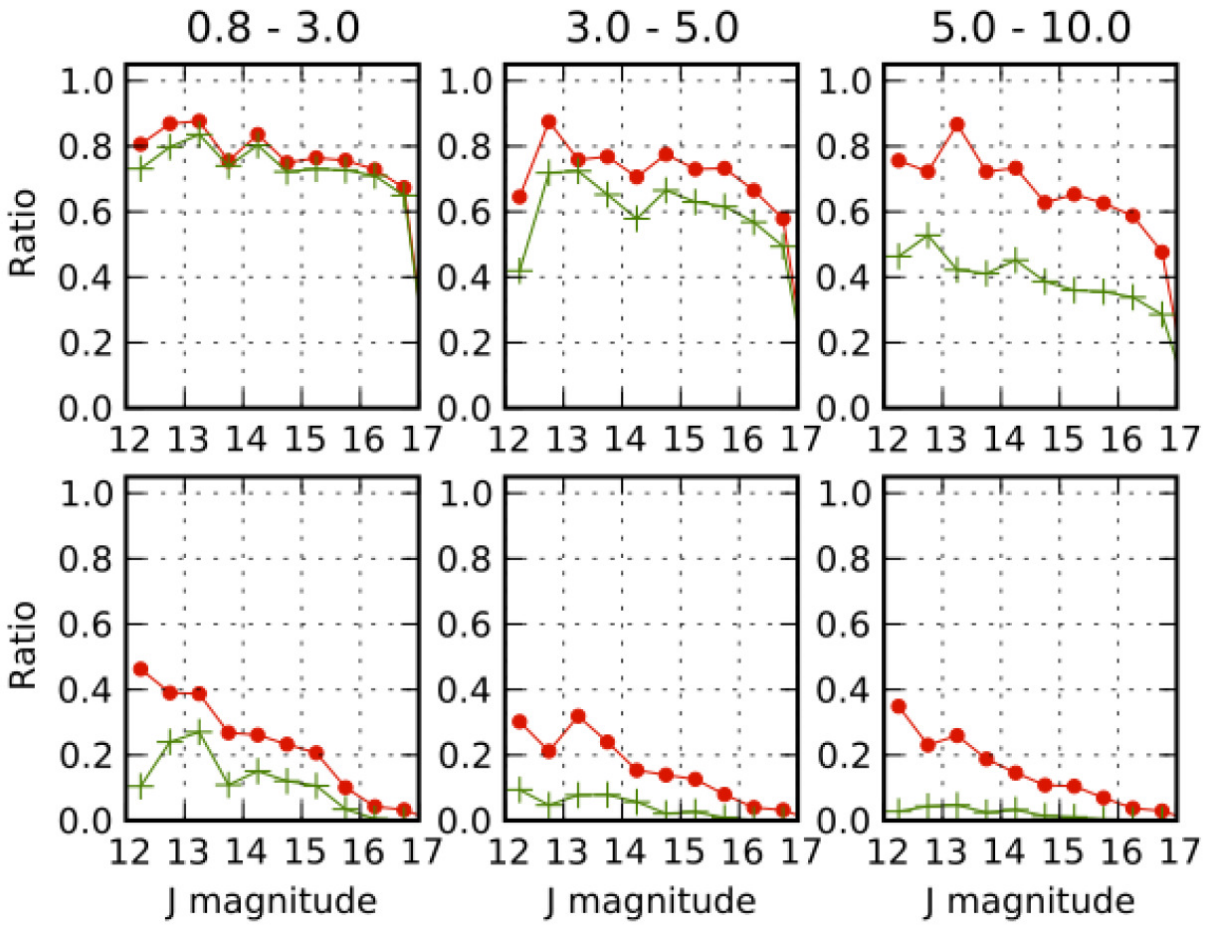

Figure 2.8: The same of Figure 2.7 for M2+Jupiter (upper row) and M2+Neptune (lower row) simulated scenarios.

Filled red circles (•) and green crosses (+) represent the optimistic and pessimistic interpretation respectively. The survey sensitivity has a maximum around J=13.5 and drops towards fainter (J < 15-16) objects. Except for the highest signal case (M2+J) it becomes a fraction ($1/8^{th}$-$1/10^{th}$) of the brighter regime value. Values are also lower at the brightest end. This is in accordance with our expectations, we have higher noise levels towards fainter objects but occasional saturations in the bright end (J < 13). The optimistic and pessimistic ratios are almost identical in the shortest period bin but the pessimistic curve shows a stronger dependence on period. In the longest period panels the optimistic ratio is about twice of the pessimistic one showing that while the SNR detection statistic can recover signals, many of these systems may be missed due to poor initial period guesses.

2.5 Results

In Sections 5.2 and 5.3 the two planets discovered by the WTS along the first five years of activity are described. The planets are two HJs orbiting around a late F-type and an early K-type stars. Both the parent stars of these two systems are hotter than an M-dwarf, the main target sample of the WTS. According to these results, the null detection of Jupiter and Neptune planets around M-stars is here reported. In Kovacs et al. (2012), the planetary occurrence fraction is analysed and discussed. The whole set of identified M-stars in the 19hr field is divided into two bins: 2844 are M0-2 stars ($T_{\rm eff}$=3400-3800 K) and 1679 are M2-4 stars ($T_{\rm eff}$=2960-3400 K). In Figure 2.9, the upper limit of the HJs planetary occurrence for the two samples of M-dwarfs are shown by green arrows. The occurrence upper limit related to the M0 bin from the *Kepler* sample (red arrow) was computed considering 1086 stars. Due to the factor of 2 higher number of early M-dwarfs, the statistical upper limit set for the WTS M0-2 bin is a stricter constraint than the one that can be derived for the *Kepler* M-dwarfs sample (see Figure 2.9). Further details and considerations can be found in Kovacs et al. (2012).

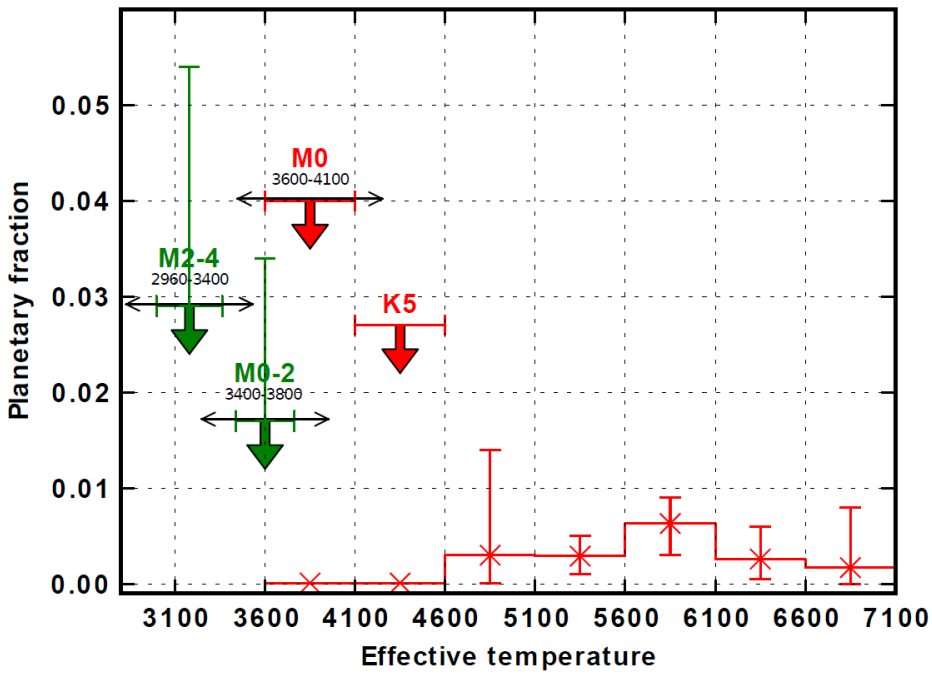

Figure 2.9: Short period (0.8-10 day) HJ planetary occurrence fractions and upper limits in case of null detections in the WTS (green) and in *Kepler* (red). *Kepler* rates are based on Howard et al. (2011). WTS upper limits (green arrows) are shown for the M0-2 and M2-4 bins. Vertical error bars cover the uncertainty of values related to the optimistic and pessimistic planet detection probability. Horizontal bars show temperature bin widths, horizontal arrows mark estimated uncertainty of bin edges where available. Red arrows in the two coolest *Kepler* bins (M0, K5) are upper limits for null detections.

Chapter 3

Instrumentation and spectroscopic observations

Figure 3.1: External view of the Hobby-Eberly telescope.

3.1 Hobby-Eberly Telescope

The Hobby-Eberly Telescope (HET, see Figure 3.1), is one of the world's largest optical telescopes, with an effective aperture of 9.2 m. The HET is named in honour of its principal benefactors, William P. Hobby and Robert E. Eberly, and is a joint project of the 'University of Texas' at Austin (Texas, USA), the 'Pennsylvania State University' (Pennsylvania, USA), the 'Stanford University' (California, USA), the 'Ludwig-Maximilians-Universität' in Munich (Germany) and the 'Georg-August-Universität' in Göttingen (Germany). The observations related to the RoPACS project could be performed thanks to the observing time granted by Prof. Dr. Ralf Bender[1].

The telescope design is revolutionary: it sits at a fixed elevation angle of 55 °, and rotates in azimuth to access 81% of the sky visible from McDonald Observatory (Texas, USA). Its primary mirror is made of an array of 91 spherically shaped hexagonal segments. Because the HET is fixed in its vertical axis, the mirror is stationary with respect to gravity. This completely eliminates the problem of variable distortion that affects the precision required of large optical mirrors for quality image resolution. It also dramatically simplifies the telescope supporting framework. Such a structure solution has two side-effects. First, an astronomical target can be observed only in two 'observable windows' during a night. According to the target coordinates, dusk or dawn can partially or totally overlap with one (of both) observable window. Then, the exposure time of a scientific frame is limited to $\lesssim$ 1 hour if neither dusk nor dawn partially occur along the available observable time.

The HET is designed for spectroscopy and hosts a trilogy of spectroscopic instruments. The Low-resolution Spectrograph (LRS) is located at prime focus on the tracker. The Medium-resolution Spectrograph (MRS) and the High-resolution Spectrograph (HRS) are located beneath the telescope in a climate controlled basement, and are fed by optical fibre.

The HET meets its specification and points to better than 30″, but because it is not designed for pointing more accurately than 10″, all targets except the brightest, most isolated ones should have a finding chart to avoid any setup ambiguity. A photomultiplier is used to locate the fiducial position of the optical fiber probe from the HRS. The limiting magnitude for such acquisition method is approximately 16 mag. For objects fainter than 16th magnitude but brighter than 19 mag the object can be placed on the fiducial marker which marks the fiber location. The focus model for the HET is determined by tracking a star all the way through its trajectory and recording focus corrections with the LRS. Objects are tracked by a moving instrument package located 13 m above the mirror at prime focus. Essentially, on the HET, it is the eyepiece that does the tracking. As a star moves overhead, its light bounces off of the large stationary mirror and the tracker package moves to catch it, always precisely at the exact location of focus. This instrument package combines focusing and tracking in a single system. The tracker must move within a six axis coordinate system (hexapod) to achieve focus as it tracks.

The HET operates a queue scheduled observing program. Under this system, operation

[1] Observatory of the Ludwig-Maximilians-Universität München, Max-Planck-Institute for Extraterrestrial Physics, Garching bei München.

of the telescope, and the acquisition of targets on the nightly observing list is the primary responsibility of the resident astronomer, who has flexibility to optimize the observing plan. This mode of operations is particularly well suited to the HET because it makes full use of the entire night for the maximum scientific output. All the observations related to the present work were taken with the HRS from 2008 to the late 2011. The instrument employed for the spectroscopic follow-up of the target, the HRS, is described in the following sections.

3.2 The HRS Spectrograph

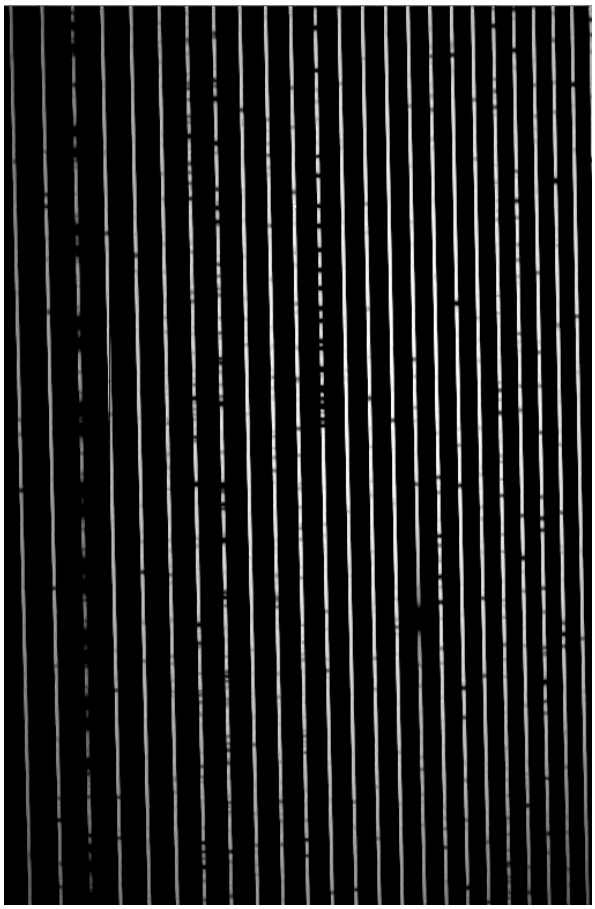

Figure 3.2: Example of a star spectrum observed with the HRS. Each nearly vertical strip corresponds to a spectral order. The wavelength grows from the bottom to the top along a single order and from left to right across the different orders.

The HRS is a single channel adaptation of the European Southern Observatory (ESO) Ultraviolet and Visual Echelle Spectrograph (UVES) as described by Tull et al. (1998). Resolving powers of R∼15 000, 30 000, 60 000 and 120 000 are available by means of four effective slit widths. It uses an R-4 echelle mosaic with cross-dispersing gratings to separate spectral orders. An all-refracting camera images onto a mosaic of two Charge Coupled Devices (CCD). Such CCDs are thinned and anti-reflection coated Marconi type, each with 2048×4100 pixels of $15\,\mu$m size. The CCDs are placed side by side along their 4K side with a ~ 72 pixel dead space between them. This dead space is approximately parallel to the spectral orders. One echelle spectral order is lost during the exposure as it falls completely onto this gap between the two CCDs.

The HRS is a "white pupil" spectrograph using the 2-mirror collimator system (see Figure 3.3): the main collimator (M1) is an off-axis paraboloid used in autocollimation, with the entrance slit at its focus. After the dispersed light is reflected from M1, the beam comes to an intermediate focus, offset from the slit by $0.8\,^\circ$. Mirror M2 has identical figure and focal length but is farther off-axis: it serves to recollimate the beam, directing all dispersed rays to the white pupil coinciding with the surface of the cross-dispersing grating and compensate for the off-axis aberrations of M1. For spectral stability, the echelle and gratings tilts can be varied only in fixed steps (see Section 3.3).

The overall wavelength coverage goes from 3000 to 10 500 Å. The flux delivered below 4000 Å drops sharply as the quantum efficiency of the blue CCD and the focus degrade. Below 3000 Å the atmospheric cut-off occurs and hence ground-based observation are not possible. The longest observable wavelength is limited by the drop in the quantum efficiency of the red CCD. Accordingly to the instrumental configuration, the wavelength range of the observed spectrum is shorter (see Section 3.3). Moreover, the wavelength range of

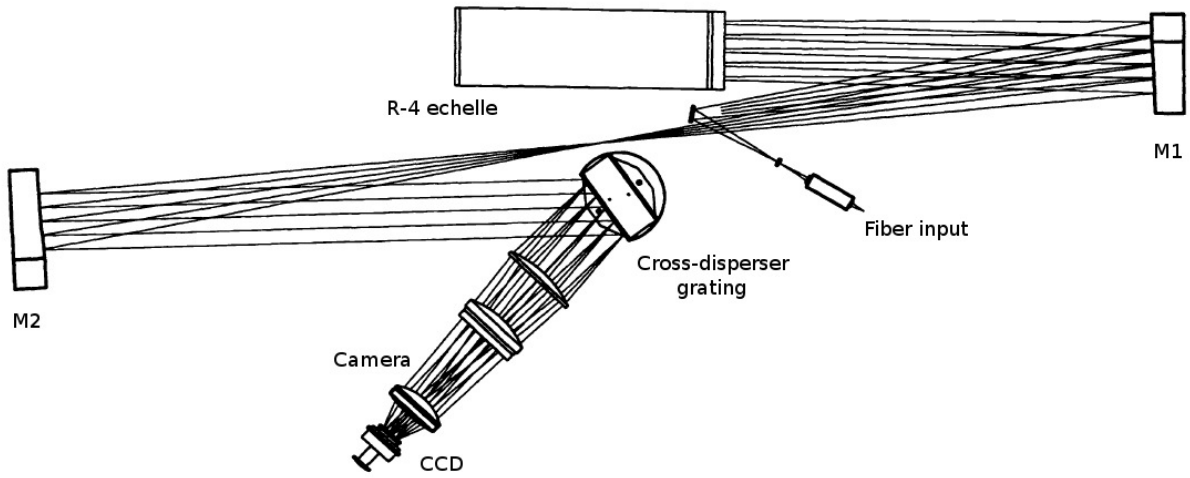

Figure 3.3: Optical design of the HRS (Tull et al., 1998).

the spectra employable in the analysis of the data is strongly limited by the SNR of the observed spectra (see Section 4.3.1).

Each scientific exposure is performed connecting the HRS, set to the desired configuration, to the focus of the HET with an optical fiber. The camera shutter is opened for the required exposure time and finally the detected signal is recorded on the output file. Each of the output files of the HRS is a *fits* file with three components. The first component (components [0]) is represented by the list of headers which describes the instrumental configuration parameters and the environmental conditions at the epoch of the acquisition of each exposure (see Table 3.1). The two frames coming from the two CCDs composing the detector are saved in two distinct components (red and blue components or components [1] and [2], respectively) of the *fits* files.

Beyond the proper science files, several calibration frames are required in order to correctly reduce the data. These files are the bias, the flat-fields and an exposure which has a 'Thorium-Argon lamp' (ThAr) as source. Examples of such calibration frames are reported in Figure 3.4. A bias frame is essentially a zero-length exposure with the shutter closed. A pre-defined constant voltage is applied to the electronic circuits that read the charges measured by the pixels of the CCDs. Such constant voltage introduces an off-set in the number of counts which is required in order to avoid null or negative values of the final measured signal. This bias level is removed from all the science and ThAr frames during the calibration phase (see Section 4.2.2).

The second kind of frames involved in the calibration is the flat-field. Each pixel has its own read out electronic noise and a different sensitivity to the photons reaching the detector. Furthermore, the optical system is characterized by a given efficiency profile, the intra-order blaze function, which depends mainly on the configuration of the spectrograph. Uniformly illuminating the detector, the effects of all these systematics can be detected and removed from the scientific frames. In order to obtain a flat illumination of all the pixels a source characterized by a flat spectrum is required. Such a white spectrum is provided by

Table 3.1: List of the headers stored in the component [0] of each file and involved in the reduction and analysis of the data. A short description of each header is reported.

Header	Description
OBJECT	Content of the file
OBSTYPE	Type of exposure: object, bias, dark, flat, comp etc.
EXPTIME	Actual integration time
DATE-OBS	Date (yyyy-mm-dd) of observation
UT	Universal time
RA	Right ascension
DEC	Declination
CCDSUM	CCD on chip binning (col row)
PROBEPOS	Input source
DISPERSE	Echelle tilt position
TILTPOS	Cross disperser tilt position
INSFOCUS	HRS focus setting

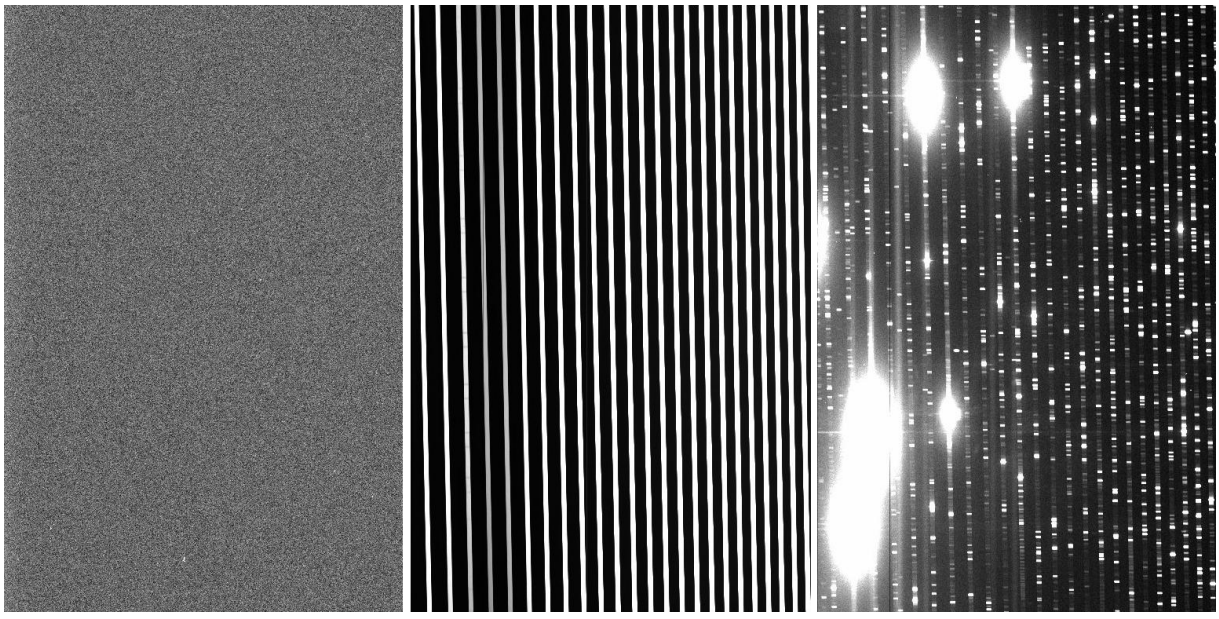

Figure 3.4: Example of the three calibration frames taken with the HRS. From left to right: bias, flat-field and ThAr frames. The bias frames are used for the detector readout noise correction; the flat-field frames for the sensitivity variation of the pixels and the definition of the orders; the ThAr spectra are required for the wavelength calibration of the science extracted spectra. The stronger lines that saturate the detector are clearly visible as white ellipses.

the 'Flat-field calibration lamp'. A dedicated fibre connects the white lamp to the HRS. This frames are also involved in the definition of the location and the inclination of all the order across the detector frame (see Section 4.2.3). The exposure time of a flat-field frame is usually as long as 6 s.

The ThAr frames are essential for the wavelength calibration of the science extracted spectra (see Section 4.2.5). The spectrum of such a lamp shows a great number of sharp emission lines which rise over a practically null continuum. The intensities of the lines can vary widely: some of them saturate the pixels of the CCDs (see Figure 3.4). Furthermore, the lines are not evenly distributed over the spectral coverage. The exposure time of a ThAr frame is usually 20 s. A set of 5 bias and 12 flat-field frames is generally taken at the begin and/or at the end of an observing night, while the ThAr frames are taken as close as possible to the science exposure (see Section 3.4). All these calibration frames requires to be taken with exactly the same instrumental set-up in order to be employable in the reduction of the scientific data.

3.3 Instrumental configurations

The HRS gives access to many different configurations accordingly to the specific requirements of the observations. Stellar RV measurements are achieved by cross-correlating the observed spectra of the star with an opportune synthetic template. Generally speaking, the higher is the dispersion and the wider is the wavelength coverage of the spectra, the higher is the precision with which the RV can be measured. This is not always true considering faint sources (m_V >10). In order to achieve a spectrum at higher resolution keeping the same SNR, a longer exposure time is required (T_{exp} goes as the square of the spectral resolution). The upper limit on the exposure time, set by the HET structure (see Section 3.1), is the real constrain on the SNR achievable observing fainter targets and, hence, limiting the RV precision.

The parameters that define the HRS configuration employed for the acquisition of the observations related to the present work are here briefly described and discussed[2]. The values of the parameters chosen for the observations are also provided:

- **ResPower**: the resolution power can be set to different values: 15 000, 30 000, 60 000, and 120 000. Almost all the observations discussed within this work were performed at a resolution of 60 000. Only one set of data was taken at 15 000 (see Section 5.4);

- **Echelle**: the echelle value can be set to `blue`, `central` and `red`. These values set the echelle rotation angle for changing the position of the orders on the detector, primarily to move spectral features of interest off the CCDs defects. `central` is the default value and is intended to centre the orders on the detector. In practice, the blaze peaks are slightly to the red side of the CCDs. `blue` causes the wavelength approximately at the blue end of the orders to be moved to the centre of the CCDs. The blaze peak of the order (peak efficiency) moves near the red edge of the CCDs. `red` causes the opposite effect. The default configuration was employed along all the observations;

- **CrossDisp**: this parameter sets the rotation of the cross disperser to select which orders fall on the detector and variate the inter-order space (fundamental in case sky fibers are used). The movement defined by this parameter is orthogonal to the movement set by the *echelle* parameter. The observations performed without the use of sky fibers were taken with this parameter set to `316g5936` (the resulting wavelength coverage is 4076-7838 Å), while in presence of sky fibers the value `600g5271` was set (4275-6263 Å);

- **Fiber**: it is the angular diameter on the sky of the fiber to be used for feeding light from the telescope to the spectrometer. It can be set to `2″` and `3″`. The 2″ fibers were employed during the observations;

[2]For clarity, the names of the parameters are the same reported on the HET webpage *http://hydra.as.utexas.edu/?a=help&h=36*, where further information can be found.

- **SkyFibers**: it is the maximum number of sky fibers that can be used without orders overlap. It critically depends upon the values of *CrossDisp* and *fiber*. In the cases in which the sky subtraction was required, 2 sky fibers were used (see Figure 3.5).

- **GasCell**: `GC1` or `GC0` specify if the iodine gas cell must be kept respectively in or out of beam during scientific or flat-field calibration exposures. The main target of the WTS are the stars in the magnitude range m_J=13-16 (see Chapter 2.2). Such sources are too faint to allow the employment of the iodine gas cell as the RV precision is not limited by systematic effects (see Chapter 5);

- **Binning**: this parameter represents the CCDs (column binning)×(row binning), where the column binning is in the cross dispersion dimension and the row binning is in the echelle dispersion dimension. The widths of the orders for *fiber*=2″ is 13 pixels (assuming column binning equal to 1). The binning value is connected to the resolution of the observations. It was 2×1 and 2×5 for the observation of the spectra taken at 60 000 and 15 000, respectively. Column binning of 1 is not recommended because in that case the read-out noise per pixel rises by a factor ∼2 (and consequently the SNR per pixel halves) with respect, for example, to the 2×1 setting.

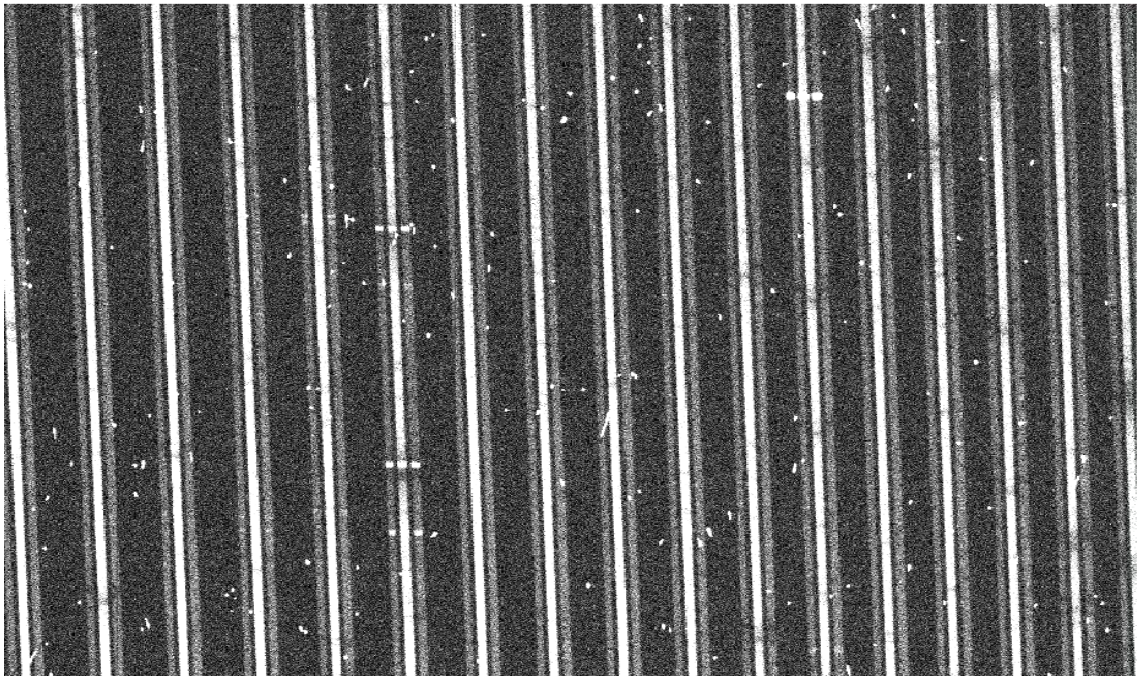

Figure 3.5: Example of a raw science frame measured with two sky fibers. The signal coming from the sky is visible as two stripes aside the central science spectral orders. During the exposure, the moon was only 60 ° away the observed star. Continuum, emission and absorption lines of the contamination sky spectrum are clearly visible.

The header OBJECT of each science file has the following format:

```
'target name' HRS_60k_central_316g5936_2as_0sky_IS0_GC0_2x1
```

and collects, in a single line, all the settings relative to the parameters just reported and described. This particular parameters combination is defined the *standard configuration* of the HRS and was used for almost all the observations when the sky subtraction was not required. The resolution and wavelength coverage related to this configuration (60 000, 4076-7838 Å) are ideal for the observation of a wide variety of stars (from M to F type, down to $\sim 16^{th}$ magnitude) and to measure with high-precision their RVs (see Chapter 5 for several examples reporting the values of the achievable RV precision). This configuration does not comprehend the employment of sky fibers as the sky contamination becomes significant only if faint object are observed and/or strong contamination sources (like the Moon) are close to the target star during the exposure.

In the cases where the subtraction of the sky contamination was required, two sky fibers and the cross disperser set to `600g5271` were used. The number of orders that fall on the detector with this configuration is lower as a larger inter-order space is required to host the two sky fibers without overlap. The spectral coverage of 4275-6263 Å allows to keep high the precision of the measured RVs. Most of the absorption stellar lines that allow to measure the Doppler shift are present in this bluer part of the stars spectrum. An example of a raw science frame taken with such configuration is reported in Figure 3.5. The contribution of the sky is visible as two stripes located aside the central science spectral orders. In this particular example, the moon was only 60 ° away the observed star during the exposure.

3.4 Visit types

Once observational time has been allocated by the Telescope Allocation Committee (TAC), the observation must be accurately programmed accordingly to the Phase II requirements. This is performed submitting a TSL (Target Submission Language) document where the project Principal Investigator PI submits a target list as an ASCII file (or several appended files). Each submission file is fundamentally structured as a series of blocks which contain parameter/value pairs defining all the information required during the data acquisition: the coordinates of the targets to be observed, the program at which the observation belongs, the instrumental configuration (see Section 3.3), the exposures time of science and calibration frames, the sky condition at the time of the observation and the overall structure of the visit.

The main visit structures adopted for the observation were two. The basic requirement for both was to get two ThAr calibration frames taken immediately before and after the science exposure. This strategy allows to keep under control any systematic effect which can occurs during the visit (see Chapter 4.3.7). The difference between the two types of visit consists in the optional split of the science exposure into two consecutive exposures (of half the exposure time each). This is recommended especially for science exposures longer than 30 minutes in order to reduce the cosmic-rays (CR) hits in each frame. The two basic visits structures (called for simplicity 'standard' and 'split' types) are therefore:

- **Standard visit**: ThAr1, science, ThAr2;
- **Split visit**: ThAr1, science1, science2, ThAr2.

All the frames taken within a visit are characterized by the same instrumental setup, as well as the flat-field and bias exposures which are usually taken at the begin and/or at the end of the nights. Due to the bias frames acquisition, only the Binning value must be the same of the other frames. Sometimes the visit structure can not be faithfully followed during the night. So it can happen, for example, that only one of the requested two ThAr frames is taken. As it will be discussed in the following two Chapters, the flexibility of the pipeline allows the data to be correctly reduced and analysed even in such cases. Usually 5 bias and 12 flat-field frames are taken along the acquisition of the calibration frames: they are combined into a master bias frame along the reduction of the data (see Section 4.2.2). The more exposures are used for the calculation of the master frames, the less noise will be introduced in the frame calibration phase.

Chapter 4

Reduction and analysis pipeline

Everything should be made as simple as possible,
but not simpler.

A. Einstein

Figure 4.1: Ancient Roman aqueducts in the Roman countryside. M. Cappetta©

4.1 Introduction

In this chapter the pipeline employed for the reduction and the analysis of the data is described and discussed. The first phase of the pipeline consists in the data reduction (DR). Generally speaking, DR usually refers to the extraction from raw files of the scientific information, corrected by any known source of systematics, and then stored in files in a suitable form. In this particular context, the scientific information we are interested in is enclosed in the position of all the absorption lines present in the spectra due to the stellar atmosphere. Several spectra of a target are observed at different epochs. The variation of the position of the stellar lines as a function of the time is the indirect signal of the presence of a stellar companion we want to detect. The first step in the reduction of the data is the filtering of the science frame in order to remove the CR hits. In case the exposure time of the science frame is longer than $\sim$10 minutes, the presence of the CRs becomes relevant and can affect the other steps of the DR and, as a consequence, also the final quality of the observed spectra. After the standard bias subtraction and flat-fielding of both the science and ThAr frames, the master flat-field frame is employed for the definition of the position and the inclination of all the echelle orders detected by the CCDs of the spectrograph. Next, the stellar and the ThAr spectra are extracted from the related frames. Each single spectral order is individually extracted. Throughout all the rest of the pipeline, the spectra extracted from all the single orders are kept separated. The ThAr spectra are then used for the definition of the dispersion function, which is required in order to assign a wavelength value to each pixel of the extracted stellar spectra.

The extracted and wavelength calibrated spectra can be considered the intermediate stage of the whole pipeline. They represent the output of the DR and the input of the following data analysis (DA). The aim of the DA is to transform the stellar spectra and make them ready for the measure of the position of the stellar lines, *i. e.* for the estimation of the RV values of the observed star. A cross-correlation (CC) between the observed spectra and a synthetic template allows to calculate the shift between the absorption lines in the observed and template spectra. This shift is first expressed in pixel and then is converted into a velocity value according to the Doppler law and the resolution with which the spectra were observed. A single RV measure is derived from each spectral order. For each epoch in which the target star was observed, the final RV estimate is computed from the set of RVs related to all the single spectral orders. Average and standard deviation are derived applying adequate statistical tools. In order to minimize the systematics that could affect the CC of the observed stellar spectra, several operations must be performed. First, as the quality of the spectra drops at the extremes, the initial and/or the final portions of the spectra are removed if the SNR is too low (SNR$\lesssim$4). Then, the continuum of the spectra is estimated in order to normalize the stellar spectra. This step simplifies the following removal of the CR peaks: taking advantage of the multiple observation of the same target, the spectra taken at different epochs are compared and the CR peaks, being randomly distributed over the spectral coverage and not falling at the same wavelength in all the spectra, are detected and removed. Next, the telluric lines are subtracted and finally the observed spectra are resampled to a common wavelength binning.

The procedure described in this chapter, the main considerations and all the figures are related to the reduction and analysis of the data taken with the standard instrumental set-up of the HRS (see Section 3.3). The files produced along the whole pipeline flow are organized and divided in several directories: the files in each directory represent the output of a given step and the input for the subsequent one. The reduction steps are performed using dedicated packages within the IRAF[1] environment. IRAF provides a wide variety of tasks fitting several different reduction and analysis requests within many fields of astronomy. In order to speed up the reduction process, the IRAF tasks are employed with specific scripts which can be run in the IRAF prompt. Such IRAF scripts, created using SHELL scripts, manage the flow of the input data, execute the required task and finally save the output files with the specified format and names. Custom MATLAB programs were instead created along this project in order to execute the analysis steps described above. Such programs are optimized to perform automatically the different phases of the analysis but allow the user to control the results and, if required, to correct the output of the programs.

Few preliminary operations must be done before the reduction of the data. The main two are i) the split of each file coming from the HRS in the red and blue components (see Section 3.2) which are saved into two distinct files and ii) the computation of the velocities of the McDonald observatory in the heliocentric rest frame at the epoch of each observation and projected along the direction of the observed star. The trajectory and the velocity of the observatory in the heliocentric rest frame is the result of the sum of three different movements: the rotation of the Earth around its proper axis, the rotation of the Earth around the Earth-Moon centre of mass and the revolution of the Earth around the Sun. The overall movement introduces a Doppler shift in the observed spectra of the order of few tens of km s^{-1} (up to $\sim$60 km s^{-1}) which varies on time-scales of $\sim$6 months. Hence, in order to detect an expected signal of few tens of m s^{-1}, the Doppler shifts due to the motion of the observatory must be accurately estimated at the time of the observations and subtracted to the measured RVs. Both these operations are performed using dedicated IRAF tasks.

[1] IRAF is distributed by National Astronomy Observatories, which is operated by the Association of Universities of Research in Astronomy, Inc., under contract to the National Science, USA.

4.2 Data reduction

4.2.1 Cosmic-rays filtering

When the exposure time of a science frames is longer than ∼10 minutes, the effect of the CRs hits can influence the following steps of the DR and affect the quality of the scientific data. Realistically, the integration time of a scientific exposure is limited to about 30 minutes due to the contamination of the CRs. The IRAF task `crutil.cosmicrays` allows to filter an input frame for the CR hits. CR events in each input image are detected and replaced by the average of the four neighbours. The task allows to remove all the pixels where the saturation level was reached due to the energy released by the cosmic particle. Almost all (∼ 80%) of the peaks that do not reach the saturation level are removed from the inter-order space too. The task is less efficient in the removal of the lower non-saturated peaks that fall on the echelle orders, where the stellar spectrum is measured by the CCD. Most of such CR hits are left and are consequently present in the extracted spectrum too. They are removed along the following DA taking advantage of the multiple observation of the same target taken at different epochs (see Section 4.3.4).

4.2.2 Frames calibration

The frame calibration is a standard procedure that removes the bias applied during the read-out of the data from the detector, as well as to fix tiny defects of the camera and of the optical system. As already reported in Section 3.2, a set of 5 bias and 12 flat-field frames is generally taken at the begin and/or at the end of an observing night with the same instrumental setting employed for the science and ThAr exposures. The master bias and the flat-field frames (both the red and the blue components) are obtained stacking the respective sets of the single bias and flat-field frames. The IRAF tasks `ccdred.zerocombine` and `ccdred.flatcombine` allows to combine and stack these two sets of frames in order to reduce the noise related to each single pixel of the master frames by a factor $\sqrt{5}$ and $\sqrt{12}$ respectively.

The master bias allows to measure the amount of digital units (ADU) added to all the frames recorded by the CCDs of the HRS during the read-out phase in order to avoid null or negative counts numbers (see Section 3.2). This bias level introduced during the read-out is removed simply subtracting from all the frames the master bias. The bias levels of the master red and blue frames are 509.9 ADU and 499.4 ADU respectively. These two values are constant over a time-scale of several years. The noise introduced by the different sensitivity to the photons of each pixel can be eliminated by applying the flat-fielding correction to the frames. This operation consists in the pixel-by-pixel division of the image to be calibrated by the master flat-field frame. Both the pixel-scale variation due to the different pixel efficiency and the intra-order blaze function (the smooth efficiency profile variation along each order) are corrected. The effect of this inter-order fringing noise can be quantified in the drop of the SNR of the extracted spectra by ∼10%. As a consequence, the SNR of a spectrum extracted from a calibrated frame results higher by ∼10% with

respect to that extracted from a non-calibrated one. The IRAF task `ccdred.ccdproc` allows to perform the calibration of a given frame, that is the bias subtraction and the flat-field correction as just described above. The master bias is subtracted from the master flat-field frame before its employment.

The 'HET Data Reduction Tips' webpage[2] report another recipe for the use of the master flat-field frame: an intermediate frame is created with the IRAF task `echelle.apflatten`. This frame is then used for the correction of the inter-order fringing only during the calibration of the science and ThAr frames. This procedure is usually preferred as the pixel values keep their linear dependence to the signal of the observed source (*i. e.* the number of photons). Such condition is not required for our purposes during the DR. In particular, because the spectra are subsequently normalized at the beginning of the following DA. In the calibration of the data related to this work, the direct employment of the master flat-field frames was preferred as it allows to remove also the blaze-function profile along each single spectral order. The overall transmission efficiency has a drop at the extremities of each orders down to ∼20% of the efficiency in the central part of the order. The removal of the inter-order transmission efficiency profile has three main effects:

- the rescue of the fainter ThAr emission lines at the edges of each order;
- the removal of the distortion of the ThAr emission lines due to the different slope of the blaze function along each single order;
- a much flatter continuum of science extracted spectra.

The first two consequences allow to get a better estimation of the dispersion function with the use of the extracted ThAr spectra (see Section 4.2.5). Concerning the third, the continuum of the science spectra depends only on: i) the true source continuum (for example a black body emission in case of a star) and ii) the deviation of the spectrum of the white-lamp from a pure flat spectrum. In any case, the resulting continuum of the scientific extracted spectra is much easier to be normalized during the following DA (see Section 4.3.2). It is worth noting that the SNR of both the observed stellar and ThAr spectra do not depend on the way the frame calibration is performed.

4.2.3 Apertures definition

Accordingly to the ECHELLE type design of the HRS, the spectrum of an observed target is broadened in both the X and Y directions above the detectors (see Section 3.2). Each diffraction order of the grating element leads to one of the stripes visible in the frames. These strips are generally called 'orders', as each of them is univocally related to a diffraction order, or 'aperture', accordingly to the IRAF context. The determination of position, thickness and inclination of each aperture is fundamental for the correct extraction of the spectra from the science and ThAr frames. Only the values of the pixels receiving the light coming from the observed target or the calibration lamp must be considered for the estimation of the spectral flux (see Section 4.2.4).

[2] *http://hydra.as.utexas.edu/?a=help&h=29#HRS*

Apertures position

The IRAF task `echelle.apedit` allows to define and edit interactively the apertures of the reference frame given as input to the task. The reference frames are the red and blue master flat-field frames. Figure 4.2 reports an example of the graphic interface with which the user can define the echelle orders. The plot shows the profiles of all the apertures across the whole length of the detector perpendicularly to the dispersion axis. The task automatically computes the centroid position of the apertures and the related limits.

The number of apertures present on the red and blue components depends on the configuration of the cross-disperser of the HRS. In the standard configuration the cross-disperser `316g5936` is used (see Section 3.3), and the apertures to be defined are 24 in the red component of the detector and 40 in the blue component. The corresponding diffraction orders are 78^{th} to 101^{st} and 103^{rd} to 142^{nd} for the red and blue components respectively. The diffraction order 102^{nd} is lost as it falls onto the junction between the two CCDs that form the detector. The number of aperture defined in the blue CCD is limited to 40 as the further 6 apertures falling inside the detector start to overlap. The overall throughput

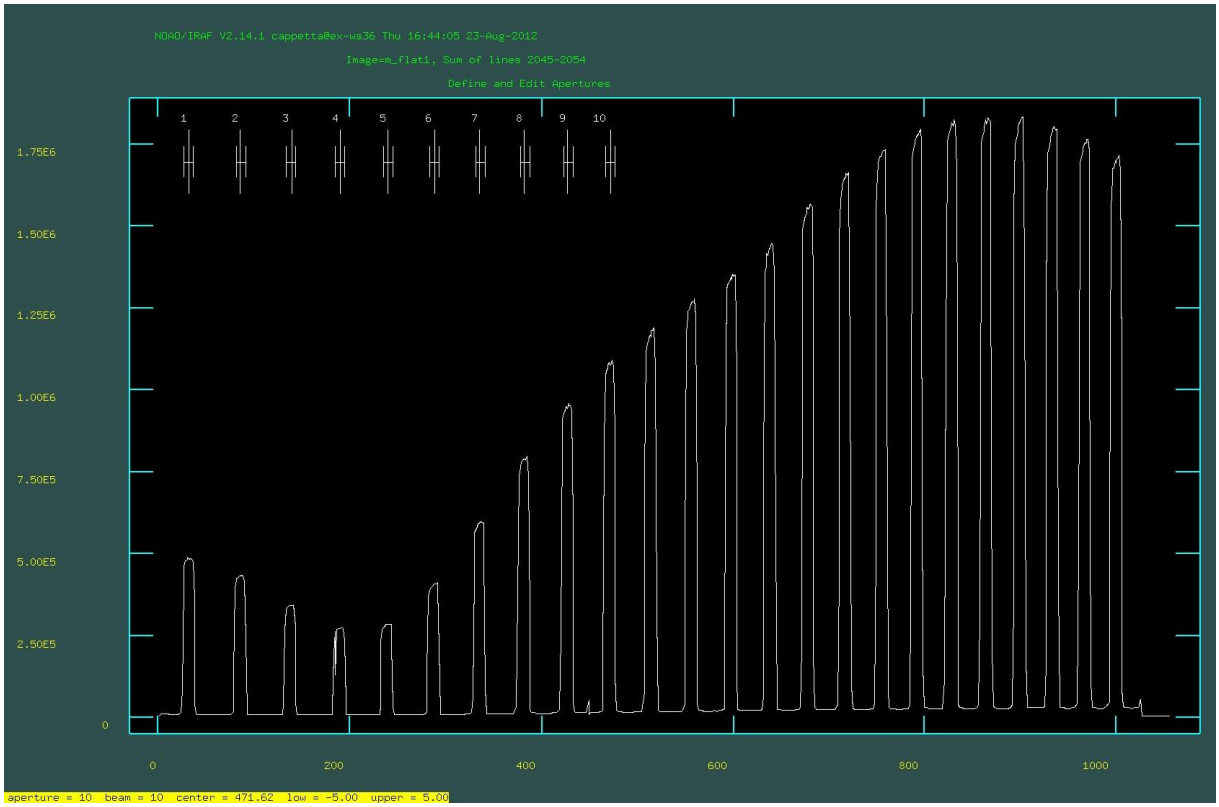

Figure 4.2: Definition of the apertures position and size on the red component of the detector performed with the IRAF task `echelle.apedit`. The operation of definition of the apertures is not complete as only the first 10 apertures are marked. The apertures on the red component are 24 if the cross-disperser `316g5936` is employed.

of the HRS for those apertures is ∼60 times smaller then its maximum efficiency, while the spectral coverage related to these apertures is 4080-4280 Å. The inter-order distance decreases as the order number grows. The distance between the last 6 orders is equal or smaller than the thickness of the orders itself. The definition of these apertures results difficult due to the overlap between the different apertures. Furthermore, the extracted spectra can suffer the contamination of the spectra related to the nearby apertures.

Apertures tracing

Once position and size of the apertures across the dispersion axis are defined, the inclination and the curvature of the orders must be determined along the dispersion axis. The IRAF task `echelle.aptrace` allows to trace and fit interactively the apertures of the reference frame given as input which are the same red and blue master flat-field frames employed previously. When the task is executed a graph appears showing the pattern across the frame of all the points, indicated by crosses, recognised to belong to the first aperture. An

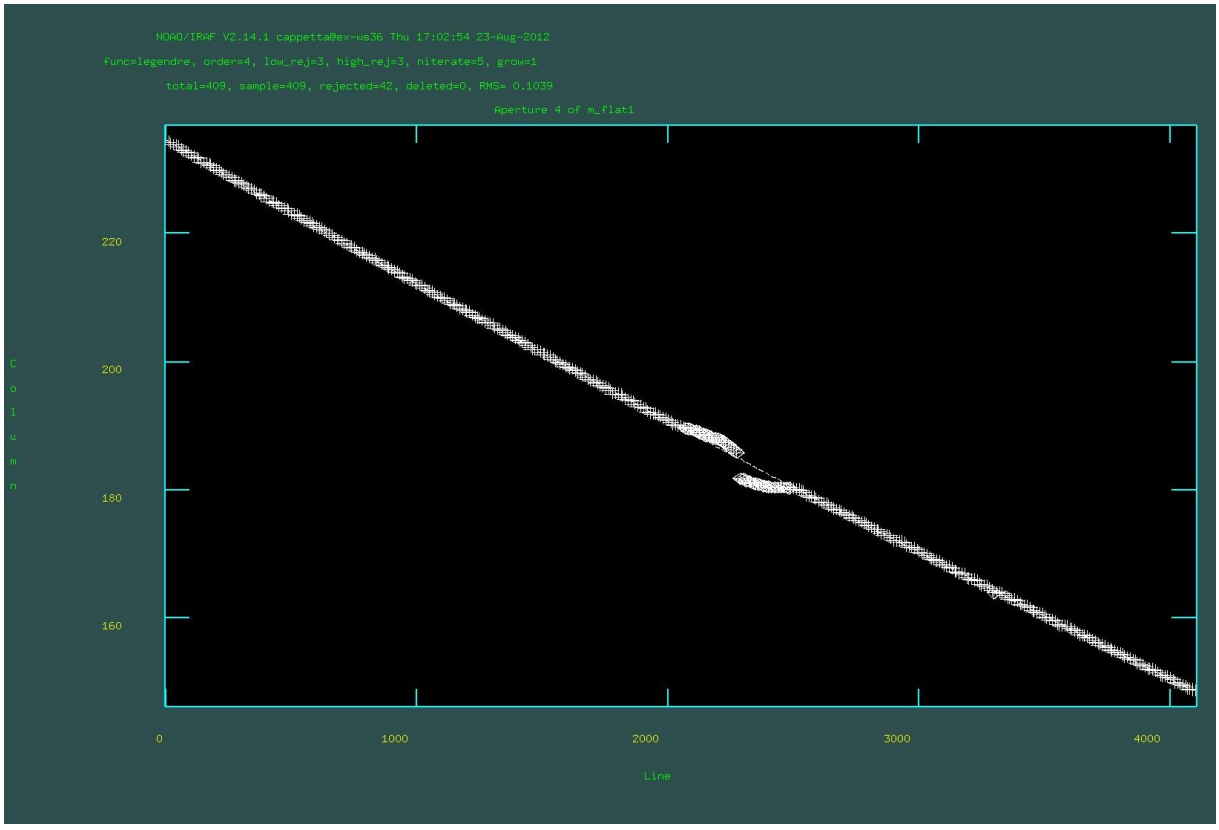

Figure 4.3: Aperture tracing performed with the IRAF task `imred.echelle.aptrace`. A low order polynomial fitting overcomes tracing problems that could rise due to dark columns or bad pixels along the apertures. In this example, a dark column crosses the echelle order at about 2200 pixels.

example is reported in Figure 4.3. The fit of the traced point positions with a 4^{th} degree Legendre polynomial function may be performed interactively. The best-fitting models can be estimated excluding one or more portions of the apertures. Several different sources of noise can so be excluded during the fitting procedure. In two cases the range taken into account by the fit should be reduced:

- when an echelle aperture does not fall completely inside the CCD (for example the 1^{st} or the 24^{th} orders in the red component).
- when the apertures are particularly faint and/or close each over. This is the case proceeding toward the left hand side of the blue component, where the instrumental throughput and the inter-order distance critically decrease (orders 35^{th}-40^{th} in the red component).

The parameters of the best-fitting function are saved and used to fully define the shape of the apertures. The whole set of quantities estimated during the definition of the apertures allows to know exactly which pixels must be considered for the extraction of the spectra from the scientific and ThAr frames (see Section 4.2.4).

4.2.4 Spectra extraction

The following step of the DR consists in the extraction of the spectra from the calibrated scientific and ThAr frames. The information related to the orders, defined in the previous step of the reduction, determines univocally which pixels contribute to the computation of the flux of the extracted spectra. The IRAF task `echelle.apall` permits to extract the spectra related to each single order in the input frame. The extraction algorithm can be customized according to the instrumental settings employed during the observations. Several corrections can be applied to the extracted spectra. The sum of the contributions of the pixels within the width of the aperture (across the dispersion axis) defines the flux value of the spectrum in that particular position along the order. This operation is repeated for each line of the frame, that is for each position along the dispersion axis. The final spectrum consists in a sequence of flux values (expressed in ADU) as a function of the position along the order (expressed in 'pixels'). In this context, the flux is not related to a physical quantity (for example a spectral flux density expressed in $erg\ s^{-1}\ m^{-2}\ \mathring{A}^{-1}$) of the observed signal. The lengths of extracted spectra equal the dimension of the input frame along the dispersion axis, that is 4100 pixels. The spectra related to the single orders are extracted separately and kept distinct in the final output files.

An example of an observed extracted spectrum related to the 16^{th} red order is plotted in Figure 4.4. As it can be seen, the continuum of the spectrum is particularly flat thanks to the choice regarding the flat-fielding step in the frame calibration (see Section 4.2.2). Accordingly to the instrumental throughput profile along each order, the SNR follows a bell trend: it has its maximum roughly in the middle of the order and decreases toward the extremities. The SNR of a spectrum can be computed considering a portion free by absorption lines, computing mean value and standard deviation of the flux in that portion

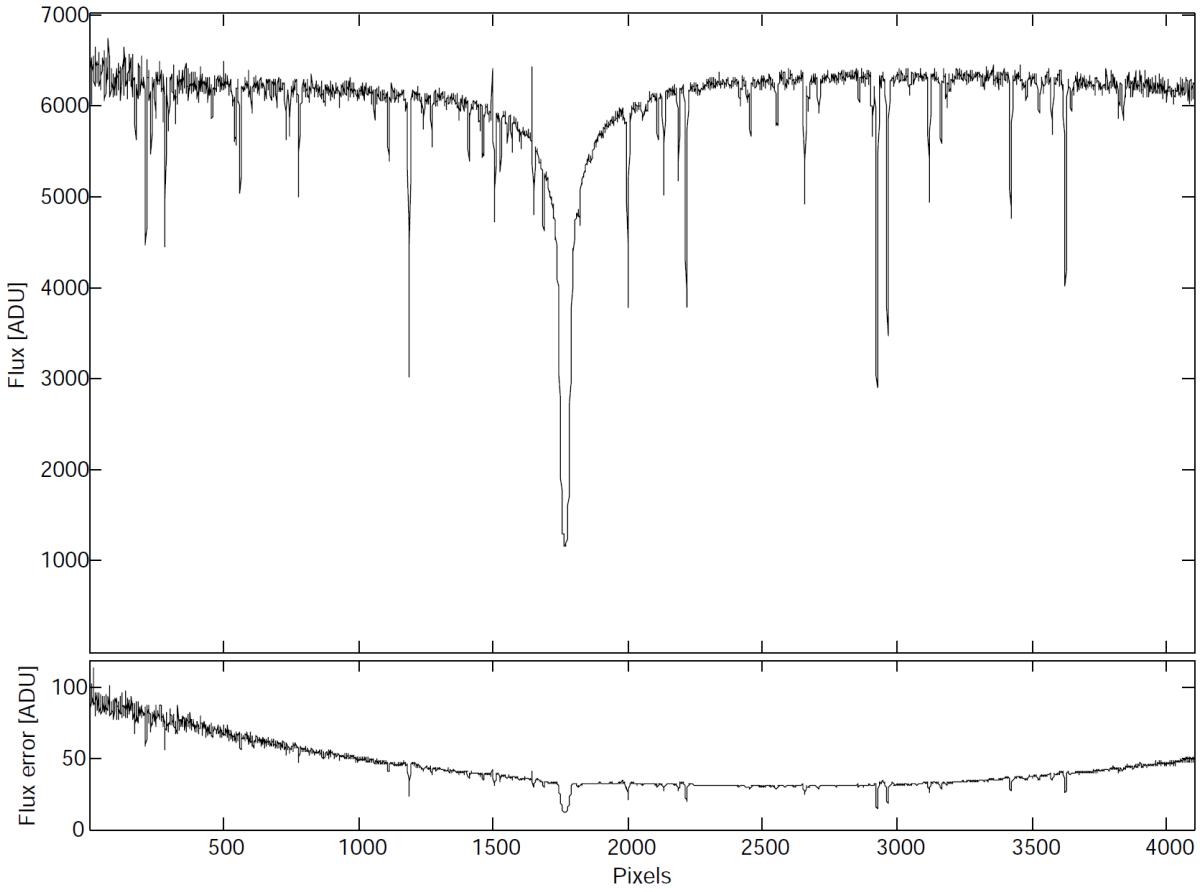

Figure 4.4: Flux (upper panel) and flux uncertainty (lower panel) related to a single echelle order (16^{th} red order) extracted with the IRAF task `echelle.apall`. The continuum of the extracted spectrum is particularly flat thanks to the particular flat-fielding procedure.

and taking the ratio between these two quantities. Providing the *gain* and the *readout noise* of the camera of the HRS (0.68 e^-/ADU and 2.8 e^- respectively, Hill et al., 2010), the IRAF task can compute the flux f and the associated uncertainty σ_f too. The flux error reported in Figure 4.4 was estimated propagating the uncertainty computed by the IRAF task and considering the division of the science frame by the master flat-field frame performed during the frame calibration. Dividing pixel-per-pixel f and σ_f gives another estimate of the SNR of a spectrum. These two methods bring to perfectly comparable measures of the SNR of a spectrum. This result was checked considering a variety of spectra characterized by a SNR ranging from 5 to 200.

As the knowledge of the pixel-per-pixel flux uncertainty is not required in the following steps of the pipeline, the task was employed for the computation of the flux only. Furthermore, this allowed to reduce the computing time required by the task and to reduce the amount of data created along this step of the DR. In order to quantify the quality of the spectra related to the observed target (see Chapter 5), the SNR was computed considering

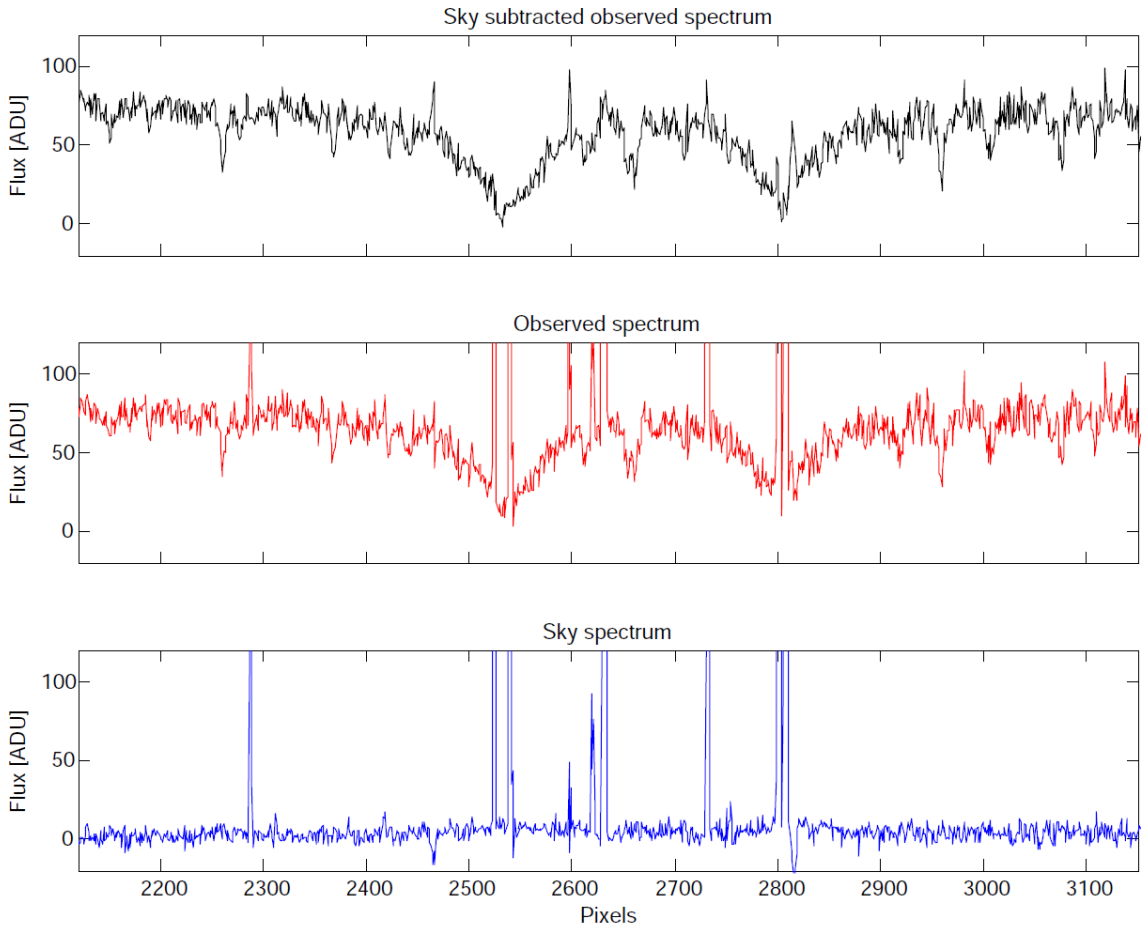

Figure 4.5: Example of the effect of the sky spectrum (lower panel) subtraction from the observed spectrum (middle panel). The resulting spectrum related to the target star only is plotted in the upper panel. The exposure time of the science frame was 1800 s.

the spectral portions free by absorption lines as described above.

If the instrumental set-up of the HRS involves the use of sky fibers (**SkyFibers**=`2sky`, see Section 3.3), then the contamination due to the sky emission can be removed from the extracted science spectrum. In this case, the task allows to extract the spectral signal related to the two sub-apertures located 11 pixels away on both sides of the science spectral orders (see Figure 3.5 in Section 3.3). The spectra registered within these two sub-apertures are the spectra of the sky observed in two positions in the observed science target neighbourhood. These two sky spectra are extracted similarly to what performed for the science spectrum. The average between the sky spectra spectra is computed and finally subtracted from the science spectrum. Such procedure is repeated for all the apertures previously defined. Figure 4.5 reports an example of the resulting observed spectrum after the subtraction of the sky spectrum. As it can be seen in the lower panel, the sky spectrum consists mainly in the strong and sharp sky emission lines and a noisy background with

an average value of about 5 ADU. The RMS of the sky spectrum, considering the noisy background regions only, is ∼3 ADU. This amount must be summed in quadrature with the flux uncertainty of the extracted observed spectrum in order to estimate the noise of the corrected stellar spectrum. The statistical noise due to the lower SNR of the corrected spectrum increases the uncertainties on the final computed RVs of few m s^{-1}. On the other hand, systematics shifts on the measured RVs due to the over-imposed sky spectrum can be as large as ∼100 m s^{-1}. The main source of contamination during a scientific exposure is the solar spectrum reflected by the surface of the Moon. The absorption lines of this contaminating spectrum affect the RV values as they are generally shifted with respect to the absorption lines of the observed star. Other sources of contamination could be present if the observed target lies in a crowded field. Sky subtraction is desirable in case the observed target is particularly faint (m_V $>12^{th}$) and/or the spectra are used for chemical abundances analysis.

Both the scientific and the ThAr spectra must be extracted from the related frames. The ThAr red and blue spectra play a key role in the next step of the DR.

4.2.5 Wavelength calibration

The wavelength calibration of the extracted science spectra represents the most critical phase of the DR. It actually comprises two steps: the computation of the dispersion function (DF) and its following application.

The DF allows to assign a wavelength value to each pixel of the extracted science spectra. Each single echelle spectrum is related to a given echelle order. Both the number associated to this order and the position of the pixel along the spectrum are mapped into the wavelength to be assigned. So, the DF has two variables as input and the wavelength value as output. This relation is usually expressed by the following formula:

$$\lambda = \frac{f(o,x)}{o} \tag{4.1}$$

where o is the number of the order, x is the position of the pixel along the order, and f is a bidimensional polynomial function. The terms $\frac{1}{o}$ present in the right hand side of the equation comes from the relationship between the central wavelength of an order and the related order number[3]. In order to estimate a DF, the extracted ThAr spectra can be employed. The positions (expressed in pixels) of the ThAr emission lines can be defined computing the centroids of the lines, while the associated central wavelength are tabulated and are a priori known from the theoretical atomic physics. An example of ThAr spectrum, related to the 99^{th} echelle order, is reported in Figure 4.6. This plot belongs to the 'HET HRS ThAr and Echelle Tilt Atlas'[4]. This document contains detailed information relatively to all the 100 echelle orders (from the 56^{th} to the 155^{th}) measurable with the different configurations of the HRS. As it can be seen in the figure, some lines are

[3]Empirically, $\lambda_c = 611400/ord$.

[4]The document is downloadable from the webpage *http://hydra.as.utexas.edu/?a=help&h=38*.

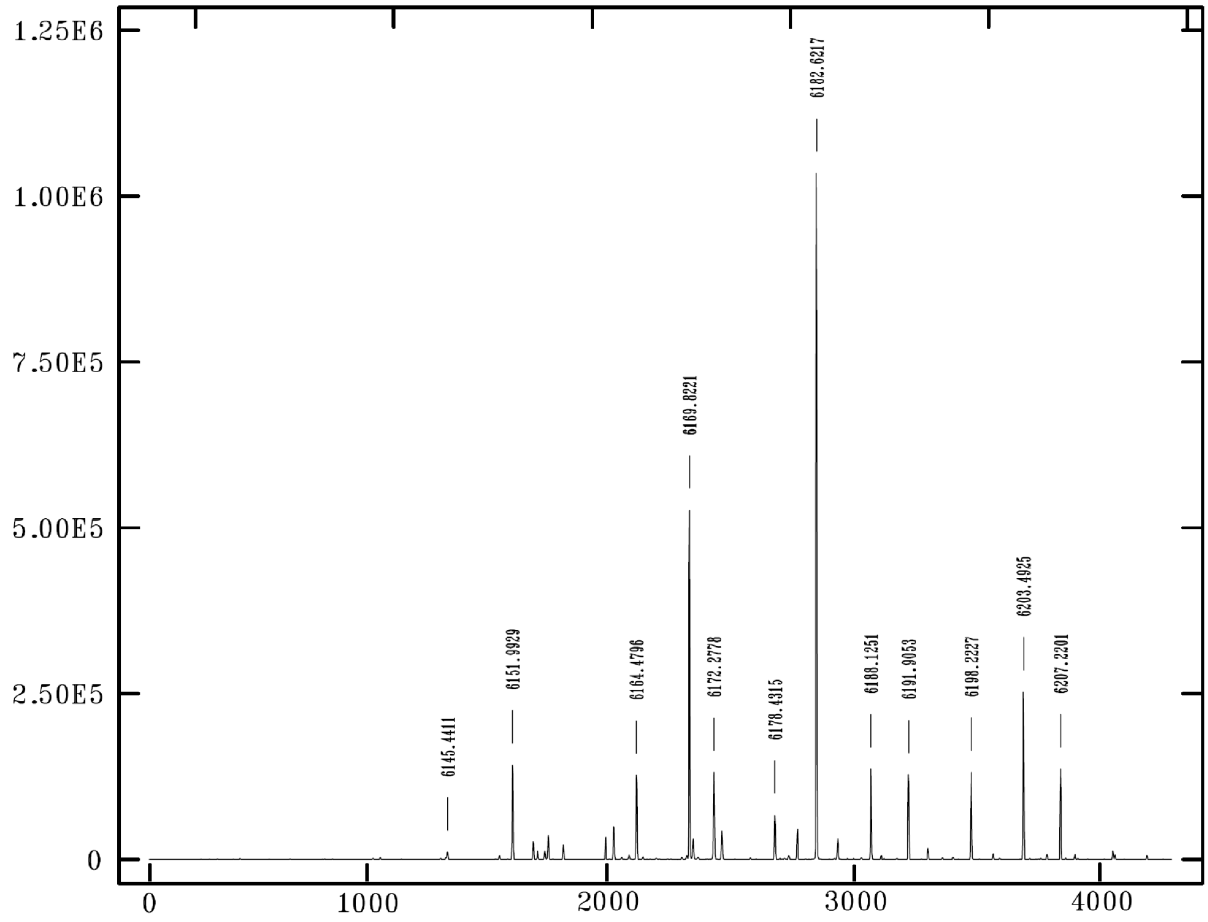

Figure 4.6: Template plot of one of the red ThAr spectral orders as reported in the atlas of the orders detectable with the HRS. The measured flux of the ThAr spectrum is as a function of the pixels along the echelle order.

marked and the related theoretical central wavelength (expressed in Å) is reported. Each emission line in the different ThAr spectral orders provides a point in the 3D space defined by o, x and λ_c. The distribution of all these points can be parametrized with the model expressed by the equation reported above. Then, the parameters related to the best fitting model can be employed for the definition of the DF with which to perform the wavelength calibration of the science spectra.

The IRAF task `echelle.ecidentify` allows to operate as just described employing the ThAr extracted spectra to generate a set of points in the (o, x, λ_c) space and computing the best fit polynomial function f. A first set of emission lines must be identified and tagged by the user. Then the task automatically recognises the other lines until almost all the detectable and unblended lines are involved in the best-fitting procedure. Once the best-fitting parameters of the bidimensional polynomial function are computed, the residuals, that is the difference between the fitted central wavelength and expected theo-

Table 4.1: Main parameters of the final DFs solutions for the red and blue components: total number of orders, initial number of lines marked by the user, final number of lines automatically tagged and RMS of the residuals are reported.

Component	Number of orders	Initial number of lines	Final number of lines	RMS
Red	24	~ 80	~ 1000	0.0035 Å
Blue	40	~ 150	~ 2200	0.0029 Å

retical wavelength of a single line, are computed. Several parameters can be set to define the fitting function *f*. The main two are the orders of the polynomial along the o and x directions. In the course of the task interactive loop, these and other parameters can be changed in order to minimize the RMS of the residuals. The lower is the dispersion of the residuals (quantified by the value of the RMS), the better is the computed DF. Two distinct DFs must be computed considering the ThAr spectra extracted from the red and the blue component of the detector. These two DFs are then employed for the wavelength calibration of the red and the blue set of scientific extracted spectra. The best results, for both the DFs related to the red and the blue components, were obtained with the orders of the polynomial along the o and x directions set respectively to 5 and 7. The main parameters of the final DFs related to the red and blue ThAr spectra are reported in Table 4.1.

The RMS of the residual allows to estimate the systematic uncertainty introduced by the use of this particular technique to perform the wavelength calibration of the spectra. Supposing that all the other systematic sources of noise are removed during the other steps of the pipeline and that the statistical noise is negligible, the RV values can not be measured with an error[5] smaller than $\sim 3\,\mathrm{m\ s^{-1}}$. The use of the master flat-field frame during the frame calibration, removing the inter-order blaze function (see Section 4.2.2), allows to rescue of the fainter ThAr lines at the extremities of each spectral order and to remove the distortions due to the blaze function itself. Both these results bring to a more precise estimation of the DFs. The RMS of the residuals is smaller by a factor $\sim$25% with respect to the case in which the ThAr spectra are not corrected for the blaze function.

The computation of the DFs is the core step of the whole DR: even small imperfections of the dispersion solutions critically influence the final RV measurements. The following step consists in the actual wavelength calibration of the extracted science spectra, performed by the IRAF task `echelle.dispcor`, employing the computed DFs. The application of the DF allows to assign a wavelength value to each pixel of a spectrum. The difference between the wavelengths of two adjacent pixels increases linearly within each single spectral order. In order to achieve a constant wavelength binning over the whole

[5] Assuming a mean RMS value of 0.003 Å, 6000 Å as the central wavelength of the whole observed wavelength range and a total of about 3000 lines, the RV uncertainty can be computed as $(c \cdot \frac{0.003}{6000})/\sqrt{3000} \sim 3\,\mathrm{m\ s^{-1}}$.

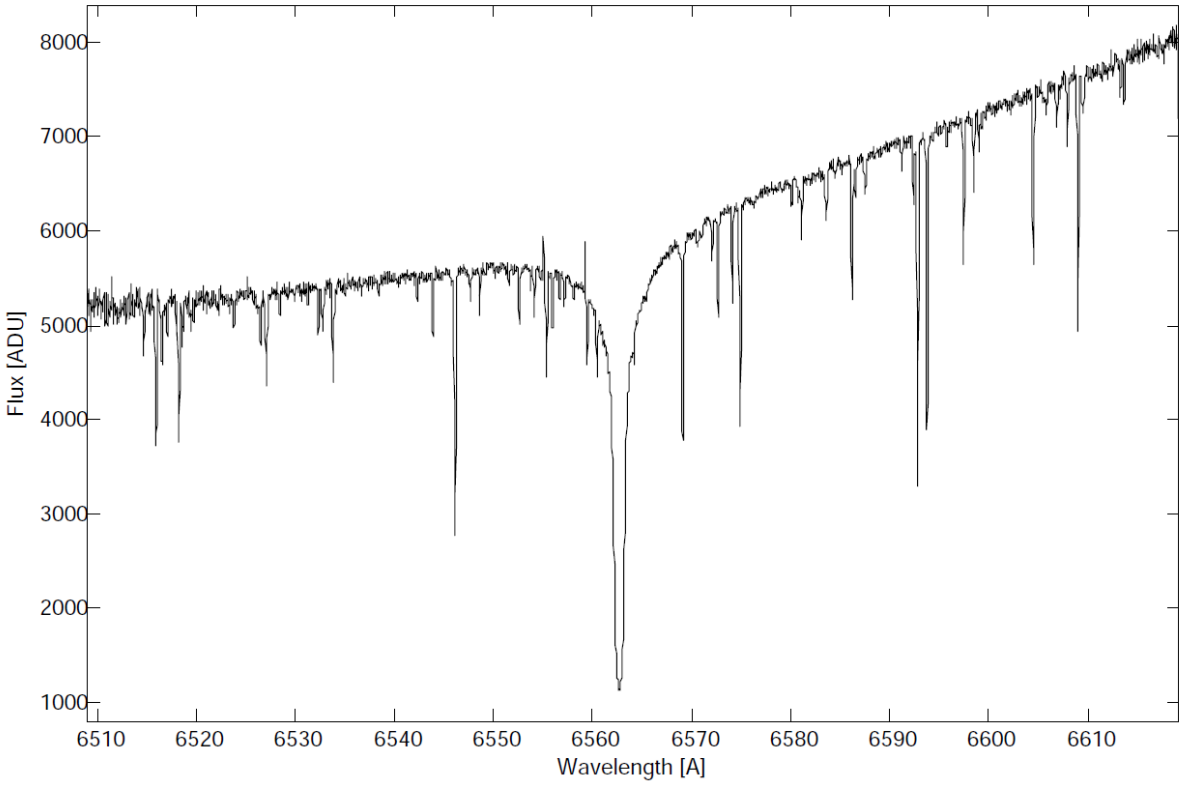

Figure 4.7: Example of an extracted wavelength calibrated spectrum. The spectrum is the same shown previously in Figure 4.4. The different trend of the continuum is due the conservation of the spectral flux density during the wavelength calibration phase. The wavelength calibration of the spectrum allows to identify the stronger absorption line at $\sim$6563.35 Å as the Hα Balmer series line.

wavelength range, each spectrum must be resampled. The conservation of the spectral flux density (flux per unit of wavelength) introduces a smooth increasing trend in the continua of the extracted spectra. The wavelength step is constant within each single spectral order but decreases from the redder to the bluer orders as the resolution power is constant. An example of a wavelength calibrated spectrum is reported in Figure 4.7. The order spectrum shown in the figure is the same reported previously in the upper panel of Figure 4.4. The strongest absorption line visible roughly in the centre of the spectral coverage can be now be identified as the Hα Balmer series line. The different continuum trend introduced by the resample of the spectrum after the wavelength calibration can be noted.

In case of 'standard visit', the ThAr calibration exposures are two (ThAr1 and ThAr2, see Section 3.4). For both, the DFs must be computed and consequently applied. This leads to two different sets of wavelength calibrated spectra starting from the only set of science extracted spectra. All the steps in the following DA are performed for both these two sets of wavelength calibrated science spectra. The final RV values related to the two different

wavelength calibrations, if no unexpected systematics occurred during the observations, are consistent within the uncertainties.

A preliminary check of the absolute wavelength calibration of the scientific spectra could be performed searching for the brightest sky emission lines in a stellar spectrum. Mainly due to the neutral Oxygen O I in the Earth atmosphere, the sky lines can be identified and fitted with a Voigt profile. Comparing the measured central wavelength of each line with those present in a stellar spectrum observed with HARPS, an overall redshift of few hundreds of m s^{-1} was measured. Each single central wavelength value was measured with a precision of few thousandths of Å, corresponding to $\sim$100 m s^{-1}. Unfortunately, the uncertainties related such redshift of the sky lines positions were too large to compute the shift to be applied to the HET spectra in order to correct for any imprecisions of the wavelength calibration. Being this small off-set between the expected and the measured wavelengths constant over the whole spectral coverage, no drift are introduced in the RV values obtained from the different spectral orders. As the orbital parameters of a stellar companion do not depends on the systemic velocity off-set required to fit the RV data, such systematic shift does not affect the characterization of any new discovered stellar companion.

A better estimation of the zero point RV correction of the HRS spectra calibrated with ThAr spectra is derived in Section 5.1.4. Further considerations and possible explanation of the physical reasons of this off-set are also reported. The knowledge of this quantity allows to combine the RV measurements with those achieved with other instruments involved in the detection and in the characterization of extrasolar planets with the RV method.

4.3 Data analysis

4.3.1 Crop of the spectra

As already discussed in Section 4.2.4, the SNR of the observed spectra is not constant over the whole spectral coverage. If the observed star is particularly faint and/or the exposure time is limited, the SNR at the extremes can be as large or smaller than 4. In such a regime, the noise hides the stellar absorption lines. Furthermore, the quality of the spectra drops critically at the extremities of the spectral coverage if the related aperture partially falls outside the edge of the CCDs. Such portions of spectrum, where the noise (both statistical and/or systematic) dominates over the signal, can critically contaminate the RV measurements. In order to obtain the highest precision and accuracy of the RVs from the observed spectra, all the sources of possible contamination must be removed.

The MATLAB program `CROP_SPECTRA` allows to visualize all the spectra, measured at different epochs, related to the same spectral order. Then, a common range free from

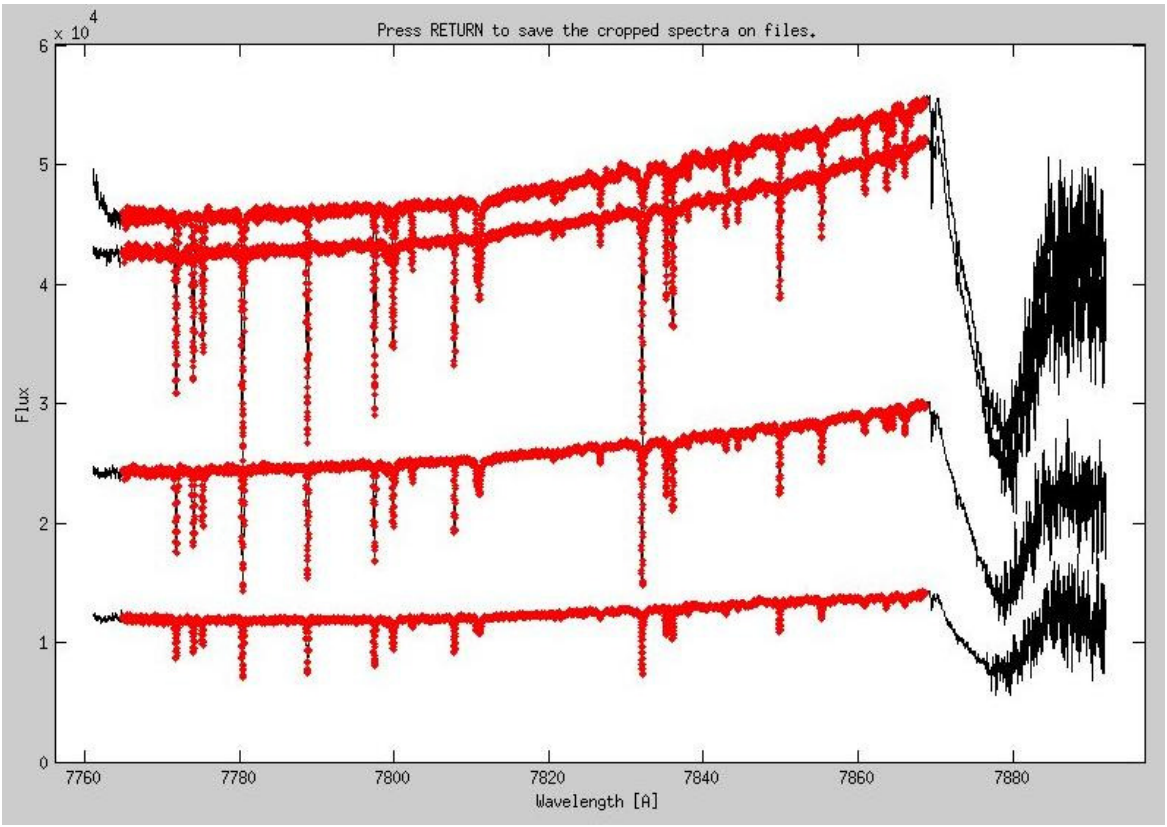

Figure 4.8: Final stage of the valid wavelength range selection. The exit of the echelle orders from the surface of the CCD can be clearly seen as a sudden linear drop of the flux followed by a pure noise region. The valid portion defined by the user and saved on the output files is highlighted in red.

Table 4.2: Wavelength ranges defining the valid portion of each spectral order.

Red orders	Range [Å]	Blue orders	Range [Å]	Blue orders	Range [Å]
1	7760.7-7868.1	1	5826.8-5917.8	21	4894.9-4963.7
2	7662.7-7791.7	2	5770.6-5861.5	22	4854.1-4922.6
3	7567.9-7694.2	3	5713.2-5807.3	23	4819.2-4884.3
4	7473.7-7593.0	4	5663.1-5752.8	24	4780.5-4846.9
5	7383.1-7506.7	5	5613.2-5699.7	25	4746.4-4806.1
6	7293.4-7416.5	6	5560.5-5647.5	26	4710.8-4770.8
7	7207.7-7328.1	7	5507.1-5596.1	27	4670.6-4735.1
8	7122.8-7241.9	8	5459.6-5545.5	28	4641.6-4697.9
9	7040.5-7157.4	9	5411.8-5496.1	29	4601.5-4663.0
10	6958.1-7075.1	10	5366.1-5446.1	30	4569.8-4628.3
11	6880.2-6995.2	11	5322.7-5399.1	31	4536.6-4593.3
12	6801.9-6916.2	12	5277.7-5352.6	32	4502.8-4559.3
13	6726.0-6839.4	13	5228.6-5306.4	33	4472.0-4525.7
14	6652.1-6764.3	14	5186.8-5261.2	34	4437.1-4493.2
15	6579.8-6690.4	15	5137.8-5216.7	35	4411.4-4460.6
16	6509.0-6619.0	16	5095.6-5170.3	36	4378.6-4428.2
17	6439.9-6548.3	17	5054.9-5129.8	37	4349.2-4396.7
18	6371.9-6479.6	18	5011.1-5086.0	38	4316.2-4365.3
19	6305.6-6412.3	19	4974.7-5045.0	39	4283.5-4334.4
20	6241.2-6345.9	20	4932.6-5004.5	40	4256.9-4301.5
21	6178.1-6276.4				
22	6114.5-6217.4				
23	6054.6-6155.8				
24	6020.6-6094.8				

any type of contaminations can be selected and the observed spectra are consequently cropped. An example of such a operation is reported in Figure 4.8. The peculiar features visible on the right side of the spectra (a sudden linear drop followed by a pure noise region) correspond to the exit of the echelle orders from the surface of the CCD. The corresponding wavelength range is removed and will not belong any more to those spectra. All the spectra related to the 24 red and the 40 blue orders are cropped in order to extract only the valid portion of spectra. In Table 4.2, the wavelength ranges of all the observed cropped spectra are collected. As it can be seen, the valid wavelength range of each spectral order partially overlaps with the ranges of the previous and following orders. One spectral order is lost as it falls in the gap between the two CCDs of the camera of the HRS (see Section 3.2). The missing order causes a gap of ~ 100 Å in the observed wavelength range. This happens with all the possible configurations of the cross disperser.

4.3.2 Spectra normalization

As the scientific information of interest resides in the absorption lines generated in the stellar atmosphere, the spectral continuum plays no role and, therefore, can be eliminated from each spectrum. The continuum is basically the black body emission of the stellar interior distorted by the residual of the optical blaze function and the quantum efficiency profile of the CCDs, not completely corrected during the calibration phase (see Section 4.2.2). Furthermore, the normalization of the spectra allows to apply the following steps of the DA (mainly the telluric lines removal and the CR peaks filtering) in a much easier way.

The continuum can be removed from a spectrum simply dividing the spectrum by an estimate of the continuum itself. To compute a function that estimates the continuum is not an easy task due to the presence of the absorption lines. These lines are due both to the outer layers of gas of the star and the different chemical species present in the Earth atmosphere (in particular water vapour). Two MATLAB programs allows to estimate the continuum of the spectra in two different ways: `CONT_AUTO` estimates automatically the continua while `CONT_USER` is based entirely on the user control for the definition of the continua. The first program is generally faster and more efficient. The latter is instead preferable in case of spectra with low SNR or over-crowded of lines (the bluer spectral orders shows both these feature).

Automatic continuum estimation

The MATLAB program `CONT_AUTO` automatically estimates at once the continua of all the spectra, measured at different epochs, related to one spectral order. The input files are the observed cropped spectra and a synthetic stellar spectrum. The latter one must be a spectrum that simulates the spectral features of a star of the same spectral class of the observed one. The resolution of the synthetic spectrum must be equal to or higher than the resolution of the observed spectra. The template spectra employed in the phase of the DA were generated employing the MAFAGS code (Grupp, 2004) and normalized with the IRAF task `onedspec.continuum`. Figure 4.9 shows the final graph produced by the program at the end of the normalization process. In the upper panel, the input observed cropped spectra are plotted. The final normalized spectra are reported in the lower panel. The difference between the levels of the spectra is caused by i) the changing atmospheric conditions at the time of the observations and ii) the various intensities of the signal in the master flat-field frames employed in the calibration of the science frames. Small temperature and pressure changes in the 'white lamp' used for the acquisition of the flat-field frames can vary the amount of light entering through the slit of the HRS.

The program performs the following operations:

1. it aligns the template spectrum and the observed spectra. The alignment is obtained performing a preliminary cross-correlation between the template and the observed spectra. The shift measured at this phase of the DA is affected by a large uncertainty. It is not usable for the precise computation of the RV, but is adequate to get a raw alignment between the observed and the template spectra;

2. it selects the wavelength ranges of the template spectrum free from absorption lines (*i. e.* where the flux $f > 0.95$);

3. in these ranges, it computes the central wavelengths and the mean values of the observed spectra flux. A σ-clipping procedure is applied in order to exclude the contributes of the CR peaks in the computation of the mean flux. These two values (λ_{cent} and $\overline{f}$) represent the coordinates of a point in the wavelength-flux space. Each spectral range without absorption line provides one point;

4. it performs a cubic *spline* interpolation over the set of points just defined. This interpolating function is the estimate of the continuum of the spectrum. This operation is performed for all the single observed spectra;

5. finally, it divides the cropped spectra by the related estimated continuum in order to obtain the normalization of the input spectra.

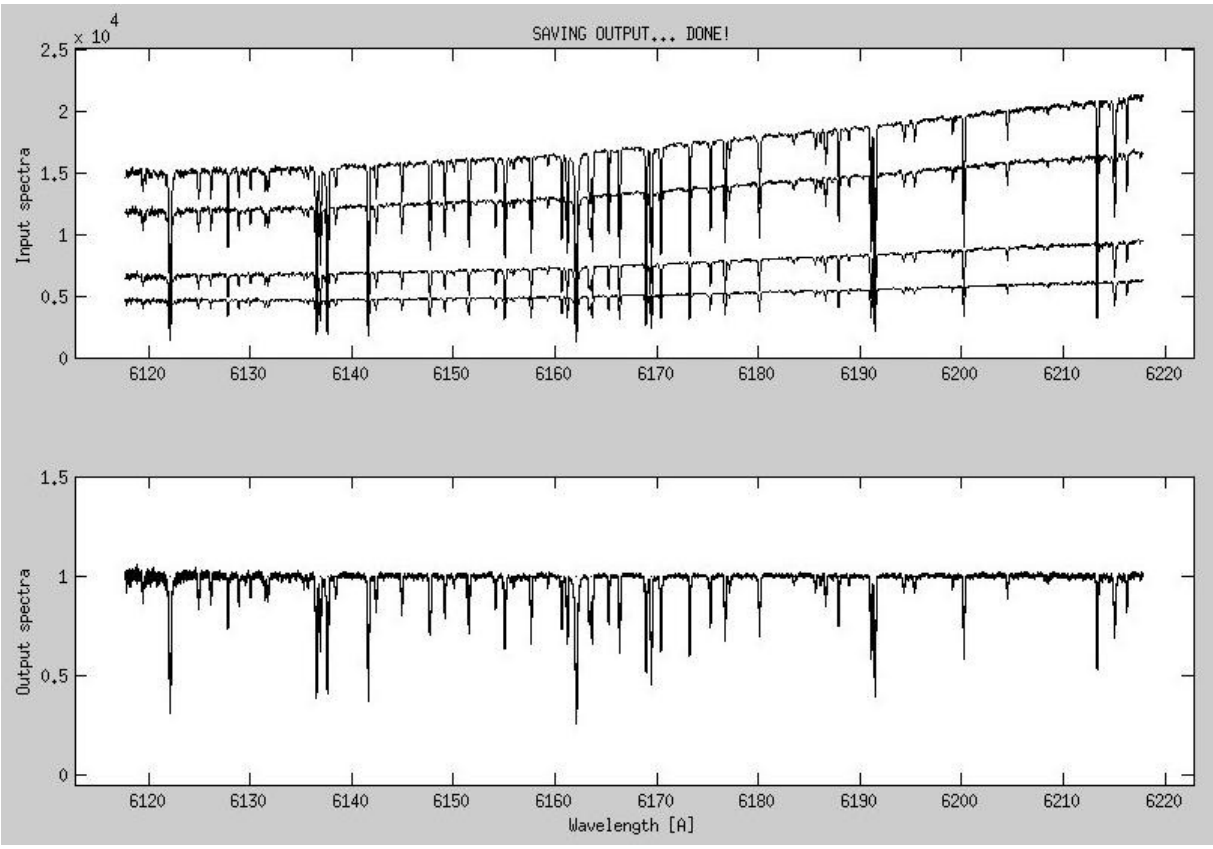

Figure 4.9: Example of the final graph produced by the program `CONT_AUTO`. The input crop spectra, reported in the upper panel, shows different continuum levels (see text for details) and an overall increasing trend. The output normalized spectra are shown in the lower panel.

All these steps are performed automatically. The user can overview all the intermediate phases and, if required, intervene and correct what has been done by the program. The efficiency of the algorithm was tested simulating several observed spectra. A synthetic spectrum of a star was multiplied by a 6^{th} degree polynomial function to simulate a continuum. Then, a random number of simulated CR peaks and random white noise accordingly to a given SNR value were added. In order to estimate the efficiency of the program for a wide range of spectral properties, the simulated spectra of different stellar type (from M to F dwarfs) were used. Moreover, the mock spectra were generated with SNR values ranging from 5 to 100. If the RMS of the difference between the 6^{th} degree polynomial function and the estimated continuum was equal or smaller than 1/SNR, then the estimation of the continuum was considered acceptable. Such condition was fulfilled in $\sim$90% of the simulated spectra considering all the spectra types and a SNR$\geq$8.

The percentage of failures rises sensibly considering spectra with SNR$\leq$8. Unfortunately, due to the algorithm with which the program operates, not only the noise can cause a bad estimation of the continuum. If the considered spectral range is crowded of absorption lines, then the portions that can be considered as line-free are only few and short. As a consequence, the points involved in the cubic *spline* interpolation are affected by the large uncertainty on the mean flux values and their number is not sufficient to correctly define the continuum. Such situation is encountered especially when the bluer spectral orders are normalized. Moreover, the normalization can not take place correctly for few red spectral orders heavily affected by the telluric lines. This happens as the stellar template spectrum involved by the program does not take into account the over-imposed telluric spectrum. In all these cases in which the normalization can not be automatically performed, another approach must be used.

User continuum definition

As discussed in the previous section, the spectral orders particularly crowded of absorption lines can be subject of incorrect normalization by the automatic algorithm of the program `CONT_AUTO`. Moreover, a low SNR can heavily affect the capability of the program to give acceptable results. The bluer spectral orders (from the blue $30th$ with the 'standard configuration') and the few red spectral orders heavily affected by the telluric lines are particularly susceptible to such weakness of the algorithm.

In all such cases, the program `CONT_USER` is preferred. It allows the user to fully manage the normalization of the input spectra.

The program performs the following operations:

1. it scales the observed spectra in order to maximize the overlap. A multiplicative factor is enough to parametrize the difference between the flux levels of the observed spectra (see previous section for details). As the spectra overlap, only one continuum, valid for all the spectra, can be defined;

2. it allows the user to mark the points where the continuum must pass;

3. analogously to what performed by the previous program, the continuum is computed performing a cubic *spline* interpolation with the set of marked positions;

4. finally, it divides the scaled spectra by the estimated continuum in order to obtain the normalization of the input spectra.

The program allows the user to iteratively define and correct the set of points involved in the definition of the continuum. Figure 4.10 shows an example of the definition of the continuum for the normalization of the spectra related to one of the bluer orders. In the upper panel the input scaled spectra are plotted with the points defined by the user and the interpolated cubic *spline* function. The result of the normalization performed with the just defined continuum is shown in the lower panel. Only few spectral orders (about 5 over the whole set of 64 orders) can not be normalized with the automatic procedure reported in the previous section and require the use of the program `CONT_USER`.

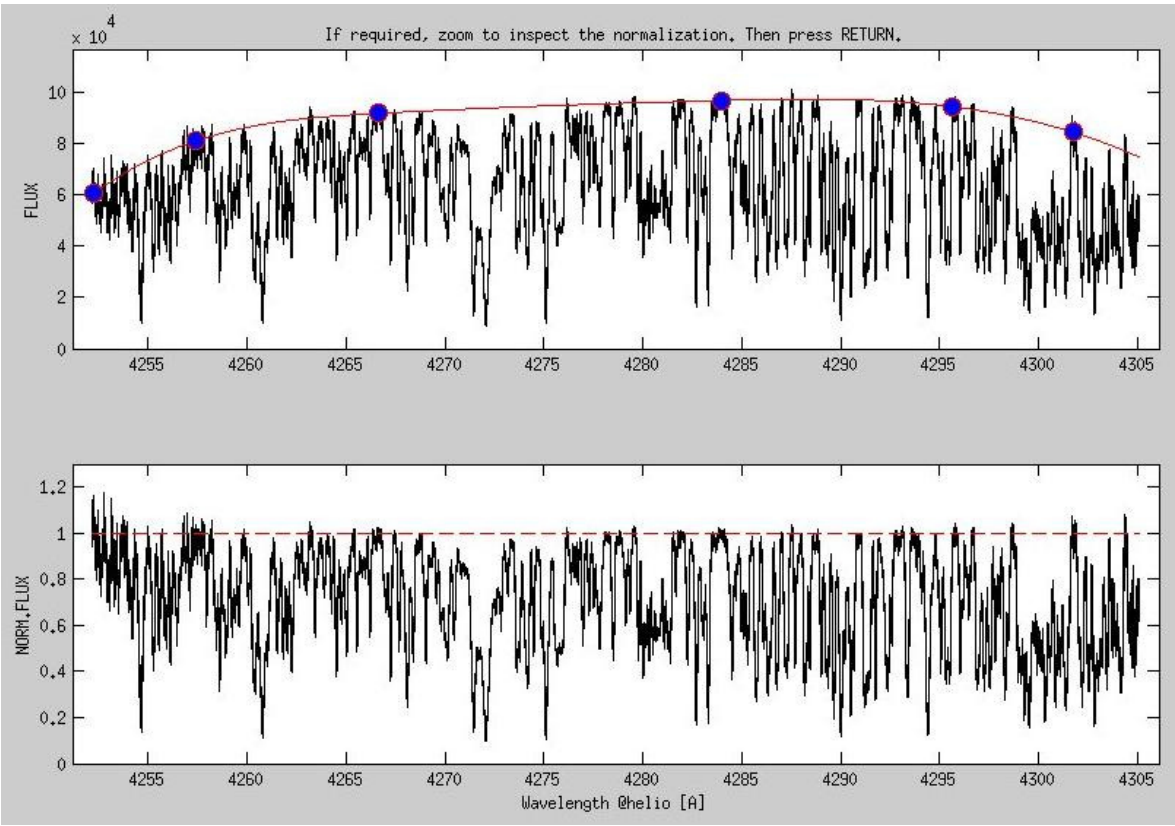

Figure 4.10: Example of the interactive loop that allows the normalization of the spectra with the program `CONT_USER`. *Upper panel*: input scaled spectra (black lines), marked points defined by the user (blue dots) and related cubic *spline* interpolation function (red line). *Lower panel*: normalized spectra (black line). The normalized spectra in the lower panel is performed with the continuum shown in the upper panel.

4.3.3 Telluric lines removal

Ground-based spectroscopic observations are affected by extinction and absorption within the Earth atmosphere. Absorption features that originate in the atmosphere are referred to as telluric features. Such features are prominent in the red end of the visible window and in the infrared domain.

Telluric features are atmospheric absorption lines generated in the Earth atmosphere. When a star is observed from the Earth, its light passes through the atmosphere and these telluric absorption features appear superimposed with the stellar spectrum. Telluric

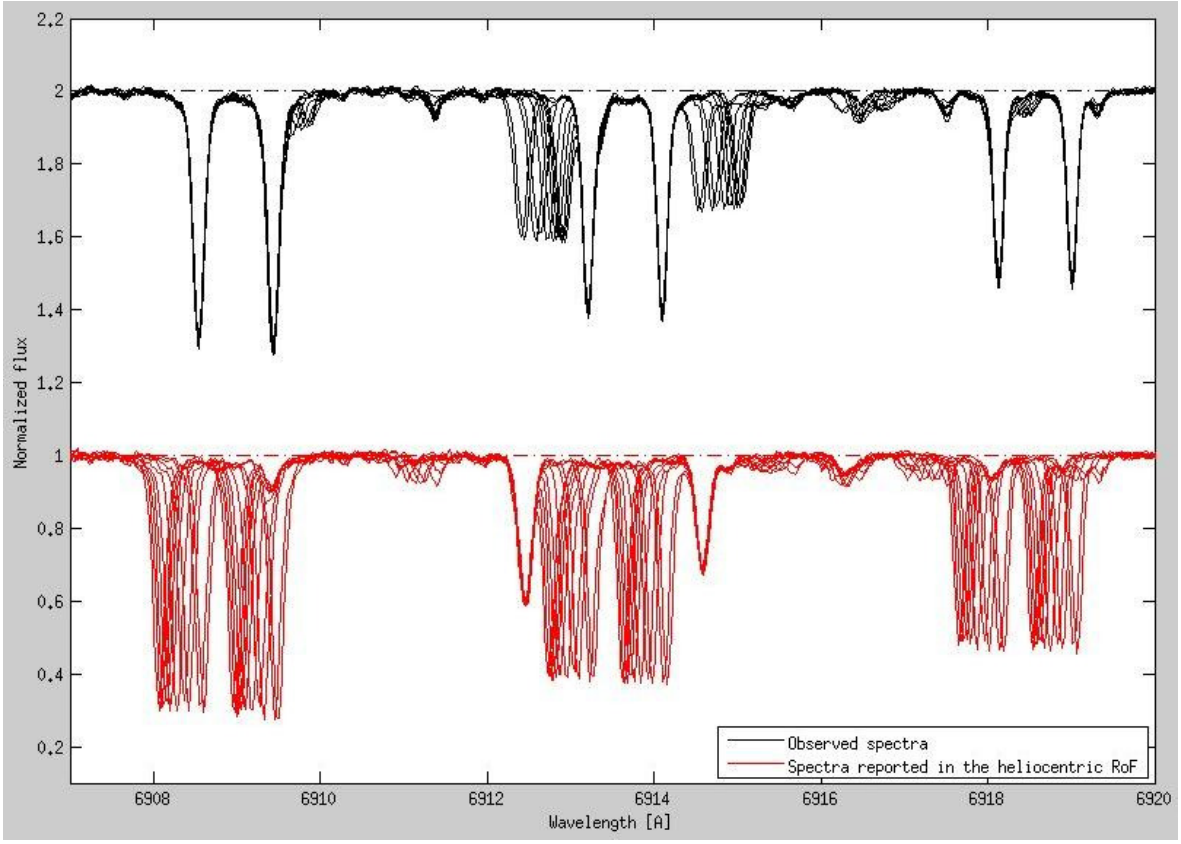

Figure 4.11: Example of telluric lines superimposed with the red 12^{th} observed spectral order. In particular, three water vapour doublets are visible. The spectra plotted in red are the observed spectra (black) shifted accordingly to the heliocentric velocities of the McDonald Observatory projected along the direction of the observations (see Section 4.1). As the observatory velocities is not constant over the epochs of the observations, the stellar lines show a displacement in the observed spectra (black) while the telluric lines overlap as the observatory and the Earth atmosphere move jointly. On the over hand, the stellar lines overlap perfectly in the spectra reported in the heliocentric rest frame (red) and the telluric lines are spread. The maximum displacement between the telluric lines corresponds to a difference of $\sim 22\,\mathrm{km\ s^{-1}}$ of the observatory heliocentric velocities.

features in the infrared region of the spectrum are mainly the result of absorption by ozone (O_3), gaseous oxygen (O_2), and water vapour (H_2O) (Adelman et al., 2002). Other lines include the Na-D lines (Lundstrom et al., 1991) and Carbon dioxide (CO_2) (Kingdon & Ferland, 1991). Of these lines, those caused by H_2O are the most problematic, varying not only with air mass but with humidity levels within the atmosphere as well. As a result, when the spectrum of the object is taken in several different exposures, the telluric features will not be identical in each spectrum (Lallement et al., 1993).

Even if the telluric features may be slightly shifted, due to the winds in the atmosphere, the displacement (10-30 m s^{-1}, Caccin et al., 1985) is fairly smaller than that the stellar lines show due to the motion of the Earth along its orbit (tens of km s^{-1}). This is clearly visible in Figure 4.11, where in the observed spectra (black spectra) three water vapour doublets overlap while the stellar lines migrate. The spectral coverage shown in the figure is only ∼10 Å. In few red orders the telluric contamination is analogous to what the figure represents and it is uniformly distributed over the whole spectral coverage (∼100 Å). Many telluric lines (in particular those related to water vapour) are much stronger than the stellar lines. As a consequence, the set of telluric lines simulate the spectrum of a mock source superimposed to the stellar spectrum. Such mock source would rest in the observatory

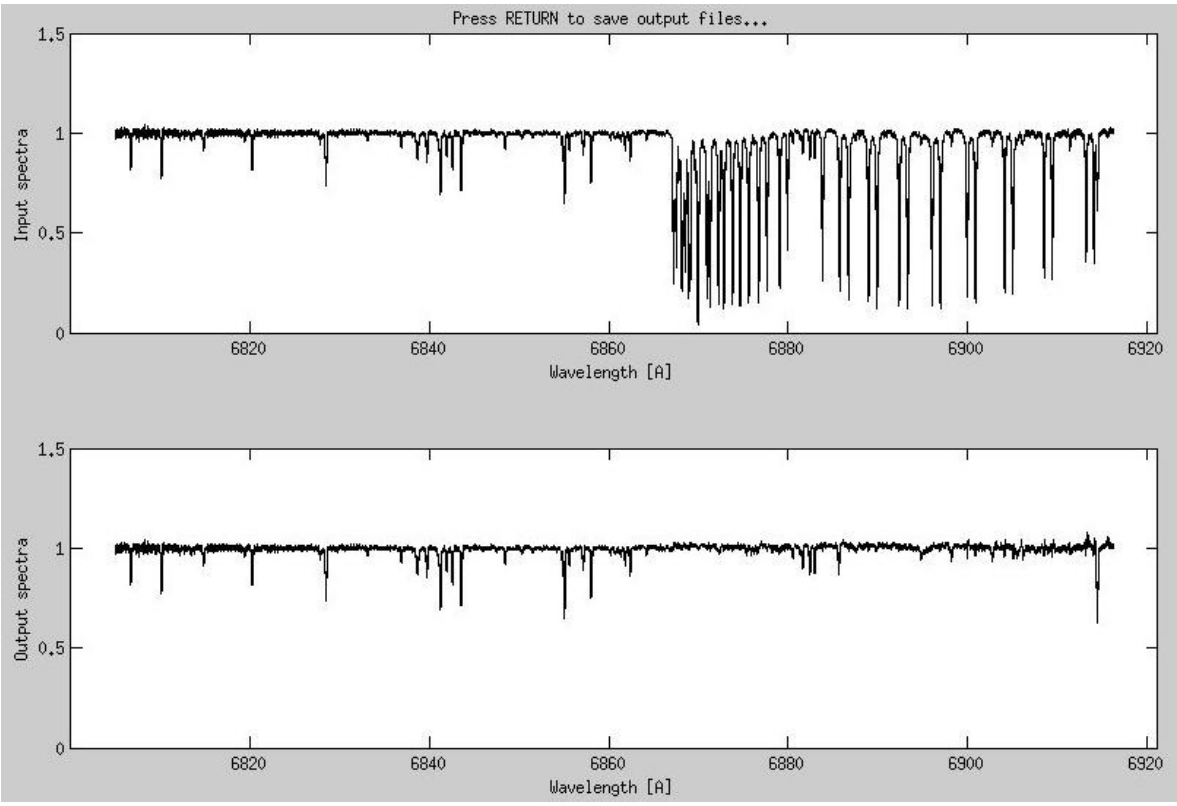

Figure 4.12: Example of the final graph produced by the program `TELL_REMOV`. The input normalized spectra (red 12^{th} spectral order) shows several strong telluric features. The output spectra are telluric-free.

rest frame. When the CC is performed, the telluric spectrum can dominate on the stellar spectrum and drive the correlation to completely wrong RV values. This happens even if the template spectrum was accurately chosen in order to be as similar as possible to the observed stellar spectra. Consequently, the set of telluric lines must be removed from the observed spectra before being cross-correlated in order to avoid systematics contamination on the final RV measurements.

The MATLAB program `TELL_REMOV` allows to perform the telluric lines removal. No user interaction is required once the program is executed. The input files are the normalized spectra of the observed star and a normalized observed spectrum of a WD. This last one is a spectrum characterized by the same (or higher) spectral resolution of the observed stellar ones. As the spectrum of a WD is essentially that of a black body, the telluric lines are not over-imposed to any stellar absorption lines. The few spectral features intrinsic to the WD are the H-Balmer series lines. These can be removed simply dividing the WD spectrum with a fitted Voigt model of each line. The resulting spectrum is assumed as template for the set of telluric lines to be removed.

First, the program shifts and scales the template spectrum in order to minimize the differences between the telluric line profiles in the template and in the observed spectra. The telluric lines are then removed from the observed spectra subtracting the shifted and scaled template to them. Figure 4.12 reports the input normalized spectra and the output telluric-free spectra. As the profile of the telluric lines changes night by night, the shifted and scaled template spectrum can not perfectly match the telluric features in the observed spectra. The RMS of the spectra after the removal of the telluric lines is of the order of $\sim$0.02. Hence, the systematic uncertainties left by a not perfect removal of the telluric features are negligible for observed spectra with SNR<50. All the blue and the red 21-24 spectral orders are completely telluric-free. The red orders most effected by the telluric features are the 3^{rd}, 11^{th} and 12^{th}.

4.3.4 Cosmic-rays peaks removal

If the observed star is particularly faint (m_V>13), the exposure time required in order to achieve spectra with an acceptable SNR ($\gtrsim$ 10) increases up to 30 minutes. For such long exposures, the effect of the CRs is large and the preliminary CRs filtering performed on the raw science frame (see Section 4.2.1) can result insufficient to remove the CR hits that fall on the echelle orders. Such hits appear as sharp peaks in the observed spectra. As in the case of the telluric lines, such peaks can affect the CC of the observed spectra with the template and introduce systematic uncertainties on the final RV measurements.

The MATLAB program `COSMIC_REMOV` removes the peaks due to the CRs in the observed spectra. The input files are the telluric-free spectra. No user interaction is required once the program is executed. First, the program shifts the spectra by an amount equal to the heliocentric velocities of the observatory at the epochs of the observations (see Section 4.1). Then, after the resample of the spectra to a common wavelength binning, it rejects the cosmic peaks for each pixel along the whole spectral length. The rejection algorithm basically consists in a σ-clipping: for each of the pixels that constitute the spectra, the

flux values related to the different spectra are sorted in decreasing order. If the first flux value is higher than $m + n_{rej} \cdot s$, where m and s are the average and the standard deviation computed on the remnant flux values, it is considered a cosmic peak and replaced with the average of the fluxes of the two adjacent pixels. n_{rej} is a parameter that can be changed by the user: its default value is 4 but it can be changed accordingly to the SNR of the spectra. The second adjustable parameter is *threes*, which define a flux limit: all the pixels with a flux higher than that limit are considered cosmic peaks, no matter the result of the σ-clipping rejection criterion. The red and blue spectral are, of course, all uniformly affected by the cosmic peaks. It is obvious that the higher is the number of the observations, the better are the results. An examples of the final graph produced by the program is reported in Figure 4.13. The input spectra reported in the upper panel were extracted from a science frame for which the exposure time was as long as 20 minutes.

The efficiency of the program was tested simulating several observed spectra. Analogously to what performed when the efficiency of the program `CONT_AUTO` was tested, the synthetic spectrum of a star was cropped in order to reproduce the spectrum related to

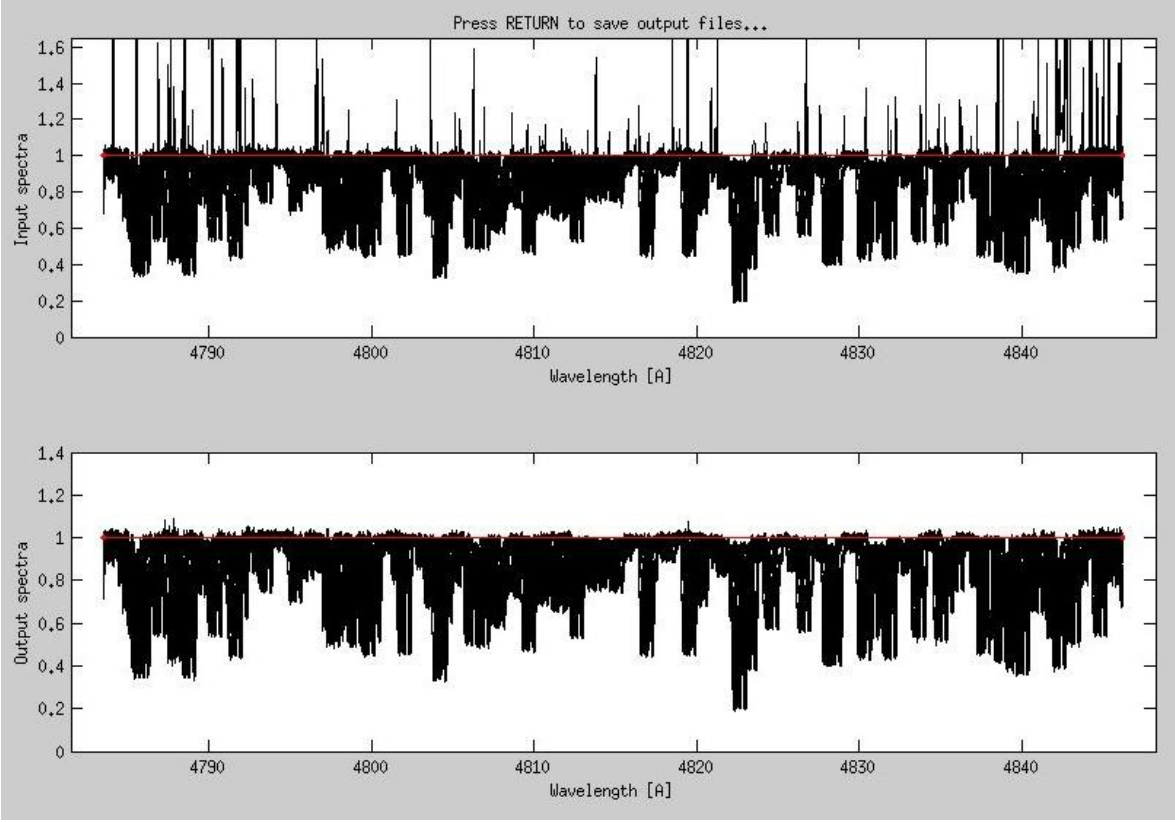

Figure 4.13: Example of the final graph produced by the program `COSMIC_REMOV`. In the input spectra (upper panel) many cosmic peaks are present due to the exposure time of 20 minutes of the science frame. In the output spectra (lower panel), almost all the peaks are removed.

a single echelle order. Then, 100 synthetic CR peaks were added in uniformly random positions within the spectral coverage. Finally, random white noise was added in order to obtain the desired SNR value. In order to estimate the efficiency of the program for a wide range of spectral properties, the simulated spectra of different stellar type (from M to F dwarfs) were used. Moreover, the mock spectra were generated with SNR values ranging from 5 to 100. Sets on N simulated spectra were then analysed by the program in order to estimate its efficiency in the removal of the CR peaks. These simulations showed that if the number of the input spectra N is equal or greater than 5, then more than 95% of the CR peaks are removed. For $N < 5$, the rate of peaks successfully removed drops critically (it is already 60% for N=4). The SNR of the input spectra only marginally influence the efficiency of the algorithm: such robust result could be achieved setting the parameter *threes* to a value equal to 1+4/SNR. The efficiency with which the CR peaks are removed does not shows a significant dependence on the spectral type of the observed star.

4.3.5 Spectra resampling

The last step of the DA, before the core CC phase, is represented by the resample of the wavelengths of the observed spectra. The extracted scientific spectra consist in a sequence of flux values as a function of the pixels position (see Section 4.2.4). When the DF is applied to the extracted spectra during the wavelength calibration (see Section 4.2.5), a wavelength value is associated to each pixel. All the extracted spectra related to a single spectral order are 4100 pixels long. But, the wavelength value of the first pixel differs from one spectrum to another. As a consequence, all the values related to the following pixels are different too. Such difference in the wavelength values is kept along all the steps of the DA previously described. As the operation of CC considers only the flux values of the spectra to correlate, both the observed spectra and the template spectrum must be resampled to a common set of wavelength values. The wavelengths usually differ by only few thousandth of Å (for example $\delta\lambda$=0.007 Å at $\lambda \sim 6200$ Å). Such a small difference can lead to systematic shifts of the order of $c \cdot \delta\lambda/\lambda \sim 340\,\mathrm{m\ s^{-1}}$, one order of magnitude larger than the final uncertainty on the measured RVs.

The resample of the wavelengths of the observed spectra is performed by the MATLAB program `RESAMPLE`. The template stellar spectra employed in the CC are also created by the program. The synthetic spectrum already employed during the normalization of the spectra (see Section 4.3.2) is cut in chunks accordingly to the spectral coverage of the single observed spectral orders (see Table 4.2). If the observed star is known to have a high proper motion along the line of sight ($RV \sim 100\,\mathrm{km\ s^{-1}}$ or higher), the synthetic template spectrum must be first shifted in order to get its absorption lines closer to those present in the observed spectra. An estimate of the mean RV of a star can be found on the SIMBAD database[6]. This operation allows to maximize the common wavelength range (and hence the number of pixels) employed for the CC (see Section 4.3.6). If such a shift of the template spectrum is required, the same amount will be afterwards added to the

[6] *http://simbad.u-strasbg.fr/simbad/*

final RV measurements (see Section 4.3.7).

The input files are the CRs filtered observed spectra and the selected template stellar spectrum. No user interaction is required once the program is executed. The program performs the following operations: computes the widest wavelength range common to all the observed spectra, defines the new set of wavelengths and resample the observed spectra accordingly to the new set of wavelength values (the same for all the spectra). If two spectra were observed within the same visit ('split type' visit, see Section 3.4), then these spectra are merged: pixel-by-pixel, the average of the two fluxes is computed. This operation implies an increase of the SNR of the spectra of a factor $\sqrt{2}$. Finally, also the template stellar spectrum is resampled with the same wavelengths set employed for the observed stellar spectra. The resampled observed and synthetic template spectra are the input files of the following CC.

4.3.6 Cross-correlation

The observed stellar spectra are now ready to be cross-correlated with the template synthetic stellar spectra. The operation of CC basically consists in the measure of the 'similarity' of two spectra as a function of the displacement applied to one of them. Such similarity is estimated by the value of the correlation function (CF) as a function of the displacement (expressed in pixel). The CF usually follows a bell curve: it reaches its maximum when the absorption lines in the template and in the observed spectra are aligned.

The IRAF task `rv.fxcor` performs the CC on the input object spectrum and the template spectrum. As the spectra are already normalized, filtered and resampled at this step of the analysis, no operation is required to further prepare the data for correlation. The peak of the CF is fitted with a Gaussian profile considering the 13 points closer to the absolute maximum of the CF as shown in Figure 4.14. The Gaussian fit allows to accurately measure the position of the centre of the peak, expressed in pixel, and therefore to obtain a RV measure accordingly to the value of the dispersion (km s^{-1} per pixel[7]). Analogously, the full width half maximum (FWHM) of the Gaussian fits determines the uncertainty associated to the RV measure.

In the example reported in Figure 4.14, the template spectrum was shifted by -80 km s^{-1} in order to maximize the number of pixels involved in the computation of the CF (see Section 4.3.5). As a consequence, the RV value of -13.069±0.143 km s^{-1} measured fitting the peak in the CF must be corrected to the final value of -93.069±0.143 km s^{-1} (see Section 4.3.7). This example refers to the star `HD195019`, a bright (m_V=6.87) G3V main sequence star. The synthetic spectrum of a G3 main sequence star ($T_{\rm eff}$=6 800 K and log g=4.5) was employed as template for the CC. It was generated employing the MAFAGS code (Grupp, 2004) and normalized with the IRAF task `onedspec.continuum`. The observed spectrum has a SNR of ~ 150.

Each single observed spectral order is cross-correlated with the related template spectrum in order to provide one RV measurement. Table 4.4 collect the RV values and the

[7]For $R = 60\,000$ and 4 pixels per resolution element, the dispersion is 1.25 km s^{-1}/pxl.

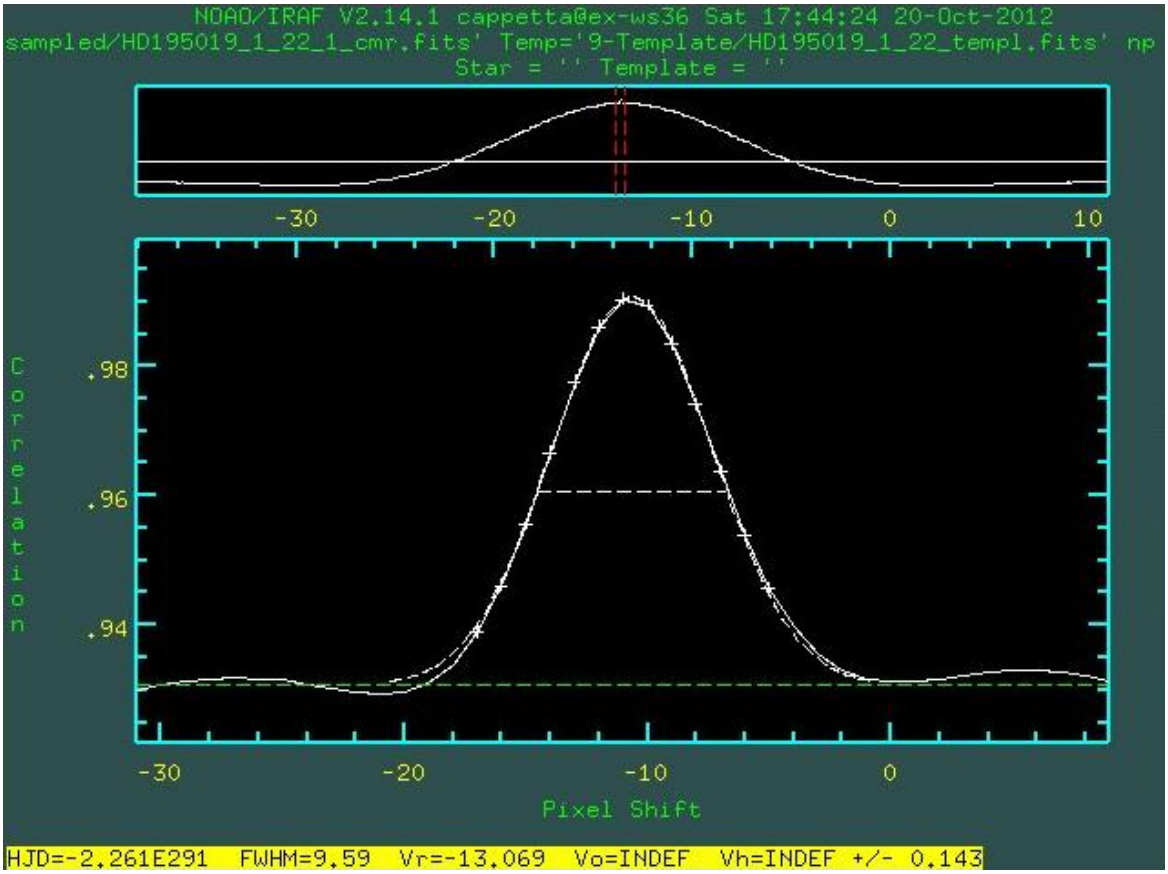

Figure 4.14: Example of the CF computed by the IRAF task `rv.fxcor`. The peak in the CF is fitted with a Gaussian profile considering the 13 points closer to the absolute maximum. The RV value and its uncertainty is computed from the best fitting parameters.

related uncertainties computed cross-correlating all the spectral order taken in the first epoch in which the star `HD195019` was observed. This and the other sets of RVs related to all the epochs are the output of the CC phase. How the final RV values are computed is described in the following section.

4.3.7 Final RV values

The last step of the DA consists in the computation of the RV mean value and its uncertainty for all the epochs in which the stellar target was observed. For a single epoch, 64 RVs are provided: 24 related to the red spectral orders and 40 to the blue ones. As discussed in Section 4.3.3, several red orders are significantly affected by the presence of strong telluric absorption lines. Even if such features were removed, it can happen that for these orders the absolute maximum of the CF occurs in correspondence of the remnants of the telluric lines (*i.e.* the measured RV value is close to zero). In these cases, the stellar lines would generate a maximum in the CF that is only a local one.

Table 4.3: RV values and related uncertainties computed cross-correlating each single spectral order of the first epoch in which the star HD195019 was observed. All the quantities are expressed in km s^{-1}.

Red	RV	σ_{RV}	Blue	RV	σ_{RV}	Blue	RV	σ_{RV}
1	-12.9846	0.199	1	-12.6633	0.346	21	-13.2825	0.109
2	-13.2301	0.099	2	-13.0117	0.180	22	-13.0330	0.079
3	-13.0426	0.186	3	-13.1445	0.138	23	-12.9829	0.158
4	-13.0505	0.156	4	-13.2466	0.151	24	-12.9140	0.529
5	-13.1493	0.115	5	-12.9001	0.210	25	-13.0742	0.207
6	-13.1022	0.407	6	-13.2764	0.107	26	-13.1549	0.246
7	-14.3246	0.308	7	-13.2070	0.174	27	-13.0769	0.164
8	-13.1658	0.566	8	-13.1225	0.164	28	-13.0695	0.144
9	-13.1820	0.165	9	-12.8544	0.126	29	-12.9240	0.102
10	-12.9696	0.155	10	-13.1279	0.151	30	-13.2960	0.140
11	-13.4412	0.533	11	-13.1943	0.152	31	-13.2500	0.059
12	-13.0287	0.163	12	-13.2490	0.123	32	-13.1865	0.337
13	-13.0170	0.151	13	-13.2004	0.079	33	-13.0961	0.062
14	-13.1599	0.135	14	-13.1243	0.165	34	-13.2842	0.229
15	-13.0831	0.113	15	-13.1432	0.106	35	-13.3775	0.096
16	-13.2811	0.125	16	-13.2513	0.087	36	-13.2991	0.189
17	-13.1031	0.214	17	-13.2705	0.071	37	-13.2403	0.203
18	-13.1827	0.235	18	-13.0272	0.185	38	-13.0119	0.311
19	-13.1137	0.146	19	-13.1201	0.066	39	-12.7594	0.155
20	-13.2327	0.131	20	-13.1390	0.086	40	-13.2008	0.200
21	-13.2118	0.179						
22	-13.0692	0.143						
23	-13.0462	0.157						
24	-12.9389	0.111						

The RVs compatible with this scenario can be easily detected as significantly deviating from the average value of the RVs over the bluer orders. Even if the SNR decrease moving toward the bluer orders, the RV uncertainties are generally larger for the redder orders. This is due to the telluric contamination and to the number of stellar lines in the red-end of the optical spectrum which is much smaller with respect to the bluer one. In Figure 4.15 the 64 raw RV values, related to all the 10 epochs in which the star HD195019 was observed, are plotted as a function of the spectral order. The medians of the RVs, computed over a single epoch, were subtracted in order to highlight the intrinsic spread of the measurements for each order. As it can be seen, the bluer orders have a smaller intrinsic scatter as the telluric contamination is not present and the spectral orders are crowded with stellar lines. The most deviating RV outliers, due to the telluric contamination, falls several km s^{-1}

outside the boundaries of the graph. The lower is the SNR of the observed spectra, the larger is the intrinsic RVs scatter of the orders.

Figure 4.16 shows the same raw data but broadened as a function on the epochs in which the observed spectra were taken. Here, the errorbars related to each single measure are reported too. As it can be seen, the RV outliers have large uncertainties and do not linger in all the epochs. This is the whole set of data with which the final RV measurements are computed. The MATLAB program `RV_COMP` allows to compute the mean value and the associated uncertainty starting from the raw RVs for all the epochs. Considering the set of RVs related to one epoch per time, the outliers are firstly rejected performing a σ-clipping algorithm. Then, the mean value is estimated computing the average value over the orders that passed the σ-clipping selection. The average is weighted with the square of the uncertainty of each single RV value. Finally, the uncertainty on the mean value is obtained computing the standard deviation of the RVs, via bootstrap of the sample, and dividing it by the square root of the number of the orders. Accordingly to the formula for

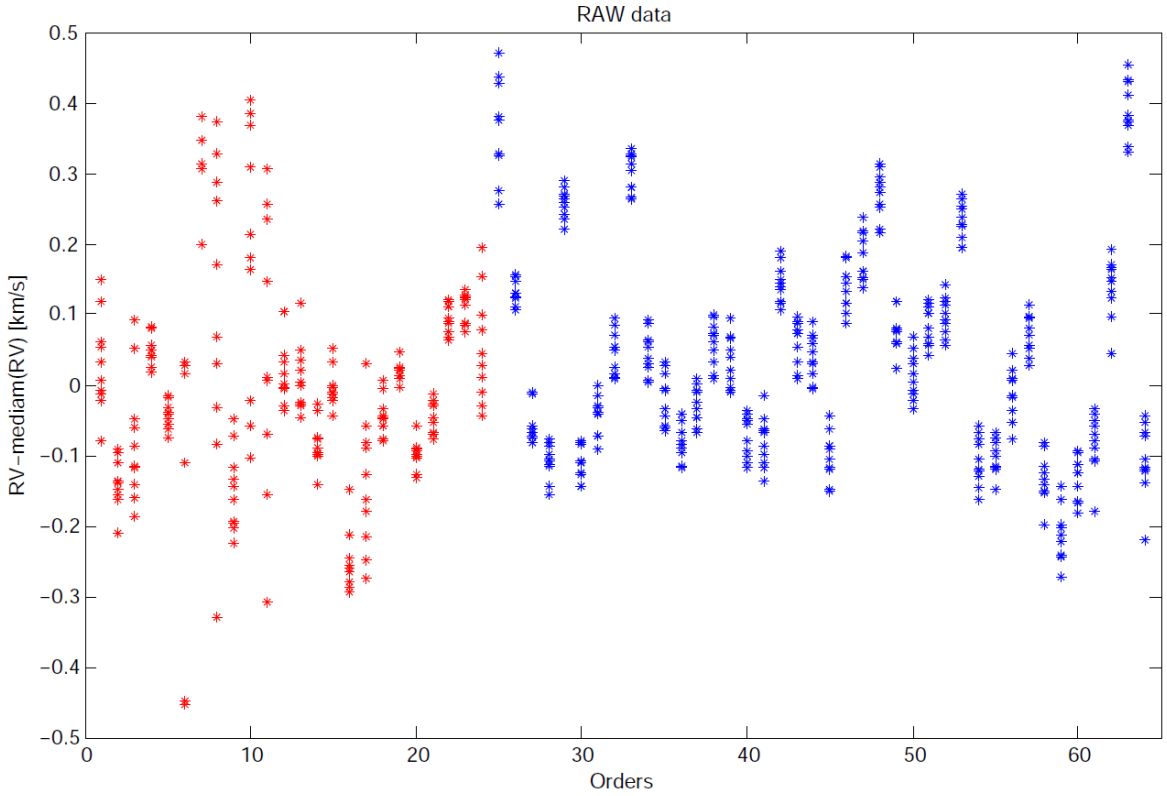

Figure 4.15: In this graph all the 64 raw RV values, related to the star `HD195019` observed in 10 epochs, are plotted as a function of the spectral order. The first 24 order are those related to the red component of the detector (red dots) and the last 40 those related to the blue component (blue dots). The medians computed over a single epoch were subtracted in order to highlight the intrinsic spread of the measurements for each order.

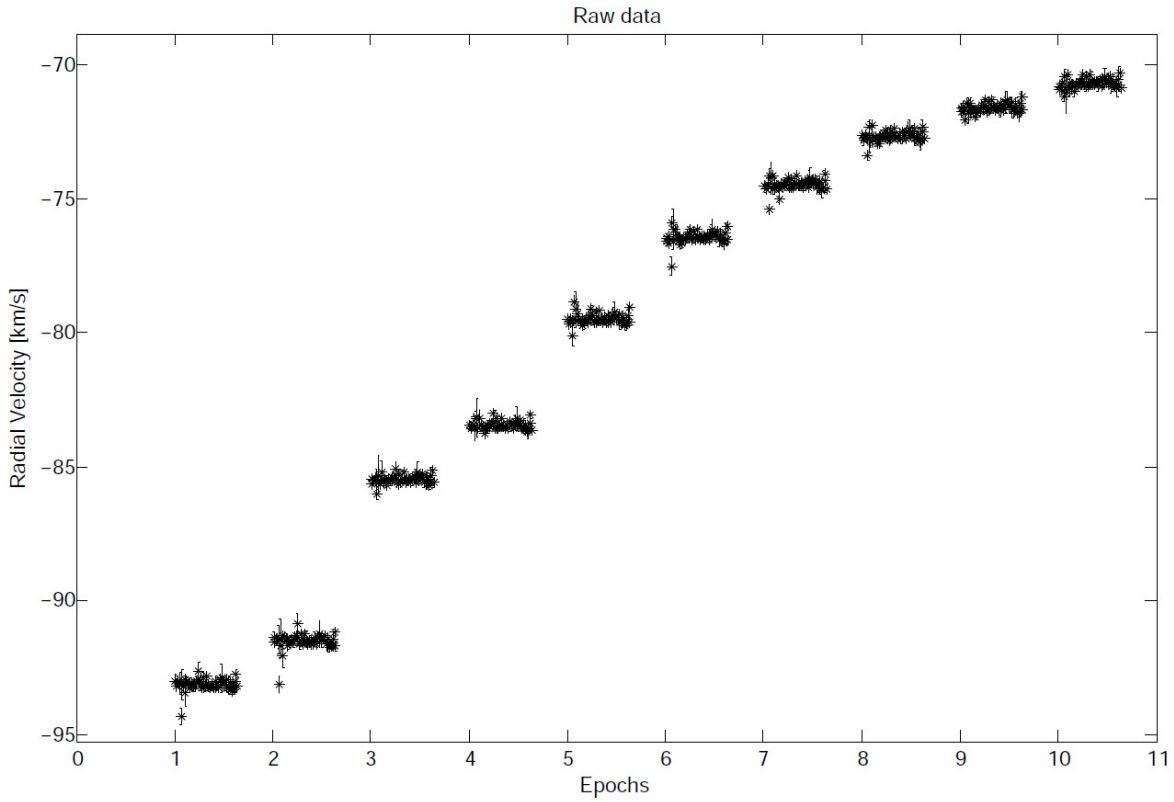

Figure 4.16: In this graph all the 64 raw RV values are plotted for all the epochs in which the star was observed (in this case, `HD195019` was observed in 10 different nights).

the computation of the standard deviation of the mean value, the higher is the square root of the number of orders considered for the computation of the final RV, the smaller is the related uncertainty. This is the reason for all the efforts performed to remove the telluric contamination in the red orders.

The RV values computed from the raw data are shown in Figure 4.17. These values represent the measures of two distinct movements projected along the line of sight: the proper motion of the observed star and the displacement of the observatory within the heliocentric rest frame as a function of the time (see Section 4.1). In order to obtain the true RV variation of the star only, the heliocentric velocities of the observatory must hence be subtracted. The final results of the computation performed by the program `RV_COMP` and related to the star `HD195019` are listed in Table 4.4 and shown in Figure 4.18. As it can be seen, the RV amplitude of the star is only of few hundreds of m s^{-1}. This indicates that the displacement of the stellar absorption lines in the observed spectra as a function of the time is almost entirely due to the motion of the observer itself and not to the observed target. The final uncertainty on the RV measures is $15-20$ m s^{-1}. This result was obtained with spectra characterized by a SNR$\sim$150 (m_V=6.87, 200 s of exposure time). As the SNR of the spectra is high, this precision is close to the limit determined by the statistical

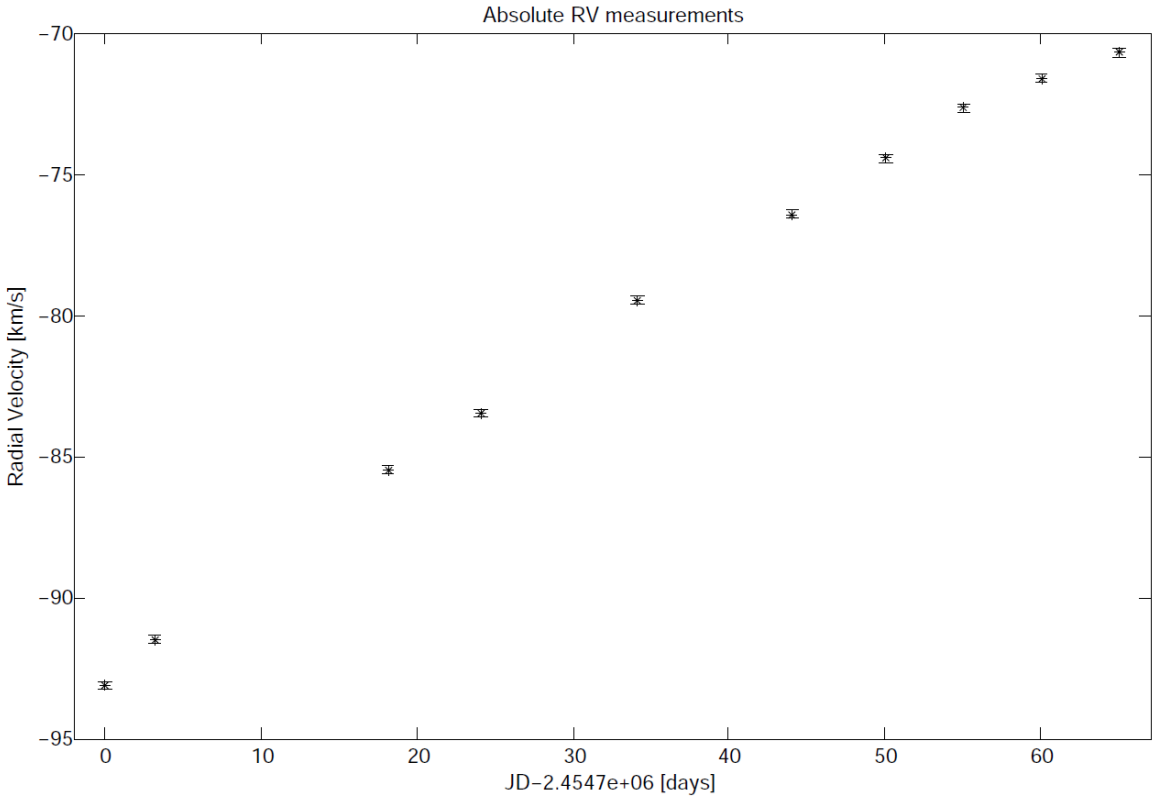

Figure 4.17: In this graph the RV values computed from the raw data, and the related standard deviations, are shown. They are the sum of the proper motion of the observed star and the motion of the observatory in the heliocentric rest frame.

uncertainties and, hence, that all the source of systematic errors were removed. A shift of $10\,\mathrm{m\ s^{-1}}$ corresponds to ~ 0.008 pixels[8], which imply a displacement of the positions of the stellar lines on the detector of only of $0.1\,\mu$m.

All the figures of this section show plots produced during the execution of the MATLAB program `RV_COMP`. For clarity, all the RVs reported in the plots were measured with the spectra wavelength calibrated using the solution related to the ThAr spectra taken before the science exposure (see Section 4.2.5). In the example related to `HD195019` here reported, the two final RVs, computed employing the two different wavelength calibrations, practically overlap (the difference of the mean values is smaller than $3\,\mathrm{m\ s^{-1}}$). The data points plotted in Figure 4.18 clearly show that the RV of `HD195019` is not constant as the standard deviation of the measures ($206\,\mathrm{m\ s^{-1}}$) is much higher than the uncertainties related to the single data points ($\sim 20\,\mathrm{m\ s^{-1}}$). Further considerations can be find in Section 5.1.1.

[8]For $R = 60\,000$ and 4 pixels per resolution element, the dispersion is $1.25\,\mathrm{km\ s^{-1}/pxl}$.

Table 4.4: Final results of the computation performed by the program `RV_COMP`. For each epoch the following data are reported: Julian date, the heliocentric velocity of the observatory, the observed RV (that is the measured shift of the stellar lines), the final RV corrected for the motion of the observatory and the RV uncertainty.

Epoch	JD [days]	V_{helio} [km s^{-1}]	RV_{obs} [km s^{-1}]	RV_{corr} [km s^{-1}]	σ_{RV} [km s^{-1}]
1	2454679.676	2.584	-93.168	-90.584	0.016
2	2454682.869	0.857	-91.514	-90.657	0.019
3	2454697.823	-5.085	-85.485	-90.570	0.016
4	2454703.800	-7.398	-83.524	-90.922	0.017
5	2454713.797	-11.209	-79.490	-90.699	0.019
6	2454723.761	-14.619	-76.440	-91.059	0.019
7	2454729.731	-16.472	-74.458	-90.930	0.019
8	2454734.726	-17.949	-72.661	-90.610	0.018
9	2454739.716	-19.294	-71.608	-90.902	0.017
10	2454744.709	-20.501	-70.431	-91.130	0.020

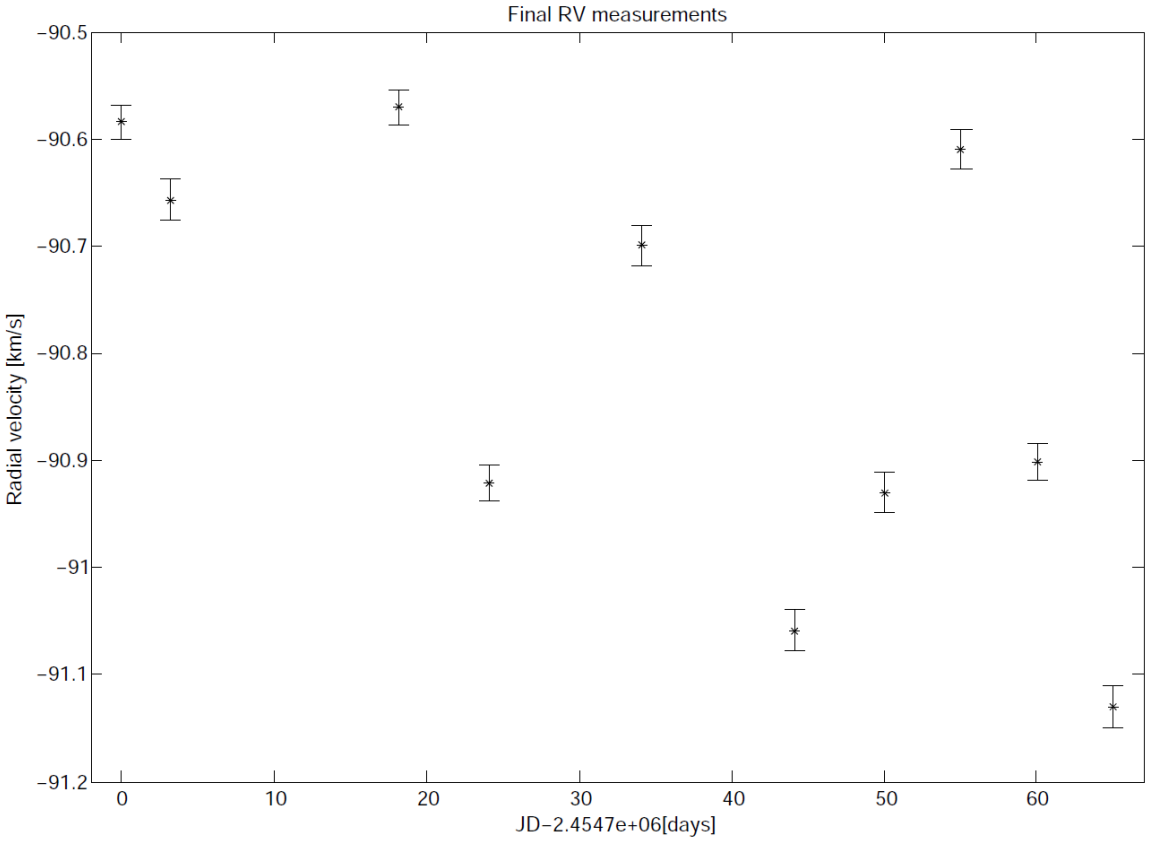

Figure 4.18: In this graph the final RV measurements related to `HD195019` are shown. The heliocentric velocities of the observatory were subtracted from the values computed from the raw data and reported in Figure 4.17.

Chapter 5

Observations and results

Everything will be all right in the end.
If it's not all right, then it's not the end.

Unknown

Figure 5.1: Rome, Sant'Angelo bridge. Angel with Sudarium... and Moon. M. Cappetta©

The processes of reduction and analysis of the data described in the previous chapter are optimized to measure the RV variations of any observed star. All the known sources of systematics (the over-imposed sky spectrum, the telluric lines, etc.) are corrected and the smaller uncertainties on the final RV measures are computed according to statistical noise present in the observed spectra.

In order to check the capability of the pipeline, in particular that all the possible systematic noise sources are correctly removed, the star HD195019 was observed. It is known that this star is orbited by a planet (Fischer et al., 1999). As the orbital parameters of the system are determined, the RVs of the star measured with the HET spectra could be compared with those expected at the epochs of the observations. This set of observations was the first benchmark with which the pipeline was tested. Several improvements could be applied in the different phases of reduction and analysis of the spectra up to the final version of the pipeline reported in this thesis. The observations of the star HD352939 allowed to detect a mechanical problem within the spectrograph. Such problem was then fixed by the technical staff of the McDonald Observatory. The following observations did not experience any more such technical problems. The observations of these two stars allowed also to estimate the highest precision with which the RV of a solar type star can measured when the systematic noise limit is reached. Analogously, the star GJ1214 was observed in order to quantify the RV uncertainty related to the observation of a moderately faint M dwarf (the main target of the WTS, see Chapter2). Finally, the spectroscopic follow-up of several stars in the open cluster M 67 allowed to precisely compute the zero point correction to be applied to the HET RVs in order to make them employable with the RV values obtained by other instruments involved in the detection and confirmation of extrasolar planets with the Doppler method.

The characterization of the pipeline allowed to optimize the results obtained within the spectroscopic follow-up of two stars observed by the WTS. These stars passed all the selection criteria for the detection of a transit in their measured LCs. The RV curves produced with the HET spectra allowed to confirm the planetary nature of the stellar companions that generated the transits. WTS1 b and WTS2 b are the first two extrasolar planets detected within the WTS. The spectra of the white dwarf NLTT 5306, which is orbited by a brown dwarf, were also observed with the HET in order to place stronger constrains on the orbital parameter of the system.

5.1 Pipeline characterization

5.1.1 HD 195019

The star HD195019, a bright G3v-star (m_V=6.87), has a known planetary companion of $M_P\ sin(i)$=3.51±0.4 M_J orbiting in P=18.27±0.14 days (Fischer et al., 1999). Fischer and collaborators performed a Keplerian best-fit (see Appendix A) on RV values measured from Keck and Lick observations ($\sigma_{RV} \sim 5\,\mathrm{m\ s^{-1}}$) obtaining a semi-amplitude value of K=275±5 m s^{-1}. The RV variation is therefore more than one order of magnitude larger than the RV precision that we expect to achieve for an observed star similar to HD195019 in brightness and spectral type.

The star was observed in 10 epochs between August and September 2008 with the HRS.

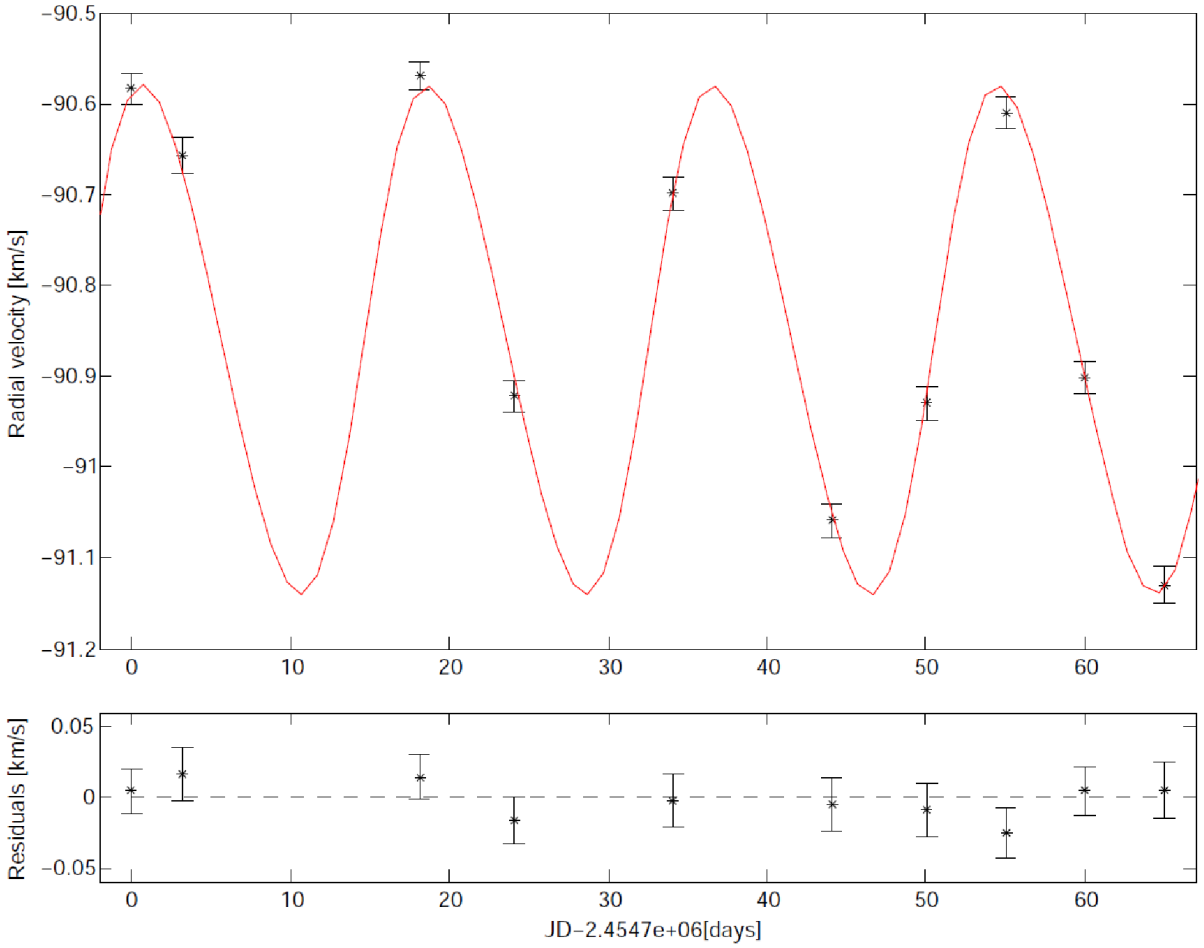

Figure 5.2: In the big panel, the measured RVs of the star HD195019 are reported (black errorbars) with the related Keplerian orbit best-fit (red line). The residuals are shown in the lower panel. The best-fit has a χ^2_ν=1.23 and the RMS of the residuals is 13 m s^{-1}. The best-fitting parameters are consistent with those obtained by Fischer et al. (1999).

The standard configuration setting (60k, 316g5936, 0sky, see Section 3.3) was employed. The brightness of the star allowed to measure spectra with SNR∼150 with 200 s of exposure time. As the orbital parameters of the planetary companion HD195019 b are known, the reflex motion of the parent star is also known. It permitted to compare the measured RVs amplitude (and the other fitted parameters) with the value expected accordingly to the presence of the companion.

The 10 RVs obtained at the end of the DA (see Table 4.4 and Figure 4.18) were fitted with a Keplerian orbit model (see Figure 5.2 and Appendix A). The values of the fitted parameters are consistent with those obtained by Fischer et al. (1999) as the fitted orbital period is P=17.9±0.2 days and the semi-amplitude K=280±10 m s^{-1}. The best-fit has a χ^2_ν=1.23 and the RMS of the residuals is 13 m s^{-1}, comparable to the size of the errorbars of the measured velocities. This result demonstrates that the pipeline works properly and that the measured RVs are not affected by systematic uncertainties larger than few m s^{-1}.

5.1.2 HD 352939

The star HD352939 is a moderately bright G0V-star (m_V=9.71) which was observed with the HRS in three different periods between 2008 and 2011. The standard configuration setting (see Section 3.3) was employed.

The first period in which HD352939 was observed goes from August to October 2008. The purpose of these observations was to estimate the RV precision achievable with the spectra of a solar type star characterized by a moderate (30-50) SNR. The exposure time of the scientific frames was 66 s. The RV measurements related to these observations are drawn in Figure 5.3 and correspond to the data within the first 100 days. The measures are characterized by an uncertainty of the order of 50 m s^{-1} and show a weak decreasing trend over the tree months of the observations.

In order to confirm the effective existence of the trend, a second series of observation was performed in the second half of 2010. The exposure time of the scientific frames was ∼1200 s in order to achieve a high precision of the RV measures. In this case the SNR of the observed spectra is 150 − 200. The epochs related to this second period are characterized by an error of the RVs of ∼10 m s^{-1}, the smallest of all the measures performed within the project. Such uncertainty can be assumed as the limit value achievable with a wavelength calibration performed with a ThAr calibration spectra taken not simultaneously to the science spectra. Surprisingly, for this set of epochs, the values related to the two different wavelength calibrations are consistently different as it can be seen in Figure 5.3. The difference between the two RVs are of the order of several hundreds of m s^{-1} (up to 0.5 km s^{-1}). After a carefully inspection of all the raw files, both the scientific and calibration frames, the reason of such drift was detected in a displacement of the echelle order positions of the two ThAr exposures. The direction of the displacement was tilted 45 ° with respect to the mash of the pixels of the CCDs. As a consequence, the component of the drift along the dispersion axis introduced a shift of the ThAr emission lines up to 0.5 pixels. Such shift between the two ThAr spectral lines caused the different measured RVs seen in the plot. Moreover, the mechanical origin of the movement of the echelle orders onto the detector was recognized

in a unexpected shift of the cross-disperser grating (see Section 3.2). According to the value of the parameter TILTPOS the cross-disperser can be placed in different predefined positions. When this component was moved during those nights to change the instrumental configuration, it required, against expectation, an amount of time of the order of 30 minutes to settle down correctly in the new position. Just after a change of the configuration, the disperser continued a slow drift toward the final location. Such scenario was confirmed by the analysis of the series of flat-field exposures taken at the end of the nights just after the change of the grating configuration. A monotonic displacement trend of the order positions was indeed detected. In this case only the component of the drift across the dispersion direction could be measured. The position of the orders showed an asymptotic movement toward the final position.

The discovery of this mechanical problem permitted to the technical staff of the Mc-

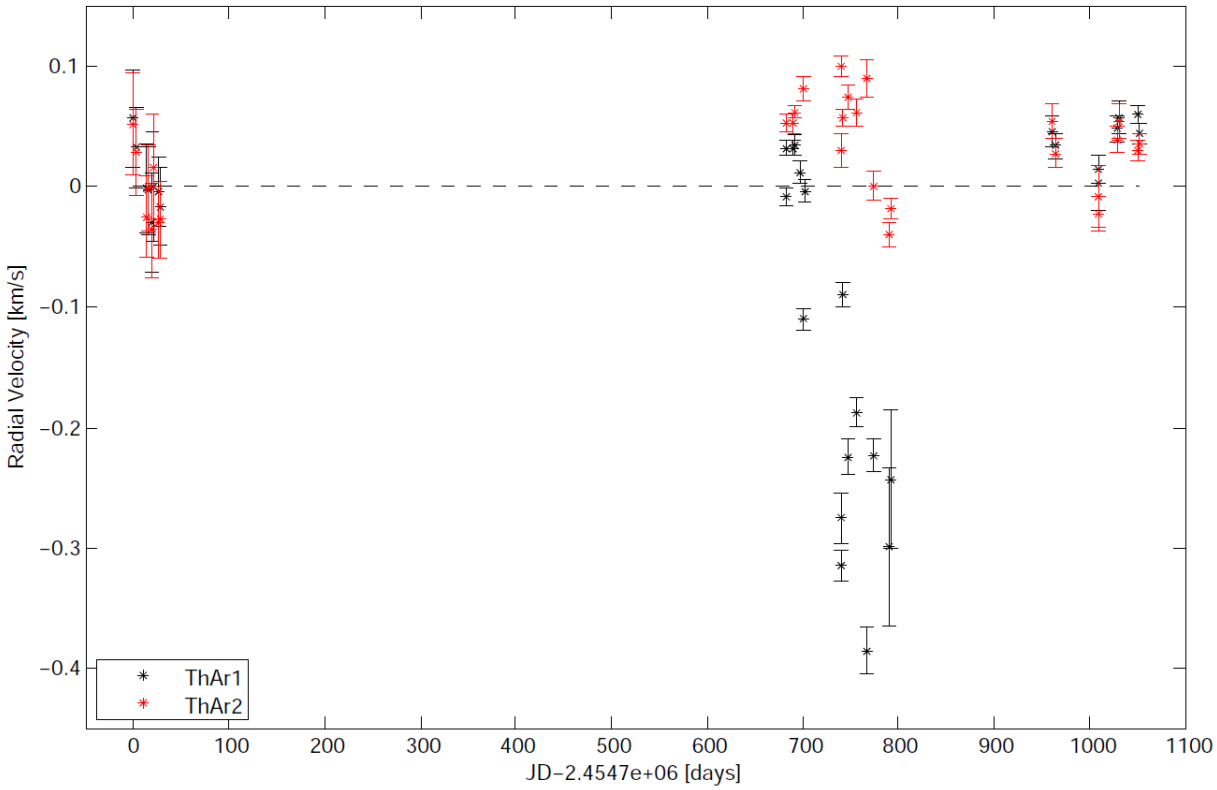

Figure 5.3: RV measurements related to the G0V-star HD352939. The star was observed first in the late 2008, then in the second half of 2010 and finally in summer 2011. For each epoch, two RV measures are shown. The two values are related to the two wavelength calibrations of the stellar spectra. The DFs were computed with the ThAr spectra taken before (black errorbars) and after (red errorbars) the science exposure. Thanks to the observations performed in the second period, we detected a mechanical problem within the spectrograph (see text for details).

Donald Observatory to fix this unexpected behaviour of the cross-disperser in the second half of 2010. Furthermore, the usage of the same configuration for a longer section of a night prevented the change of the position of any internal component of the HRS (not only the disperser) and, consequently, to exclude *a priori* any possible drift which could affect the observations.

The star was observed again between June and August 2011 and the difference between the two RV values related to a single epoch is negligible as the systematic drift of the cross-disperser did not occur. As it can be seen in Figure 5.3, the RVs do not show a variation larger than $\sim$20 m s^{-1} over a time baseline of almost 3 years. Thanks to the follow-up of `HD352939`, all the observations performed from the second half of 2010 are not affected by the drift of the cross-disperser occurring after a change of the instrumental setup.

5.1.3 GJ 1214

In order to define the RV precision achievable observing cooler and fainter stars, `GJ1214` was observed in 8 nights along spring 2010 with the HRS set to the standard configuration (see Section 3.3). The star is a faint (m_V=14.67) M4-dwarf. A super-Earth planet of 6.55 $M_\oplus$ orbits the observed star in 1.58 days (Charbonneau et al., 2009). The presence of this companion generates a semi-amplitude variation of 12 m s^{-1} in the RV of the parent star.

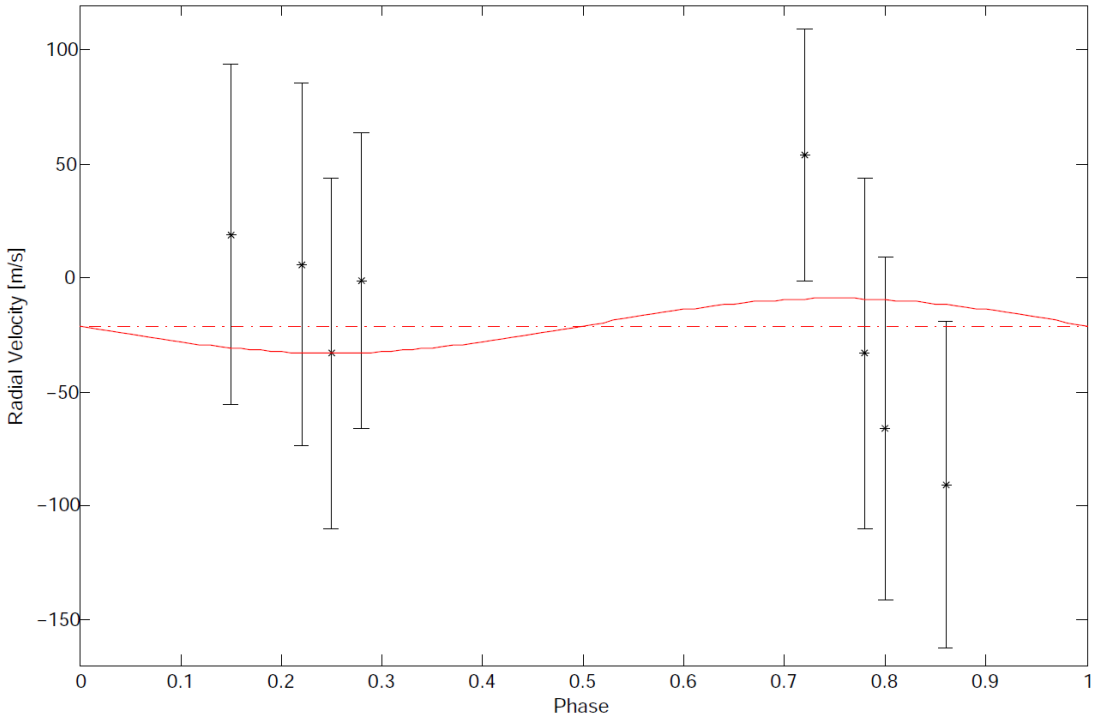

Figure 5.4: Phase folded RV measures of `GJ1214` (black errorbars). The red line represents the expected RV variation of K=12 m s^{-1} due to the presence of the super-Earth `GJ1214 b`. The RMS of the residuals is $\sim$60 m s^{-1}.

This RV excursion is comparable to the precision achieved for the two stars discussed in the previous sections. Being GJ1214 several magnitudes fainter, the expected RV precision does not allows the detection of such small amplitude due to the planet. The spectra extracted by the science frames (the exposure time was ∼40 minutes) are characterized by a SNR of $10 - 30$. The final measured RVs are reported in Figure 5.4. The data were phase folded accordingly to period and transiting epochs computed by Charbonneau et al. (2009). The RMS of the residuals is $\sim 60\,\mathrm{m\ s^{-1}}$, comparable to the size of the errorbars of the measured velocities.

As the WTS is optimized to search for transiting companions orbiting M-dwarf stars, the observations of GJ1214 defined the lower limit of the RV variation measurable with the HET spectroscopic follow-up of an M star. As the peak of the instrumental throughput of the HRS falls in the visible (∼6000 Å), the spectra taken with the HET do not represent the best data set with which to compute the RVs of such cool stars. Indeed, their emissivity decreases in the considered wavelength range (4300-7800 Å). It would be preferable to perform spectroscopic observations in the near infrared as them allow to achieve better results being more sensitive to the peak of the stellar emissivity at ∼10 000 Å.

5.1.4 M 67

The HET was employed for the observation of different stars in the open cluster M 67. This star cluster is one of the most studied as it has been comprehensively observed to establish astrometric membership and to achieve precise photometry and RVs curves of its stars. Its chemical composition and age are very close to solar values and it hosts very good candidates for solar twins. For an open cluster, M 67 is quite rich in stars, and its colour-magnitude diagram is well populated in the main sequence, in the sub-giant and red-giant branches.

As fully described in Pasquini et al. (2012), 70 observing runs with the HET were dedicated to the observation of 13 stars between November 2010 and April 2011. The targets were selected from the main sample with the following magnitude cut: $9.0 \leq m_V \leq 14.6$. Each visits consisted of two exposures of 1320 s and the standard instrumental configuration was employed. The SNR of the spectra related to the faintest stars is ∼10 and the uncertainties on the single RVs are in the range 20-40 $\mathrm{m\ s^{-1}}$ (see Pasquini et al., 2012). All the stars were also observed with the 'High Accuracy Radial velocity Planet Searcher' (HARPS, Mayor et al., 2003).

Six of the 13 observed stars showed a flat trend of the RVs measured with both the HET and HARPS. Unsurprisingly, a large offset was found between the two data series, with the HET RVs systematically higher than the HARPS ones. The characterization of the pipeline employed for the reduction and analysis of the HET observations could not be complete without an estimate of the zero-point offset of the RV measurements with respect to the other instruments involved in the detection and confirmation of the extrasolar planets with the Doppler method. As the wavelength calibration of the spectra observed with HARPS

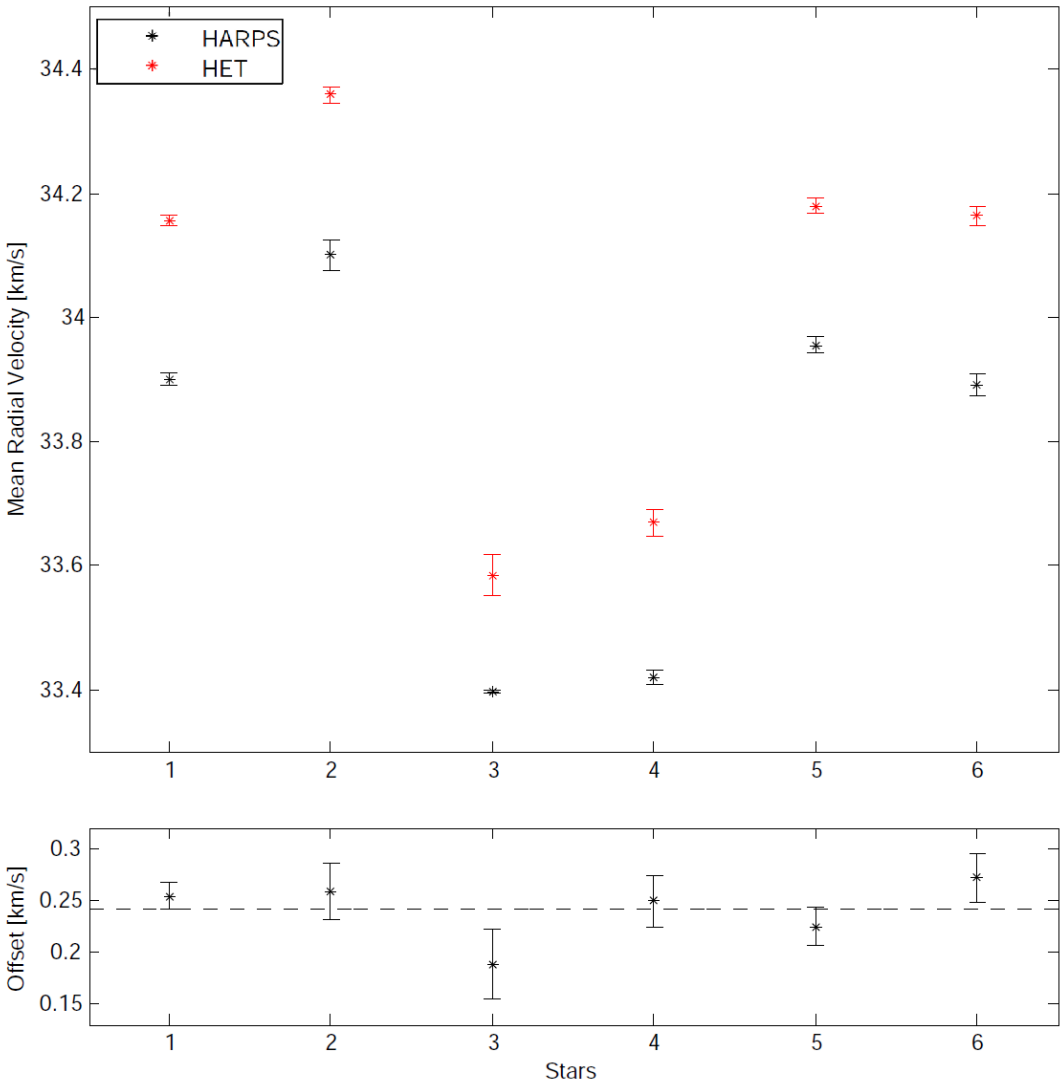

Figure 5.5: *Upper panel*: mean values of the HARPS (black) and HET (red) RVs for the 6 stars observed in `M 67` and showing a flat trend of the RVs. *Lower panel*: offsets between the HARPS and HET mean RV values. The dashed line represents the zero-point mean value weighted on the squares of the single offset uncertainties.

is an 'absolute wavelength calibration'[1], the HARPS measures are commonly assumed for the computation of the offsets related to the other instruments. The RVs of the stars of `M 67` were hence employed for the estimation of the HET RVs zero-point correction.

For each of the six stars, the average value of the RVs related to the HET spectra was computed. The associated error was calculated dividing the standard deviation of the RV

[1]The wavelength calibration is 'absolute' if no systematic shift is present between the measured and the theoretical central wavelength of the observed lines (for example in the spectrum of a calibration lamp or in the emission spectrum of the sky).

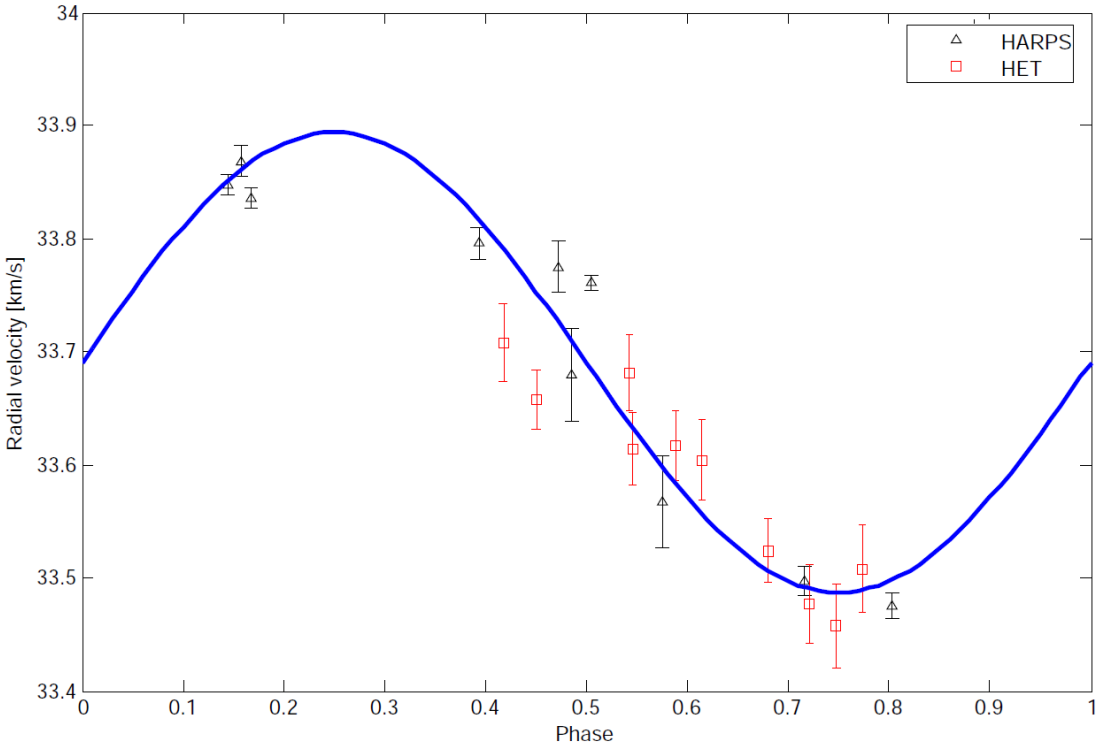

Figure 5.6: RV of a star in M 67 measured with HARPS (black triangles) and HET (red squares) spectra. The Equation 5.1 was used to shift the HET RVs.

values by the square root of the number of data points related to a single star, accordingly to the formula for the estimation of the mean value uncertainty. The same was performed for the sets of the HARPS RVs related to the single stars. The mean values of the HET and HARPS RVs are shown in Figure 5.5. In the lower panel of the figure, the difference between the two mean values are plotted. The uncertainties related to the differences were computed summing in quadrature the mean value errors. The average of the differences gives the estimate of the offset correction to be applied to the HET measurements. The uncertainty on the zero-point correction was computed as before, accordingly to to the formula for the estimation of the mean value uncertainty. The following formula can be used to report the RVs measured with the HET spectra in the absolute system of HARPS:

$$RV_{HARPS} = RV_{HET} - (242 \pm 12\,\mathrm{m\ s^{-1}}) \tag{5.1}$$

This equation was used in order to collect in a unique data set the RVs measured with both the HET and HARPS. In Figure 5.6 an example in which the previous formula was applied is reported. The HET and HARPS spectra employed for the computation of the RVs were observed $\sim$1 year aside.

Such RV offset is caused by several reasons. First, small imperfections of the dispersion

function could have affected the wavelength calibration of the observed spectra. The positions of the Oxygen O I emission line at 5577.34 Å observed in the HET spectra show a redshift of few hundreds on m s^{-1} with respect to those observed in the HARPS spectra (see Section 4.2.5). Unfortunately, the precision with which the positions of that and the other strong sky emission lines[2] are measured is not better than $\sim$100 m s^{-1}. So, it was impossible to estimate the shift to be applied to the HET spectra in order to correct for any systematics of the wavelength calibration. Then, the spectrograph resolutions employed for the observations of HARPS were higher (R=115 000) than that used with the HET (R=60 000). Moreover, no optical scrambling (Avila & Singh, 2008) is provided for the optical fibers connection between the HET focus and the entrance slit of the HRS, whereas HARPS uses this device. Finally, the pipeline for the data reduction and analysis are different. In particular, a binary mask is employed for the CC of the spectra observed with HARPS. A binary mask is a spectrum in which the flux can assume only the values 0 and 1. According to the spectral type of the observed star, the flux goes to 0 for the pixels in correspondence of the stellar absorption lines. Such masks substitute the synthetic stellar spectrum used for the correlation of the HET spectra.

[2] O I 6300.30 Å, 6363.78 Å; Na I 5889.95 Å, 5895.92 Å

5.2 WTS1 b

In this section, the discovery of WTS1 b[3], the first extrasolar planet found by the WTS is reported. The host star WTS1 (see Table 5.1), before the discovery and the following confirmation of its planetary companion, was labelled 19d_1_09358 as it falls in the paw-print 'd' of the 19hr field (see Section 2.1). The combined analysis of the light curves and spectroscopic data resulted in an orbital period of the sub-stellar companion of 3.35 day, a planetary mass of $4.01 \pm 0.35\, M_J$, and a planetary radius of $1.49^{+0.16}_{-0.18}\, R_J$. WTS1 b has one of the largest radius anomalies among the known HJ in the mass range 3-5 M_J.

Table 5.1: The host star WTS1.

Parameter	Value
RA[a]	19h 35m 58.37s
Dec[a]	+36d 17m 25.17s
l[a]	+70.0140 deg
b[a]	+7.5486 deg
$\mu_\alpha cos\delta$[b]	-7.7±2.4 mas yr^{-1}
μ_δ[b]	-2.8±2.4 mas yr^{-1}

[a] Epoch J2000;
[b] Proper motion from SDSS.

5.2.1 Observations

Photometric data

The instrument used for the J-band observations, the steps involved in the data reduction and the following transit detection algorithm are described in Chapter 2. The unfolded J-band LC for WTS1 is shown in Figure 5.7 (all the measurements are reported in Table 5.2) and its final out-of-transit RMS is 0.0064 (equivalent to 6.92 mmag).

In addition to the WFCAM J-band LC, we observed one half transit of the WTS1 system in the i'-band (see Section 2.3) on July 23, 2010. A total of 82 images, sampling the ingress of the transit, were taken with an integration time of 60 seconds. The data were reduced with the CASU INT/WFC data reduction pipeline as described in detail by Irwin & Lewis (2001b) and Irwin et al. (2007). The pipeline performs a standard CCD reduction, including bias correction, trimming of the overscan and non-illuminated regions, a non-linearity correction, flat-fielding and defringing, followed by astrometric and photometric calibration. A master catalogue for the i'-band filter was then generated by stacking 20

[3]Published in Cappetta et al. (2012).

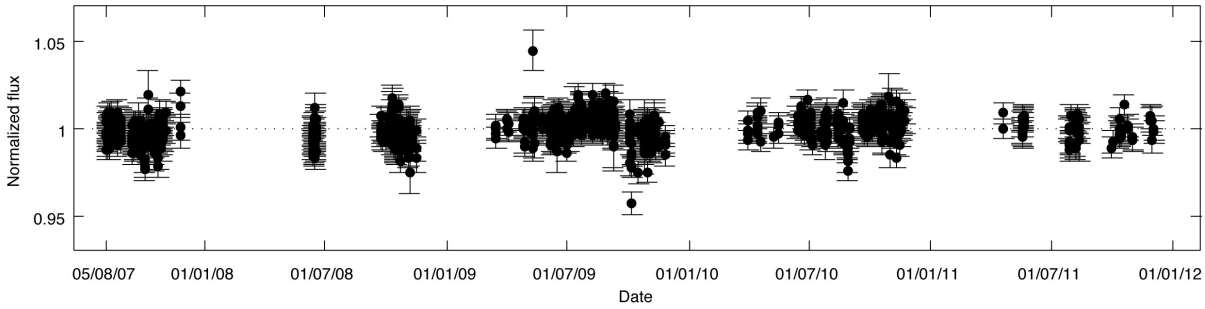

Figure 5.7: The unfolded J-band LC for `WTS1`.

frames taken under the best conditions (seeing, sky brightness and transparency) and running source detection software on the stacked image. The extracted source positions were used to perform variable aperture photometry on all of the images, resulting in a time-series of differential photometry. The final out-of-transit RMS in the `WTS1` i'-band light curve is 0.0026 (equivalent to 2.87 mmag) and is used to refine the transit model fitting procedure in Section 5.2.4. The i'-band light curve for `WTS1` is given in Table 5.3.

Table 5.2: WFCAM J-band LC of `WTS1`. The full epoch list, which contains 1 182 entries, will be available electronically.

HJD -2 400 000	Normalized flux	Error
54317.8138166	1.0034	0.0057
54317.8258565	0.9971	0.0056
...	...	...
55896.7105702	0.9979	0.0064

Table 5.3: INT i'-band LC of `WTS1`. The full epoch list, which contains 82 entries, will be available electronically.

HJD -2 400 000	Normalized flux	Error
55401.3703254	1.0244	0.0109
55401.3809041	1.0205	0.0034
...	...	...
55401.4894461	0.9936	0.0022

Broad band photometry

The WFCAM and SDSS photometric data for `WTS1` are reported in Table 5.4 with other single epoch broad band photometric observations. Johnson B V R bands were observed for `WTS1` on the night of 6th April 2012 at the University of Hertfordshire's Bayfordbury Observatory. A Meade LX200GPS 16-inch f/10 telescope fitted with an SBIG STL-6303E CCD camera was used, and the integration times was 300 s for each band. Images were bias, dark, and flat-field corrected, and extracted aperture photometry was calibrated using three bright reference stars within the image. Photometric uncertainties combine contributions from the SNR of the source (typically ∼20) with the scatter in the zero point from the calibration stars. The Two Micron All Sky Survey (2MASS, Skrutskie et al., 2006) and the Wide-field Infrared Survey Explorer (WISE, Wright et al., 2010) provide further NIR data points (J H Ks bands and $W1$ $W2$ bands respectively).

Table 5.4: Broad band photometric data of WTS1 measured within the WFCAM (Vega), SDSS (AB), 2MASS (Vega) and WISE (Vega) surveys. Johnson magnitudes in the visible are provided too (Vega). Effective wavelength λ_{eff} (mean wavelength weighted by the transmission function of the filter), equivalent width (EW) and magnitude are given for each single pass-band. The bands are sorted by increasing λ_{eff}.

Band	λ_{eff}[Å]	EW[Å]	Magnitude
SDSS-u	3546	558	18.007 (±0.014)
Johnson-B	4378	970	17.0 (±0.1)
SDSS-g	4670	1158	16.785 (±0.004)
Johnson-V	5466	890	16.5 (±0.1)
SDSS-r	6156	1111	16.434 (±0.004)
Johnson-R	6696	2070	16.1 (±0.1)
SDSS-i	7471	1045	16.249 (±0.004)
UKIDSS-Z	8817	879	15.742 (±0.005)
SDSS-z	8918	1124	16.189 (±0.008)
UKIDSS-Y	10305	1007	15.642 (±0.007)
2MASS-J	12350	1624	15.375 (±0.052)
UKIDSS-J	12483	1474	15.387 (±0.005)
UKIDSS-H	16313	2779	15.103 (±0.006)
2MASS-H	16620	2509	15.187 (±0.081)
2MASS-Ks	21590	2619	15.271 (±0.199)
UKIDSS-K	22010	3267	15.048 (±0.009)
WISE-W1	34002	6626	15.041 (±0.044)
WISE-W2	46520	10422	15.886 (±0.157)

5.2.2 Spectroscopic data

ISIS/WHT

We carried out intermediate-resolution spectroscopy of the star WTS1 over two nights between July 29 − 30, 2010, as part of a wider follow-up campaign of the WTS planet candidates, using the William Herschel Telescope (WHT) at Roque de Los Muchachos, La Palma. We used the single-slit Intermediate dispersion Spectrograph and Imaging System (ISIS). The red arm with the R1200R grating centred on 8500 Å was employed. We did not use the dichroic during the ISIS observations because it can induce systematics and up to 10% efficiency losses in the red arm, which we wanted to avoid given the relative faintness of our targets. The four spectra observed have a wavelength coverage of 8100-8900 Å. The wavelength range was chosen to be optimal for the majority of the targets for our spectroscopic observation which were low-mass stars. The slit width was chosen to match the approximate seeing at the time of observation giving an average spectral resolution $R \sim 9000$. An additional low-resolution spectrum was taken on July 16, 2010,

using the ISIS spectrograph with the R158R grating centred on 6500 Å. This spectrum has a resolution ($R \sim 1000$), a SNR of ~ 40 and a wider wavelength coverage (5000–9000 Å). The spectra were processed using the IRAF.CCDPROC package for instrumental signature removal. We optimally extracted the spectra and performed wavelength calibration using the semi-automatic KPNO.DOSLIT package. The dispersion function employed in the wavelength calibration was performed using CuNe arc lamp spectra taken after each set of exposures.

CAFOS/2.2-m Calar Alto

Two spectra of WTS1 were obtained with CAFOS at the 2.2-m telescope at the Calar Alto observatory (as a Directors Discretionary Time) in June, 2011. CAFOS is a 2k×2k CCD SITe#1d camera at the RC focus, and it was equipped with the grism R-100 that gives a dispersion of ~ 2.0 Å/pix and a wavelength coverage from 5850 to 9500 Å, approximately. Their resolving power is of around $R \sim 1900$ at 7500 Å, with a $SNR \sim 25$. The data reduction was performed following a standard procedure for CCD processing and spectra extraction with IRAF. The spectra were finally averaged in order to increase the SNR.

KPNO

A low resolution spectrum of WTS1 was observed in September 2011 with the Ritchey-Chretien Focus Spectrograph at the 4-m telescope at the Kitt Peak National Observatory (KPNO, Arizona, USA). The grism BL-181, which gives a dispersion of ~ 2.8 Å/pix, was used. Calibration, sky subtraction, wavelength and flux calibration were performed following a standard procedure for long slit observations using dedicated IRAF tasks. The ThAr arc lamp and the standard star spectra, employed for the wavelength and the flux calibration respectively, were taken directly after the science exposure. The measured spectrum covers the wavelength range 6000-9000 Å with SNR$\sim$40 at 7500 Å and has a resolution of $R \sim 1000$. This is the only flux calibrated spectrum available.

HET

In the late 2010 and in the second half of the 2011 the star WTS1 was observed during 11 nights with the HET. One science fiber was used to get the spectrum of the target star and two sky fibers were used in order to subtract the sky contamination. The cross disperser configuration '600g5271' allowed to achieve a spectral coverage of 4300-6260 Å. Only the spectral orders covering a wavelength longer than 4830 Å were analysed as the SNR was too low in the bluer part of the whole spectral range. Each science observation except one was split in two exposures, of about half an hour each. A total of 40 orders (18 from the red CCD and 22 from the blue one) cover the wavelength range 4400-6300 Å. The spectra have a SNR between 8 and 15.

5.2.3 Stellar parameters

Spectral energy distribution

Johnson (empty dots), each

A first characterization of the parent star can be performed comparing the shape of the Spectral Energy Distribution (SED), constructed from broad band photometric observations, with a grid of synthetic theoretical spectra. The data relative to the photometric bands, collected in Table 5.4, were analysed with the application VOSA (Virtual Observatory SED Analyser, Bayo et al., 2008, 2012). VOSA offers a valuable set of tools for the SED analysis, allowing the estimation of the stellar parameters. It can be accessed through its web-page interface and accepts as input file an ASCII table with the following data: source identifier, coordinates of the source, distance to the source in parsecs, visual extinction (A_V), filter label, observed flux or magnitude and the related uncertainty. Only the main intrinsic parameters of the star were fitted: effective temperature, surface gravity and metallicity. The extinction A_V was assumed as a further free parameter.

The synthetic photometry is calculated by convolving the response curve of the used filter set with the theoretical synthetic spectra. Then a statistical test is performed, via χ^2_ν minimization, to estimate which set of synthetic photometry best reproduces the observed data. The Kurucz ATLAS9 templates set (Castelli et al., 1997) were employed to fit our photometric data. These templates reproduce the SEDs in the high temperature regime better than the NextGen models (Baraffe et al., 1998), more suitable at lower temperatures ($< 4500\,K$).

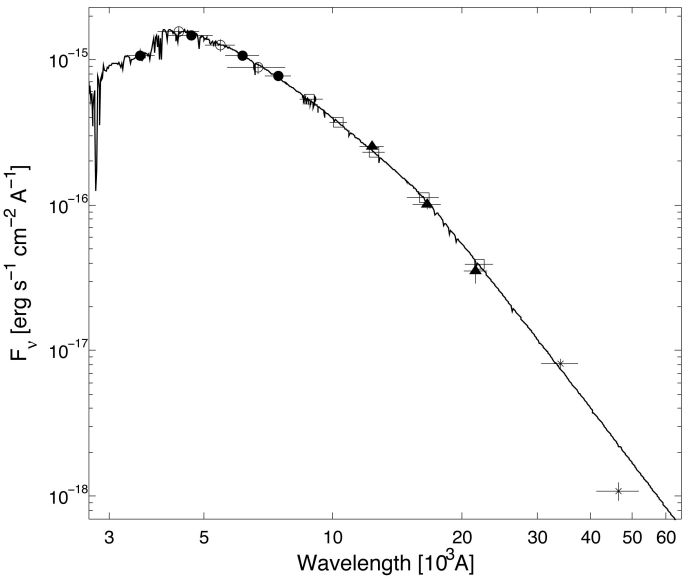

Figure 5.8: Broad band photometric data of `WTS1`: SDSS (filled dots), Johnson (empty dots), WFCAM (squares), 2MASS (triangles) and WISE (stars). The best fitting template (black line) is the ATLAS9 Kurucz $T_{\rm eff}$=6500 K, log g=4.5, [Fe/H]=-0.5 model with A_V=0.44. Vertical errorbars correspond to the flux uncertainties while those along the X-axis represent the EW of each band (see Table 5.4).

In order to speed up the fitting procedure, the range of $T_{\rm eff}$ and log g were restricted to 3500-8000 K and 3.0-5.0, respectively. These constrains in the parameter space did not affect the final results as it was checked a posteriori that the same results were obtained considering the full available range for both parameters. The resulting best fitting synthetic template, plotted in Figure 5.8 with the photometric data, corresponds to the $T_{\rm eff}$=6500 K, log g=4.5 and [Fe/H]=-0.5 Kurucz model with

A_V=0.44. Uncertainties on the parameters were estimated both using χ^2_ν statistical analysis and a bayesian (flat prior) approach. The related errors result to be of the order of 250 K, 0.2, 0.5 and 0.07 for $T_{\rm eff}$, log g, [Fe/H] and A_V, respectively.

As it can be seen in Figure 5.8, the WISE $W2$ data point is not consistent with the best fitting model. Firstly, it is worth noting that the observed value of $W2 = 15.886$ ($\pm$0.157) is below the 5 sigma point source sensitivity expected in the $W2$-band (> 15.5). The number of single source detections used for the $W2$-band measurement is also considerably less than that of the $W1$-band (4 and 19 respectively) increasing the uncertainty in the measurement. Finally, the poor angular resolution of WISE in the $W2$-band (6.4″) could add further imprecisions to the final measured flux, especially in a field as crowded as the WTS 19hrs field. For these reasons, the WISE $W2$ data point was not considered in the fitting procedure.

Once the magnitude values were corrected for the interstellar absorption according to the best fitting value (A_V=0.44$\pm$0.07), colour – temperature relations were used to further check the effective temperature and spectral type of the host star. From the SDSS g and r magnitudes, we obtained a value of $(B\text{-}V)_0$=0.43$\pm$0.04 (Jester et al., 2005) which imply $T_{\rm eff}$=6300$\pm$600 K assuming log g=4.4 and [Fe/H]=-0.5 (Sekiguchi & Fukugita, 2000). Following the appendix B of Collier Cameron et al. (2007), the 2MASS $(J - H)$ index of 0.23$\pm$0.09 leads to a value of $T_{\rm eff}$=6200$\pm$400 K while Table 3 of Covey et al. (2007) suggests the host star to be a late-F considering different colour indices at once. These results are all compatible within the uncertainties.

Spectroscopic analysis

The spectroscopic spectral type determination was done firstly by comparing the spectrum observed with CAFOS with a set of spectra of template stars. Stars of different spectral types, uniformly spanning the F5 to G2 range, were observed with the same instrumental setting. Since the observed spectrum has a relatively low SNR, the analysis focused on the strongest features present which are the Hα (6562.8 Å) and the Ca II triplet (8498.02 Å, 8542.09 Å, 8662.14 Å). The best match was obtained, via minimization of the RMS of the difference between the `WTS1` and template star spectra, with the spectrum of an F6V star with solar metallicity.

Afterwards, the estimation of the stellar parameters was performed comparing the observed spectrum with a simulated spectrum with known parameters. For that aim, a library of high resolution synthetic stellar spectra by Coelho et al. (2005) was used, created by the PFANT code (Barbuy, 1982; Cayrel et al., 1991; Barbuy et al., 2003) that computes a synthetic spectrum assuming local thermodynamic equilibrium (LTE). The synthetic spectra were achieved using the model atmospheres presented by Castelli & Kurucz (2003). Since the core of these lines are strongly affected by cumulative effects of the chromosphere, non-LTE and inhomogeneity of velocity fields, a spectrum of the Sun observed with HIRES spectrograph at the Keck telescope (Vogt et al., 1994) was first compared. The spectrum of the Sun was degraded to lower resolution and resampled to match the CAFOS spectrum specifications to see how such effects appear at this resolution and

how different the solar spectrum is from a synthetic spectrum from the library by Coelho and collaborators. Looking at the upper plots in Figure 5.9, we concluded that the cores of the lines in the simulated spectrum are systematically higher than those in the observed spectrum of the Sun. Nevertheless, the Ca II triplet line at 8498.02 Å seems to be less affected by the above-mentioned problems. Considering these differences between central depth of the observed and simulated spectra in the best fitting procedure, we estimated that the synthetic model with $T_{\rm eff}$=6250 K, log g=4.5 and [Fe/H]=0.0 best reproduces the observed spectrum of `WTS1`. The expected uncertainties are of the order of the step size of the used library ($\delta T_{\rm eff}$=250 K, δlog g=0.5 and δ[Fe/H]=0.5).

synthetic spectra match

The high resolution HET spectra were employed to attempt a more detailed spectroscopic analysis of the host star. The spectra observed each single night were stacked together obtaining a final spectrum with a SNR of about 12, calculated over a 1 Å region at 5000 Å. To compute model atmospheres, LLmodels stellar model atmosphere code (Shulyak et al., 2004) was used. For all the calculations, LTE and plane-parallel geometry were as-

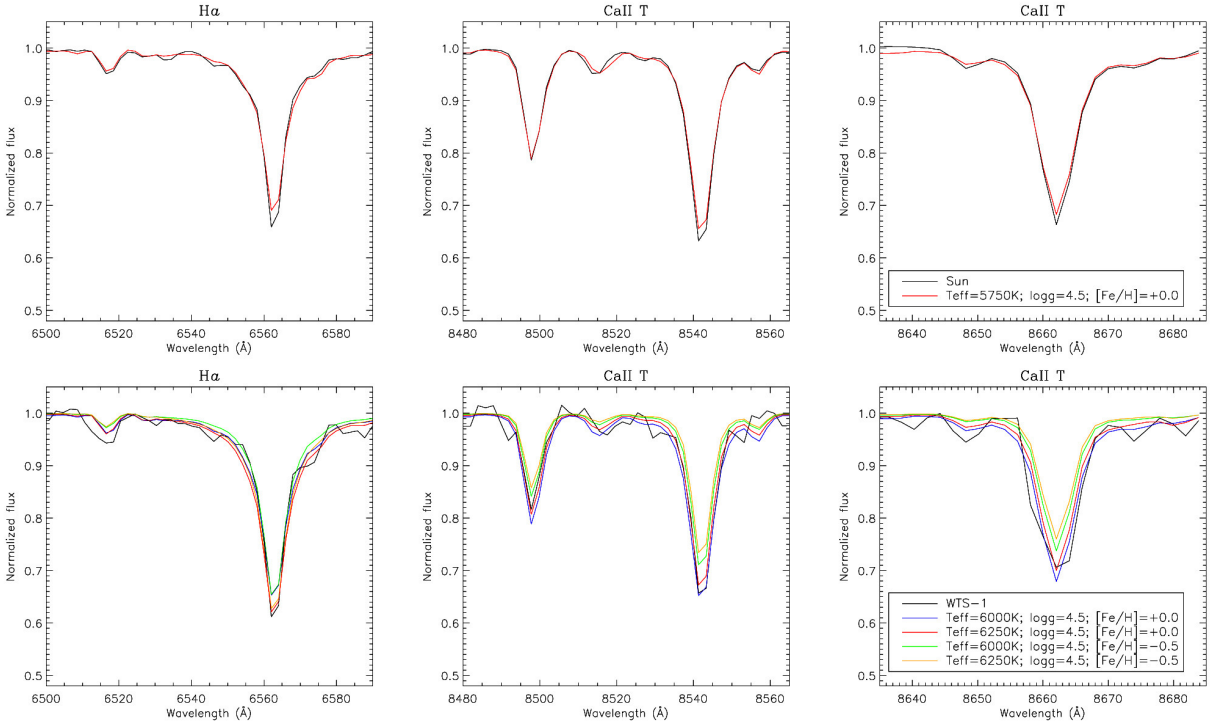

Figure 5.9: *Upper row*: comparison of a degraded spectrum of the Sun (black) with a synthetic spectrum (red) computed with $T_{\rm eff}$=5750 K, log g=4.5 and [Fe/H]=0.0. *Lower row*: comparison of the `WTS1` spectrum (black) with different synthetic spectra (colours). The comparison between the observed `WTS1` spectrum and the synthetic models took into account the differences of the core of the lines shown in the upper row plots. From this analysis, the best fitting model is the one with $T_{\rm eff}$=6250 K, log g=4.5 and [Fe/H]=0.0.

sumed. The VALD database (Piskunov et al., 1995; Kupka et al., 1999; Ryabchikova et al., 1999) was used as a source of atomic line parameters for opacity calculations with the LLmodels code. Finally, convection was implemented according to the Canuto & Mazzitelli (1991) model of convection.

The parameter determination and abundance analysis were performed iteratively, self-consistently recalculating a new model atmosphere any time one of the parameters, including the abundances, changed. As a starting point, the parameters derived from the CAFOS spectrum was adopted. The atmospheric parameter determination was performed by imposing the iron excitation and ionization equilibria making use of equivalent widths measured for all available unblended and weakly blended lines. The equivalent width of each line was converted into an abundance value with a modified version (Tsymbal, 1996) of the WIDTH9 code (Kurucz, 1993). Unfortunately, the faintness of the observed star, coupled with the calibration process (including the sky subtraction), led to a distortion of the stronger lines, weakening their cores. For this reason, the analysis took into account only the measurable weak lines, making therefore impossible a determination of the microturbulence velocity (v_{mic}), which was fixed at a value of 0.85 km s^{-1} (Valenti & Fisher et al.,

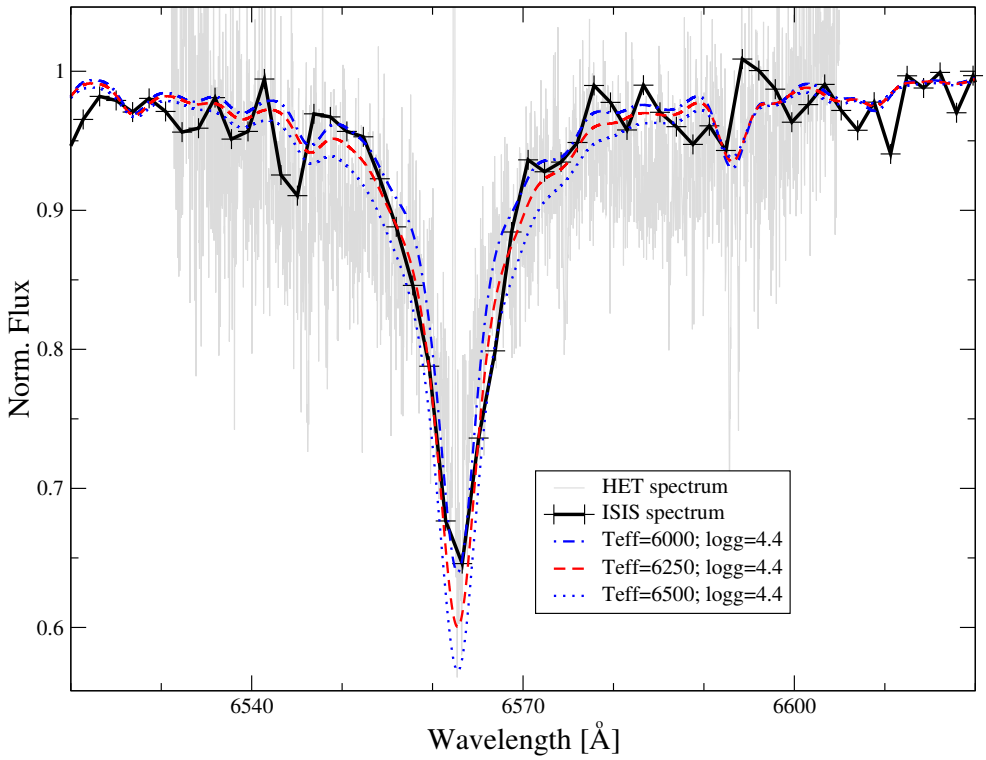

Figure 5.10: Intermediate resolution ISIS spectrum (black line) and high resolution HET spectrum (grey line) of the Hα line of WTS1 in comparison with synthetic spectra calculated with different effective temperatures of 6000 K (blue dash-dotted line), 6250 K (dashed line; finally adopted $T_{\rm eff}$), and 6500 K (blue dotted line). The synthetic spectra were convolved in order to match the resolution of the ISIS spectrum.

2005). With the fixed v_{mic}, the Fe excitation and ionization equilibria were imposed, which led to an effective temperature of 6000±400 K and a surface gravity of 4.3±0.4. Imposing the ionization equilibrium the expected non-LTE effects for Fe I (∼0.05 dex, Mashonkina, 2011) were taken into account, while for Fe II non-LTE effects are negligible.

In this temperature regime, the ionization equilibrium is sensitive to both $T_{\rm eff}$ and $\log g$ variations, therefore it is important to simultaneously and independently further constrain temperature and/or gravity. For this reason we looked at the Hα line to further constrain $T_{\rm eff}$, as in this temperature regime Hα is sensitive primarily to temperature variations (Fuhrmann et al., 1993). We did this by fitting synthetic spectra, calculated with SYNTH3 (Kochukhov, 2007), to the Hα line profile observed in the HET high resolution and in the ISIS/WHT low resolution spectra. As the Hα line of the HET spectrum was also affected by the before mentioned reduction problems, only the wings of the line were considered. Although we could calculate synthetic line profiles of Hα on the basis of atmospheric models with any $T_{\rm eff}$, because of the low SNR of our spectra, we performed the line profile fitting on the basis of models with a temperature step of 100 K (Fuhrmann et al., 1993, small variations in gravity and metallicity are negligible). From the fit of the Hα line we obtained a best fitting $T_{\rm eff}$ of 6100±400 K. Further details on method, codes

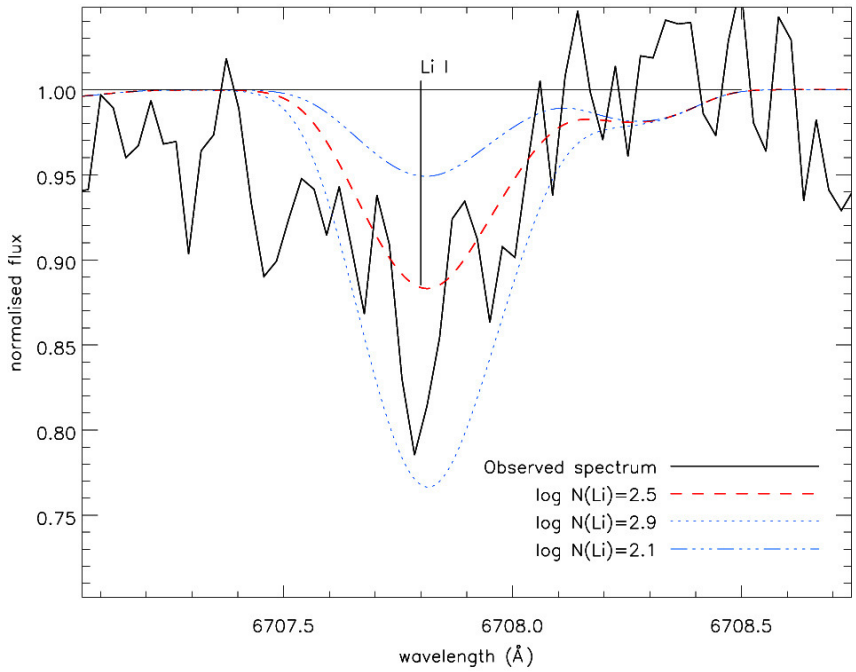

Figure 5.11: High-resolution HET stacked spectrum (black full line) of the WTS1 Li I line at ∼6707 Å in comparison with three synthetic spectra calculated with the final adopted stellar parameters and lithium abundances (log N(Li)) of 2.5 (red dashed line), 2.9 (blue dotted line), and 2.1 (blue dash-dotted line). The vertical line indicates the position of the centre of the multiplet.

and techniques can be found in Fossati et al. (2009), Ryabchikova et al. (2009), Fossati et al. (2011) and references therein. Figure 5.10 shows the Hα line profile observed with ISIS and HET in comparison with synthetic spectra calculated assuming a reduced set of stellar parameters. On the basis of the previous analysis, we finally adopted Teff=6250±250 K, log g=4.4±0.1. With this set of parameters and the equivalent widths measured with the HET spectrum, a final metallicity of -0.5±0.5 dex dex was derived, where the uncertainty takes into account the internal scatter and the uncertainty on the atmospheric parameters. By fitting synthetic spectra, calculated with the final atmospheric parameters and abundances, to the observation, we derived a projected rotational velocity v $sin(i)$=7±2 km s^{-1}.

The HET spectrum allowed us to measured the atmospheric lithium abundance from the Li I line at ∼6707 Å. Lithium abundance is important as it can constrain the age of the star (see Section 5.2.3). As this line presents a strong hyperfine structure and is slightly blended by a nearby Fe I line, we measured the Li I abundance by means of spectral synthesis, instead of equivalent widths. By adopting the meteoritic/terrestrial isotopic ratio Li6/Li7=0.08 by Rosman & Taylor (1998), we derived log N(Li)=2.5±0.4 (corresponding to an equivalent width of 41.12±24.40 mÅ), where the uncertainty takes into account the uncertainty on the atmospheric parameters, $T_{\rm eff}$ in particular (see Figure 5.11).

The low resolution spectrum obtained at the KPNO observatory, being the only flux calibrated spectrum, was compared to the Kurucz ATLAS9 templates set (the same employed in the SED analysis in Section 5.2.3). The limited wavelength range covered by the observed spectrum (3000 Å), allowed to achieve usable results fitting only one parameter of the template spectra. We therefore decided to leave $T_{\rm eff}$ as a free parameter, fixing the other quantities to log g=4.5, [Fe/H]=-0.5 and A_V=0.44. We concluded that the temperature range 6000-6500 K brackets the $T_{\rm eff}$ with 95% confidence level.

Properties of the host star WTS-1

The atmospheric parameters of the star `WTS1` were computed combining the results coming from the analysis described in the previous sections. We finally obtained an effective temperature of 6250±200 K, a surface gravity of 4.4±0.1 and a metallicity range $-0.5 \div 0.0$ dex. As described in Section 5.2.3, the faintness of the star and the reduction process led to a distortion of the stronger lines in the HET high resolution spectrum, reducing the number of reliable lines employed in the measure of the metallicity. For these reasons, the relative uncertainty on the metallicity is larger with respect to those of the other parameters. Further observations would be needed to pin down the exact value of the star metallicity.

In order to determine the parameters of the stellar companion, mass and radius of the host star must be known. The fit of the transit in the light curves provides important constrains on the mean stellar density (see Section 5.2.4). Joining this quantity to the effective temperature, we could place `WTS1` in the modified $\rho_s^{-1/3}$ vs. $T_{\rm eff}$ H-R diagram and compare its position with evolutionary tracks and isochrones models (Girardi et al., 2000) in order to estimate stellar mass and age. In this way, we estimated the stellar mass to be 1.2±0.1 $M_\odot$ and the age of the system to range between 200 Myr and 4.5 Gyr.

Table 5.5: Properties of the WTS1 host star.

Parameter	Value
Spectral type	F6-8
$T_{\rm eff}$	6250±200 K
log g	4.4±0.1
[Fe/H]	[-0.5, 0] dex
M_s	1.2±0.1 $M_\odot$
R_s	$1.15^{+0.10}_{-0.12}$ $R_\odot$
m_V	16.13±0.04
M_V	$3.55^{+0.27}_{-0.38}$
v $sin(i)$[a]	7±2 km s^{-1}
ρ_s	$0.79^{+0.31}_{-0.18}$ $\rho_{\rm sun}$
Age	[0.6, 4.5] Gyr
Distance	$3.2^{+0.9}_{-0.4}$ kpc
True space motion U[c]	13±28 km s^{-1}
True space motion V[c]	20±38 km s^{-1}
True space motion W[c]	-12±26 km s^{-1}

[a] We assumed v_{mic}=0.85 km s^{-1};
[b] Epoch J2000;
[c] Left-handed coordinates system (see text).

Further constrains on the stellar age can be fixed considering the measured Li I line abundance. Depletion of lithium in stars hotter than the Sun is thought to be due to a not yet clearly identified slow mixing process during the main-sequence evolution, because those stars do not experience pre-main sequence depletion (Martin, 1997). Comparison of the lithium abundance of WTS1 (log N(Li)=2.5±0.4) with those of open clusters rise the lower limit on the age to 600 Myr, because younger clusters do not show lithium depletion in their late-F members (Sestito & Randich, 2005). On the other hand, it is not feasible to derive an age constrain from the WTS1 rotation rate (v $sin(i)$=7±2 km s^{-1}) because stars with spectral types earlier than F8 show no age-rotation relation (Wolff et al., 1986) and thus they are left out from the formulation of the spin down rate of low-mass stars (Stepien, 1988).

The true space motion knowledge of WTS1 allows to determine to which component of our Galaxy it belongs. In order to compute the U, V and W components of the motion,

the following set of quantities was required: distance, systemic velocity (from the RV fit, see Section 5.2.4), proper motion (from SDSS 7^{th} release, Munn et al., 2004, 2008) and coordinates of the star. The distance to the observed system was estimated according to the extinction, fitted in the SED analysis (A_V=0.44 ± 0.07), and a model of dust distribution in the galaxy (Amôres & Lépine, 2005, axis-symmetric model). The UVW values and their errors are calculated using the method in Johnson & Soderblom (1987), with respect to the Sun (heliocentric) and in a left-handed coordinate system, so that they are positive away from the Galactic centre, Galactic rotation and the North Galactic Pole respectively. All the quantities here discussed are listed in Table 5.5. Considering the uncertainties on the derived quantities, maily affected by the error on the distance, the host star is consistent with both the definitions of Galactic young-old disk and young disk populations (metallicity between -0.5 and 0 dex, solar-metallicity respectively, Leggett, 1992). But we could assess that `WTS1` is not a halo member.

Combining ρ_s and M_s, a value of $1.15^{+0.10}_{-0.12}\,R_\odot$ was computed for the stellar radius. The same result was obtained considering the stellar mass and the surface gravity measured from the spectroscopic analysis. Scaling by the distance the apparent V magnitude calculated from the SDSS g and r magnitudes (Jester et al., 2005), we computed an absolute V magnitude of $3.55^{+0.27}_{-0.38}$. This value and all the other derived stellar parameters are consistent with each other and with the typical quantities expected for an F6-8 main-sequence star (Torres & Lacy, 2009). They are collected in Table 5.5.

5.2.4 Planetary parameters

Transit fit

The light curves in J- and i'-band were fitted with analytic models presented by Mandel & Agol (2002) (see Appendix B). We used quadratic limb-darkening coefficients for a star with effective temperature $T_{\rm eff}$=6250 K, surface gravity log g=4.4 and metallicity [Fe/H]=-0.5 dex, calculated as linear interpolations in $T_{\rm eff}$, log g and [Fe/H] of the values tabulated in Claret & Bloemen (2011). We use their table derived from ATLAS atmospheric models using the flux conservation method which gave a slightly better fit than the ones derived using the least-squares method. The values of the limb-darkening coefficients we used in our fitting are given in Table 5.6. Scaling factors were applied to the error values of the J- and i'-band light curves (0.94 and 0.9 respectively) in order to achieve a reduced χ^2 of

Table 5.6: Quadratic limb-darkening coefficients used for the transit fitting, for a star with effective temperature $T_{\rm eff}$=6250 K, surface gravity log g=4.4 and metallicity [Fe/H]=-0.5 dex (Claret & Bloemen, 2011).

filter	γ_1	γ_2
J	0.14148	0.24832
i′	0.25674	0.26298

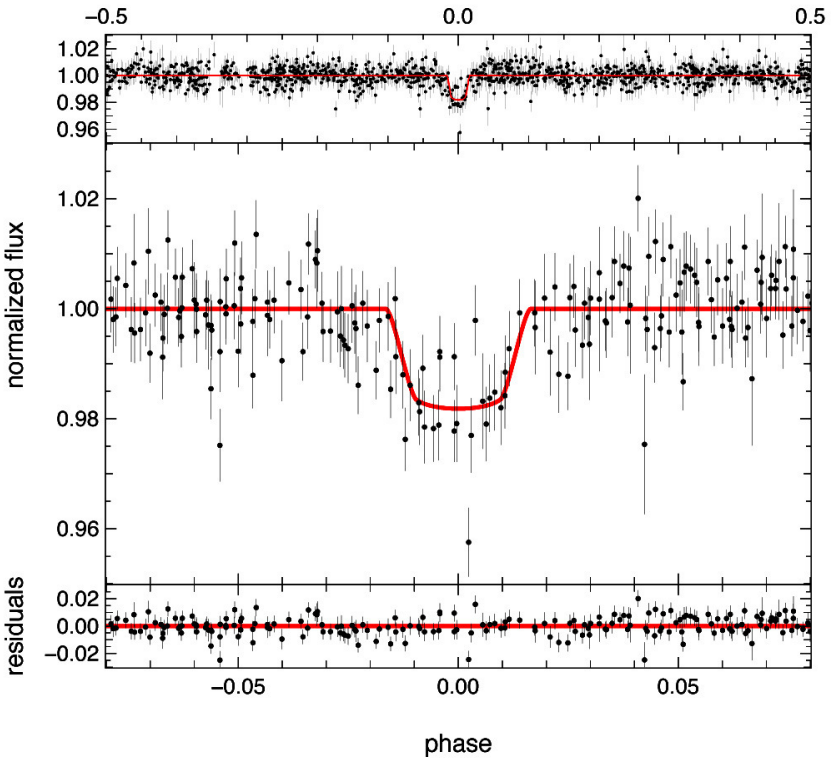

Figure 5.12: WFCAM J-band light curve data of WTS1. *Upper panel*: whole set of the folded WFCAM J-band data points. *Middle panel*: folded photometric data centred in the transit and best model (red line) fitted in combination with the INT i′-band data. *Lower panel*: residuals of the best fit.

the constant out-of-transit part equal to 1.

Using a simultaneous fit to both light curves, we fitted the period P, the time of the central transit t_0, the radius ratio R_p/R_s, the mean stellar density, $\rho_s = M_s/R_s^3$ in solar units and the impact parameter $\beta_{\rm impact}$ in units of R_s. The light curves and the model fit are shown in Figures 5.12 and 5.13, while the resulting parameters are listed in Table 5.7. The errors were calculated using a multi-dimensional grid on which we search for extreme grid points with $\Delta\chi^2$=1 when varying one parameter and simultaneously minimizing over the others.

Considering the solar metallicity scenario, with different limb-darkening coefficients, the change in the final fitting parameters is smaller than 1% of their uncertainties. Note that the combined fit assumes a fixed radius ratio although in a hydrogen-rich atmosphere, molecular absorption and scattering processes could result in different radius ratios in each band (an attempt to detect such variations has recently been undertaken by de Mooij et al., 2012). In our case, the uncertainties are too large to see this effect in the light curves and the assumption of a fixed radius ratio is a good approximation. The estimated stellar density of the host star ($0.79^{+0.31}_{-0.18}$ $\rho_{\rm sun}$) is consistent with the expected value based on its

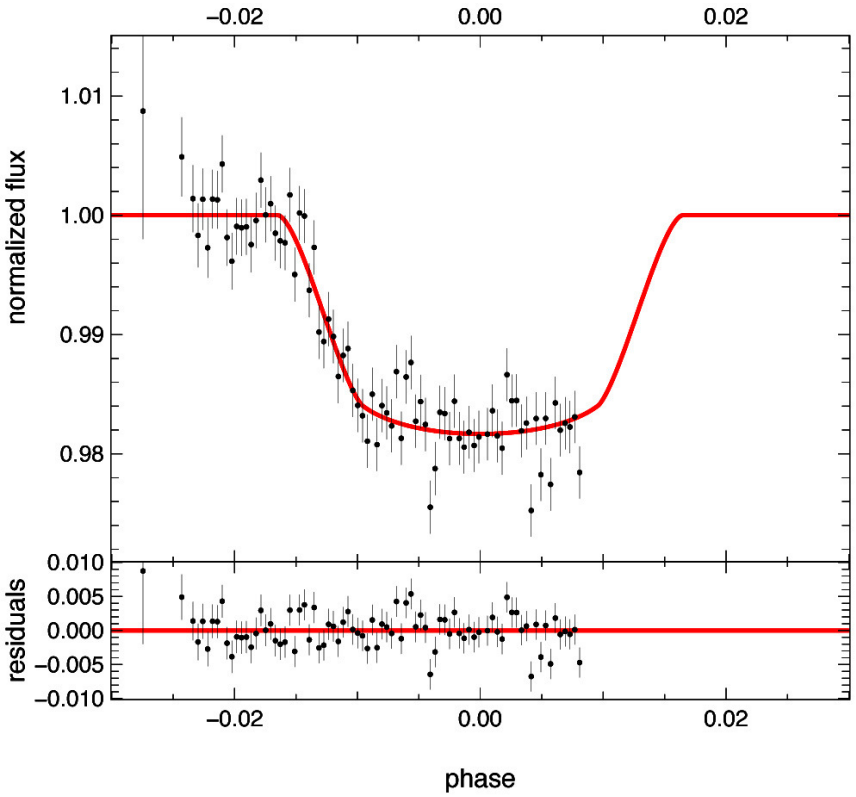

Figure 5.13: INT i'-band light curve data of `WTS1`. *Upper panel*: photometric data and best model (red line) fitted in combination with the WFCAM J-band data. *Lower panel*: residuals of the best fit.

spectral type (Seager & Mallén-Ornelas, 2003). The noise in the data did not allow a secondary transit detection.

Subsequently, we searched for further periodic signals in the light curve after the removal of the data points related to the transit. No significant signals were detected in the Lomb-Scargle periodogram up to a period of 400 days. Since `WTS1` is a late F-star, there are not many spots on the surface and they do not live long enough to produce a stable signal over a timescale of several years.

Radial velocity

One of the most pernicious transit mimics in the WTS are eclipsing binaries. On one hand, a transit can be mimicked by an eclipsing binary that is blended with foreground or background star. On the other hand, grazing eclipsing binaries with near-equal radius stars also have shallow, near-equal depth eclipses that can phase-fold into transit-like signals at half the binary orbital period. In order to rule out the eclipsing binaries scenarios, the RV variation of the WTS-1 system were first measured using the ISIS/WHT intermediate resolution spectra. Eclipsing binaries systems typically show RV amplitudes of tens of km s^{-1},

Table 5.7: Fitted parameters of the WTS1 system as determined from the simultaneous fit of the J- and i'-band light curves. Scaling factors to the uncertainties of the J and i' data points (0.94 and 0.9 respectively) were applied in order to achieve a reduced χ^2=1 in the constant out-of-transit part of the light curves.

Parameter		Value
P_{orb}	=	$3.352059^{+1.2\times10^{-5}}_{-1.4\times10^{-5}}$ days
t_0	=	$2\,454\,318.7472^{+0.0043}_{-0.0036}$ HJD
R_p/R_s	=	$0.1328^{+0.0032}_{-0.0035}$
ρ_s	=	$0.79^{+0.31}_{-0.18}$ $\rho_{\rm sun}$
$\beta_{\rm impact}$	=	$0.69^{+0.05}_{-0.09}$

while the measured RVs were all consistent with a flat trend within the RV uncertainties of $\sim 1\,\mathrm{km\ s^{-1}}$.

Afterwards, we analysed the high-resolution HET spectra in order to accurately investigate the properties of the sub-stellar companion of WTS1. The spectra related to each single night were cross-correlated using the IRAF.RV.FXCORR task with the synthetic spectrum of

Table 5.8: RVs and BSs measurements for WTS1 obtained by HET spectra. The phases were computed from the epochs of the observations expressed in Julian date and using the P and t_0 values found with the transit fit.

HJD -2 400 000	Phase	RV [km s^{-1}]	BS [km s^{-1}]
55477.676	0.74	-1.46 ± 0.12	-0.31 ± 0.40
55479.666	0.33	-1.80 ± 0.10	-0.77 ± 0.39
55499.608	0.28	-2.03 ± 0.10	0.76 ± 0.51
55513.586	0.45	-2.06 ± 0.17	0.87 ± 0.63
55522.556	0.13	-2.09 ± 0.44	-0.39 ± 0.35
55523.542	0.42	-1.70 ± 0.16	-0.13 ± 0.44
55742.729	0.26	-1.97 ± 0.15	0.27 ± 0.68
55760.673	0.79	-1.11 ± 0.12	-0.47 ± 0.59
55782.837	0.22	-2.23 ± 0.07	0.41 ± 0.39
55824.722	0.25	-2.31 ± 0.06	0.16 ± 0.56
55849.650	0.75	-1.19 ± 0.06	0.18 ± 0.31

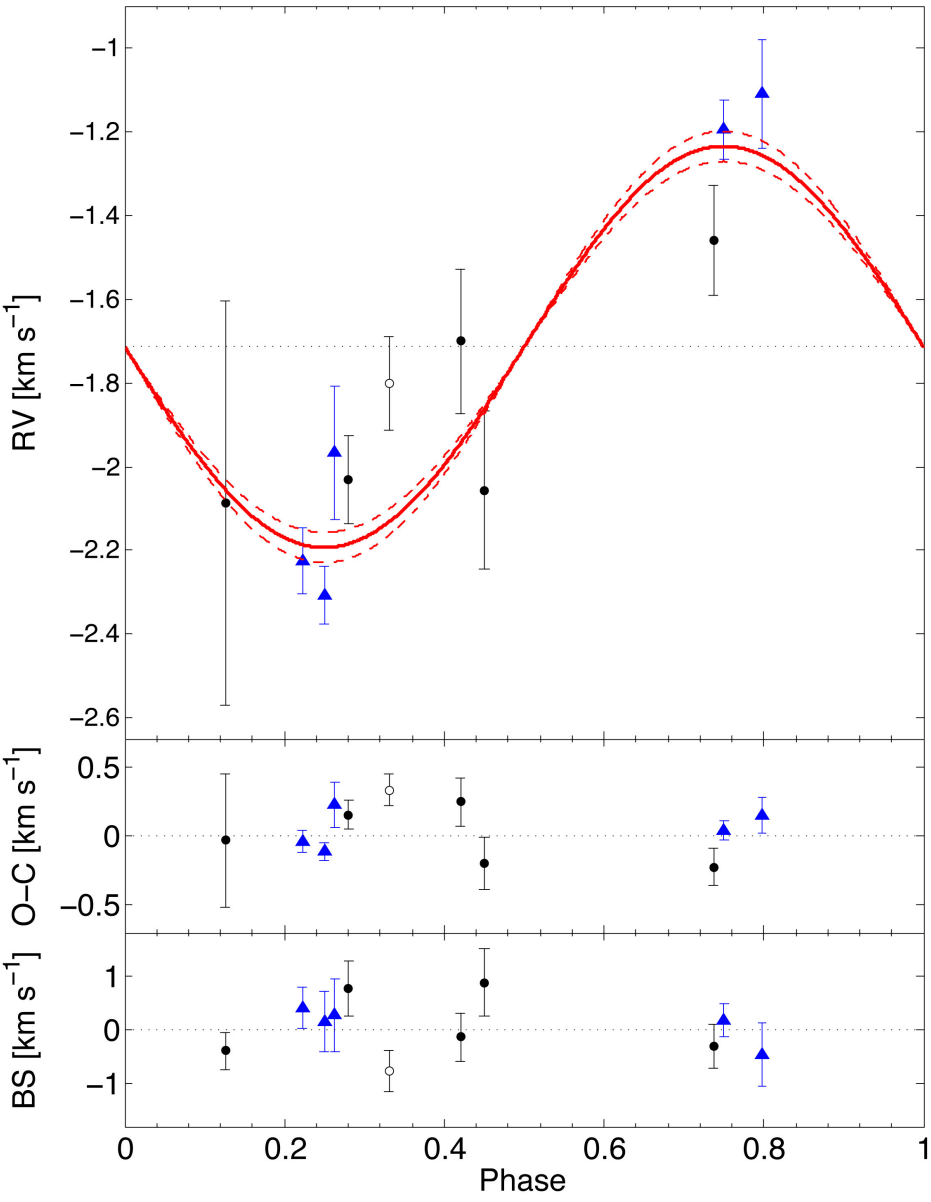

Figure 5.14: *Top panel*: RV values measured with the high-resolution HET spectra of `WTS1` as a function of the orbital phase. Black dots and blue triangles refers to observations performed in 2010 and 2011 respectively. The data point at $\phi = 0.33$, empty dot, was excluded from the fitting procedure (see text for details). Best-fit circular orbit model (χ^2_ν=1.45) and 1σ uncertainty of the semi-amplitude ($K_\star$=479±34 m s^{-1}) are indicated with solid and dashed red lines respectively. The black dotted line refers to the fitted radial systemic velocity (γ=-1 714±35 m s^{-1}). Zero phase corresponds to the mid-transit time. *Middle panel*: Phase folded O-C residuals from the best-fit. The residual scatter is of the order of $\sim$ 150 m s^{-1}, consistent with the RVs uncertainties. *Bottom panel*: Bisector spans. No significant deviations from zero and no correlation with the RVs were found.

a star with $T_{\rm eff}$=6250 K, log g=4.4 and [Fe/H]=-0.5. Changes in the effective temperature of the synthetic templates, even of the order of several hundreds of Kelvin, cause variations of the measured RV values smaller than the statistical uncertainties due to noise in the spectra (suggesting the absence of contamination of back/foreground stars of different spectral type). Even smaller variations occur changing surface gravity and metallicity of the template. The 40 single RV values, each one coming from a different order, were used to compute the RVs and related uncertainty at each epoch of the observations. Resampling statistical tools were used in order to better estimate mean value, standard deviation and possible bias in the sample of measured RVs. Finally, the measured RVs were corrected for the Earth orbital movements and reduced to the heliocentric rest frame. The phase values ϕ were computed from the epochs of the observations, expressed in Julian date, and using the extremely well determined P and t_0 values (relative uncertainties are of the order of 10^{-6} and 10^{-9} respectively) obtained from the photometric fit (see Table 5.7).

The data, listed in Table 5.8, were then fitted with a simple two parameters sinusoid of the form:

$$RV = \gamma + K_{\star} sin(2\pi\phi) \tag{5.2}$$

where $K_{\star}$ is the RV semi-amplitude of the host star and γ is the systemic velocity of the system. Thanks to the acquisition of two ThAr calibration exposures (before and after the science exposure, see Section 5.2.2), we detected a small drift between the ThAr lines occurring during the science exposures on November 22, 2010. In the presence of a suspected systematic trend, which could affect the measured RV value, we performed the fitting procedure excluding the data point related to that night (at $\phi = 0.33$). The larger RV error of the data point at $\phi = 0.13$ is due to the integration time (half hour) of the science frame which is shorter than those of all the other data points (one hour). The best fitting model (χ^2_{ν}=1.45) was obtained for $K_{\star}$=479±34 m s^{-1}and γ=-1 714±35 m s^{-1}and is plotted in Figure 5.14 with the RV data. We imposed the orbit to be circular as the eccentricity was compatible with zero when a Keplerian orbit fit (see Appendix A) was performed (see Anderson et al. (2012) for a discussion of the rationale for this). In accordance to the RV uncertainties, a relatively loose upper limit can be plaved on the eccentricity ($e < 0.1$, C.L.= 95%). The fitted RV semi-amplitude implies a planet mass of 4.01±0.35 M_J assuming a host star mass of 1.2±0.1 $M_{\odot}$ (see Section 5.2.3). The uncertainty on the planet mass in mainly driven by the uncertainty on the mass of the host star. As can be seen in Figure 5.14, the RVs related to observations performed in late 2010 and in the second half of 2011 are consistent, showing no significant long term trends in our measurements.

The HET spectra were employed also to investigate the possibility that the measured RVs are not due to true Doppler motion in response to the presence of a planetary companion. Similar RV variations can rise in case of distortions in the line profiles due to stellar atmosphere oscillations (Queloz et al., 2001). To assert that this is not our case, we used the same cross-correlation profiles produced previously for the RV calculation to compute the bisector spans (BS) which are reported in Table 5.8. Following Torres et al. (2005), we measured the difference between the bisector values at the top and at the bottom of the correlation function for the different observation epochs. In case of contaminations, we

would have expected to measure BS values consistently different from zero and a strong correlation with the measured RVs (Queloz et al., 2001; Mandushev et al., 2005). As it can be seen in the bottom panel of Figure 5.14, the measured BS do not show significant deviation from zero within the uncertainties. No correlation was detected between the BS and the RV values. In this way, contaminations that could mimic the effect of the presence of a planet were ruled out.

5.2.5 Discussion

The parameters of the new transiting extrasolar planet `WTS1 b` are collected in Table 5.9. It is a $\sim$4 M_J planet orbiting in 3.35 days a late F-star with possibly slightly subsolar metallicity. With a radius of $1.49^{+0.16}_{-0.18}$ R_J, it is located in the upper part of the mass – radius diagram of the known extrasolar planets in the mass range 3-5 M_J (see Figure 5.15). The parameters of the other planets are taken from *www.exoplanet.eu* at the time of this work. Planets with only an upper limit on the mass and/or on the radius are not shown. It is worth noting that only a cut-off of the transit depth, different for each survey, could act as a selection effect against the detection of planets in this upper portion of the diagram. Larger planetary radii imply a deeper transit feature in the light curves and thus, within this mass range, larger object are more easily detectable. The properties of `WTS1 b`, as well as those of the other two planets present in the upper part of the diagram, CoRoT-2b (Alonso et al., 2008) and OGLE2-TR-L9b (Snellen et al., 2009), are not explained within standard formation and evolution models of isolated gas giant planets (Guillot, 2005).

Table 5.9: Properties of the new extrasolar planet `WTS1 b`.

Parameter	Value
M_p	4.01 ± 0.35 M_J
R_p	$1.49^{+0.16}_{-0.18}$ R_J
P_{rot}	$3.352057^{+1.3\times10^{-5}}_{-1.5\times10^{-5}}$ d
a	0.047 ± 0.001 AU
e	< 0.1 (C.L.= 95%)
inc	$85.5^{+1.0}_{-0.7}$ °
$\beta_{\rm impact}$	$0.69^{+0.05}_{-0.09}$
t_0	$2\,454\,318.7472^{+0.0043}_{-0.0036}$ HJD
ρ_p	1.61 ± 0.56 $g\ cm^{-3}$, 1.21 ± 0.42 ρ_J
T_{eq} [a]	1500 ± 100 K

[a] We assumed a Bold albedo A_B=0 and re-irradiating fraction F= 1;

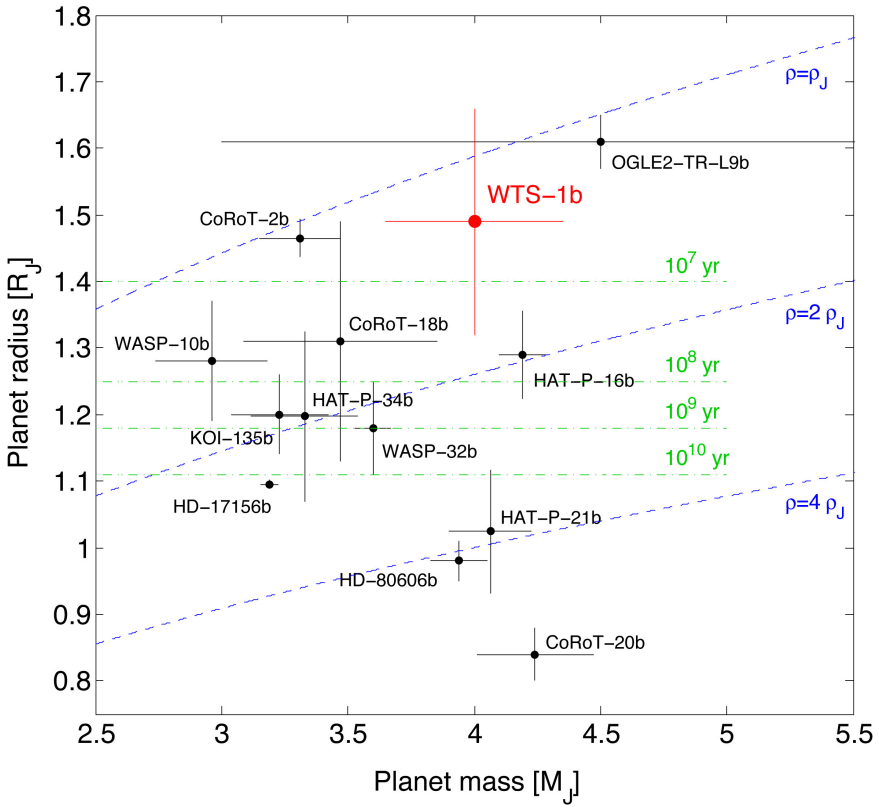

Figure 5.15: Mass – Radius diagram of the known planets with a mass in the range 3-5 M_J (black dots). Labels with the related planet name are shown for an easier identification. Planets with only an upper limit on mass and/or radius are not shown. The blue dashed lines represent the iso-density curves. The green dot-dashed lines indicate the planetary radii at different ages accordingly to Fortney et al. (2007) (see text for details). Masses, radii of the planets are taken from *www.exoplanet.eu* at the time of this work, while the related uncertainties were found in the refereed publication. `WTS1 b` is shown in red.

The radius anomaly is at the $\sim 2\sigma$ level considering the stellar irradiation that retards the contraction of the planets, the distance of the planet from the host star and the age of the planet (Fortney et al., 2007). The models of Fortney and collaborators predict indeed a radius of 1.2 R_J for a 600 Myr-old planet (see their Figure 5, 3 M_J and 0.045 AU model). This radius estimate is an upper limit as 600 Myr is the lower limit on the age of the `WTS1` system due to the Li abundance (see Section 5.2.3). The radius trend shown in the figure would suggest an age for `WTS1 b` less than 10 Myr. The same significance on the radius anomaly is obtained considering empirical relationships coming from the fit of the observed radii as a function of the physical properties of the star-planet system, such as mass, equilibrium temperature and tidal heating (Enoch et al., 2012, eq. 10). In any case, a rapid migration of `WTS1 b` inward to the highly-irradiated domain after its formation seems required.

Surface day/night temperature gradients due to the strong incident irradiation, are likely to generate strong wind activity through the planet atmosphere. Recently, Wu & Lithwick (2012) showed how the Ohmic heating proposal (Batygin & Stevenson, 2010b; Perna et al., 2010) can effectively bring energy in the interior of the planet and slow down the cooling contraction of a HJ even on timescales of several Gyr: a surface wind blowing across the planetary magnetic field acts as a battery that rises Ohmic dissipation in the deeper layers. In Huang & Cumming (2012), the Ohmic dissipation in HJs is treated decoupling the interior of the planet and the wind zone. In this scenario, the radius evolution for an irradiated HJ planet (see their Figure 9, $3\,M_J$) leads to a value consistent with our observation up to 3 Gyr.

Accordingly to Fortney et al. (2008), the incident flux (the amount of energy from the host star irradiation, per unit of time and surface, that heats the surface of the planet) computed for `WTS1 b` ($1.12\pm0.26 \cdot 10^9$ erg s^{-1} cm^{-2}) assigns it to the so called pM class of HJs. This classification considers the day-side atmospheres of the highly-irradiated HJs that are somewhat analogous to the M- and L-type dwarfs. In particular, the predictions of equilibrium chemistry for pM planet atmospheres are similar to M-dwarf stars, where absorption by TiO, VO, H_2O, and CO is prominent (Lodders, 2002). Planets in this class are warmer than required for condensation of titanium (Ti)- and vanadium (V)-bearing compounds and will possess a temperature inversion (which could lead to a smaller inflation due to Ohmic heating accordingly to Heng (2012)) due to absorption of incident flux by TiO and VO molecules. Fortney et al. (2008) propose that these planets will have large day/night effective temperature contrasts and an anomalous brightness in secondary eclipse at mid-infrared wavelengths. Unfortunately, the SNR in the J-band light curve, due to the faintness of the parent star `WTS1`, is not high enough for such kind of detection (see Section 5.2.4).

To conclude, the discovery of `WTS1 b` demonstrates the capability of WTS to find planets, even if it operates in a back-up mode during dead time on a queue-schedule telescope and despite of the somewhat randomised observing strategy. Moreover, `WTS1 b` is an inflated HJ orbiting a late F-star even if the project is designed to search for extrasolar planets hosted by M-dwarfs.

5.3 WTS2 b

After the confirmation of the planetary nature of WTS1 b, a second extrasolar planet WTS2 b[4] was detected by the WTS around the star labelled as 19c_4_06396. The observations performed on the parent star are analogous to those of WTS1. Here, the observational data and the main results are reported. Detailed descriptions of the data acquisition and their following analysis can be found in the previous section. The combined analysis of the light curves and spectroscopic data allowed the estimation of the main properties and orbital parameters of WTS2 b. The planet has a mass of $1.08 \pm 0.11\, M_J$, a radius of $1.350^{+0.051}_{-0.055}$ R_J and an orbital period of 1.018 days. The basic properties of WTS2 b, mass, radius, and equilibrium temperature, are concordant with the general population of HJs. In particular, its radius is inflated above that of Jupiter, but is within the scatter of other known HJs. As WTS2 b orbits very close to its host star, it receives a high level of incident radiation. Hence, a secondary eclipses is expected to be detectable in the Ks-band.

Table 5.10: Broad band photometry for WTS2. All reported magnitudes are in the Vega system except the SDSS photometry, which is in the AB magnitude system. These magnitudes have not been corrected for reddening. $\lambda_{\rm eff}$ is the effective wavelength defined as the mean wavelength weighted by the transmission function of the filter, and EW is the equivalent width of the bandpass.

Filter	$\lambda_{\rm eff}$ (Å)	EW (Å)	Magnitude
SDSS-u	3546	558	18.361 ± 0.039
Johnson-B	4378	1158	16.8 ± 0.1
SDSS-g	4670	1158	16.283 ± 0.004
Johnson-V	5466	890	15.9 ± 0.1
SDSS-r	6156	1111	15.464 ± 0.003
Johnson-R	6696	2070	15.3 ± 0.1
SDSS-i	7471	1045	15.146 ± 0.003
WFCAM-Z	8817	879	14.501 ± 0.003
SDSS-z	8918	1124	14.959 ± 0.005
WFCAM-Y	10305	1007	14.352 ± 0.004
2MASS-J	12350	1624	13.928 ± 0.025
WFCAM-J	12483	1474	13.963 ± 0.003
WFCAM-H	16313	2779	13.470 ± 0.002
2MASS-H	16620	2509	13.464 ± 0.026
2MASS-K_s	21590	2619	13.414 ± 0.039
WFCAM-K	22010	3267	13.360 ± 0.003
WISE-$W1$	34002	6626	13.123 ± 0.040
WISE-$W2$	46520	10422	13.119 ± 0.055

[4]Published in Birkby et al. (2012), *in prep*

5.3.1 Stellar parameters

In order to obtain a first estimate of the spectral properties of WTS2 the SED analysis was performed with VOSA. The available broadband photometry for WTS2 is reported in Table 5.10 and plotted in Figure 5.16.

We opted to use a grid of Kurucz ATLAS9 model spectra (Castelli et al., 1997) in the range $T_{\rm eff}$=3500-6000 K in steps of 100 K, with log g=4.0-4.5, [Fe/H]=-0.5; 0.0; 0.2; 0.5, and A_V=0-0.5 in steps of 0.05. The upper limit on the extinction range was chosen to approximately match the total integrated line-of-sight extinction for the 2 ° region around the centre of the 19hr field (A_V=0.44 mag) calculated using the infrared dust maps of Schlegel et al. (1998). The best-fit values were as follows: $T_{\rm eff}$=5000 K, log g=4.5, [Fe/H]=0.2 and A_V=0.225 mag. The SED fit (see Figure 5.16) did not indicate an infrared excess.

The analysis of the intermediate and high-resolution spectra of WTS2, the same described in the previous section, allowed to confirm these estimates of the main stellar parameters and to reduce the related uncertainties. Moreover, this further analysis constrained several

Table 5.11: Properties of the host star WTS2. The proper motions $\mu_\alpha \cos\delta$ and μ_{delta} are from the SDSS DR7 database. The space velocities U, V, W are with respect to the Sun (heliocentric) but for a left-handed coordinate system, i.e. U is positive away from the Galactic centre, V is positive in the direction of Galactic rotation and W is positive in the direction of the north Galactic pole.

Parameter	Value
RA	19h 34m 55.87s
Dec	+36d 48m 55.79s
Spectral Type	K2V
$T_{\rm eff}$	5000 ± 100 K
log g	4.45 ± 0.25
[Fe/H]	0.0 ± 0.2
$v \sin(i)$	2.2 ± 1.0 km s^{-1}
v_{mic}	0.75 ± 0.5 km s^{-1}
$\log N(Li)$	< 1.8 dex
$\rho_\star$	1.697 ± 0.11 $\rho_{\rm sun}$
$M_\star$	0.815 ± 0.035 $M_\odot$
$R_\star$	0.775 ± 0.025 $R_\odot$
A_V	0.238 ± 0.013 mag
Distance	~ 1 kpc
Age	> 1 Gyr
$\mu_\alpha \cos\delta$	2.8 ± 2.40 mas yr^{-1}
μ_{delta}	-1.5 ± 2.35 mas yr^{-1}
U	-13.6 ± 5.7 km s^{-1}
V	-0.5 ± 8.1 km s^{-1}
W	-14.9 ± 5.4 km s^{-1}

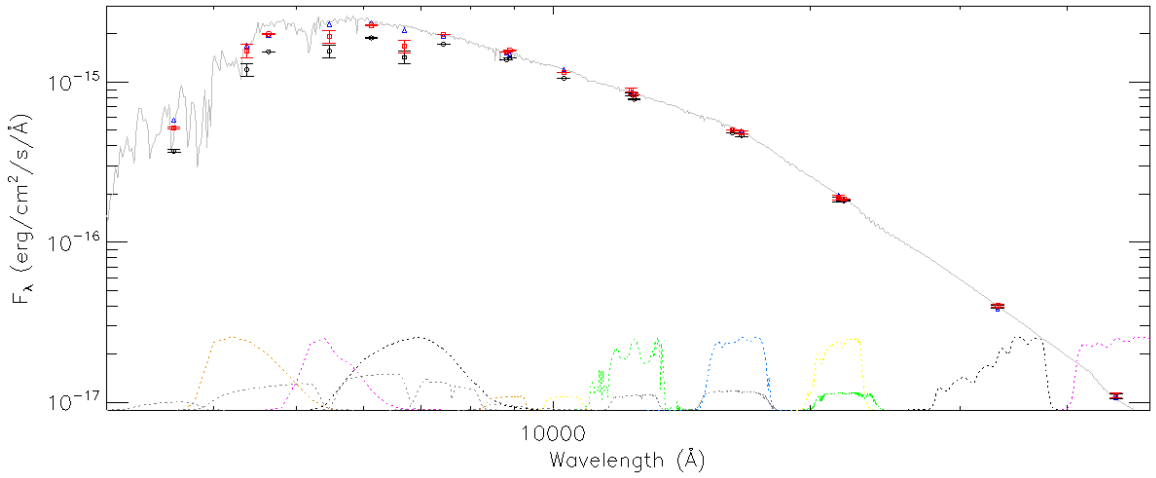

Figure 5.16: The spectral energy distribution of WTS2. The best-fitting Kurucz model spectrum ($T_{\rm eff}$=5000 K, log g=4.5, [Fe/H]=0.2 and A_V=0.225 mag) is overlaid in grey, while the integrated model fluxes for each of our observed bands are shown by the blue open triangles. The observed data are shown by the black open circles and the de-reddened photometry, according to the best-fit A_V , is shown by the red open squares. The filter transmission profiles for the various wavebands listed in Table 5.10 are shown by the dotted lines at the bottom of the plot.

properties of the host star (age, distance, proper motion, etc.). Table 5.11 collects all the quantities derived for the host star WTS2, a K2V main sequence ∼1 Gyr old star of $0.815 \pm 0.035\,M_\odot$.

5.3.2 Planetary parameters

Light curves analysis

The J-band and i-band light curves of WTS2 were fitted simultaneously with analytic models based on those presented by Mandel & Agol (2002) (see Appendix B). Limb-darkening coefficients were obtained from a linear interpolation of the tabulated values in (Claret & Bloemen, 2011), adopting the ATLAS atmospheric models and the flux conversion method. We assumed $T_{\rm eff}$=5000 K, log g=4.5, and solar metallicity, which gave limb-darkening coefficients of γ_1=0.2667, γ_2=0.2401 for the J-band and γ_1=0.4670, γ_2=0.1706 for the i-band.

The light curves and their combined best-fit model are shown in Figure 5.17, and the resulting best-fit model parameters are listed in Table 5.12. The errors were calculated using a multi-dimensional grid in which we searched for extreme grid points with $\Delta\chi^2$=1 when varying one parameter and simultaneously minimising over the others. Note that the radius ratio was assumed to be the same in both the J-band and i-band transit models. Although the planet's atmospheric properties could theoretically give different depths at these two wavelengths, due to possible absorbing molecular species or scattering processes,

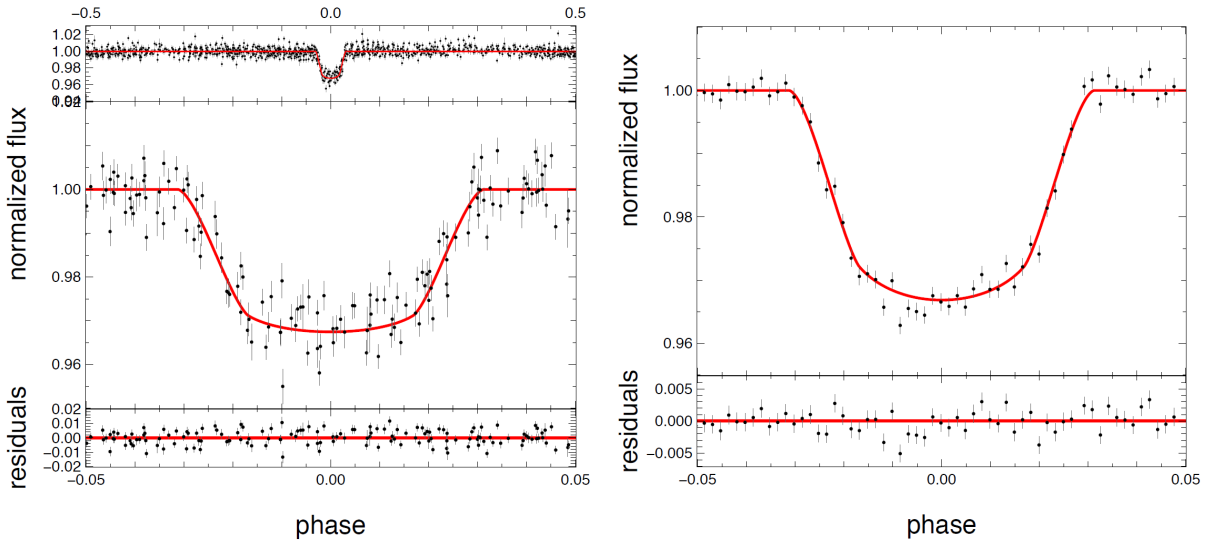

Figure 5.17: *Left*: WTS J-band LC for WTS2.The middle panel shows the data phase-folded on the best-fitting period from a simultaneous fit to the J-band and i-band LCs, zoomed around the transit. The best-fit model is shown by the solid red line. The upper panel shows the full-phase LC. The lower panel shows the residuals to the best-fit. *Right*: The INT i-band light curve for WTS2. All the available data is shown with the best-fit model shown by the solid red line. The lower panels shows the residuals to the best-fit.

Table 5.12: Fitted parameters of the WTS2 system as determined from the LCs and RVs fitting. Assuming a primary mass of $0.85\,M_{\odot}$we calculate the orbital inclination as well as the stellar and planetary radius.

	Light curve analysis		Radial velocity analysis
P	$1.01870700^{+6.9\times10^{-7}}_{-7.0\times10^{-7}}$ days	K	-0.242 ± 0.027 km s^{-1}
T_0	$2454317.81309^{+6.9\times10^{-4}}_{-6.8\times10^{-4}}$ HJD	V_γ	-20.026 ± 0.021 km s^{-1}
$\rho_\star$	$1.724^{+0.173}_{-0.141}\ \rho_\odot$	e	0 (fixed)
$Rp/R_\star$	$0.17547^{+0.00187}_{-0.00204}$	M_P	$1.08 \pm 0.11\,M_J$
b	$0.6108^{+0.0269}_{-0.0355}$	ρ_P	$0.43\,\rho_{jup}$
i	$83.10^{+0.60}_{-0.51}$ °	χ^2_ν	1.46
R_p	$1.350^{+0.051}_{-0.055}\ R_J$		
$R_\star$	$0.790^{+0.023}_{-0.025}\ R_\odot$		
a	0.0185082 ± 0.00026 AU		
	$5.136 \pm 0.074\,R_\star$		

the precision of our data is not sufficient to measure this effect, hence a constant radius ratio is a reasonable assumption in this case. The derived planetary radius is $1.350^{+0.051}_{-0.055}\,R_J$.

Radial velocity analysis

The host star was observed with the HET in 7 nights during Autumn 2010. The cross-disperser configuration of the HRS was '600g5271' and 2 sky fibers were employed to measure the sky contamination. The reduction and the analysis of the data are described in Chapter 4. The RVs were computed cross-correlating the observed spectra with a synthetic template of a $T_{\rm eff}$=5000 K, log g=4.5, solar metallicity star. Table 5.13 reports the RV measurements for `WTS2`.

In order to measure the semi-amplitude of the RV variation in the host star, the measured RVs were modelled with a simple sinusoid, assuming a circular orbit. The period was fixed to the value derived in the light curve solution and the phases were calculated using period and T_0 (see Table 5.13). The period-folded RVs and the best-fit circular orbit model are plotted in Figure 5.18.The best-fitting parameters of the RV data are collected in Table 5.12. The derived planet mass is 1.08±0.11 M_J.

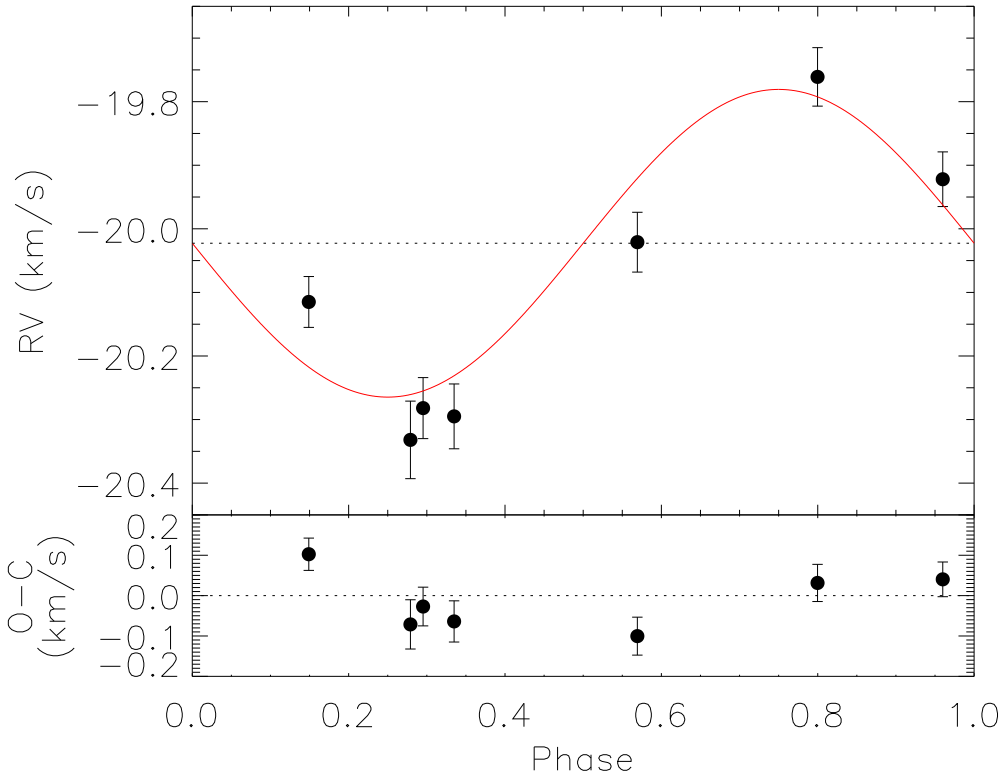

Figure 5.18: *Top panel*: phase folded RVs values measured with the high resolution HET spectra of `WTS2` as a function of the orbital phase. The best-fit circular orbit model (χ^2_ν=1.46) is indicated with the red solid line. The black dotted line refers to the fitted radial systemic velocity (V_γ=-20.026 km s^{-1}). Zero phase corresponds to the mid-transit time. *Bottom panel*: phase folded O-C residuals from the best-fit. The residual scatter is of the order of 150 m s^{-1}, consistent with the RVs uncertainties.

Table 5.13: Radial velocity data for WTS2 derived from the HET spectra. The phases are calculated using the best-fitting period and T_0 from the simultaneous LC analysis (see Table 5.12).

HJD	Phase	RV (km/s)	σ_{RV} (km/s)
2455790.83253	0.9599	-19.922	0.043
2455822.73790	0.2790	-20.332	0.061
2455845.68006	0.7997	-19.761	0.046
2455856.65080	0.5693	-20.021	0.047
2455867.61787	0.3349	-20.295	0.051
2455869.61445	0.2952	-20.282	0.048
2455876.59697	0.1490	-20.115	0.040

5.3.3 Discussion

Radius inflation

The basic properties of WTS2 b, such as its mass, radius, and equilibrium temperature are concordant with the general population of HJs. Figure 5.19 shows WTS2 b in the mass-radius plane. Its radius is inflated above that of Jupiter, but is within the scatter of other known HJs. For example, using the empirical relationships presented by Enoch et al. (2012) for the given mass of WTS2 b, we would predict a radius of $1.272 \pm 0.106\,R_J$, which is within 1σ of our measured value. An inflated radius is unsurprising given that WTS2 b receives an incident stellar irradiation of $1.29{\cdot}10^9$ erg/s/cm^2, which is well above the observed minimum value ($\sim 2{\cdot}10^8$ erg/s/cm^2) required to inflate the radius, according to Demory & Seager (2011).

Follow-up potential

WTS2 b orbits very close to its host star and receives a high level of incident radiation (F_{inc}=$1.29{\cdot}10^9$ erg/s/cm^2). If we assume that its atmosphere has no reflection (Bond albedo $A_B = 0$) and that it instantaneously re-radiates the incident stellar flux ($f = 2/3$), then we can calculate the planet's equilibrium temperature and estimate the deepest eclipse depths we would expect to find in the $IZJHKs-$bands. Following the prescription of López-Morales & Seager (2007) the equilibrium temperature is: $T_{eq} = T_\star\,(R_\star/a)^{1/2}\,[f(1-A_B)]^{1/4} = 2000 \pm 100$ K. Further assuming that the star and planet behave as black bodies at optical and infrared wavelengths, the predicted secondary eclipses depths in the $IZJHKs-$bands are $(F_P/F_\star)_I \sim 0.14 \cdot 10^{-3}$, $(F_P/F_\star)_Z \sim 0.19 \cdot 10^{-3}$, $(F_P/F_\star)_J \sim 0.82 \cdot 10^{-3}$, $(F_P/F_\star)_H \sim 1.7 \cdot 10^{-3}$, and $(F_P/F_\star)_K \sim 3.0 \cdot 10^{-3}$, respectively (integrating over the bandpasses). The typical RMS of the WTS J-band light curves at J=13.9 mag, and indeed the RMS of the out-of-eclipse data for WTS2 b, is $\sim$4 mmag. In the J-band phase-folded light curve of WTS2 b there are 88 data points in the secondary eclipse phase, which corresponds to a noise-to-signal ratio of $\sim 0.43{\cdot}10^{-3}$, meaning that the WTS LC cannot place meaningful

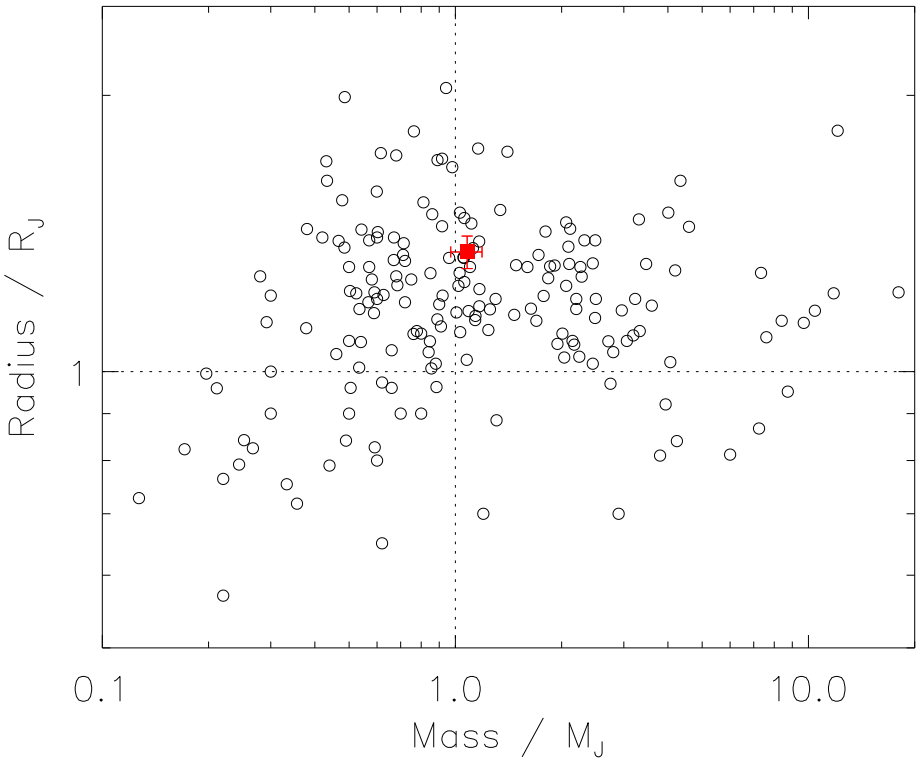

Figure 5.19: Planetary radius as a function of planetary mass for known transiting planets (open circles) and WTS2 b (filled red square). WTS2 b is inflated above 1 R_J but is within the observed scatter. Data from *http://exoplanet.eu*.

constraints secondary eclipse depth in the J-band, so we do not draw any conclusions about its atmospheric properties here. In principle WFCAM could be used to detect the J-band secondary eclipse, however we expect one of the main limitations in the survey data is the random nature of the observing strategy. This makes it difficult to control the systematics in the LC to the precision needed to robustly detect secondary eclipses, and in practice one would need a dedicated night of observations.

However, if we compare the predicted Ks-band secondary eclipse depth of WTS2 b to the other known transiting exoplanets, assuming each planet has A_B=0 and f=2/3, (see Figure 5.20), we find that WTS2 b has one of the deepest predicted Ks-band secondary eclipses amongst the known exoplanet population. Although the host star is relatively faint, such a deep secondary eclipse could potentially be detected with ground-based infrared facilities. For example, both the Long-slit Intermediate Resolution Infrared Spectrograph at the 4-m William Herschel Telescope in La Palma, and WFCAM at the 3.8-m UKIRT in Hawaii have a proven record for detecting these event (see e.g. Snellen, 2007; de Mooij & Snellen, 2009, 2011). Note that Figure 5.20 does not include actual measurements of

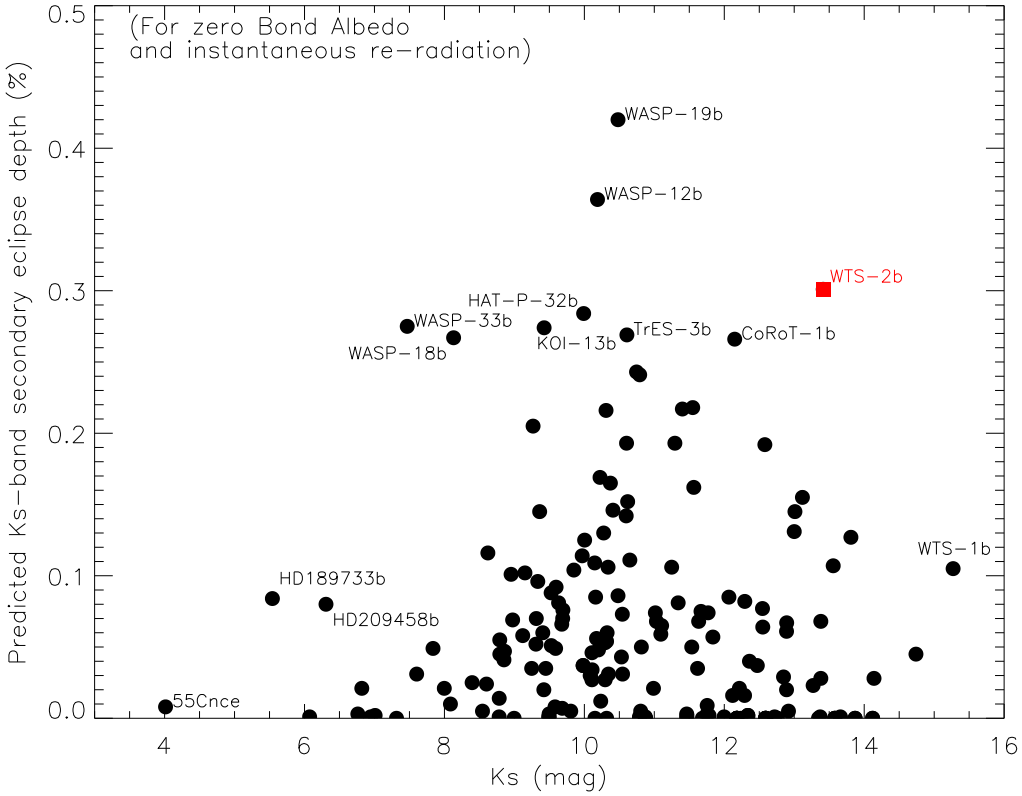

Figure 5.20: Predicted Ks-band secondary eclipse depths for known exoplanets as a function of Ks-band magnitude, assuming zero Bond albedo ($A_B = 0$) and instantaneous re-radiation ($f = 2/3$) for all planets. `WTS2 b` is marked by the red square and is one of the deepest predicted Ks-band secondary eclipse depths, making it more favourable for ground-based atmospheric characterisation studies. However, note that these are only predicted eclipse depths. Some of these exoplanets have measured eclipse depths that are smaller e.g. HD189733b (0.039%, Swain et al. 2009) and recall we have assumed the deepest eclipse case for A_B and f. Magnitudes from *http://exoplanet.eu*.

Ks-band secondary eclipses depths from the literature, and is shown purely to emphasise the follow-up potential of `WTS2 b` in comparison to other systems.

The secondary eclipses of `WTS2 b` will allow us to study a highly irradiated planet but around a cooler host star than many of the currently known very hot-Jupiters, providing an insight to the affect of the stellar spectrum on the composition and structure of hot-Jupiter atmospheres. Further discussion on the `WTS2` system can be find in Birkby et al. (2012), *in prep.*

5.4 NLTT 5306

In this section the system NLTT 5306[5], a brown dwarfs (BDs) orbiting a white dwarfs (WDs) is reported. The detection and study of BDs mass companions to WDs is of great importance in the study of high mass ratio binary formation and evolution. A large deficit of BD companions to main-sequence stars, known as the 'brown dwarfs desert', has been detected analysing the companions of nearby Sun-like stars (McCarthy & Zuckerman, 2004; Grether & Lineweaver, 2006).

As detached companions to H-rich WDs (as know as DA WDs), BDs are rare (∼0.5%, Steele et al., 2011; Girven et al., 2011). Only a handful of such systems have thus far been spectroscopically confirmed. For e.g. GD165 (DA+dL4, Becklin & Zuckerman, 1988), GD1400 (DA+dL6-7, Farihi & Christopher, 2004; Dobbie et al., 2005), WD0137349 (DA+dL8, Maxted et al., 2006; Burleigh et al., 2006), PHL 5038 (DA+dL8, Steele et al., 2009) and LSPM1459+0857 (DA+T4.5, Day-Jones et al., 2011). GD165, PHL 5038 and LSPM1459+0857 can be classed as widely orbiting with projected separations of 120 AU, 55 AU and 16500-26500 AU respectively. WD0137349 and GD1400 have much shorter orbital periods of 116 minutes and ∼10 hours (Burleigh et al., *in prep.*) respectively, and have both undergone a common envelope evolution.

These two distinct populations are thought to be the outcome of stellar evolution; the wide pairs where the secondary has migrated outwards due to the mass loss of the WDs progenitor (Farihi et al., 2006; Nordhaus et al., 2010), and the close systems in which the secondary has survived a stage of common envelope evolution and may eventually lead to the formation of a cataclysmic variable. In these close binaries, the BD is expected to be irradiated by the WD high UV flux, leading to substantial differences in the 'day' and 'night' side hemispheres. These systems can additionally be used for testing models of irradiated HJ atmospheres (e.g. HD189733b, Knutson et al., 2007).

NLTT 5306 (=SDSS J 013532.98+144555.8) was first identified as a candidate WD+BD binary in Steele et al. (2011) and Girven et al. (2011). The former used an estimate

Table 5.14: SDSS and UKIDSS magnitudes of NLTT 5306.

Band	Magnitude
u'	17.51 ± 0.01
g'	17.03 ± 0.00
r'	16.95 ± 0.00
i'	16.96 ± 0.01
z'	17.00 ± 0.01
Y	16.49 ± 0.01
J	16.24 ± 0.01
H	15.86 ± 0.01
K	15.56 ± 0.02

[5]Published in Steele et al. (2012), MNRAS accepted

of the WD atmospheric parameters ($T_{\rm eff}$=8083±22 and log g=8.08±0.04, Eisenstein et al., 2006) in combination with cooling models for DA WDs (Holberg & Bergeron, 2006; Kowalski & Saumon, 2006; Tremblay et al., 2011; Bergeron et al., 2011) to predict the near-infrared photometry of the star. A comparison was then made with the UKIDSS observations identifying NLTT 5306 as having a near-infrared excess consistent with a red companion. The SDSS and UKIDSS magnitudes are given in Table 5.14. Further fitting of the photometry yielded an estimated spectral type of dL5 for the secondary, with a mass of 58±2 M_J at a distance of 60±10 pc. The system was unresolved with an upper limit of <57 AU between components.

5.4.1 Observations

INT photometry

NLTT 5306 was observed photometrically for two hours in the Sloan i-band on the night of October 23^{th}, 2009 with the Wide Field Camera (WFC) on the 2.5 Isaac Newton Telescope (INT) in La Palma, Spain. The data were reduced using the INT Wide Field Survey (WFS) pipeline (Irwin & Lewis, 2001b) developed by the Cambridge Astronomical Survey Unit. For a detailed description of the reduction process, see Irwin et al. (2007). In brief a standard CCD reduction was performed by correcting for the bias, trimming the frames, correcting non-linearity, flat-fielding and correcting for the gain. The flux was measured in each observation using aperture photometry and the result converted to magnitudes.

SDSS Spectroscopy

NLTT 5306 was observed on multiple occasions by the SDSS. From the SDSS archive we extracted a total of 17 spectra taken over the period from December 1^{st} to 20^{th}, 2000. All but three of these spectra had exposure times of 15 minutes; the three spectra acquired on December 4^{th} were exposed for 20 minutes.

HET high-resolution spectroscopy

NLTT 5306 was observed using the HRS between December 2010 and February 2011. The ephemeris of the system was unknown at the time and so six random observations were taken in order to establish if the primary has a measurable RV, and then to estimate the orbital period. Each observation was split into 2 separate exposures of 1320 s. The cross disperser setting was 316g5936 corresponding to a wavelength range of 4076-7838 A, in order to cover the Hα, Hβ and Hγ Balmer lines.

The instrumental configuration of the HRS was set in order to employ two sky fibers to simultaneously record the sky background and to achieve a resolution of the observed spectra of R=15 000. The Balmer lines generated by the neutral hydrogen in the atmosphere of the WD are the only spectral features in its spectrum. Due to the high log g value of NLTT 5306 (log g=8.08±0.04, Eisenstein et al., 2006) the line profiles extend for tens of Å in the observed spectra. A higher resolution of the spectra (for e.g. 60 000) is not required

to resolve these lines as their broadening is much larger than the width of the resolution element (∼0.4 Å at 6563 Å) at R=15 000. The lower resolution of the spectra allows also to obtain a higher SNR as a 2×5 binning can be employed, reducing by a factor ∼5 the read-out-noise with respect to the 2×1 binning used in combination with a resolution of 60 000.

X-Shooter Spectroscopy

NLTT 5306 was observed using X-Shooter (D'Odorico et al., 2006) mounted at the VLT-UT2 telescope on the night of September 5^{th}, 2010. X-Shooter is a medium-resolution spectrograph capable of observing using 3 independent arms simultaneously: the ultraviolet (UV), optical (VIS) and the near-infrared (NIR) arms covering a wavelength range of 0.3-2.5 μm. For our observations we used slit widths of 0.8″, 0.9″and 0.9″in the UV, VIS and NIR arms respectively. Exposure times for each arm were 1200 s in the UV, 1200 s in the VIS and 12×150 s in the NIR. We nodded between each exposure along the NIR slit to improve sky subtraction. Reduction of the raw frames was carried out using the standard pipeline release of the ESO X-Shooter Common Pipeline Library recipes (version 1.3.7) within GASGANO[6], version 2.4.0. The standard recipes were used with the default settings to reduce and wavelength calibrate the 2-dimensional spectrum for each arm. The extraction of the science and spectrophotometric standard and telluric spectra were carried out using `apall` within IRAF. The instrumental response was then removed by dividing the associated standard star by its corresponding flux table.We also used this method to apply the telluric correction. Finally, the spectra were flux calibrated using the SDSS and UKIDSS magnitudes (see Table 5.14).

5.4.2 Analysis

INT i'-band LC

The INT i'-band LC of NLTT 5306 (see Figure 5.21) shows low-level photometric variability with a peak-to-peak amplitude of ∼0.8%. The analysis leading to this result is here outlined. A 'floating-mean' periodogram was used to search for periodicity in the target (Cumming et al., 1999). This method involves fitting the time-series data with a sinusoid plus a constant A in the form of:

$$A + Bsin\left[2\pi f(t - t_0)\right] \tag{5.3}$$

where f is the frequency and t is the time of observation. The errors associated with the best-fitting frequency were estimated as the 2σ frequency range from the global minimum (corresponding to a change in χ^2 of four, assuming only one useful fitted parameter). To evaluate the significance of the best-fitting period, a false alarm probability (FAP) was estimated using 1000 Monte Carlo trials and an analytical approach for comparison. Fake

[6] *http://www.eso.org/sci/software/gasgano*

light curve datasets were generated for the Monte Carlo tests at the same timings as the observations with the mean magnitude as the observed data. Random Gaussian noise was then added to the flux distributed with the same variance as observed magnitudes. The FAP was determined from the number of trials where the maximum power in the periodogram (from the fake dataset) exceeded the maximum power from the observed dataset. A small FAP indicates that variability present in the light curve is less likely to have arisen solely from noise fluctuations. A significant detection threshold was set at 99% (FAP$\leqslant$0.01). The probability was also determined analytically using the equation given in Table 1 in Zechmeister & Kürster (2009) for the residual variance normalisation (also see Appendix B in Cumming et al., 1999). Further details on the significance tests can be found in Cumming et al. (1999) and Lawrie et al. (2012, *in prep.*).

A global minimum in the periodogram is found at a frequency of $14.1^{+0.9}_{-1.4}$ cycles/day, a period of $102.2^{+11.3}_{-6.4}$ minutes. A fitted sine wave to the data gives a reduced χ^2 of 2.03. It shows low-level photometric variability with a peak-to-peak amplitude of 0.84%. The FAP statistics are well within the limit for a significant detection, with a FAP of <0.001 from the Monte Carlo tests and a FAP of 1.020×10^{-5} from the analytical estimation. This suggests that it is significantly unlikely that the variability seen in the light curve is due to noise fluctuations alone. The probability that this system has an alignment that would result in an eclipse as viewable from Earth is ∼20%, with an eclipse duration of ∼7 minutes (Faedi et al., 2011). No eclipse or grazing transit is immediately obvious in the phase folded LC

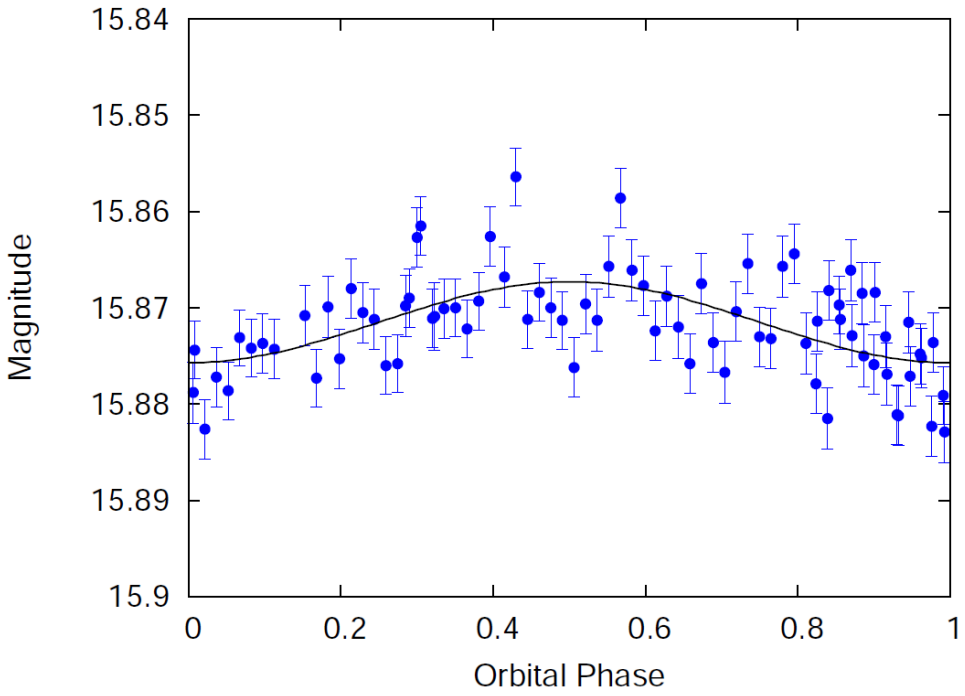

Figure 5.21: Phase folded INT *i*'-band LC of NLTT 5306 showing a variability of ∼1% with a period of $102.2^{+11.3}_{-6.4}$ minutes.

of NLTT 5306 (see Figure 5.21). Given the total time between exposures of ∼90 s and the coverage of ∼1.5 orbital periods, it seems unlikely that we would have missed an eclipse.

WD spectroscopy

Figure 5.22 shows the extracted X-Shooter spectrum for NLTT 5306 observed with the UV and VIS arms. This clearly shows the WD primary dominating the optical wavelengths and the BD companion dominating the near-infrared wavelengths. A closer inspection of the Hα absorption line in individual exposures revealed a core emission line was present.

The Balmers series lines in both the X-Shooter and SDSS spectra were fitted with atmospheric models of hydrogen atmosphere of DA WDs (Koester, 2008). The average of the best fitting parameters yield to an effective temperature and a surface gravity of $T_{\rm eff}$=7756±35 K and log g=7.68±0.08 respectively. We interpolated these values over a grid of synthetic colours and evolutionary sequences of DA WDs[7] to calculate a mass of M_{WD}=0.44±0.04 $M_{\odot}$ and a distance of 71±4 pc. The results are summarised in Table 5.15. The region within Hα containing the core emission was excluded from this fit. A model spectrum calculated using these values is over-plotted in Figure 5.22.

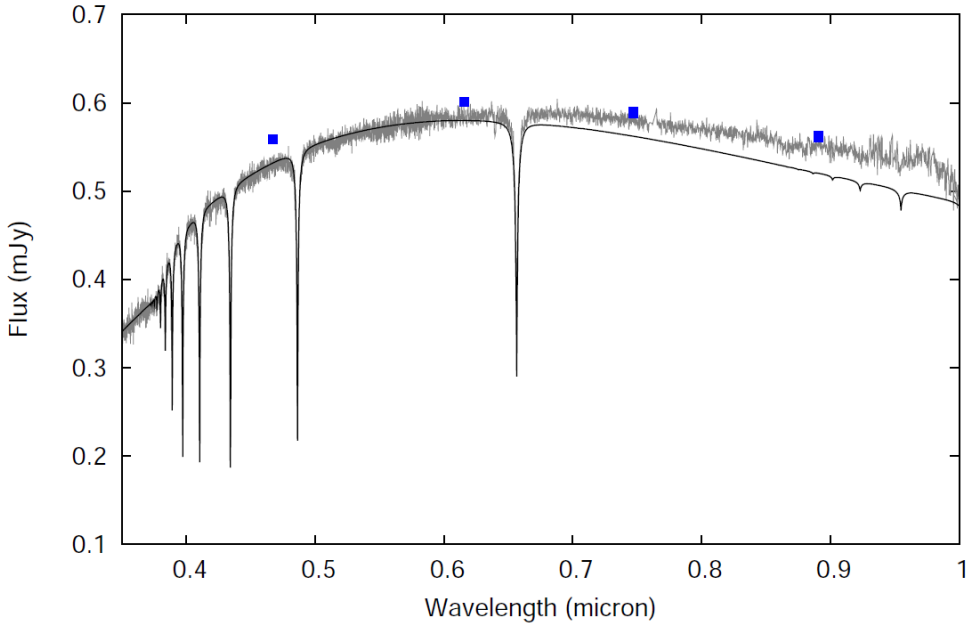

Figure 5.22: X-Shooter spectrum (grey) of NLTT 5306 covering the UV and VIS arms where the WD primary dominates. SDSS *griz* photometry is over-plotted (squares). The WD model SED (black) begins to diverge from the observed spectrum at longer wavelengths due to the added flux from the secondary BD. The absorption lines visible in the spectrum are the Balmer series lines from the Hα to the Hη.

[7] *http://www.astro.umontreal.ca/bergeron/CoolingModels/*

Table 5.15: Properties of the WD NLTT 5306.

Parameter	Value
$T_{\rm eff}$	7756±35 K
log g	7.68±0.08
$M_\star$	0.44±0.04 $M_\odot$
$R_\star$	0.0156±0.0016 $R_\odot$
Distance	71±4 pc

It should be noted that the spectroscipic fit may have lead to an overestimate of the WD mass, due to the difficulty in modelling the hydrogen line profiles below $T_{\rm eff}$=12000-13000 K. The Tremblay et al. (2011) analysis of SDSS WDs suggest an overestimate at the level of 10%, although this is largely based on WDs with a mass of around 0.6 $M_\odot$. A lower WD mass would decrease the minimum value for the mass of the secondary, relaxing the need for the system to have a high inclination for the mass to be consistent with the spectral type of dL4-7 and given the non-detection of an eclipse or grazing transit.

Radial velocity analysis

Each SDSS spectrum is a combination of separate red and blue spectra. We split these into spectra covering Hα and spectra covering the higher Balmer series. We fitted multiple Gaussian components to these lines, using two Gaussian per line (see Marsh et al., 1995, for details of this process). Once profiles to the mean spectra had been fitted, then for the final fit we held all shape parameters fixed and simply allowed the radial velocity to be fitted, giving us our final radial velocities. The HET observation obtained in one of the six nights was affected by contamination (probably due to a pointing problem) and hence was not considered in the analysis. Four of the five observations left consisted of 2 separate exposures of 1320s each, with the final observation only producing one such exposure. As these exposures represented a significant fraction of the orbital period of NLTT 5306 b, each observation was fitted separately, giving a total of 9 data points. The absorption lines were fitted using a combination of 2 Gaussian and 2 Lorentzian using the program FITSB2 written by Ralf Napiwotzki. The best fitting shape parameters were fixed and then fitted for velocity shifts. The precision of such RV measures is of the order of $\sim$1 km s^{-1}. Four more radial velocities were measured by extracting individually the spectra which were combined to make the final X-Shooter spectrum. Theses were measured using the same method outlined above.

The SDSS data were shifted so that the mean velocity matched that of the higher resolution and therefore superior HET and X-Shooter data. The low resolution of the SDSS data made measurement of the systemtic velocity with just the SDSS data unreliable, with a significant difference measured in the mean velocites ($\sim$20 km s^{-1}) even between the blue and red arms. The mean velocity measured from HET and X-Shooter is consistent with the systemic velocity of -15 $\pm$ 36 km s^{-1} previously measured in Adelman-McCarthy et al. (2008).

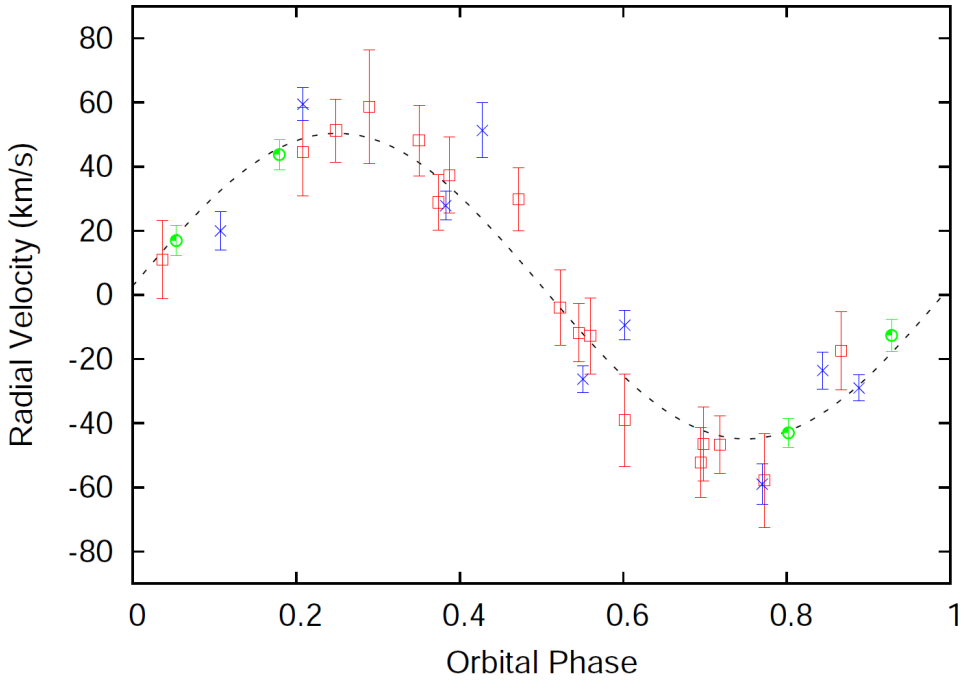

Figure 5.23: Phase folded RV curve for the favoured period of 101.87±0.04 minutes of the H absorption lines of NLTT 5306 a showing the HET (crosses), SDSS (squares) and X-Shooter (circles) data. The curve representing the best fitting orbital parameters is over-plotted (dashed).

The high resolution of HET and X-Shooter spectra allowed for the detection of the line emission in the core of Hα lines. The fit to the Hα absorption lines in the WD spectra was used to subtract the contribution of the WD. The emission line was then fitted with a single Gaussian to measure the RV. This was possible in all 4 X-Shooter exposures and 8 of the 9 HET exposures, with the final exposure being too noisy to accurately identify the emission.

Periodicity was searched for in the combined RV data of the WD (SDSS, X-Shooter and HET) and for the line emission (X-Shooter and HET) using the same method discussed previously for the analysis of the INT LC. For the WD, 30 unique data points were used as measured from the Balmer series absorption lines visible in the observed spectra, and for the BD, 12 as measured from the Hα core emission.

The analysis of the WD data resulted in 2 favoured aliases with periods of 109.96 $\pm$ 0.02 minutes (χ^2=72.6) and 101.88 $\pm$ 0.02 minutes (χ^2=66.5). The χ^2 value slightly favours the high frequency shorter period alias which would be consistent with the period measured from the INT LC. However, the lower frequency longer period alias produces a period which is also within errors of this value. Therefore, it was not possible to determine the period accurately just utilising the available WD data only.

The same analysis was repeated considering the RV variation measured from the Hα

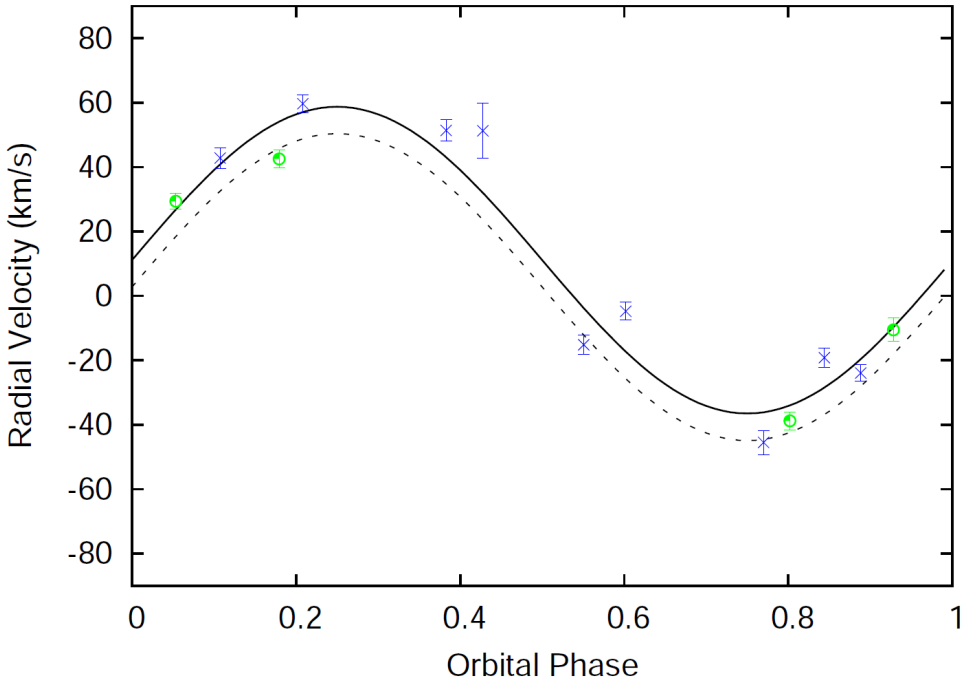

Figure 5.24: Phase folded radial velocity curve for the favoured period of 101.87±0.04 minutes of the Hα emission line showing the HET (crosses) and X-Shooter (circles) data. The curve representing the best fitting orbital parameters is over-plotted (solid) as well as the best fitting model for the absorption lines (dashed).

core emission profiles too. In this case, the 2 most favoured periods of 101.87 ± 0.04 minutes (χ^2=78.5) and 109.64 ± 0.04 minutes (χ^2=93.0) are indeed consistent with those obtained for both the light curve and the RV fit of the WD. However, the χ^2 value is much more in favour of the higher frequency shorter period alias in this case. Therefore, it is this value of P=101.88 ± 0.02 minutes that we take for the period of the system. Figures 5.23 and 5.24 show the phase folded RV measures related to the WD and the Hα core emission.

An attempt was made to measure the RV of the BD component using the four individual X-Shooter observations in the NIR arm. Each spectrum was extracted and flux calibrated, and the telluric correction applied. The model WD spectrum (see Figure 5.22) was then subtracted from each spectrum. We then cross correlated each spectrum with a dL5 template using the IRAF package FXCOR. However the SNR in the individual exposures was such that the cross correlation with the template did not produce any sensible results. We also suspect that we were not entirely able to remove the WD contribution satisfactorily, and it is also possible that the BD spectrum undergoes short term changes in overall shape due to the irradiation form the primary.

5.4.3 Discussion

The stellar/sub-stellar nature of an object is dependent on its mass. The commonly used limit to distinguish between low mass main-sequence stars and BDs is $0.075\,M_{\odot}$ ($75\,M_{J}$, Burrows et al., 1997; Chabrier & Baraffe, 2000), below which hydrogen fusion does not occur.

Figures 5.23 and 5.24 show the RV measurements in phase space for NLTT 5306. The parameters of the spectroscopic orbit are summarised in Table 5.16. The period measured using the RV data is consistent with the period measured using the variability of the INT *i*'-band LC. Using the calculated value for the mass of the primary, M_{WD}=0.44±0.04 $M_{\odot}$ (see Table 5.15), the minimum mass of the secondary is 56±3 M_{J} consistent with the measured spectral type of dL4-7 and confirming NLTT 5306 b is a bona fide BD. Given this consistency, we suspect that this system has a relatively high inclination, even though no eclipse was detected. It also confirms NLTT 5306 is the shortest period detached WD+BD binary. Parsons et al. (2012) detected a detached WD binary system with a period of only 94 minutes (CSS 03170). However, in this case the secondary has a mass above the hydrogen burning limit and so is classed as a main sequence star. The most similar known system is WD0137-349 which has an orbital period of 116 minutes (Maxted et al., 2006) and a slightly higher mass secondary ($53 \pm 6\,M_{J}$, Burleigh et al., 2006).

One might assume that the Hα emission seen in our spectroscopy was likely to arise from the irradiation of the BDs atmosphere by the WD primary, as was the case for WD0137-349. If this were true, then the RV measurements would be in anti-phase with those measured from the Hα absorption, and the amplitude would allow us to solve for the masses of both binary components. However, Figure 5.24 shows the emission is clearly in phase with the absorption, and with a similar measured amplitude of 48.9±1.8 km s^{-1}, its origin must be associated with the WD. The most likely cause of such emission is accretion, either via Roche Lobe overflow or wind from the sub-stellar companion.

Burleigh et al. (2006) observed a similar situation in the magnetic WD+BD binary SDSS J 121209.31+013627.7 ($P_{orb} \sim 90$ minutes). In this case the system is considered to be in a semi-detached state with a magnetic cataclysmic variable (polar) in a low state of accretion from a BD onto a magnetic WD. Although NLTT 5306 shows no evidence of a detectable magnetic field and at $P_{orb} \sim 102$ minutes is probably not in semi-detached contact, it may be accreting from a weak wind from the BD. Therefore, NLTT 5306 is more akin to the wind accreting system LTT 560 (Tappert et al., 2007, 2011), albeit in this system the secondary is a much earlier spectral type of dM5.

The Hα emission seen in LTT 560 consists of two anti-phased components, one originating in the secondary and the other from a chromosphere on the WD as a result of accretion via the companion stellar wind. NLTT 5306 only shows the emission component associated with the WD, and so we conclude we may be observing a similar situation where there is only chromospheric emission and no obvious activity from the secondary (which is to be expected given the estimated spectral type). The origin of this emission line component in post-common-envelope binaries is briefly discussed in Tappert et al. (2011), although given the rarity of systems where the Hα emission line component is located on the WD,

it is presently unclear under what conditions chomospheric emission occurs.

If NLTT 5306 is accreting via a stellar wind onto a chromosphere then this would occur some distance above the WD. The systemic velocity of the observed emission is similar in value to that of the RV measured using the WDs Balmer absorption lines. Some difference would be expected due to the gravitational redshift of the WD if the emission was chromospheric in origin. Adopting the measured atmospheric parameters from this work, this amounts to a redshift of v_{gr}=17.9±3.5 km s^{-1}. Figure 5.24 shows the systemic velocity of the emission feature is ∼5-10 km s^{-1} greater than that measured from Balmer absorption. If anything we would expect it to be less (*i. e.* redshifted compared to the WD) but given the low SNR of the emission detected in the HET data (from which the fit heavily relies), this value should not be trusted. In all likelihood the emission forming region is somewhere above the WDs photosphere. This could be further constrained with more accurate measurements of the RV of the absorption and emission features, and should be considered as a future project for the VLT + X-Shooter.

The effective temperature of the BD can be estimated to be ∼1700 K from its measured spectral type of dL4-7, and comparison with observed L-dwarfs (Vrba et al., 2004). Using this effective temperature and the cooling age of the WD (see Table 5.15) as a minimum value for the age of the system, we have estimated the radius of NLTT 5306 b to be R_{BD} = 0.95 ± 0.04 R_J by interpolating the Lyon group atmospheric models (Chabrier et al., 2000; Baraffe et al., 2002).

The systemic velocity of the WD allows us to discuss the kinematics of the system, in particular the U velocity (see also Section 5.2.3). This gives a good indication of whether the WD is a thin disc, thick disc or halo object, and thus allows for further constraints on the age of the primary. Using the equations of Johnson & Soderblom (1987) and the values given in Tables 5.16 and 5.14, we calculate Usim70 km s^{-1} for NLTT 5306. This would seem to suggest that the WD is a member of the thick disk population (see Figure 4 of Pauli et al., 2006) and is likely much older than the minimum cooling age suggests (>5 Gyr). At this age the Lyon group models give a mass of closer to 70 M_J for the companion, still well within the accepted BD range.

The asymmetric heating and rotation of the BD produces a modulation of brightness known as the 'reflection effect' (Wilson, 1990). This has been detected at the order of ∼1% in the INT *i*'-band LC. Since the BD is tidally locked with the WD, this has allowed us to estimate the binary orbital period independently of the RV measurements. A more accurate spectral typing of the companion would require further measurements of this effect at longer wavelengths (*i. e.* the near-infrared) where this variation would be more pronounced (Burleigh et al., 2008).

Variability has also been observed in the *i*'-band for WD0137349, but of the order of ∼2% (Burleigh, private communication). WD0137349 a is hotter than NLTT 5306 (∼16000 K) so there are more UV photons, and more flux overall by approximately an order of magnitude. Therefore, we would not necessarily expect to observe such a strong effect on NLTT 5306 b, which may also depend on local conditions and chemistry in the BD atmosphere, but a variation of ∼1% seems consistent with the effects of irradiation.

The progenitor system of NLTT 5306 a & b consisted of a main-sequence star and a BD

Table 5.16: Spectroscopic orbit of NLTT 5306 where the WD RV at a time T is given by γ_1 + K_1 sin[2πf(T - T_0)], and the emission line radial velocity γ_2 + K_2 sin[2πf(T - T_0)], where f = 1/P is the frequency.

Parameter	Value
P	101.88±0.02 minutes
T_0	2453740.1408±0.0005 HJD
K_1	48.1±1.3 km s^{-1}
K_2	46.9±1.1 km s^{-1}
γ_1	2.7±1.3 km s^{-1}
γ_1	11.1±1.0 km s^{-1}
a	0.566±0.005 $R_\odot$

with an orbital separation sufficiently small for the progenitor of NLTT 5306 a to fill its Roche lobe as it evolved off the main sequence. As a consequence of the ensuing unstable mass transfer the BD was engulfed in the envelope of the progenitor of NLTT 5306 a, leading to a rapid reduction in the orbital period and the ejection of the envelope. The low mass of NLTT 5306 a suggests that the core-growth was truncated by this common envelope evolution, and that this WD may contain a He core (Webbink, 1984; Iben & Tutukov, 1986; Rebassa-Mansergas et al., 2011). Therefore, the evolution of NLTT 5306 a likely terminated on the red giant branch (RGB) rather the the asymptotic giant branch (AGB).

Following the emergence from the common envelope, the binary continued to evolve towards shorter periods. Given the low mass of NLTT 5306 b gravitational wave radiation is likely to be the only relevant agent of orbital angular momentum loss. Adopting the stellar parameters for the WD and the BD determined above, and using the formalism outlined by Schreiber & Gänsicke (2003), we calculate the orbital period at the end of the common envelope to have been $P_{CE} \simeq 120$ minutes. The orbital period of NLTT 5306 will continue to decrease for another ≃900 Myr, until the BD will eventually fill its Roche lobe and initiate stable mass transfer onto the WD. This transformation into a cataclysmic variable (CV) will occur at an orbital period of ≃68 minutes, near the orbital period minimum of CVs (Gänsicke et al., 2009).

The existence of WD0137-349 b (Maxted et al., 2006; Burleigh et al., 2006) and NLTT 5306 b demonstrate that BDs can survive common envelope evolution (see also Nordhaus et al., 2010), and their short orbital periods and low WD masses are in line with the statistics of the much larger sample of post-common envelope binaries containing low-mass M-dwarfs (Zorotovic et al., 2011b). Binary population models predict both the existence of CVs born at very short periods with BD donors (Politano, 2004), and CV containing low-mass He-core WDs (e.g. de Kool, 1992; Politano, 1996). Yet, among the sample of known CVs, there is no compelling evidence for either systems that were born with a BD donor (see the discussion in Littlefair et al., 2007; Uthas et al., 2011; Breedt et al., 2012) or CVs containing low mass WDs (Zorotovic et al., 2011a; Savoury et al., 2011). We conclude that

WD0137-349 and NLTT 5306 represent nearby bona fide progenitors of CVs with low-mass WDs and BD donors, and that the lack of such systems among the CV population reflects that the present-day population of pre-CVs is not fully representative of the progenitors of the present-day population of CVs.

Chapter 6

Conclusions

This Ph.D. Thesis is devoted to the confirmation, by means of the radial velocity (RV) technique, of the candidate planets detected with the transit method by the WFCAM Transit Survey (WTS). The high-resolution spectra employed for the computation of the RV measures were observed with the 9.2-m Hobby-Eberly Telescope (HET). The pipeline for the reduction and analysis of the spectroscopic data has been created and tested during the Ph.D.. The results obtained with this pipeline allowed to confirm the planetary nature of two transiting candidates detected by the WTS.

An introduction to the extrasolar planets is given in Chapter 1. The main methods for their detection, in particular photometric transit and Doppler method, are shown. The formation of both rocky and gaseous planets is discussed within the 'Solar Nebular Disk Model'. The first are thought to form in the inner part of the Proto-planetary Disk (PPD), where the temperature is high enough to prevent condensation of water ice resulting in the coagulation of purely rocky grains.

A more complicated process leads to the formation of giant planets. It occurs beyond the so-called 'snow line', where planetary embryos are mainly made of various ices. As a result, they are several times more massive than in the inner part of the PPD, allowing the accretion of the hydrogen and helium from the disk to start. The gas accretion stops when a gap in the disk opens as a result of the exhaustion of the gas in the neighbourhood of the planet. Another model, the 'disk instability' one, states instead that giant planets form in the massive PPD as a result of its gravitational fragmentation. Such process is very similar to the initial stage of the formation of a star. The three main hypothesis for planetary migration are discussed too. Gas disk interaction, planetesimal-driven migration and planet-planet scattering have been proposed in order to explain the discovery of several giant gaseous planets orbiting their parent stars in just few days. Due to the small distance from the stars, the planet formation could not take place where the planets are observed now. A statistical analysis of the main properties of the nearly 800 extrasolar planets detected so far concludes the chapter.

The WTS survey, an on-going photometric monitoring campaign making use of the Wide Field Camera on the United Kingdom Infrared Telescope, is described in Chapter 2. The survey operates as a back-up program in the highly efficiently queue-scheduled operational mode of the telescope, observing in sky conditions unemployable by the other programs (*e. g.* seeing $> 1.3''$). The photometric observations are obtained in the J-band (1.25 μm) as the survey was primarily designed to find planets transiting M-dwarf stars. This wavelength is indeed near to the peak of the spectral energy distribution of a typical M-dwarf.

The strategies that characterize the observations are discussed with the general procedure employed for the detection of the transits among the thousands of J-band light curves related to all the stars in the observed fields. The efficiency of the observations (according to the back-up nature of the program) is quantified simulating transiting systems and applying the transit detection algorithm. The candidate transiting planets detected in the J-band light curves that passed all the selection criteria progressed to the candidate

confirmation phase.

The spectroscopic follow-up of the stars with the detected transits, was performed with the High Resolution Spectrograph (HRS) housed in the basement of the HET. The main properties of telescope and spectrograph are outlined in Chapter 3. Technical details of the HRS and its configurations employed for the acquisition of the high-resolution spectra are discussed. The structure of the visits with which the target stars were observed are described too.

Chapter 4 is dedicated to a complete description of the pipeline dedicated to the reduction of the HET high-resolution spectra and their following analysis for the computation of the RVs. The first step of the reduction consists in the calibration of the science and ThAr frames. In this phase, a particular procedure has been adopted for the flat-fielding of the frames, different from the commonly used approach. Such choice results into several advantages in the following steps of the pipeline and in an overall improvement on the final RV precision. The definition of the echelle apertures allows the following extraction of both the stellar and ThAr spectra. This latter data set is then involved in the computation of the dispersion function, which is finally employed for the wavelength calibration of the science stellar spectra.

After their normalization, the spectra are filtered for the cosmic-rays hits. The removal of the telluric lines and the resample of the spectra to a common wavelength binning are the last steps before the cross-correlation between the observed and the template spectra. Statistical tools are finally applied for the computation of the RV mean value and uncertainty related to all the epochs in which a star was observed.

The observation of several target stars, characterized by different apparent magnitude and spectral type, allowed to debug, optimize and test the pipeline. The first part of Chapter 5 collects the results coming from such observations.

The star `HD195019`, a bright G3V-star (m_V=6.87), has a known planetary companion which causes a variation of the stellar RV with a semi-amplitude value of $\sim$275 m s^{-1}. The RVs obtained with the HET spectra reveal the presence of the planet and the parameters derived from the Keplerian fit of the data are consistent with those obtained by previous works. The SNR of the observed spectra is $\sim$150 with 200 s of exposure time. Both the mean size of the errorbars and the RMS of the residuals of the best fitting model are of the order of $\sim$13 m s^{-1}. This result demonstrates that the pipeline works properly and that the measured RVs are not affected by systematic uncertainties larger than few m s^{-1}.

A technical problem occurring under given instrumental configuration could be identified thanks to the observation of `HD352939`, a moderately bright G0V-star (m_V=9.71). The exposure time of the scientific frames was $\sim$1200 s in order to achieve a high precision of the RV measures. In this case the SNR of the observed spectra is $\sim$ 200, leading to an uncertainty on the RVs of only $\sim$10 m s^{-1}. Such uncertainty, the smallest of all the measures performed within the project, can be assumed as the limit value achievable with a not simultaneous wavelength calibration. Surprisingly, a significant deviation was found

between the RV values obtained employing the two different wavelength calibrations related to the ThAr exposures taken just before and after the scientific one. The discovery of this mechanical problem, due to an unexpected movement of the cross-disperser inside the HRS, permitted to the technical staff to fix the problem. In this way, a possible source of systematic was removed from any later scientific observation.

As the WTS searches for transiting planets around M-dwarf stars in the magnitude range m_V=13-16, the M4V star GJ1214 (m_V=14.67) was observed in order to define the RV precision achievable with such cooler and fainter stars. The spectra extracted by the science frames (∼40 minutes of exposure time) are characterized by a SNR of 10-30. The errorbars size of the final measured RVs result to be ∼60 m s^{-1}. Such precision is limited by the instrument employed for the spectroscopic follow-up. As the peak of the instrumental throughput of the HRS falls in the visible (∼6000 Å), the spectra taken with the HET do not represent the best data set with which to compute the RVs of such cool stars. It would be preferable to perform spectroscopic observations in the near infrared as them allow to achieve better results being more sensitive to the peak of the stellar emissivity at ∼10 000 Å.

Finally, the characterization of the pipeline employed for the reduction and analysis of the HET observations could not be complete without an estimate of the zero-point offset of the RV measurements with respect to the other instruments involved in the detection and confirmation of the extrasolar planets with the Doppler method. The observation of different stars in the open cluster M 67 permitted to estimate the offset with respect to the HARPS data. The wavelength calibration of the spectra observed with HARPS is an 'absolute wavelength calibration'. Hence, the HARPS measures are commonly assumed for the computation of the offsets related to the other instruments. This zero-point correction (resulting of 242±12 m s^{-1}) allows the comparison of the HET measures with those related to any other instruments involved in radial velocity follow-up.

In the second part of Chapter 5, the achieved scientific results are discussed. The RVs computed from the HET high-resolution spectra allowed to confirm the detection of the first two extrasolar planet performed by the WTS. WTS1 b is a ∼4 M_J planet orbiting in 3.35 days a late F-star with possibly slightly sub-solar metallicity. With a radius of 1.49 R_J, it is the third largest planet of the known extrasolar planets in the mass range 3-5 M_J. Its unusual large radius can not be explained within the standard evolution models, even considering the strong radiation that the planet receives from the parent star. Ohmic heating could be a possible mechanism able to bring energy in the deeper layers of WTS1 b and hence explaining its radius anomaly.

WTS2 b is instead a ∼1 M_J planet orbiting an early K-star in about 1 day only. The basic properties of WTS2 b, such as its mass, radius, and equilibrium temperature are concordant with the general population of HJs. Its radius (1.35 R_J) is inflated above that of Jupiter, but is within the scatter of other known HJs. As WTS2 b orbits very close to its host star, it receives a high level of incident radiation. Hence, the detection of a secondary eclipses is expected in the Ks-band. Such observation will allow to study a highly irradiated planet but around a cool star, cooler than many of the currently known very hot-Jupiters host

stars. An insight to the effect of the stellar spectrum on the composition and structure of hot-Jupiter atmospheres would be provided.

Beyond the RoPACS network, the pipeline has been employed for the reduction and analysis of the HET spectra related to the white dwarf NLTT 5306. The radial velocity follow-up of this object allowed to confirm the presence of a brown dwarf companion of $56\pm3\,M_J$ orbiting in $\sim$102 minutes, the shortest period ever observed in such systems.

To conclude, the discoveries of WTS1 b and WTS2 b demonstrate the capability of WTS to find planets, even if it operates in a back-up mode during dead time on a queue-schedule telescope and despite of the somewhat randomised observing strategy. Moreover, the two new discovered planets are hot-Jupiters orbiting an F and a K-star even if the project was designed to search for extrasolar planets hosted by M-dwarfs.

Currently, the most efficient instrument employed for the detection of extrasolar planets is *Kepler*, a space observatory launched by NASA (Borucki et al., 2010). The mission was specifically designed to survey a portion of our region of the Milky Way galaxy to detect Earth-size planets with the photometric transit method. The scientific objective of the *Kepler* Mission is to explore the structure and diversity of planetary systems. This is achieved by surveying a large sample of stars in order to determine the percentage of terrestrial and larger planets in or near the habitable zone. As of December 2012, more than 100 confirmed extrasolar planets have been discovered by *Kepler*, while almost 3000 are the detected candidates planets waiting for confirmation[1]. Among the 10^5 stars observed by *Kepler*, about a thousand are M stars. Accordingly to the detection of no Jupiter-like planets around this sample of stars, the upper limit of the very hot-Jupiter planetary occurrence around M-darfs can be estimated, resulting in a value of 0.04. This is a looser constrain than the one derived for the WTS M-dwarfs sample (0.017). Such better estimation of the occurrence fraction is a consequence of the number of stars observed by the WTS which is a factor of 2 higher than those in the *Kepler* field of view.

As the candidates detected by *Kepler* are all transiting companions, the confirmation via radial velocity measurements is favoured as the inclination of the orbit i is known. The information obtained by both methods, transit and radial velocity, allows to fully characterize the newly discovered planetary systems. Nowadays, programs involved in the spectroscopic follow-up are operating with precisions as good as $0.5\,\mathrm{m\ s^{-1}}$ on 4-m class telescopes, but more routinely at $1\,\mathrm{m\ s^{-1}}$ (Mayor & Udry, 2008). There are several sources of noise that contribute to limit the precision of radial velocity measurements, including those intrinsic to the instrumentation and measurement process, and those associated with the star itself. The ESO – ESPRESSO echelle spectrograph (Pepe et al., 2010) that will be commissioned at the VLT, using up to four of the 8.2-m telescopes, is designed to achieve a precision and long-term stability better than $0.1\,\mathrm{m\ s^{-1}}$ (Mayor & Udry, 2008). At this level of precision, detection (and confirmation) of Earth-sized planets around Sun-like stars is possible.

The transit and Doppler methods are most sensitive in the detection of planets with

[1] *http://kepler.nasa.gov/Mission/discoveries/*

an edge-on orbit respect to line of sight. The astrometry method can thus be considered complementary as it best performs in the detection of stellar wobbles due to the presence of planets in a face-on orbit. The space astrometry mission *Gaia* (Lindegren et al., 2012), planned to be launched by the European Space Agency (ESA) in 2013, will determine accurate astrometric data for about one billion objects in the magnitude range from 6 to 20. Accuracies of $\sim 8\,\mu$as are typically expected for the trigonometric parallaxes, positions at mean epoch, and annual proper motions of simple (*i. e.* apparently single) stars down to 15^{th} magnitude. *Gaia* will provide unprecedented positional measurements with the accuracies needed to produce a stereoscopic and kinematic census of about one billion stars in our Galaxy. Combined with astrophysical information for each star, these data will have the precision necessary to quantify the early formation, and subsequent dynamical, chemical and star formation evolution of our Galaxy. Based on current estimates of the distribution of planets and their orbits, *Gaia* will also be capable of discovering thousands of extra-solar planets through the detection of the parent star position wobble. This astrometry method is suitable for detecting long-period planets, but requires precise measurements and long time spans.

All the efforts in the detection of extrasolar planets will allow to enlarge even more the statistical sample of planets. The determination of the distribution of the physical properties of the planets, mostly mass and radius; the characterization of their orbit; the occurrence ratio of rocky and gaseous planets in each systems will allow to better understand the processes involved in the formation and evolution of a planetary system, comprised our own Solar System.

The investigation of exoplanetary atmospheres represents a landmark in placing our Solar System in context within the Universe and by addressing the suitability of planets for the presence of life. In the past ten years, we have learned how to obtain the first spectra of exoplanets using transit transmission and emission spectroscopy. With the high stability of Spitzer, Hubble, and large ground-based telescopes the spectra of bright close-in massive planets can be obtained and species like water vapour, methane, carbon monoxide and dioxide have been detected. The Exoplanet Characterisation Observatory (EChO Tinetti et al., 2012) is a mission under the ESA discussion specifically geared for this purpose (possible launch in 2022). EChO will simultaneously observe a broad spectral region (from the visible to the mid-infrared) to constrain from one single spectrum the temperature structure of the atmosphere, the abundances of the major carbon and oxygen bearing species, the expected photochemically-produced species and magnetospheric signatures. The spectral range and resolution are optimized to distinguish features belonging to up to 30 molecules and retrieve the composition and temperature structure of planetary atmospheres. The identification of potential biosignatures in the atmospheres of super-Earths in the habitable zone of stars cooler than the Sun will challenge the paradigm of the Earth-twin orbiting a Sun-twin as the only possible environment that allows the formation of life.

Appendix A

Keplerian orbit model[†]

In this appendix, the model employed in the best-fitting procedure of the radial velocity (RV) data is explained. The complete expression for the RV of a star due to the presence of a single orbiting planet is:

$$V_r = \frac{2\pi a}{P\sqrt{1-e^2}} \frac{m_p sin(i)}{(M_\star + M_p)} [cos(f+\omega) + e \cdot cos\omega] + V_0 \tag{A.1}$$

where a is the semi-major axis of the orbit of the planet, P is the orbital period, m_p is the mass of the planet, $M_\star$ is the mass of the star, i is the inclination of the orbital plane, e is the eccentricity of the orbit, f is the true anomaly, ω is the argument of the periastron and V_0 is the systemic velocity off-set of the star-planet system.

In order to fit the data, the RV is usually parametrized as a function of the time t as follow:

$$V_r(t) = K \cdot [cos(f(t)+\omega) + e \cdot cos(\omega)] + V_0 \tag{A.2}$$

where:

$$K = \frac{m_p sin(i)}{(M_\star + m_p)} \frac{2\pi a}{P\sqrt{1-e^2}} \tag{A.3}$$

In Eq. A.2 only the true anomaly f results to be a function of the time t. In the case of circular orbits (e=0), it results to be a linear function of time. On the other hand, in the general elliptic case, it is the mean anomaly l to be a linear function of the time: $l=\frac{2\pi}{P}(t\text{-}\tau)$ where τ is the time of passage through the periastron. The relationship between the true anomaly f and the mean anomaly l is given in terms of the intermediate eccentric anomaly u. The relation between these three quantities is expressed by the following equations:

$$tan(f/2) = \sqrt{\frac{1+e}{1-e}} \cdot tan(u/2); \qquad l = u - e \cdot sin(u) \tag{A.4}$$

[†]Based on Beaugé et al. (2007)

The latter is the classical Kepler equation, and must be solved iteratively to obtain the passage from l (or the time t) to the eccentric anomaly u and, consequently, to the true anomaly f that appears in Eq. A.2.

Figure A.1 shows the phase folded RV measurements of HD80606 (Moutou et al., 2009). The fit of the data with a Keplerian orbit model allowed Moutou and collaborators to estimate the orbital parameters of HD80606 b, amongst which the eccentricity (e=0.934±0.003), the second highest measured value among the eccentricities of the known extrasolar planets. Due to the high eccentricity, the best fitting model heavily deviates from a sinusoid profile (circular orbit) as can be clearly seen in the figure.

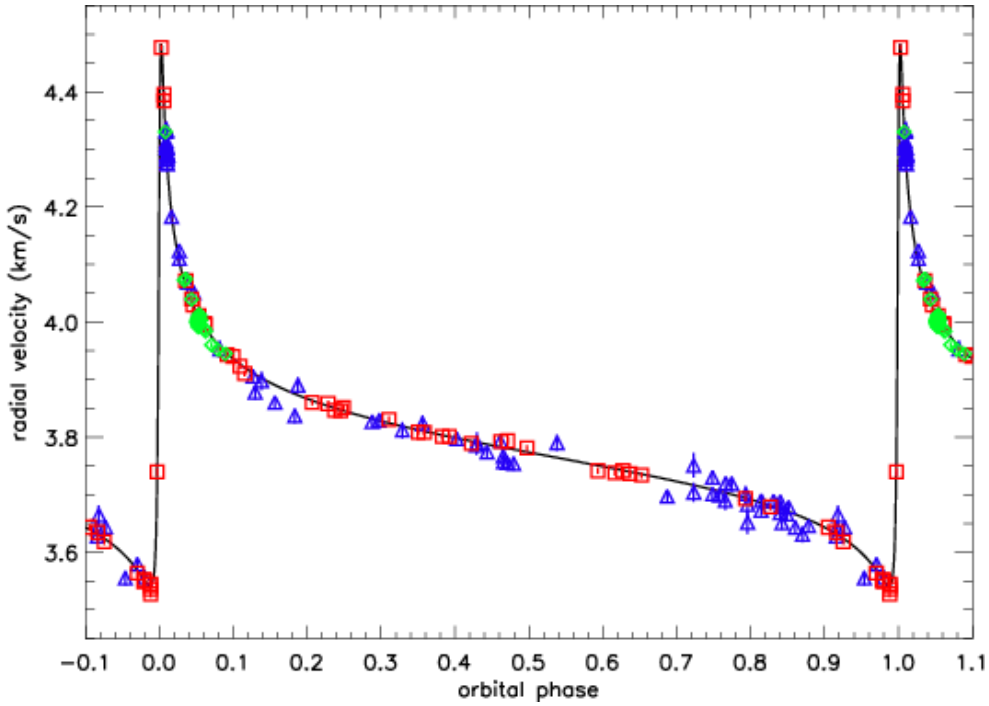

Figure A.1: Phase folded RV measurements of HD80606 as a function of the orbital phase. ELODIE data in blue, Keck data in red, SOPHIE data in green. The best-fitting Keplerian model (solid line) is characterized by e=0.934±0.003 (Moutou et al., 2009).

Appendix B

Analytic light curve transit[‡]

In this appendix, the model employed in the best-fitting procedure of the photometric data is explained. The transit method is based on the observation of small drops in the brightness of the observed star. Each drop occurs when the orbit of a planets passes ('transits') in front of the star. There are four key points in a transit referred to as 1^{st} to 4^{th} contacts. The first contact begins when the front edge of the planet just touches the edge of the star. The second contact occurs as the planet passes fully in front of the star. After the 2^{nd} contact, the planet is fully in front of the star. Starting from the third contact, the planet is no longer fully in front of the star and finally the fourth contact occurs as the back edge of the planet touches the far edge of the star, the last moment that the planet is occulting the star. These important points naturally divide a transit into 4 distinct stages: 'ingress', 'full eclipse', 'egress' and 'out of transit' elsewhere.

B.1 Uniform source

As a first approximation, the transit of a planet can be simply modelled as an eclipse of a spherical star, with a constant luminosity across the disc, by an opaque, dark sphere. In what follows, d is the centre-to-centre distance between the star and the planet, r_p is the radius of the planet, $r_\star$ is the stellar radius, z=d/r is the normalized separation of the centres, and p=$r_p/r_\star$ is the size ratio (Figure B.1b). The flux relative to the unobscured flux is F. For a uniform source, the ratio of obscured to unobscured flux is $F^e(p,z)$=1-$\lambda^e(p,z)$, where:

$$\lambda^e(p,z) = \begin{cases} 0, & 1+p<z \\ \frac{1}{\pi}\left[p^2\kappa_0 + \kappa_1 - \frac{1}{2}\sqrt{4z^2-(1+z^2-p^2)^2}\right], & |1-p|<z<1+p \\ p^2, & z \le 1-p \end{cases} \quad \text{(B.1)}$$

with κ_0=$\cos^{-1}[(p^2$+z^2-1)/2pz] and κ_1=$\cos^{-1}[(1$-p^2+$z^2)/2z]$. The first case (when $1+p<z$) describes the out of transit flux of the system. The second case describes the flux during

[‡]Based on Mandel & Agol (2002) and Seager & Mallén-Ornelas (2003)

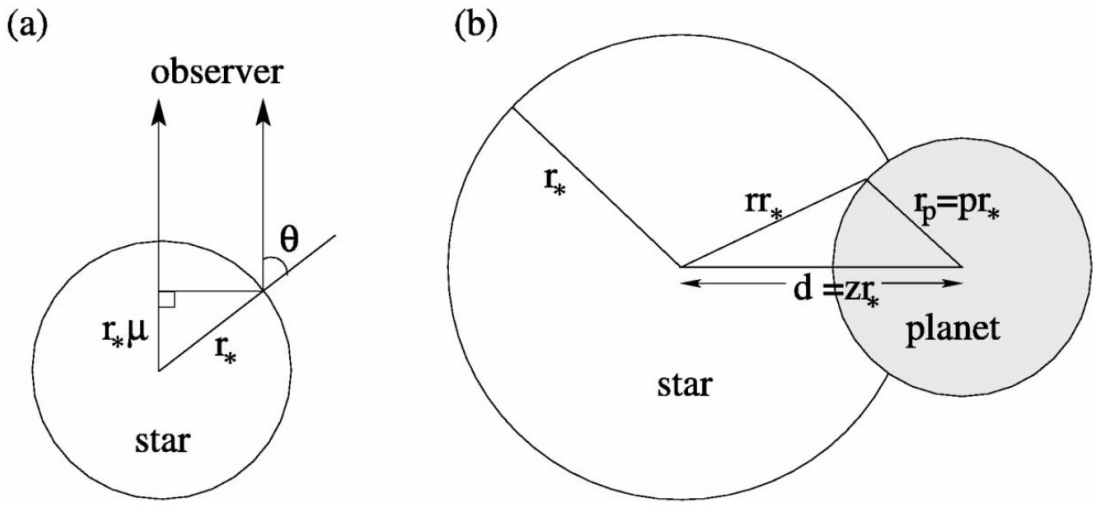

Figure B.1: (a) Geometry of limb darkening. The star is seen edge-on, with the observer off the top of the page. The star has radius $r_\star$, and θ is defined as the angle between the observer and the normal to the stellar surface, while μ=cos(θ). (b) Transit geometry from the perspective of the observer.

ingress and egress. The third case describes the flux during full eclipse. In the situation in which the planet is large enough to occult the entire star at once, of course λ^e=1 but this case is not relevant for exoplanets.

The transit shape defined by the previous set of equations can be parametrize in terms of transit depth ΔF, total transit duration t_T (first to fourth contact), and duration of the transit within ingress and egress t_F (second to third contact). Figure B.2 gives an illustrative definition of these three quantities. Three equations describe the geometry of the transit and depend on four observables: the period P, the transit depth ΔF, t_F, and t_T. Four combinations of the physical parameters of the system (stellar mass $m_\star$, semi-major axis of the orbit a, inclination of the orbit i, $r_\star$ and r_p) can be found directly from the observables described above using the the three geometrical equations coupled with the Kepler's third law (assuming $m_p \ll m_\star$ and a circular orbit[1]). The four combinations of parameters are as follows. The planet-star radius ratio, which trivially follows from the third case in Equation B.1:

$$\frac{r_p}{r_\star} = \sqrt{\Delta F}; \tag{B.2}$$

the impact parameter b, defined as the projected distance between the planet and star centres during mid-transit in units of $r_\star$:

$$b \equiv \frac{a}{r_\star}\, cos(i) = \left\{ \frac{(1-\sqrt{\Delta F})^2 - [sin^2(t_F\pi/P)/sin^2(t_T\pi/P)]\,(1+\sqrt{\Delta F})^2}{1-[sin^2(t_F\pi/P)/sin^2(t_T\pi/P)]} \right\}^{1/2}; \tag{B.3}$$

[1]Circular orbits are expected for short-period planets as a result of their short tidal circularization timescale.

the ratio between the semi-major axis and the stellar radius:

$$\frac{a}{r_\star} = \left\{ \frac{(1+\sqrt{\Delta F})^2 - b^2\,[1 - sin^2(t_T\pi/P)]}{sin^2(t_T\pi/P)} \right\}^{3/2} ; \tag{B.4}$$

and the stellar density $\rho_\star$, which can be derived from the above equation for $a/r_\star$ and the Kepler's third law:

$$\rho_\star \equiv \frac{m_\star}{r_\star^3} = \left(\frac{4\pi^2}{P^2 G}\right) \left\{ \frac{(1+\sqrt{\Delta F})^2 - b^2\,[1 - sin^2(t_T\pi/P)]}{sin^2(t_T\pi/P)} \right\}^{3/2} \tag{B.5}$$

The parameters b and $a/r_\star$ are dimensionless. The density can be written in units of $\rho_\odot$ by substituting $4\pi^2/G = 365.25^2/215^2\,\mathrm{day}^2\ m_\odot/r_\odot^3$.

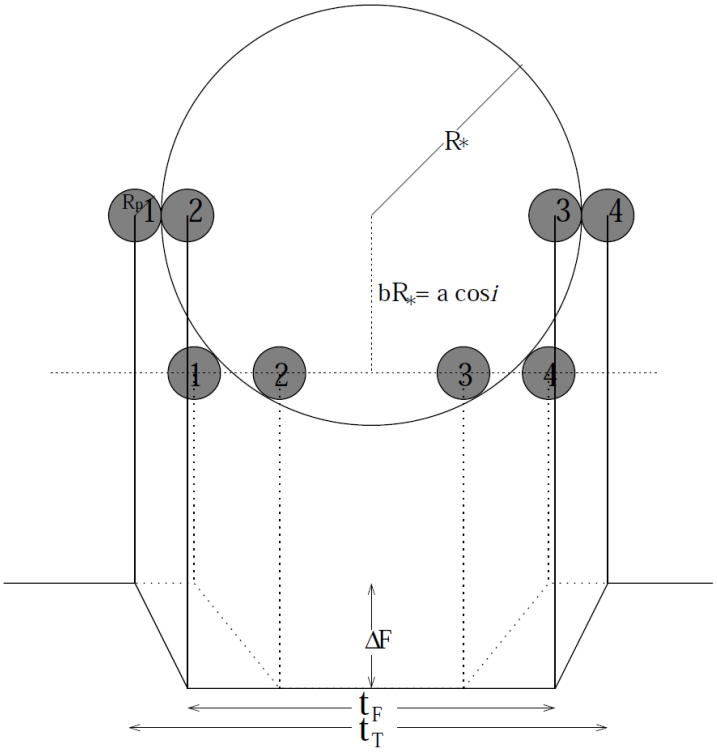

Figure B.2: Definition of transit light curve observables. Two schematic light curves are shown on the bottom (solid and dotted lines), and the corresponding geometry of the star and planet is shown on the top. Indicated on the solid light curve are the transit depth ΔF, the total transit duration t_T, and the transit duration between ingress and egress t_F. First, second, third, and fourth contacts are noted for a planet moving from left to right. Also defined are $R_\star$, R_p, and the impact parameter b corresponding to orbital inclination i. Different impact parameters b (or different i) will result in different transit shapes, as shown by the transits corresponding to the solid and dotted lines.

It is interesting to consider the geometrical and physical origin of these combinations of parameters. The impact parameter b depends almost entirely on the transit shape (parametrized by t_F/t_T) and the ratio of planet and star sizes. The term $a/r_\star$ is the ratio of orbital semi-major axis to planet radius; to first order it is related to the ratio of transit duration to total period. The term $a/r_\star$ is also dependent on the impact parameter b and planet-star size ratio because these parameters affect the transit duration. The stellar density, $\rho_\star$, comes from Kepler's third law and the transit duration t_T; Kepler's third law describes how much mass is enclosed inside the planetary orbit, and the stellar radius is described by the transit duration with a physical scale set by Kepler's third law. Again, $\rho_\star$ is also dependent on the impact parameter b and the planet-star size ratio because these parameters affect the transit duration.

The five physical parameters $m_\star$, $r_\star$, a, i and r_p can be derived from the above solution for $r_p/r_\star$, b, $a/r_\star$, and $\rho_\star$ by using one additional equation: the stellar mass-radius relation. Such relation can be expressed as:

$$r_\star = \kappa \, m_\star^x \tag{B.6}$$

where κ is a constant coefficient for each stellar sequence (main sequence, giants, etc.) and x describes the power law of the sequence (e.g., $x \simeq 0.8$ for K, G and F main sequence stars, Cox, 2000). It is worth noting that the Kepler's third law and the stellar mass-radius relationship are the two physical equations required to break the degeneracy of the mathematical description given by Equation B.1, by setting a physical scale. This physical scale, together with the geometrical description, allows to achieve a unique solution for the parametrization of the transiting system.

B.2 Limb-darkening

As a star is not uniformly bright across its entire surface, the previous assumption is not enough to model the transit feature in the observed light curves. Modelling an exoplanet transit, the effect called 'limb darkening' must be taken into account. Limb darkening causes the edges of a star to appear darker than the centre. It results from the fact that the optical depth is different at the edges of the star than at the centre. A star becomes opaque at a specific optical depth which is uniform across the star, but the radius at which this optical depth is reached increases towards the edge. As a result, the effective temperature of the star appears to decrease towards the edge, causing it to appear fainter. Hence, a transiting planet will block more light as it transits the centre of the star than when it passes close to the edges. A comparison between the expected light curve transit shape related to the uniform brightness assumption and the model computed considering the limb darkening is reported in Figure B.3

A non-linear limb darkening law fits well a wide range of stellar models and observational bands (Claret, 2000). The specific intensity on the disk of the star, as a function of

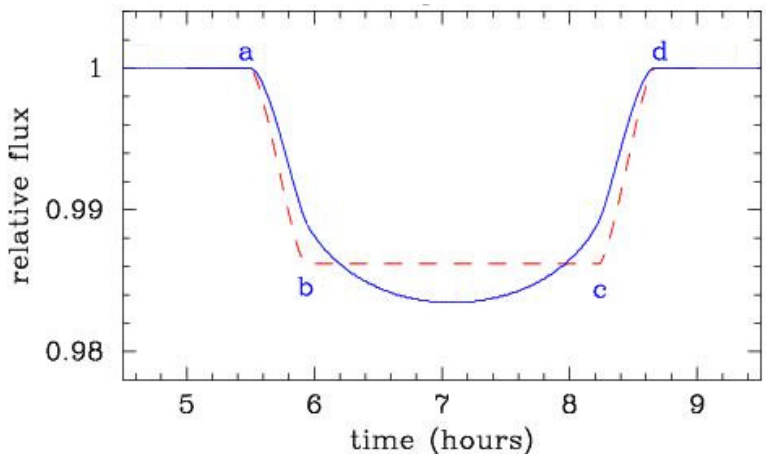

Figure B.3: Models of an exoplanet transit relative to the uniform star brightness (dashed red line) and considering the stellar limb-darkening (blue solid line). The letters, a to d, refer to the four contact points.

the normalized radial coordinate r, can be written as:

$$I(r) = 1 - \sum_{n=1}^{4} c_n \left(1 - \mu^{n/2}\right) \tag{B.7}$$

where μ=cos(θ)=(1-r^2)$^{1/2}$ and with $I(0)$=1. Figure B.1a shows the geometry of limb-darkening and the definition of μ. The light curve described previously by the three cases in Equation B.1 is now substituted, considering the limb-darkening, by the following expression:

$$F(p,z) = \left[\int_0^1 dr 2r I(r)\right]^{-1} \int_0^1 dr I(r) \frac{d\left[F^e(p/r, z/r)r^2\right]}{dr} \tag{B.8}$$

where $F^e(p,z)$ is the light curve of a uniform source previously defined. Figure B.4 shows five light curves, the first of which has c_n=0 (n=1,4), while the other four have c_n=1 and c_m=0 ($m \neq n$) for p=0.1. These may be thought of as a basis set for any non linear limb darkening profiles. Note that the higher order functions have flux which is concentrated more strongly toward the centre of the star, and thus have a more gradual ingress and a deeper minimum as more flux is blocked at the centre than the edge.

Claret (2000) has found that the most suitable limb-darkening functions are the quadratic law in μ. In such case, the expression of $I(r)$ that appears in Equation B.8 becomes:

$$I(r) = 1 - \gamma_1(1-\mu) - \gamma_2(1-\mu)^2 \tag{B.9}$$

Where γ_1+γ_2 <1. This parametrization of the specific intensity on the disk of the star, $I(r)$, is a particular case of the non linear Equation B.7. Modelling in this way the transit in the observed light curve does not allow to derive analytically the five physical parameters ($m_\star$, $r_\star$, a, i and r_p) of the system. Hence, the data are best fitted via χ^2 minimization performed

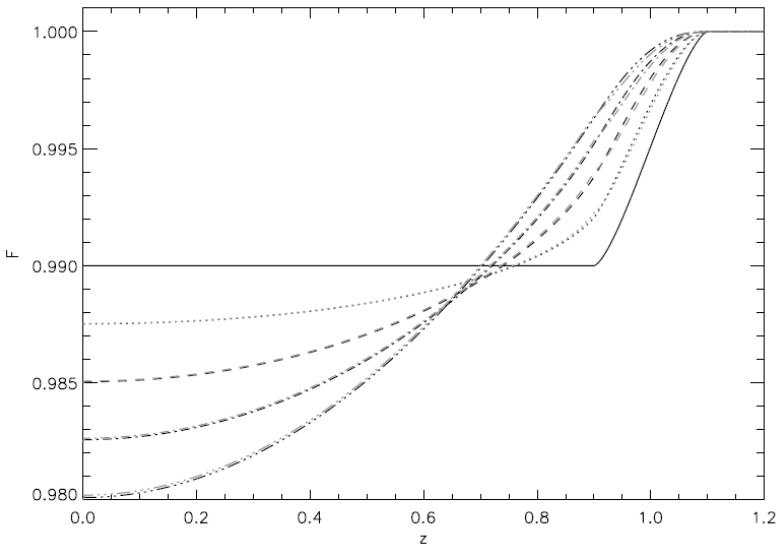

Figure B.4: Transit light curves for p=0.1 and c_1=c_2=c_3=c_4=0 (solid line), and all coefficients equal zero but c_1=1 (dotted line), c_2=1 (dashed line), c_3=1 (dash-dot line), or c_4=1 (dash, triple-dot line). The lighter lines (nearly indistinguishable) show the approximation discussed in Section B.3.

over a five parameters space. Figure B.5 reports four examples of the correlation plots of the quantities derived from the fit of a transit. The plots show the pairs of parameters that most correlate. The parameters γ_1 and γ_2 are considered as fixed parameters. Claret & Bloemen (2011) give the tabulated values of such parameters as a function of the photometric band of the measured light curve and the spectral information ($T_{\rm eff}$, log g and [Fe/H]) of the observed star. An example of the values of such parameters is reported in Table B.1. The values are related to a solar metallicity star with $T_{\rm eff}$=5000-7500 K and log g=3.5-4.5 observed in the J-band.

B.3 Small planets

For a small planet, $p \lesssim 0.1$, the interior of the light curve (between second and third contact, or third case in Equation B.1) can be approximated by assuming the surface brightness of the star is constant under the disk of the planet. If the limb-darkening coefficients, γ_1 and γ_2, of the star are known (from, for example, spectral information), and if the semi-major axis a is much larger than the size of the star $r_\star$ so that the orbit can be approximated by a straight line, then the shape of the eclipse for $p \lesssim 0.1$ is simply determined by the smallest impact parameter, b=$(a/r_\star)$ cos(i). This is a very fast means of computing transit light curves with reasonable accuracy (see Figure B.4) and may be used for any limb-darkening function.

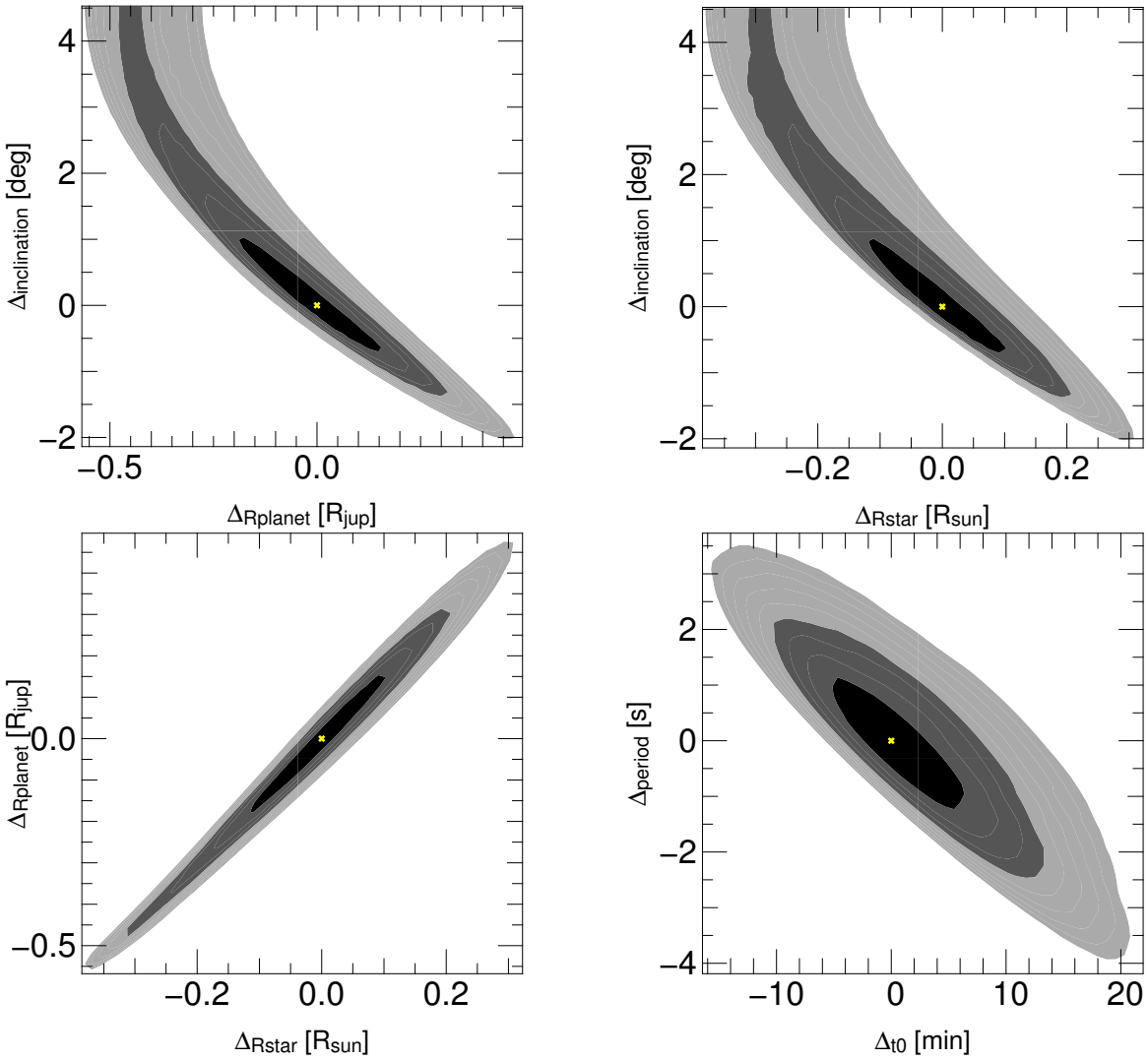

Figure B.5: Examples of correlation plots related the quantities derived from the fit of a transit. The χ^2 minima are indicated by crosses while the different tones of grey correspond to the 68%, 95% and 99% confidence level (darker to lighter respectively). The other couples of parameters do not show significant correlations.

Table B.1: Limb-darkening coefficients γ_1 and γ_2 for a solar metallicity star with $T_{\rm eff}$=5000-7500 K and log g=3.5-4.5. The values are related to a light curve observed in the J-band (Claret & Bloemen, 2011).

	log g=3.5		log g=4.0		log g=4.5	
$T_{\rm eff}$	γ_1	γ_2	γ_1	γ_2	γ_1	γ_2
5000	0.2270	0.2748	0.2312	0.2730	0.2348	0.2718
5250	0.1972	0.2848	0.2031	0.2823	0.2060	0.2823
5500	0.1703	0.2925	0.1764	0.2899	0.1793	0.2900
5750	0.1453	0.2983	0.1508	0.2963	0.1563	0.2946
6000	0.1231	0.3008	0.1300	0.2988	0.1349	0.2978
6250	0.1054	0.3008	0.1125	0.2989	0.1167	0.2982
6500	0.0913	0.2994	0.0978	0.2978	0.1016	0.2972
6750	0.0777	0.2998	0.0844	0.2970	0.0889	0.2954
7000	0.0675	0.2983	0.0726	0.2962	0.0777	0.2942
7250	0.0596	0.2880	0.0642	0.2934	0.0683	0.2921
7500	0.0765	0.2716	0.0575	0.2894	0.0614	0.2889

Curriculum vitae

Personal

Date of birth	28 November 1984
Place of birth	Bolzano (BZ), Italy
Nationality	Italian

Education

2009 - present	PhD student of the International Max Planck Research School at the Max-Planck-Institut für extraterrestrische Physik (Garching bei München, Germany). Thesis topic: Radial velocity curves with high-resolution spectra from the HRS at the Hobby-Eberly Telescope Supervisor: Prof. Dr. Roberto Philip Saglia
2009	Master degree in Astrophysics and Space Science at the University of Trieste. Grade: 110/110 cum Laude. Thesis Topic: Tomography of the inter galactic medium with high-resolution spectra of QSO pairs at high red-shift. Supervisor: Prof. Dr. Stefano Cristiani
2006	Bachelor degree in Physics at the University of Trieste. Grade: 109/110. Thesis topic: Atomic configuration and periodic table in a mean-field theory. Supervisor: Prof. Dr. Raffaele Resta
2001	High School Diploma. Grade: 90/100

Publications

1. 2013 - *WTS-2 b: a hot Jupiter orbiting near its tidal destruction radius around a K-dwarf*
   Birkby, J.; **Cappetta, M.**; Cruz, P.; J. Koppenhöfer, J.; Ivanyuk, O.; Mustill, A. J.; Hodgkin, S. T.; Pinfield, D. J.; Saglia, R. P.; Sipöcz, B.; Gàbor, K.; Pavlenko, Y. V.; Barrado, D.; Bayo, A. M.; Campbell, D. A.; Catalan, S.; Fossati, L.; Gàlvez-Ortiz, M. C.; Kenworthy M.; Martín, E. L.; Mislis, D.; de Mooij, E. J. W.; Nefs, B.; Snellen, I. A. G.; Stoev, H.; Zendejas, J.; del Burgo, C.; Barnes, J.; Goulding, N.; Haswell, C.; Jones, H.; Kuznetsov, M.; Lodieu, N.; Marocco, F.; Moya, A.; Murgas, F.; Napiwotzki, R.; Palle, E.; Pollacco, D.; Solano, E.; Steele, P.; Tata, R., MNRAS submitted

2. 2013 - *Searching for transits in the WTS with difference imaging light curves*
   Zendejas, J.; Koppenhöfer, J.; Saglia, R. P.; Birkby, J.; Hodgkin, S. T.; Gàbor, K.; Pinfield, D. J.; Sipöcz, B.; Barrado, D.; Bender, R.; del Burgo, C.; **Cappetta, M.**; Martín, E. L.; Nefs, B.; Riffeser, A.; Steele, P., A&A submitted

3. 2012 - *A sensitivity analysis of the WFCAM Transit Survey for short-period giant planets around M dwarfs*
   Gàbor, K.; Hodgkin, S.; Sipöcz, B.; Pinfield, D.; Barrado, D.; Birkby, J.; **Cappetta, M.**; Cruz, P.; Koppenhöfer, J.; Martín, E.; Murgas, F.; Nefs, B.; Saglia, R. P.; Zendejas, J., MNRAS submitted

4. 2012 - *NLTT5306: The shortest Period Detached White Dwarf + Brown Dwarf Binary*
   Steele, P. R.; Saglia, R. P.; Burleigh, M. R.; Marsh, T. R.; Gnsicke, B. T.; Lawrie, K.; **Cappetta, M.**; Girven, J.; Napiwotzki, R., MNRAS in press, astro-ph/1212.2899S

5. 2012 - *The first planet detected in the WTS: an inflated hot-Jupiter in a 3.35 day orbit around a late F-star*
   Cappetta, M.; Saglia, R. P.; Birkby, J. L.; Koppenhoefer, J.; Pinfield, D. J.; Hodgkin, S. T.; Cruz, P.; Kovàcs, G.; Sipöcz, B.; Barrado, D.; Nefs, B.; Pavlenko, Y. V.; Fossati, L.; del Burgo, C.; Martín, E. L.; Snellen, I.; Barnes, J.; Bayo, A. M.; Campbell, D. A.; Catalan, S.; Gàlvez-Ortiz, M. C.; Goulding, N.; Haswell, C.; Ivanyuk, O.; Jones, H.; Kuznetsov, M.; Lodieu, N.; Marocco, F.; Mislis, D.; Murgas, F.; Napiwotzki, R.; Palle, E.; Pollacco, D.; Sarro Baro, L.; Solano, E.; Steele, P.; Stoev, H.; Tata, R.; Zendejas, J., MNRAS in press, astro-ph/1210.1217

6. 2012 - *Discovery and characterization of detached M dwarf eclipsing binaries in the WFCAM Transit Survey*
   Birkby, J. L.; Nefs, B.; Hodgkin, S.; Kovàcs, G.; Sipöcz, B.; Pinfield, D. J.; Snellen, I.; Mislis, D.; Murgas, F.; Lodieu, N.; de Mooij, E.; Goulding, N.; Cruz, P.; Stoev, H.; **Cappetta, M.**; Palle, E; Barrado, D; Saglia, R. P.; Martin, E.; Pavlenko, Y., MNRAS 426, 1507B, astro-ph/1206.2773

7. 2012 - *Four ultra-short-period eclipsing M-dwarf binaries in the WFCAM Transit Survey*
   Nefs, S. V.; Birkby, J. L.; Snellen, I. A. G.; Hodgkin, S. T.; Pinfield, D. J.; Sipöcz, B.; Kovàcs, G.; Mislis, D.; Saglia, R. P.; Koppenhoefer, J.; Cruz, P.; Barrado, D.; Martin, E. L.; Goulding, N.; Stoev, H.; Zendejas, J.; del Burgo, C.; **Cappetta, M.**; Pavlenko, Y. V., MNRAS 425, 950N, astro-ph/1206.1200

8. 2010 - *High-resolution spectroscopy of the 3D cosmic web with close QSO groups*
   Cappetta, M.; D'Odorico, V.; Cristiani, S.; Saitta, F.; Viel, M., MNRAS 407, 1290C, astro-ph/1004.0221

Bibliography

Absil, O. & Mawet, D. (2010). Formation and evolution of planetary systems: the impact of high-angular resolution optical techniques. *A&AR*, **18**, 317–382.

Adams, F. C. & Laughlin, G. (2003). Migration and dynamical relaxation in crowded systems of giant planets. *ICARUS*, **163**, 290–306.

Adelman, S., Bikmaev, Gulliver, I., & A.; Smalley, B. (2002). *Round Table on Instrumentation and Data Processing*, pages 1–14.

Adelman-McCarthy, J. K., Agüeros, M. A., Allam, S. S., Allende Prieto, C., Anderson, K. S. J., Anderson, S. F., Annis, J., Bahcall, N. A., Bailer-Jones, C. A. L., Baldry, I. K., Barentine, J. C., Bassett, B. A., Becker, A. C., Beers, T. C., Bell, E. F., Berlind, A. A., Bernardi, M., Blanton, M. R., Bochanski, J. J., Boroski, W. N., Brinchmann, J., Brinkmann, J., Brunner, R. J., Budavári, T., Carliles, S., Carr, M. A., Castander, F. J., Cinabro, D., Cool, R. J., Covey, K. R., Csabai, I., Cunha, C. E., Davenport, J. R. A., Dilday, B., Doi, M., Eisenstein, D. J., Evans, M. L., Fan, X., Finkbeiner, D. P., Friedman, S. D., Frieman, J. A., Fukugita, M., Gänsicke, B. T., Gates, E., Gillespie, B., Glazebrook, K., Gray, J., Grebel, E. K., Gunn, J. E., Gurbani, V. K., Hall, P. B., Harding, P., Harvanek, M., Hawley, S. L., Hayes, J., Heckman, T. M., Hendry, J. S., Hindsley, R. B., Hirata, C. M., Hogan, C. J., Hogg, D. W., Hyde, J. B., Ichikawa, S.-i., Ivezić, Ž., Jester, S., Johnson, J. A., Jorgensen, A. M., Jurić, M., Kent, S. M., Kessler, R., Kleinman, S. J., Knapp, G. R., Kron, R. G., Krzesinski, J., Kuropatkin, N., Lamb, D. Q., Lampeitl, H., Lebedeva, S., Lee, Y. S., Leger, R. F., Lépine, S., Lima, M., Lin, H., Long, D. C., Loomis, C. P., Loveday, J., Lupton, R. H., Malanushenko, O., Malanushenko, V., Mandelbaum, R., Margon, B., Marriner, J. P., Martínez-Delgado, D., Matsubara, T., McGehee, P. M., McKay, T. A., Meiksin, A., Morrison, H. L., Munn, J. A., Nakajima, R., Neilsen, Jr., E. H., Newberg, H. J., Nichol, R. C., Nicinski, T., Nieto-Santisteban, M., Nitta, A., Okamura, S., Owen, R., Oyaizu, H., Padmanabhan, N., Pan, K., Park, C., Peoples, Jr., J., Pier, J. R., Pope, A. C., Purger, N., Raddick, M. J., Re Fiorentin, P., Richards, G. T., Richmond, M. W., Riess, A. G., Rix, H.-W., Rockosi, C. M., Sako, M., Schlegel, D. J., Schneider, D. P., Schreiber, M. R., Schwope, A. D., Seljak, U., Sesar, B., Sheldon, E., Shimasaku, K., Sivarani, T., Smith, J. A., Snedden, S. A., Steinmetz, M., Strauss, M. A., SubbaRao, M., Suto, Y., Szalay, A. S., Szapudi, I., Szkody, P., Tegmark, M., Thakar, A. R., Tremonti, C. A., Tucker, D. L.,

Uomoto, A., Vanden Berk, D. E., Vandenberg, J., Vidrih, S., Vogeley, M. S., Voges, W., Vogt, N. P., Wadadekar, Y., Weinberg, D. H., West, A. A., White, S. D. M., Wilhite, B. C., Yanny, B., Yocum, D. R., York, D. G., Zehavi, I., & Zucker, D. B. (2008). The Sixth Data Release of the Sloan Digital Sky Survey. *ApJS*, **175**, 297–313.

Aigrain, S. & Irwin, M. (2004). Practical planet prospecting. *MNRAS*, **350**, 331–345.

Alonso, R., Auvergne, M., Baglin, A., Ollivier, M., Moutou, C., Rouan, D., Deeg, H. J., Aigrain, S., Almenara, J. M., Barbieri, M., Barge, P., Benz, W., Bordé, P., Bouchy, F., de La Reza, R., Deleuil, M., Dvorak, R., Erikson, A., Fridlund, M., Gillon, M., Gondoin, P., Guillot, T., Hatzes, A., Hébrard, G., Kabath, P., Jorda, L., Lammer, H., Léger, A., Llebaria, A., Loeillet, B., Magain, P., Mayor, M., Mazeh, T., Pätzold, M., Pepe, F., Pont, F., Queloz, D., Rauer, H., Shporer, A., Schneider, J., Stecklum, B., Udry, S., & Wuchterl, G. (2008). Transiting exoplanets from the CoRoT space mission. II. CoRoT-Exo-2b: a transiting planet around an active G star. *A&A*, **482**, L21–L24.

Amôres, E. B. & Lépine, J. R. D. (2005). Models for Interstellar Extinction in the Galaxy. *AJ*, **130**, 659–673.

Anderson, D. R., Collier Cameron, A., Gillon, M., Hellier, C., Jehin, E., Lendl, M., Maxted, P. F. L., Queloz, D., Smalley, B., Smith, A. M. S., Triaud, A. H. M. J., West, R. G., Pepe, F., Pollacco, D., Ségransan, D., Todd, I., & Udry, S. (2012). WASP-44b, WASP-45b and WASP-46b: three short-period, transiting extrasolar planets. *MNRAS*, **422**, 1988–1998.

Anglada-Escudé, G., López-Morales, M., & Chambers, J. E. (2010). How Eccentric Orbital Solutions Can Hide Planetary Systems in 2:1 Resonant Orbits. *ApJ*, **709**, 168–178.

Armitage, P. J. (2010). *Astrophysics of Planet Formation*.

Armitage, P. J., Livio, M., Lubow, S. H., & Pringle, J. E. (2002). Predictions for the frequency and orbital radii of massive extrasolar planets. *MNRAS*, **334**, 248–256.

Avila, G. & Singh, P. (2008). Optical fiber scrambling and light pipes for high accuracy radial velocities measurements. In *Society of Photo-Optical Instrumentation Engineers (SPIE) Conference Series*, volume 7018 of *Society of Photo-Optical Instrumentation Engineers (SPIE) Conference Series*.

Baraffe, I., Chabrier, G., Allard, F., & Hauschildt, P. H. (1998). Evolutionary models for solar metallicity low-mass stars: mass-magnitude relationships and color-magnitude diagrams. *A&A*, **337**, 403–412.

Baraffe, I., Chabrier, G., Allard, F., & Hauschildt, P. H. (2002). Evolutionary models for low-mass stars and brown dwarfs: Uncertainties and limits at very young ages. *A&A*, **382**, 563–572.

Baraffe, I., Selsis, F., Chabrier, G., Barman, T. S., Allard, F., Hauschildt, P. H., & Lammer, H. (2004). The effect of evaporation on the evolution of close-in giant planets. *A&A*, **419**, L13–L16.

Baraffe, I., Chabrier, G., & Barman, T. (2008). Structure and evolution of super-Earth to super-Jupiter exoplanets. I. Heavy element enrichment in the interior. *A&A*, **482**, 315–332.

Baraffe, I., Chabrier, G., & Barman, T. (2010). The physical properties of extra-solar planets. *Reports on Progress in Physics*, **73**(1), 016901.

Barbuy, B. (1982). Ph.D. thesis, PhD thesis, Université de Paris VII, (1982).

Barbuy, B., Perrin, M.-N., Katz, D., Coelho, P., Cayrel, R., Spite, M., & Van't Veer-Menneret, C. (2003). A grid of synthetic spectra and indices Fe5270, Fe5335, Mgb and Mg_2 as a function of stellar parameters and [alpha/Fe]. *A&A*, **404**, 661–668.

Batalha, N. M., Borucki, W., Caldwell, D. A., Chandrasekaran, H., Gautier, T. N., Jenkins, J., & Koch, D. G. (2006). Optimization of the Kepler Field of View. In *American Astronomical Society Meeting Abstracts*, volume 38 of *Bulletin of the American Astronomical Society*, page #210.08.

Batygin, K. & Stevenson, D. J. (2010a). Inflating Hot Jupiters with Ohmic Dissipation. *ApJ*, **714**, L238–L243.

Batygin, K. & Stevenson, D. J. (2010b). Inflating Hot Jupiters with Ohmic Dissipation. *ApJ*, **714**, L238–L243.

Bayo, A., Rodrigo, C., Barrado Y Navascués, D., Solano, E., Gutiérrez, R., Morales-Calderón, M., & Allard, F. (2008). VOSA: virtual observatory SED analyzer. An application to the Collinder 69 open cluster. *A&A*, **492**, 277–287.

Bayo, A., Barrado, D., Huélamo, N., Morales-Calderón, M., Melo, C., Stauer, J., & Stelzer, B. (2012). Spectroscopy of Very Low Mass Stars and Brown Dwarfs in the Lambda Orionis Star Forming Region. *ArXiv e-prints*.

Beaugé, C., Ferraz-Mello, S., & Michtchenko, T. A. (2007). *Planetary Masses and Orbital Parameters from Radial Velocity Measurements*, page 1.

Becklin, E. E. & Zuckerman, B. (1988). A low-temperature companion to a white dwarf star. *Nature*, **336**, 656–658.

Bergeron, P., Wesemael, F., Dufour, P., Beauchamp, A., Hunter, C., Saffer, R. A., Gianninas, A., Ruiz, M. T., Limoges, M.-M., Dufour, P., Fontaine, G., & Liebert, J. (2011). A Comprehensive Spectroscopic Analysis of DB White Dwarfs. *ApJ*, **737**, 28.

Birkby, J., Pinfield, D., & et al. (2012).

Bodenheimer, P., Lin, D. N. C., & Mardling, R. A. (2001). On the Tidal Inflation of Short-Period Extrasolar Planets. *ApJ*, **548**, 466–472.

Bodenheimer, P., Laughlin, G., & Lin, D. N. C. (2003). On the Radii of Extrasolar Giant Planets. *ApJ*, **592**, 555–563.

Borucki, W. J., Koch, D. G., Brown, T. M., Basri, G., Batalha, N. M., Caldwell, D. A., Cochran, W. D., Dunham, E. W., Gautier, III, T. N., Geary, J. C., Gilliland, R. L., Howell, S. B., Jenkins, J. M., Latham, D. W., Lissauer, J. J., Marcy, G. W., Monet, D., Rowe, J. F., & Sasselov, D. (2010). Kepler-4b: A Hot Neptune-like Planet of a G0 Star Near Main-sequence Turnoff. *ApJ*, **713**, L126–L130.

Boss, A. (2009). *The Crowded Universe: The Search for Living Planets*.

Boss, A. P. (2003). Rapid Formation of Outer Giant Planets by Disk Instability. *ApJ*, **599**, 577–581.

Boss, A. P. (2005). Evolution of the Solar Nebula. VII. Formation and Survival of Protoplanets Formed by Disk Instability. *ApJ*, **629**, 535–548.

Bottke, W. F., Durda, D. D., Nesvorný, D., Jedicke, R., Morbidelli, A., Vokrouhlický, D., & Levison, H. F. (2005). Linking the collisional history of the main asteroid belt to its dynamical excitation and depletion. *ICARUS*, **179**, 63–94.

Breedt, E., Gänsicke, B. T., Girven, J., Drake, A. J., Copperwheat, C. M., Parsons, S. G., & Marsh, T. R. (2012). The evolutionary state of short-period magnetic white dwarf binaries. *MNRAS*, **423**, 1437–1449.

Bromley, B. C. & Kenyon, S. J. (2011). A New Hybrid N-body-coagulation Code for the Formation of Gas Giant Planets. *ApJ*, **731**, 101.

Burleigh, M., Dobbie, P., Maxted, P., & Napiwotzki, R. (2008). A roasted brown dwarf in an old binary. *Anglo-Australian Observatory Epping Newsletter*, **114**, 17.

Burleigh, M. R., Hogan, E., Dobbie, P. D., Napiwotzki, R., & Maxted, P. F. L. (2006). A near-infrared spectroscopic detection of the brown dwarf in the post common envelope binary WD0137-349. *MNRAS*, **373**, L55–L59.

Burrows, A. & Orton, G. (2009). Giant Planet Atmospheres and Spectra. *ArXiv e-prints*.

Burrows, A., Marley, M., Hubbard, W. B., Lunine, J. I., Guillot, T., Saumon, D., Freedman, R., Sudarsky, D., & Sharp, C. (1997). A Nongray Theory of Extrasolar Giant Planets and Brown Dwarfs. *ApJ*, **491**, 856.

Burrows, A., Hubeny, I., Budaj, J., & Hubbard, W. B. (2007). Possible Solutions to the Radius Anomalies of Transiting Giant Planets. *ApJ*, **661**, 502–514.

Butler, R. P., Vogt, S. S., Marcy, G. W., Fischer, D. A., Wright, J. T., Henry, G. W., Laughlin, G., & Lissauer, J. J. (2004). A Neptune-Mass Planet Orbiting the Nearby M Dwarf GJ 436. *ApJ*, **617**, 580–588.

Caccin, B., Cavallini, F., Ceppatelli, G., Righini, A., & Sambuco, A. M. (1985). Terrestrial O2 lines used as wavelength references Experimental profiles and asymmetries vs. model computations. *A&A*, **149**, 357–364.

Calabretta, M. R. & Greisen, E. W. (2002). Representations of celestial coordinates in FITS. *A&A*, **395**, 1077–1122.

Canuto, V. M. & Mazzitelli, I. (1991). Stellar turbulent convection - A new model and applications. *ApJ*, **370**, 295–311.

Capobianco, C. C., Duncan, M., & Levison, H. F. (2011). Planetesimal-driven planet migration in the presence of a gas disk. *ICARUS*, **211**, 819–831.

Cappetta, M., Saglia, R. P., & et al. (2012). The first planet detected in the WTS: an inflated hot-Jupiter in a 3.35 day orbit around a late F-star.

Casali, M., Adamson, A., Alves de Oliveira, C., Almaini, O., Burch, K., Chuter, T., Elliot, J., Folger, M., Foucaud, S., Hambly, N., Hastie, M., Henry, D., Hirst, P., Irwin, M., Ives, D., Lawrence, A., Laidlaw, K., Lee, D., Lewis, J., Lunney, D., McLay, S., Montgomery, D., Pickup, A., Read, M., Rees, N., Robson, I., Sekiguchi, K., Vick, A., Warren, S., & Woodward, B. (2007). The UKIRT wide-field camera. *A&A*, **467**, 777–784.

Castelli, F. & Kurucz, R. L. (2003). New Grids of ATLAS9 Model Atmospheres. In N. Piskunov, W. W. Weiss, and D. F. Gray, editors, *Modelling of Stellar Atmospheres*, volume 210 of *IAU Symposium*, page 20P.

Castelli, F., Gratton, R. G., & Kurucz, R. L. (1997). Notes on the convection in the ATLAS9 model atmospheres. *A&A*, **318**, 841–869.

Cayrel, R., Perrin, M.-N., Barbuy, B., & Buser, R. (1991). A grid of synthetic spectra for the determination of effective temperature, gravity and metallicity of F, G, and K stars. I - Description of the method. II - Application to 41 stellar spectra taken in the Basel field of SA 141. *A&A*, **247**, 108–129.

Chabrier, G. & Baraffe, I. (2000). Theory of Low-Mass Stars and Substellar Objects. *ARAA*, **38**, 337–377.

Chabrier, G. & Baraffe, I. (2007). Heat Transport in Giant (Exo)planets: A New Perspective. *ApJ*, **661**, L81–L84.

Chabrier, G., Baraffe, I., Allard, F., & Hauschildt, P. (2000). Evolutionary Models for Very Low-Mass Stars and Brown Dwarfs with Dusty Atmospheres. *ApJ*, **542**, 464–472.

Charbonneau, D., Brown, T. M., Latham, D. W., & Mayor, M. (2000). Detection of Planetary Transits Across a Sun-like Star. *ApJ*, **529**, L45–L48.

Charbonneau, D., Berta, Z. K., Irwin, J., Burke, C. J., Nutzman, P., Buchhave, L. A., Lovis, C., Bonfils, X., Latham, D. W., Udry, S., Murray-Clay, R. A., Holman, M. J., Falco, E. E., Winn, J. N., Queloz, D., Pepe, F., Mayor, M., Delfosse, X., & Forveille, T. (2009). A super-Earth transiting a nearby low-mass star. *Nature*, **462**, 891–894.

Chauvin, G., Lagrange, A.-M., Dumas, C., Zuckerman, B., Mouillet, D., Song, I., Beuzit, J.-L., & Lowrance, P. (2004). A giant planet candidate near a young brown dwarf. Direct VLT/NACO observations using IR wavefront sensing. *A&A*, **425**, L29–L32.

Claret, A. (2000). A new non-linear limb-darkening law for LTE stellar atmosphere models. *A&A*, **363**, 1081–1190.

Claret, A. & Bloemen, S. (2011). Gravity and limb-darkening coefficients for the Kepler, CoRoT, Spitzer, uvby, UBVRIJHK, and Sloan photometric systems. *A&A*, **529**, A75.

Coelho, P., Barbuy, B., Meléndez, J., Schiavon, R. P., & Castilho, B. V. (2005). A library of high resolution synthetic stellar spectra from 300 nm to 1.8 μm with solar and α-enhanced composition. *A&A*, **443**, 735–746.

Collier Cameron, A., Wilson, D. M., West, R. G., Hebb, L., Wang, X.-B., Aigrain, S., Bouchy, F., Christian, D. J., Clarkson, W. I., Enoch, B., Esposito, M., Guenther, E., Haswell, C. A., Hébrard, G., Hellier, C., Horne, K., Irwin, J., Kane, S. R., Loeillet, B., Lister, T. A., Maxted, P., Mayor, M., Moutou, C., Parley, N., Pollacco, D., Pont, F., Queloz, D., Ryans, R., Skillen, I., Street, R. A., Udry, S., & Wheatley, P. J. (2007). Efficient identification of exoplanetary transit candidates from SuperWASP light curves. *MNRAS*, **380**, 1230–1244.

Covey, K. R., Ivezić, Ž., Schlegel, D., Finkbeiner, D., Padmanabhan, N., Lupton, R. H., Agüeros, M. A., Bochanski, J. J., Hawley, S. L., West, A. A., Seth, A., Kimball, A., Gogarten, S. M., Claire, M., Haggard, D., Kaib, N., Schneider, D. P., & Sesar, B. (2007). Stellar SEDs from 0.3 to 2.5 μm: Tracing the Stellar Locus and Searching for Color Outliers in the SDSS and 2MASS. *AJ*, **134**, 2398–2417.

Cox, A. N. (2000). *Allen's astrophysical quantities*.

Cumming, A., Marcy, G. W., & Butler, R. P. (1999). The Lick Planet Search: Detectability and Mass Thresholds. *ApJ*, **526**, 890–915.

Day-Jones, A. C., Pinfield, D. J., Ruiz, M. T., Beaumont, H., Burningham, B., Gallardo, J., Gianninas, A., Bergeron, P., Napiwotzki, R., Jenkins, J. S., Zhang, Z. H., Murray, D. N., Catalán, S., & Gomes, J. (2011). Discovery of a T dwarf + white dwarf binary system. *MNRAS*, **410**, 705–716.

de Kool, M. (1992). Statistics of cataclysmic variable formation. *A&A*, **261**, 188–202.

de Mooij, E. & Snellen, I. (2011). Ground-based Detection of the Secondary Eclipse of TrES-3b. In J. P. Beaulieu, S. Dieters, and G. Tinetti, editors, *Astronomical Society of the Pacific Conference Series*, volume 450 of *Astronomical Society of the Pacific Conference Series*, page 59.

de Mooij, E. J. W. & Snellen, I. A. G. (2009). Ground-based K-band detection of thermal emission from the exoplanet TrES-3b. *A&A*, **493**, L35–L38.

de Mooij, E. J. W., Brogi, M., de Kok, R. J., Koppenhoefer, J., Nefs, S. V., Snellen, I. A. G., Greiner, J., Hanse, J., Heinsbroek, R. C., Lee, C. H., & van der Werf, P. P. (2012). Optical to near-infrared transit observations of super-Earth GJ 1214b: water-world or mini-Neptune? *A&A*, **538**, A46.

Demory, B.-O. & Seager, S. (2011). Lack of Inflated Radii for Kepler Giant Planet Candidates Receiving Modest Stellar Irradiation. *ApJS*, **197**, 12.

Dobbie, P. D., Burleigh, M. R., Levan, A. J., Barstow, M. A., Napiwotzki, R., Holberg, J. B., Hubeny, I., & Howell, S. B. (2005). A near-infrared spectroscopic search for very-low-mass cool companions to notable DA white dwarfs. *MNRAS*, **357**, 1049–1058.

D'Odorico, S., Dekker, H., Mazzoleni, R., Vernet, J., Guinouard, I., Groot, P., Hammer, F., Rasmussen, P. K., Kaper, L., Navarro, R., Pallavicini, R., Peroux, C., & Zerbi, F. M. (2006). X-shooter UV- to K-band intermediate-resolution high-efficiency spectrograph for the VLT: status report at the final design review. In *Society of Photo-Optical Instrumentation Engineers (SPIE) Conference Series*, volume 6269 of *Society of Photo-Optical Instrumentation Engineers (SPIE) Conference Series*.

Eisenstein, D. J., Liebert, J., Harris, H. C., Kleinman, S. J., Nitta, A., Silvestri, N., Anderson, S. A., Barentine, J. C., Brewington, H. J., Brinkmann, J., Harvanek, M., Krzesiński, J., Neilsen, Jr., E. H., Long, D., Schneider, D. P., & Snedden, S. A. (2006). A Catalog of Spectroscopically Confirmed White Dwarfs from the Sloan Digital Sky Survey Data Release 4. *ApJS*, **167**, 40–58.

Enoch, B., Collier Cameron, A., & Horne, K. (2012). Factors affecting the radii of close-in transiting exoplanets. *A&A*, **540**, A99.

Faedi, F., West, R. G., Burleigh, M. R., Goad, M. R., & Hebb, L. (2011). Detection limits for close eclipsing and transiting substellar and planetary companions to white dwarfs in the WASP survey. *MNRAS*, **410**, 899–911.

Farihi, J. & Christopher, M. (2004). A Possible Brown Dwarf Companion to the White Dwarf GD 1400. *AJ*, **128**, 1868–1871.

Farihi, J., Hoard, D. W., & Wachter, S. (2006). White Dwarf-Red Dwarf Systems Resolved with the Hubble Space Telescope. I. First Results. *ApJ*, **646**, 480–492.

Fischer, D. A., Marcy, G. W., Butler, R. P., Vogt, S. S., & Apps, K. (1999). Planetary Companions around Two Solar-Type Stars: HD 195019 and HD 217107. *PASP*, **111**, 50–56.

Ford, E. B. & Rasio, F. A. (2006). On the relation between hot-Jupiters and the Roche limit. In L. Arnold, F. Bouchy, and C. Moutou, editors, *Tenth Anniversary of 51 Peg-b: Status of and prospects for hot Jupiter studies*, pages 303–310.

Ford, E. B. & Rasio, F. A. (2008). Origins of Eccentric Extrasolar Planets: Testing the Planet-Planet Scattering Model. *ApJ*, **686**, 621–636.

Ford, E. B., Havlickova, M., & Rasio, F. A. (2001). Dynamical Instabilities in Extrasolar Planetary Systems Containing Two Giant Planets. *ICARUS*, **150**, 303–313.

Ford, E. B., Rasio, F. A., & Yu, K. (2003). Dynamical Instabilities in Extrasolar Planetary Systems. In D. Deming and S. Seager, editors, *Scientific Frontiers in Research on Extrasolar Planets*, volume 294 of *Astronomical Society of the Pacific Conference Series*, pages 181–188.

Fortier, A., Benvenuto, O. G., & Brunini, A. (2007). Oligarchic planetesimal accretion and giant planet formation. *A&A*, **473**, 311–322.

Fortney, J. J., Marley, M. S., & Barnes, J. W. (2007). Planetary Radii across Five Orders of Magnitude in Mass and Stellar Insolation: Application to Transits. *ApJ*, **659**, 1661–1672.

Fortney, J. J., Lodders, K., Marley, M. S., & Freedman, R. S. (2008). A Unified Theory for the Atmospheres of the Hot and Very Hot Jupiters: Two Classes of Irradiated Atmospheres. *ApJ*, **678**, 1419–1435.

Fortney, J. J., Ikoma, M., Nettelmann, N., Guillot, T., & Marley, M. S. (2011). Self-consistent Model Atmospheres and the Cooling of the Solar System's Giant Planets. *ApJ*, **729**, 32.

Fossati, L., Ryabchikova, T., Bagnulo, S., Alecian, E., Grunhut, J., Kochukhov, O., & Wade, G. (2009). The chemical abundance analysis of normal early A- and late B-type stars. *A&A*, **503**, 945–962.

Fossati, L., Ryabchikova, T., Shulyak, D. V., Haswell, C. A., Elmasli, A., Pandey, C. P., Barnes, T. G., & Zwintz, K. (2011). The accuracy of stellar atmospheric parameter determinations: a case study with HD 32115 and HD 37594. *MNRAS*, **417**, 495–507.

Fressin, F., Torres, G., Rowe, J. F., Charbonneau, D., Rogers, L. A., Ballard, S., Batalha, N. M., Borucki, W. J., Bryson, S. T., Buchhave, L. A., Ciardi, D. R., Désert, J.-M., Dressing, C. D., Fabrycky, D. C., Ford, E. B., Gautier, III, T. N., Henze, C. E., Holman, M. J., Howard, A., Howell, S. B., Jenkins, J. M., Koch, D. G., Latham, D. W., Lissauer,

J. J., Marcy, G. W., Quinn, S. N., Ragozzine, D., Sasselov, D. D., Seager, S., Barclay, T., Mullally, F., Seader, S. E., Still, M., Twicken, J. D., Thompson, S. E., & Uddin, K. (2012). Two Earth-sized planets orbiting Kepler-20. *Nature*, **482**, 195–198.

Fuhrmann, K., Axer, M., & Gehren, T. (1993). Balmer lines in cool dwarf stars. 1. Basic influence of atmospheric models. *A&A*, **271**, 451.

Gänsicke, B. T., Dillon, M., Southworth, J., Thorstensen, J. R., Rodríguez-Gil, P., Aungwerojwit, A., Marsh, T. R., Szkody, P., Barros, S. C. C., Casares, J., de Martino, D., Groot, P. J., Hakala, P., Kolb, U., Littlefair, S. P., Martínez-Pais, I. G., Nelemans, G., & Schreiber, M. R. (2009). SDSS unveils a population of intrinsically faint cataclysmic variables at the minimum orbital period. *MNRAS*, **397**, 2170–2188.

Girardi, L., Bressan, A., Bertelli, G., & Chiosi, C. (2000). Low-mass stars evolutionary tracks & isochrones (Girardi+, 2000). *VizieR Online Data Catalog*, **414**, 10371.

Girven, J., Gänsicke, B. T., Steeghs, D., & Koester, D. (2011). DA white dwarfs in Sloan Digital Sky Survey Data Release 7 and a search for infrared excess emission. *MNRAS*, **417**, 1210–1235.

Goldreich, P. & Tremaine, S. (1980). Disk-satellite interactions. *ApJ*, **241**, 425–441.

Gomes, R., Levison, H. F., Tsiganis, K., & Morbidelli, A. (2005). Origin of the cataclysmic Late Heavy Bombardment period of the terrestrial planets. *Nature*, **435**, 466–469.

Gould, A. & Loeb, A. (1992). Discovering planetary systems through gravitational microlenses. *ApJ*, **396**, 104–114.

Goulding, N. T., Pinfield, D., & et al. (2012). J band Variability of M Dwarfs in the WFCAM Transit Survey.

Greisen, E. W. & Calabretta, M. R. (2002). Representations of world coordinates in FITS. *A&A*, **395**, 1061–1075.

Grether, D. & Lineweaver, C. H. (2006). How Dry is the Brown Dwarf Desert? Quantifying the Relative Number of Planets, Brown Dwarfs, and Stellar Companions around Nearby Sun-like Stars. *ApJ*, **640**, 1051–1062.

Grupp, F. (2004). MAFAGS-OS: New opacity sampling model atmospheres for A, F and G stars. I. The model and the solar flux. *A&A*, **420**, 289–305.

Guillot, T. (2005). THE INTERIORS OF GIANT PLANETS: Models and Outstanding Questions. *Annual Review of Earth and Planetary Sciences*, **33**, 493–530.

Hahn, J. M. & Malhotra, R. (1999). Orbital Evolution of Planets Embedded in a Planetesimal Disk. *AJ*, **117**, 3041–3053.

Haisch, Jr., K. E., Lada, E. A., & Lada, C. J. (2001). Disk Frequencies and Lifetimes in Young Clusters. *ApJ*, **553**, L153–L156.

Hartman, J. D., Gaudi, B. S., Holman, M. J., McLeod, B. A., Stanek, K. Z., Barranco, J. A., Pinsonneault, M. H., Meibom, S., & Kalirai, J. S. (2009). Deep MMT Transit Survey of the Open Cluster M37 IV: Limit on the Fraction of Stars with Planets as Small as $0.3R_J$. *ApJ*, **695**, 336–356.

Heng, K. (2012). The Influence of Atmospheric Scattering and Absorption on Ohmic Dissipation in Hot Jupiters. *ApJ*, **748**, L17.

Hill, G. J., MacQueen, P. J., Ramsey, L. W., & Shetrone, M. D. (2010). Performance of the Hobby-Eberly telescope and facility instruments. *spie*, **5492**, 10.

Hodgkin, S. T., Irwin, M. J., Hewett, P. C., & Warren, S. J. (2009). The UKIRT wide field camera ZYJHK photometric system: calibration from 2MASS. *MNRAS*, **394**, 675–692.

Holberg, J. B. & Bergeron, P. (2006). Calibration of Synthetic Photometry Using DA White Dwarfs. *AJ*, **132**, 1221–1233.

Howard, A. W., Marcy, G. W., Bryson, S. T., & et al. (2011). Planet occurrence within 0.25 AU of solar-type stars from KEPLER. *ApJ*.

Huang, X. & Cumming, A. (2012). Ohmic Dissipation in the Interiors of Hot Jupiters. *ApJ*, **757**, 47.

Hubickyj, O., Bodenheimer, P., & Lissauer, J. J. (2005). Core Accretion - Gas Capture Model for Gas Giant Planet Formation. *AGU Fall Meeting Abstracts*, page A7.

Iben, Jr., I. & Tutukov, A. V. (1986). On the formation and evolution of a helium degenerate dwarf in a close binary. *ApJ*, **311**, 742–752.

Inaba, S., Wetherill, G. W., & Ikoma, M. (2003). Formation of gas giant planets: core accretion models with fragmentation and planetary envelope. *ICARUS*, **166**, 46–62.

Irwin, J., Irwin, M., Aigrain, S., Hodgkin, S., Hebb, L., & Moraux, E. (2007). The Monitor project: data processing and light curve production. *MNRAS*, **375**, 1449–1462.

Irwin, M. & Lewis, J. (2001a). INT WFS pipeline processing. *New Astron. Rev.*, **45**, 105–110.

Irwin, M. & Lewis, J. (2001b). INT WFS pipeline processing. *New Astron. Rev.*, **45**, 105–110.

Irwin, M. J. (1985). Automatic analysis of crowded fields. *MNRAS*, **214**, 575–604.

Irwin, M. J. (1997). *Detectors and data analysis techniques for wide field optical imaging.*, pages 35–74.

Ivanov, P. B. & Papaloizou, J. C. B. (2007). Dynamic tides in rotating objects: orbital circularization of extrasolar planets for realistic planet models. *MNRAS*, **376**, 682–704.

Jackson, B., Greenberg, R., & Barnes, R. (2008). Tidal Evolution of Close-in Extrasolar Planets. *ApJ*, **678**, 1396–1406.

Janson, M., Bonavita, M., Klahr, H., Lafrenière, D., Jayawardhana, R., & Zinnecker, H. (2011). High-contrast Imaging Search for Planets and Brown Dwarfs around the Most Massive Stars in the Solar Neighborhood. *ApJ*, **736**, 89.

Jester, S., Schneider, D. P., Richards, G. T., Green, R. F., Schmidt, M., Hall, P. B., Strauss, M. A., Vanden Berk, D. E., Stoughton, C., Gunn, J. E., Brinkmann, J., Kent, S. M., Smith, J. A., Tucker, D. L., & Yanny, B. (2005). The Sloan Digital Sky Survey View of the Palomar-Green Bright Quasar Survey. *AJ*, **130**, 873–895.

Ji, J., Kinoshita, H., Liu, L., & Li, G. (2003). Could the 55 Cancri Planetary System Really Be in the 3:1 Mean Motion Resonance? *ApJ*, **585**, L139–L142.

Jiang, I.-G. & Ip, W.-H. (2001). The planetary system of upsilon Andromedae. *A&A*, **367**, 943–948.

Jiang, I.-G. & Yeh, L.-C. (2004a). Dynamical Effects from Asteroid Belts for Planetary Systems. *International Journal of Bifurcation and Chaos*, **14**, 3153–3166.

Jiang, I.-G. & Yeh, L.-C. (2004b). The drag-induced resonant capture for Kuiper Belt objects. *MNRAS*, **355**, L29–L32.

Jiang, I.-G. & Yeh, L.-C. (2007). A Possible Correlation between the Gaseous Drag Strength and Resonant Planetesimals in Planetary Systems. *ApJ*, **656**, 534–544.

Jiang, I.-G., Yeh, L.-C., Chang, Y.-C., & Hung, W.-L. (2009). Construction of Coupled Period-Mass Functions in Extrasolar Planets Through a Nonparametric Approach. *AJ*, **137**, 329–336.

Jiang, I.-G., Yeh, L.-C., Chang, Y.-C., & Hung, W.-L. (2010). On the Fundamental Mass-Period Functions of Extrasolar Planets. *ApJS*, **186**, 48–62.

Johnson, D. R. H. & Soderblom, D. R. (1987). Calculating galactic space velocities and their uncertainties, with an application to the Ursa Major group. *AJ*, **93**, 864–867.

Kingdon, J. & Ferland, G. J. (1991). The effect of telluric absorption on the intensity of He I 10830. *PASP*, **103**, 752–758.

Kinoshita, H. & Nakai, H. (2001). Stability of the GJ 876 Planetary System. *PASJ*, **53**, L25–L26.

Kirsh, D. R., Duncan, M., Brasser, R., & Levison, H. F. (2009). Simulations of planet migration driven by planetesimal scattering. *ICARUS*, **199**, 197–209.

Knutson, H. A., Charbonneau, D., Allen, L. E., Fortney, J. J., Agol, E., Cowan, N. B., Showman, A. P., Cooper, C. S., & Megeath, S. T. (2007). A map of the day-night contrast of the extrasolar planet HD 189733b. *Nature*, **447**, 183–186.

Kochukhov, O. P. (2007). Spectrum synthesis for magnetic, chemically stratified stellar atmospheres. In I. I. Romanyuk, D. O. Kudryavtsev, O. M. Neizvestnaya, and V. M. Shapoval, editors, *Physics of Magnetic Stars*, pages 109–118.

Koester, D. (2008). White Dwarf Spectra and Atmosphere Models. *ArXiv e-prints*.

Kokubo, E. & Ida, S. (2002). Formation of Protoplanet Systems and Diversity of Planetary Systems. *ApJ*, **581**, 666–680.

Kovacs, B., Hodgkin, S., Sipocz, B., Pinfield, D., Barrado, D., Birkby, J., Cappetta, M., Cruz, P., Koppenhofer, J., Martin, E., Murgas, F., Nefs, B., Saglia, R. P., & Zendejas, J. (2012). A sensitivity analysis of the WFCAM Transit Survey for short-period giant planets around M dwarfs.

Kowalski, P. M. & Saumon, D. (2006). Found: The Missing Blue Opacity in Atmosphere Models of Cool Hydrogen White Dwarfs. *ApJ*, **651**, L137–L140.

Kupka, F., Piskunov, N., Ryabchikova, T. A., Stempels, H. C., & Weiss, W. W. (1999). VALD-2: Progress of the Vienna Atomic Line Data Base. *A&AS*, **138**, 119–133.

Kurucz, R. L. (1993). A New Opacity-Sampling Model Atmosphere Program for Arbitrary Abundances. In M. M. Dworetsky, F. Castelli, and R. Faraggiana, editors, *IAU Colloq. 138: Peculiar versus Normal Phenomena in A-type and Related Stars*, volume 44 of *Astronomical Society of the Pacific Conference Series*, page 87.

Lallement, R., Bertin, P., Chassefiere, E., & Scott, N. (1993). Correction of spectra for telluric absorption lines with the help of a molecular data bank and high resolution forward modelling: H,O lines around the sodium doublet at 589.5 NM. *A&A*, **271**, 734.

Laughlin, G., Crismani, M., & Adams, F. C. (2011). On the Anomalous Radii of the Transiting Extrasolar Planets. *ApJ*, **729**, L7.

Leconte, J. & Chabrier, G. (2012). A new vision of giant planet interiors: Impact of double diffusive convection. *A&A*, **540**, A20.

Leggett, S. K. (1992). Infrared colors of low-mass stars. *ApJS*, **82**, 351–394.

Levison, H. F. & Agnor, C. (2003). The Role of Giant Planets in Terrestrial Planet Formation. *AJ*, **125**, 2692–2713.

Lin, D. N. C. & Ida, S. (1997). On the Origin of Massive Eccentric Planets. *ApJ*, **477**, 781.

Lin, D. N. C. & Papaloizou, J. (1986). On the tidal interaction between protoplanets and the protoplanetary disk. III - Orbital migration of protoplanets. *ApJ*, **309**, 846–857.

Lindegren, L., Lammers, U., Hobbs, D., O'Mullane, W., Bastian, U., & Hernández, J. (2012). The astrometric core solution for the Gaia mission. Overview of models, algorithms, and software implementation. *A&A*, **538**, A78.

Littlefair, S. P., Dhillon, V. S., Marsh, T. R., Gänsicke, B. T., Baraffe, I., & Watson, C. A. (2007). SDSS J150722.30+523039.8: a cataclysmic variable formed directly from a detached white dwarf/brown dwarf binary? *MNRAS*, **381**, 827–834.

Lodders, K. (2002). Titanium and Vanadium Chemistry in Low-Mass Dwarf Stars. *ApJ*, **577**, 974–985.

López-Morales, M. & Seager, S. (2007). Thermal Emission from Transiting Very Hot Jupiters: Prospects for Ground-based Detection at Optical Wavelengths. *ApJ*, **667**, L191–L194.

Lundstrom, I., Ardeberg, A., Maurice, E., & Lindgren, H. (1991). A synthetic telluric spectrum in the wavelength region surrounding the D1 and D2 lines of sodium. *A&AS*, **91**, 199–208.

Maciejewski, G., Dimitrov, D., Neuhäuser, R., Niedzielski, A., Raetz, S., Ginski, C., Adam, C., Marka, C., Moualla, M., & Mugrauer, M. (2010). Transit timing variation in exoplanet WASP-3b. *MNRAS*, **407**, 2625–2631.

Malhotra, R. (1995). The Origin of Pluto's Orbit: Implications for the Solar System Beyond Neptune. *AJ*, **110**, 420.

Mandel, K. & Agol, E. (2002). Analytic Light Curves for Planetary Transit Searches. *ApJ*, **580**, L171–L175.

Mandushev, G., Torres, G., Latham, D. W., Charbonneau, D., Alonso, R., White, R. J., Stefanik, R. P., Dunham, E. W., Brown, T. M., & O'Donovan, F. T. (2005). The Challenge of Wide-Field Transit Surveys: The Case of GSC 01944-02289. *ApJ*, **621**, 1061–1071.

Mann, A. W., Gaidos, E., Lépine, S., & Hilton, E. J. (2012). They Might be Giants: Luminosity Class, Planet Occurrence, and Planet-Metallicity Relation of the Coolest Kepler Target Stars. *ApJ*, **753**, 90.

Marcy, G., Butler, R. P., Fischer, D., Vogt, S., Wright, J. T., Tinney, C. G., & Jones, H. R. A. (2005). Observed Properties of Exoplanets: Masses, Orbits, and Metallicities. *Progress of Theoretical Physics Supplement*, **158**, 24–42.

Marois, C., Macintosh, B., Barman, T., Zuckerman, B., Song, I., Patience, J., Lafrenière, D., & Doyon, R. (2008). Direct Imaging of Multiple Planets Orbiting the Star HR 8799. *Science*, **322**, 1348–.

Marsh, K. A., Kirkpatrick, J. D., & Plavchan, P. (2010). A Young Planetary-Mass Object in the ρ Oph Cloud Core. *ApJ*, **709**, L158–L162.

Marsh, T. R., Dhillon, V. S., & Duck, S. R. (1995). Low-Mass White Dwarfs Need Friends - Five New Double-Degenerate Close Binary Stars. *MNRAS*, **275**, 828.

Martin, E. L. (1997). Quantitative spectroscopic criteria for the classification of pre-main sequence low-mass stars. *A&A*, **321**, 492–496.

Martin, E. L., Spruit, H. C., & Tata, R. (2011). A binary merger origin for inflated hot Jupiter planets. *A&A*, **535**, A50.

Marzari, F. & Weidenschilling, S. J. (2002). Eccentric Extrasolar Planets: The Jumping Jupiter Model. *ICARUS*, **156**, 570–579.

Mashonkina, L. (2011). Non-LTE Line Formation for Fe I and Fe II in the Atmospheres of A-F Type Stars. In *Magnetic Stars*, pages 314–321.

Maxted, P. F. L., Napiwotzki, R., Dobbie, P. D., & Burleigh, M. R. (2006). Survival of a brown dwarf after engulfment by a red giant star. *Nature*, **442**, 543–545.

Mayor, M. & Queloz, D. (1995). A Jupiter-mass companion to a solar-type star. *Nature*, **378**, 355–359.

Mayor, M. & Udry, S. (2008). The quest for very low-mass planets. *Physica Scripta Volume T*, **130**(1), 014010.

Mayor, M., Pepe, F., Queloz, D., Bouchy, F., Rupprecht, G., Lo Curto, G., Avila, G., Benz, W., Bertaux, J.-L., Bonfils, X., Dall, T., Dekker, H., Delabre, B., Eckert, W., Fleury, M., Gilliotte, A., Gojak, D., Guzman, J. C., Kohler, D., Lizon, J.-L., Longinotti, A., Lovis, C., Megevand, D., Pasquini, L., Reyes, J., Sivan, J.-P., Sosnowska, D., Soto, R., Udry, S., van Kesteren, A., Weber, L., & Weilenmann, U. (2003). Setting New Standards with HARPS. *The Messenger*, **114**, 20–24.

Mayor, M., Marmier, M., Lovis, C., Udry, S., Ségransan, D., Pepe, F., Benz, W., Bertaux, J. ., Bouchy, F., Dumusque, X., Lo Curto, G., Mordasini, C., Queloz, D., & Santos, N. C. (2011). The HARPS search for southern extra-solar planets XXXIV. Occurrence, mass distribution and orbital properties of super-Earths and Neptune-mass planets. *ArXiv e-prints*.

McArthur, B. E., Endl, M., Cochran, W. D., Benedict, G. F., Fischer, D. A., Marcy, G. W., Butler, R. P., Naef, D., Mayor, M., Queloz, D., Udry, S., & Harrison, T. E. (2004). Detection of a Neptune-Mass Planet in the ρ^1 Cancri System Using the Hobby-Eberly Telescope. *ApJ*, **614**, L81–L84.

McCarthy, C. & Zuckerman, B. (2004). The Brown Dwarf Desert at 75-1200 AU. *AJ*, **127**, 2871–2884.

Montmerle, T., Augereau, J.-C., Chaussidon, M., Gounelle, M., Marty, B., & Morbidelli, A. (2006). From Suns to Life: A Chronological Approach to the History of Life on Earth 3. Solar System Formation and Early Evolution: the First 100 Million Years. *Earth Moon and Planets*, **98**, 39–95.

Mordasini, C., Alibert, A., Benz, W., & Naef, D. (2007). Extrasolar Planet Population Synthesis - Predictions for RV and Transit Surveys. In *JENAM-2007, "Our Non-Stable Universe"*.

Moutou, C. & Pont, F. (2006). Detection and characterization of extrasolar planets: the transit method. *Ecole de Goutelas*, **28**, 55–79.

Moutou, C., Hébrard, G., Bouchy, F., Eggenberger, A., Boisse, I., Bonfils, X., Gravallon, D., Ehrenreich, D., Forveille, T., Delfosse, X., Desort, M., Lagrange, A.-M., Lovis, C., Mayor, M., Pepe, F., Perrier, C., Pont, F., Queloz, D., Santos, N. C., Ségransan, D., Udry, S., & Vidal-Madjar, A. (2009). Photometric and spectroscopic detection of the primary transit of the 111-day-period planet HD 80 606 b. *A&A*, **498**, L5–L8.

Munn, J. A., Monet, D. G., Levine, S. E., Canzian, B., Pier, J. R., Harris, H. C., Lupton, R. H., Ivezić, Ž., Hindsley, R. B., Hennessy, G. S., Schneider, D. P., & Brinkmann, J. (2004). An Improved Proper-Motion Catalog Combining USNO-B and the Sloan Digital Sky Survey. *AJ*, **127**, 3034–3042.

Munn, J. A., Monet, D. G., Levine, S. E., Canzian, B., Pier, J. R., Harris, H. C., Lupton, R. H., Ivezić, Ž., Hindsley, R. B., Hennessy, G. S., Schneider, D. P., & Brinkmann, J. (2008). Erratum: "an Improved Proper-Motion Catalog Combining Usno-B and the Sloan Digital Sky Survey" (2004, AJ, 127, 3034). *AJ*, **136**, 895.

Nash, T. (1996). The SLOAN digital sky survey. In J. Tran Thanh Van, editor, *The Sun and Beyond*, page 477.

Nordhaus, J., Spiegel, D. S., Ibgui, L., Goodman, J., & Burrows, A. (2010). Tides and tidal engulfment in post-main-sequence binaries: period gaps for planets and brown dwarfs around white dwarfs. *MNRAS*, **408**, 631–641.

Pál, A. (2008). Properties of analytic transit light-curve models. *MNRAS*, **390**, 281–288.

Papaloizou, J. C. B., Nelson, R. P., Kley, W., Masset, F. S., & Artymowicz, P. (2007). Disk-Planet Interactions During Planet Formation. *Protostars and Planets V*, pages 655–668.

Parsons, S. G., Marsh, T. R., Gänsicke, B. T., Dhillon, V. S., Copperwheat, C. M., Littlefair, S. P., Pyrzas, S., Drake, A. J., Koester, D., Schreiber, M. R., & Rebassa-Mansergas,

A. (2012). The shortest period detached white dwarf + main-sequence binary. *MNRAS*, **419**, 304–313.

Pasquini, L., Brucalassi, A., Ruiz, M. T., Bonifacio, P., Lovis, C., Saglia, R., Melo, C., Biazzo, K., Randich, S., & Bedin, L. R. (2012). Search for giant planets in M 67. I. Overview. *A&A*, **545**, A139.

Pauli, E.-M., Napiwotzki, R., Heber, U., Altmann, M., & Odenkirchen, M. (2006). 3D kinematics of white dwarfs from the SPY project. II. *A&A*, **447**, 173–184.

Pepe, F., Lovis, C., Ségransan, D., Benz, W., Bouchy, F., Dumusque, X., Mayor, M., Queloz, D., Santos, N. C., & Udry, S. (2011). The HARPS search for Earth-like planets in the habitable zone. I. Very low-mass planets around ¡ASTROBJ¿HD 20794¡/ASTROBJ¿, ¡ASTROBJ¿HD 85512¡/ASTROBJ¿, and ¡ASTROBJ¿HD 192310¡/ASTROBJ¿. *A&A*, **534**, A58.

Pepe, F. A., Cristiani, S., Rebolo Lopez, R., Santos, N. C., Amorim, A., Avila, G., Benz, W., Bonifacio, P., Cabral, A., Carvas, P., Cirami, R., Coelho, J., Comari, M., Coretti, I., de Caprio, V., Dekker, H., Delabre, B., di Marcantonio, P., D'Odorico, V., Fleury, M., García, R., Herreros Linares, J. M., Hughes, I., Iwert, O., Lima, J., Lizon, J.-L., Lo Curto, G., Lovis, C., Manescau, A., Martins, C., Mégevand, D., Moitinho, A., Molaro, P., Monteiro, M., Monteiro, M., Pasquini, L., Mordasini, C., Queloz, D., Rasilla, J. L., Rebordão, J. M., Santana Tschudi, S., Santin, P., Sosnowska, D., Spanò, P., Tenegi, F., Udry, S., Vanzella, E., Viel, M., Zapatero Osorio, M. R., & Zerbi, F. (2010). ESPRESSO: the Echelle spectrograph for rocky exoplanets and stable spectroscopic observations. In *Society of Photo-Optical Instrumentation Engineers (SPIE) Conference Series*, volume 7735 of *Society of Photo-Optical Instrumentation Engineers (SPIE) Conference Series*.

Perna, R., Menou, K., & Rauscher, E. (2010). Ohmic Dissipation in the Atmospheres of Hot Jupiters. *ApJ*, **724**, 313–317.

Petit, J.-M., Morbidelli, A., & Chambers, J. (2001). The Primordial Excitation and Clearing of the Asteroid Belt. *ICARUS*, **153**, 338–347.

Piskunov, N. E., Kupka, F., Ryabchikova, T. A., Weiss, W. W., & Jeffery, C. S. (1995). VALD: The Vienna Atomic Line Data Base. *A&AS*, **112**, 525.

Politano, M. (1996). Theoretical Statistics of Zero-Age Cataclysmic Variables. *ApJ*, **465**, 338.

Politano, M. (2004). The Formation of Cataclysmic Variables with Brown Dwarf Secondaries. *ApJ*, **604**, 817–826.

Pont, F., Zucker, S., & Queloz, D. (2006). The effect of red noise on planetary transit detection. *MNRAS*, **373**, 231–242.

Queloz, D., Henry, G. W., Sivan, J. P., Baliunas, S. L., Beuzit, J. L., Donahue, R. A., Mayor, M., Naef, D., Perrier, C., & Udry, S. (2001). No planet for HD 166435. *A&A*, **379**, 279–287.

Rasio, F. A. & Ford, E. B. (1996). Dynamical instabilities and the formation of extrasolar planetary systems. *Science*, **274**, 954–956.

Raymond, S. N., Quinn, T., & Lunine, J. I. (2006). High-resolution simulations of the final assembly of Earth-like planets I. Terrestrial accretion and dynamics. *ICARUS*, **183**, 265–282.

Raymond, S. N., Quinn, T., & Lunine, J. I. (2007). High-Resolution Simulations of The Final Assembly of Earth-Like Planets. 2. Water Delivery And Planetary Habitability. *Astrobiology*, **7**, 66–84.

Raymond, S. N., Armitage, P. J., Moro-Martín, A., Booth, M., Wyatt, M. C., Armstrong, J. C., Mandell, A. M., Selsis, F., & West, A. A. (2011). Debris disks as signposts of terrestrial planet formation. *A&A*, **530**, A62.

Rebassa-Mansergas, A., Nebot Gómez-Morán, A., Schreiber, M. R., Girven, J., & Gänsicke, B. T. (2011). Post-common envelope binaries from SDSS-X: the origin of low-mass white dwarfs. *MNRAS*, **413**, 1121–1131.

Rice, W. K. M., Armitage, P. J., & Hogg, D. F. (2008). Why are there so few hot Jupiters? *MNRAS*, **384**, 1242–1248.

Rodigas, T. J. & Hinz, P. M. (2009). Which Radial Velocity Exoplanets Have Undetected Outer Companions? *ApJ*, **702**, 716–723.

Rodler, F., Lopez-Morales, M., & Ribas, I. (2012). Weighing the Non-transiting Hot Jupiter τ Boo b. *ApJ*, **753**, L25.

Rodríguez, A., Ferraz-Mello, S., Michtchenko, T. A., Beaugé, C., & Miloni, O. (2011). Tidal decay and orbital circularization in close-in two-planet systems. *MNRAS*, **415**, 2349–2358.

Ryabchikova, T., Piskunov, N., Savanov, I., Kupka, F., & Malanushenko, V. (1999). Eu III identification and Eu abundance in CP stars. *A&A*, **343**, 229–236.

Ryabchikova, T., Fossati, L., & Shulyak, D. (2009). Improved fundamental parameters and LTE abundances of the CoRoT solar-type pulsator HD 49933. *A&A*, **506**, 203–211.

Santos, N. C., Bouchy, F., Mayor, M., Pepe, F., Queloz, D., Udry, S., Lovis, C., Bazot, M., Benz, W., Bertaux, J.-L., Lo Curto, G., Delfosse, X., Mordasini, C., Naef, D., Sivan, J.-P., & Vauclair, S. (2004). The HARPS survey for southern extra-solar planets. II. A 14 Earth-masses exoplanet around μ Arae. *A&A*, **426**, L19–L23.

Savoury, C. D. J., Littlefair, S. P., Dhillon, V. S., Marsh, T. R., Gänsicke, B. T., Copperwheat, C. M., Kerry, P., Hickman, R. D. G., & Parsons, S. G. (2011). Cataclysmic variables below the period gap: mass determinations of 14 eclipsing systems. *MNRAS*, **415**, 2025–2041.

Schlegel, D. J., Finkbeiner, D. P., & Davis, M. (1998). Maps of Dust Infrared Emission for Use in Estimation of Reddening and Cosmic Microwave Background Radiation Foregrounds. *ApJ*, **500**, 525.

Schneider, J., Dedieu, C., Le Sidaner, P., Savalle, R., & Zolotukhin, I. (2011). Defining and cataloging exoplanets: the exoplanet.eu database. *A&A*, **532**, A79.

Schreiber, M. R. & Gänsicke, B. T. (2003). The age, life expectancy, and space density of Post Common Envelope Binaries. *A&A*, **406**, 305–321.

Seager, S. & Mallén-Ornelas, G. (2003). A Unique Solution of Planet and Star Parameters from an Extrasolar Planet Transit Light Curve. *ApJ*, **585**, 1038–1055.

Seager, S., Kuchner, M., Hier-Majumder, C. A., & Militzer, B. (2007). Mass-Radius Relationships for Solid Exoplanets. *ApJ*, **669**, 1279–1297.

Sekiguchi, M. & Fukugita, M. (2000). A Study of the B-V Color-Temperature Relation. *AJ*, **120**, 1072–1084.

Sestito, P. & Randich, S. (2005). Time scales of Li evolution: a homogeneous analysis of open clusters from ZAMS to late-MS. *A&A*, **442**, 615–627.

Shaver, P. (2006). Report on the XXXVIth IAU General Assembly (held in Prague, Czech Republic, 14-25 August 2006). *The Messenger*, **125**, 51.

Showman, A. P. & Guillot, T. (2002). Atmospheric circulation and tides of "51 Pegasus b-like" planets. *A&A*, **385**, 166–180.

Showman, A. P., Fortney, J. J., Lian, Y., Marley, M. S., Freedman, R. S., Knutson, H. A., & Charbonneau, D. (2009). Atmospheric Circulation of Hot Jupiters: Coupled Radiative-Dynamical General Circulation Model Simulations of HD 189733b and HD 209458b. *ApJ*, **699**, 564–584.

Shulyak, D., Tsymbal, V., Ryabchikova, T., Stütz, C., & Weiss, W. W. (2004). Line-by-line opacity stellar model atmospheres. *A&A*, **428**, 993–1000.

Sipocz, B., Pinfield, D., & et al. (2012).

Skrutskie, M. F., Cutri, R. M., Stiening, R., Weinberg, M. D., Schneider, S., Carpenter, J. M., Beichman, C., Capps, R., Chester, T., Elias, J., Huchra, J., Liebert, J., Lonsdale, C., Monet, D. G., Price, S., Seitzer, P., Jarrett, T., Kirkpatrick, J. D., Gizis, J. E., Howard, E., Evans, T., Fowler, J., Fullmer, L., Hurt, R., Light, R., Kopan, E. L.,

Marsh, K. A., McCallon, H. L., Tam, R., Van Dyk, S., & Wheelock, S. (2006). The Two Micron All Sky Survey (2MASS). *AJ*, **131**, 1163–1183.

Snellen, I. (2007). Transit and Secondary Eclipse Photometry in the Near-Infrared. In C. Afonso, D. Weldrake, and T. Henning, editors, *Transiting Extrapolar Planets Workshop*, volume 366 of *Astronomical Society of the Pacific Conference Series*, page 236.

Snellen, I. A. G., Koppenhoefer, J., van der Burg, R. F. J., Dreizler, S., Greiner, J., de Hoon, M. D. J., Husser, T. O., Krühler, T., Saglia, R. P., & Vuijsje, F. N. (2009). OGLE2-TR-L9b: an exoplanet transiting a rapidly rotating F3 star. *A&A*, **497**, 545–550.

Sotin, C., Grasset, O., & Mocquet, A. (2007). Mass radius curve for extrasolar Earth-like planets and ocean planets. *ICARUS*, **191**, 337–351.

Sozzetti, A. (2012). Astrometry and Exoplanet Characterization: Gaia and Its Pandora's Box. In F. Arenou and D. Hestroffer, editors, *Proceedings of the workshop "Orbital Couples: Pas de Deux in the Solar System and the Milky Way". Held at the Observatoire de Paris, 10-12 October 2011. Editors: F. Arenou, D. Hestroffer. ISBN 2-910015-64-5, p. 25-31*, pages 25–31.

Spiegel, D. S., Burrows, A., & Milsom, J. A. (2010). Planet or Brown Dwarf? Bringing the Deuterium-Burning Criterion into Focus. In *AAS/Division for Planetary Sciences Meeting Abstracts #42*, volume 42 of *AAS/Division for Planetary Sciences Meeting Abstracts*, page 27.

Steele, P. R., Burleigh, M. R., Farihi, J., Gänsicke, B. T., Jameson, R. F., Dobbie, P. D., & Barstow, M. A. (2009). PHL 5038: a spatially resolved white dwarf + brown dwarf binary. *A&A*, **500**, 1207–1210.

Steele, P. R., Burleigh, M. R., Dobbie, P. D., Jameson, R. F., Barstow, M. A., & Satterthwaite, R. P. (2011). White dwarfs in the UKIRT Infrared Deep Sky Survey Large Area Survey: the substellar companion fraction. *MNRAS*, **416**, 2768–2791.

Steele, P. R., Saglia, R. P., Burleigh, M. R., Marsch, T. R., Gänsicke, B. T., Lawrie, K., Cappetta, M., Girven, J., & Napiwotzki, R. (2012). NLTT5306: The shortest Period Detached White Dwarf + Brown Dwarf Binary. *MNRAS*.

Stepien, K. (1988). Spin-down of cool stars during their main-sequence life. *ApJ*, **335**, 907–913.

Swain, M. R., Vasisht, G., Tinetti, G., Bouwman, J., Chen, P., Yung, Y., Deming, D., & Deroo, P. (2009). Molecular Signatures in the Near-Infrared Dayside Spectrum of HD 189733b. *ApJ*, **690**, L114–L117.

Tanaka, H., Takeuchi, T., & Ward, W. R. (2002). Three-Dimensional Interaction between a Planet and an Isothermal Gaseous Disk. I. Corotation and Lindblad Torques and Planet Migration. *ApJ*, **565**, 1257–1274.

Tappert, C., Gänsicke, B. T., Schmidtobreick, L., Mennickent, R. E., & Navarrete, F. P. (2007). K-band spectroscopy of pre-cataclysmic variables. *A&A*, **475**, 575–583.

Tappert, C., Gänsicke, B. T., Schmidtobreick, L., & Ribeiro, T. (2011). Accretion in the detached post-common-envelope binary LTT 560. *A&A*, **532**, A129.

Thommes, E. W., Duncan, M. J., & Levison, H. F. (1999). The formation of Uranus and Neptune in the Jupiter-Saturn region of the Solar System. *Nature*, **402**, 635–638.

Thommes, E. W., Duncan, M. J., & Levison, H. F. (2003). Oligarchic growth of giant planets. *ICARUS*, **161**, 431–455.

Tinetti, G., Beaulieu, J. P., Henning, T., Meyer, M., Micela, G., Ribas, I., Stam, D., Swain, M., Krause, O., Ollivier, M., Pace, E., Swinyard, B., Aylward, A., van Boekel, R., Coradini, A., Encrenaz, T., Snellen, I., Zapatero-Osorio, M. R., Bouwman, J., Cho, J. Y.-K., Coudé de Foresto, V., Guillot, T., Lopez-Morales, M., Mueller-Wodarg, I., Palle, E., Selsis, F., Sozzetti, A., Ade, P. A. R., Achilleos, N., Adriani, A., Agnor, C. B., Afonso, C., Prieto, C. A., Bakos, G., Barber, R. J., Barlow, M., Batista, V., Bernath, P., Bézard, B., Bordé, P., Brown, L. R., Cassan, A., Cavarroc, C., Ciaravella, A., Cockell, C., Coustenis, A., Danielski, C., Decin, L., Kok, R. D., Demangeon, O., Deroo, P., Doel, P., Drossart, P., Fletcher, L. N., Focardi, M., Forget, F., Fossey, S., Fouqué, P., Frith, J., Galand, M., Gaulme, P., Hernández, J. I. G., Grasset, O., Grassi, D., Grenfell, J. L., Griffin, M. J., Griffith, C. A., Grözinger, U., Guedel, M., Guio, P., Hainaut, O., Hargreaves, R., Hauschildt, P. H., Heng, K., Heyrovsky, D., Hueso, R., Irwin, P., Kaltenegger, L., Kervella, P., Kipping, D., Koskinen, T. T., Kovács, G., La Barbera, A., Lammer, H., Lellouch, E., Leto, G., Lopez Morales, M., Lopez Valverde, M. A., Lopez-Puertas, M., Lovis, C., Maggio, A., Maillard, J. P., Maldonado Prado, J., Marquette, J. B., Martin-Torres, F. J., Maxted, P., Miller, S., Molinari, S., Montes, D., Moro-Martin, A., Moses, J. I., Mousis, O., Nguyen Tuong, N., Nelson, R., Orton, G. S., Pantin, E., Pascale, E., Pezzuto, S., Pinfield, D., Poretti, E., Prinja, R., Prisinzano, L., Rees, J. M., Reiners, A., Samuel, B., Sánchez-Lavega, A., Forcada, J. S., Sasselov, D., Savini, G., Sicardy, B., Smith, A., Stixrude, L., Strazzulla, G., Tennyson, J., Tessenyi, M., Vasisht, G., Vinatier, S., Viti, S., Waldmann, I., White, G. J., Widemann, T., Wordsworth, R., Yelle, R., Yung, Y., & Yurchenko, S. N. (2012). EChO. Exoplanet characterisation observatory. *Experimental Astronomy*, **34**, 311–353.

Torres, G. & Lacy, C. H. S. (2009). Absolute Dimensions of the F-Type Eclipsing Binary Star VZ Cephei. *AJ*, **137**, 507–516.

Torres, G., Konacki, M., Sasselov, D. D., & Jha, S. (2005). Testing Blend Scenarios for Extrasolar Transiting Planet Candidates. II. OGLE-TR-56. *ApJ*, **619**, 558–569.

Tremblay, P.-E., Bergeron, P., & Gianninas, A. (2011). An Improved Spectroscopic Analysis of DA White Dwarfs from the Sloan Digital Sky Survey Data Release 4. *ApJ*, **730**, 128.

Tsiganis, K., Gomes, R., Morbidelli, A., & Levison, H. F. (2005). Origin of the orbital architecture of the giant planets of the Solar System. *Nature*, **435**, 459–461.

Tsymbal, V. (1996). STARSP: A Software System For the Analysis of the Spectra of Normal Stars. In S. J. Adelman, F. Kupka, and W. W. Weiss, editors, *M.A.S.S., Model Atmospheres and Spectrum Synthesis*, volume 108 of *Astronomical Society of the Pacific Conference Series*, page 198.

Tull, R. G., MacQueen, P. J., Good, J., Epps, H. W., & HET HRS Team (1998). High Resolution Spectrograph for the Hobby-Eberly Telescope. **30**, 1263.

Unwin, S., Boden, A., & Shao, M. (1997). Space Interferometry Mission. In M. S. El-Genk, editor, *Space Technology and Applications*, volume 387 of *American Institute of Physics Conference Series*, pages 63–72.

Uthas, H., Knigge, C., Long, K. S., Patterson, J., & Thorstensen, J. (2011). The cataclysmic variable SDSS J1507+52: an eclipsing period bouncer in the Galactic halo. *MNRAS*, **414**, L85–L89.

Valencia, D., O'Connell, R. J., & Sasselov, D. (2006). Internal structure of massive terrestrial planets. *ICARUS*, **181**, 545–554.

Veras, D. & Armitage, P. J. (2006). Predictions for the Correlation between Giant and Terrestrial Extrasolar Planets in Dynamically Evolved Systems. *ApJ*, **645**, 1509–1515.

Voelzke, M. R. & de Araújo, M. S. T. (2010). Pluto: Planet or "Dwarf Planet"? *Revista de Ensino de Ciências e Matemática (ISSN 2179-426X), vol. 1, p. 66-79*, **1**, 66–79.

Vogt, S. S., Allen, S. L., Bigelow, B. C., Bresee, L., Brown, B., Cantrall, T., Conrad, A., Couture, M., Delaney, C., Epps, H. W., Hilyard, D., Hilyard, D. F., Horn, E., Jern, N., Kanto, D., Keane, M. J., Kibrick, R. I., Lewis, J. W., Osborne, J., Pardeilhan, G. H., Pfister, T., Ricketts, T., Robinson, L. B., Stover, R. J., Tucker, D., Ward, J., & Wei, M. Z. (1994). HIRES: the high-resolution echelle spectrometer on the Keck 10-m Telescope. In D. L. Crawford and E. R. Craine, editors, *Society of Photo-Optical Instrumentation Engineers (SPIE) Conference Series*, volume 2198 of *Society of Photo-Optical Instrumentation Engineers (SPIE) Conference Series*, page 362.

Vrba, F. J., Henden, A. A., Luginbuhl, C. B., Guetter, H. H., Munn, J. A., Canzian, B., Burgasser, A. J., Kirkpatrick, J. D., Fan, X., Geballe, T. R., Golimowski, D. A., Knapp, G. R., Leggett, S. K., Schneider, D. P., & Brinkmann, J. (2004). Preliminary Parallaxes of 40 L and T Dwarfs from the US Naval Observatory Infrared Astrometry Program. *AJ*, **127**, 2948–2968.

Wagner, F. W., Tosi, N., Sohl, F., Rauer, H., & Spohn, T. (2012). Rocky super-Earth interiors. Structure and internal dynamics of CoRoT-7b and Kepler-10b. *A&A*, **541**, A103.

Ward, W. R. (1997). Protoplanet Migration by Nebula Tides. *ICARUS*, **126**, 261–281.

Webbink, R. F. (1984). Double white dwarfs as progenitors of R Coronae Borealis stars and Type I supernovae. *ApJ*, **277**, 355–360.

Wilson, R. E. (1990). Accuracy and efficiency in the binary star reflection effect. *ApJ*, **356**, 613–622.

Wolff, S. C., Boesgaard, A. M., & Simon, T. (1986). Activity in F stars. *ApJ*, **310**, 360–370.

Wolszczan, A. & Frail, D. A. (1992). A planetary system around the millisecond pulsar PSR1257 + 12. *Nature*, **355**, 145–147.

Woolfson, M. M. (1993). The Solar - Origin and Evolution. *QJRAS*, **34**, 1–20.

Wright, E. L., Eisenhardt, P. R. M., Mainzer, A. K., Ressler, M. E., Cutri, R. M., Jarrett, T., Kirkpatrick, J. D., Padgett, D., McMillan, R. S., Skrutskie, M., Stanford, S. A., Cohen, M., Walker, R. G., Mather, J. C., Leisawitz, D., Gautier, III, T. N., McLean, I., Benford, D., Lonsdale, C. J., Blain, A., Mendez, B., Irace, W. R., Duval, V., Liu, F., Royer, D., Heinrichsen, I., Howard, J., Shannon, M., Kendall, M., Walsh, A. L., Larsen, M., Cardon, J. G., Schick, S., Schwalm, M., Abid, M., Fabinsky, B., Naes, L., & Tsai, C.-W. (2010). The Wide-field Infrared Survey Explorer (WISE): Mission Description and Initial On-orbit Performance. *AJ*, **140**, 1868–1881.

Wright, J. T., Fakhouri, O., Marcy, G. W., Han, E., Feng, Y., Johnson, J. A., Howard, A. W., Fischer, D. A., Valenti, J. A., Anderson, J., & Piskunov, N. (2011). The Exoplanet Orbit Database. *PASP*, **123**, 412–422.

Wu, Y. & Lithwick, Y. (2012). Ohmic Heating Suspends, not Reverses, the Cooling Contraction of Hot Jupiters. *ArXiv e-prints*.

Wuchterl, G., Guillot, T., & Lissauer, J. J. (2000). Giant Planet Formation. *Protostars and Planets IV*, page 1081.

Youdin, A. N. & Mitchell, J. L. (2010). The Mechanical Greenhouse: Burial of Heat by Turbulence in Hot Jupiter Atmospheres. *ApJ*, **721**, 1113–1126.

Zapolsky, H. S. & Salpeter, E. E. (1969). The Mass-Radius Relation for Cold Spheres of Low Mass. *ApJ*, **158**, 809.

Zechmeister, M. & Kürster, M. (2009). The generalised Lomb-Scargle periodogram. A new formalism for the floating-mean and Keplerian periodograms. *A&A*, **496**, 577–584.

Zorotovic, M., Schreiber, M. R., & Gänsicke, B. T. (2011a). Post common envelope binaries from SDSS. XI. The white dwarf mass distributions of CVs and pre-CVs. *A&A*, **536**, A42.

Zorotovic, M., Schreiber, M. R., Gänsicke, B. T., Rebassa-Mansergas, A., Nebot Gómez-Morán, A., Southworth, J., Schwope, A. D., Pyrzas, S., Rodríguez-Gil, P., Schmidtobreick, L., Schwarz, R., Tappert, C., Toloza, O., & Vogt, N. (2011b). Post common envelope binaries from SDSS. XIII. Mass dependencies of the orbital period distribution. *A&A*, **536**, L3.